Development and optimisation of a method for assessment of porosity in additively manufactured parts using x-ray tomography

AHMED SALAH BAKR TAWFIK

A thesis submitted to the University of Huddersfield in partial fulfilment of the requirements for the degree of Doctor of Philosophy

December 2021

Copyright statement

I. The author of this thesis (including any appendices and/or schedules to this thesis) owns any copyright in it (the "Copyright") and s/he has given The University of Huddersfield the right to use such copyright for any administrative, promotional, educational and/or teaching purposes.

II. Copies of this thesis, either in full or in extracts, may be made only in accordance with the regulations of the University Library. Details of these regulations may be obtained from the Librarian. This page must form part of any such copies made.

III. The ownership of any patents, designs, trademarks and any and all other intellectual property rights except for the Copyright (the "Intellectual Property Rights") and any reproductions of copyright works, for example graphs and tables ("Reproductions"), which may be described in this thesis, may not be owned by the author and may be owned by third parties. Such Intellectual Property Rights and Reproductions cannot and must not be made available for use without the prior written permission of the owner(s) of the relevant Intellectual Property Rights and/or Reproductions.

Abstract

Additive manufacturing (AM) is a process whereby components are built layer-by-layer by means of powder or wire. The AM process provides clear benefits over conventional subtractive machining primarily in terms of part complexity. The technology continues to be the subject of rapid development and consequently, the geometrical repeatability and mechanical properties of AM parts are subject of research. AM technologies have evolved rapidly in the last decade enabling manufacturers to acquire additive manufacturing machines at costs comparable to multi-axis computer numerical control (CNC) machines. Additionally, the process offers the possibility of utilising high-performance engineering materials and super alloys, such as Titanium and Inconel; attracting special interest from aerospace and medical (orthopaedic implant) applications.

There are several drawbacks in the process preventing manufacturers from widely adopting this technology. A significant barrier is the lack of understanding and assessment technologies for the structural integrity of AM components. The evaluation of a component functional performance is the most important stage of any component development. Generally, the mechanical performance could be assessed by means of destructive and non-destructive testing methods. However, the destructive testing methods can be both expensive and time consuming.

In this thesis, the non- destructive testing method used is X-ray computed tomography (XCT), which is being utilised in characterising and measuring external and internal defects/features of metallic components made by AM technologies. XCT is capable of providing information about pore position, location and volume. While XCT is promising, there are several difficulties stopping industry from utilizing the technology. One of the main obstacles is the level of subjectivity within the process; this is problematic for assessment of internal process defect features such as process porosity.

This thesis reports on the process of developing the inspection techniques, which are capable of detecting and characterising internal defects; approaching the size of a single AM powder particle. In order to duplicate internal AM defects and features, a series of small porosity characterisation specific artefacts were developed. These artefacts contained micro defects, semi-fused powder and unfused powder. The artefacts were used to identify the challenges in the XCT process and determine the optimum XCT scan parameters for detecting and measuring internal defect/features. Furthermore, in this thesis, the limitations and challenges faced when attempting to identify such features in AM component are reported, and the XCT results repeatability and reproducibility was investigated. Additionally, SLM AM build chamber internal feature printing resolution was investigated, and defect analysis results were verified.

The results of studies/experiments carried out as part of this thesis had shown that XCT is an effective method for porosity detection, with a resolution approaching a single powder particle (15µm). Furthermore, based the different studies reported in this thesis; the recommended scan strategy was using a magnification as low as 38-µm voxel size to identify the location of the defects and then confirm the area where the defect is located using a high magnification scan.

It was also noted that surface determination is playing a vital rule in the results reliability. The results of several experiments reported that the ISO50% surface determination threshold is not the appropriate threshold for porosity analysis and custom surface determination protocol was developed. The results showed that selecting the appropriate scan parameters combined with the optimisation of surface determination could enhance the XCT defect characterisation process.

Based on the experience and knowledge gained from this research, a best practice method was developed, the best practice guide enhanced the efficacy of the method was demonstrated on and industrial NIKON XTH 225 machine.

The work carried out as part of this thesis were designed to be industry relevant and representative of actual internal defects, especially those found in AM components. This research was intended to be universal for all XCT machines and all powder-based AM processes. Although XCT process is capable of detecting internal defects within AM components the process requires high level of experience. At this stage, although highly informative, is not suitable in high volume manufacturing environment that requires 100% inspection, it is more suitable for low volume high value components found in medical and aerospace applications.

Statement of authenticity.

I confirm, that the work reported in this thesis is all authors own work and does not include any work completed by anyone other than the author. The work completed in this thesis is in accordance with the University of Huddersfield awarding instructions and within the time limits set by the University.

Contents

List of figures

Statement of Publications Arising from This Work

In the following publications the author performed all the practical research and wrote the entire manuscript with research guidance and editorial changes from co-authors, it is indicated where text from publications has been reproduced in this thesis.

1. *Detection of unmelted powder in additive manufactured components using computed tomography DXCT Conference, 13 July 2017, University of Warwick, UK [1].*
2. Method for characterizing defects/porosity in additive manufactured components using computed tomography. Euspen conference 10 October 2017 Leuven university, Belgium [2].
3. Characterisation of powder-filled defects in additive manufactured surfaces using X-ray CT, 8th Conference on Industrial Computed Tomography, 6 February 2018, Wels, Austria.[3]
4. Optimization of surface determination strategies to enhance detection of unfused powder in metal additive manufactured components, Proceedings - 2018 ASPE and EUSPEN Summer Topical Meeting, 24 July 2018, san Francisco, USA [4].
5. Development of an AM artefact to characterize unfused powder using computed tomography.' EUSPEN 18th International Conference & Exhibition, 4 June 2018, Venice, Italy [5].
6. Utilizing detector filters for noise reduction in XCT scanning for the inspection of structural integrity of additive manufactured metal parts', ASTM International Journal Smart and Sustainable Manufacturing Systems. 2019, USA [6].
7. Optimisation of surface determination to improve the accuracy of detecting unfused powder in AM aluminium component. 9th International Conference on Industrial Computed Tomography, 13 February 2019, Padova, Italy [7].
8. Development of an AM artefact to characterize unfused powder using computed tomography'. International Journal of Automation Technology 10 March 2019, OSAKA JAPAN [8].
9. The challenges in edge detection and porosity analysis for dissimilar materials additive manufactured components 19th International Conference and Exhibition, EUSPEN 3 June 2019, Bilbao Spain [9].
10. Challenges in Inspecting Internal Features for SLM Additive Manufactured Build Artefacts. In *Structural Integrity of Additive Manufactured Materials and Parts*, 11 October 2019, Washington USA [10].
11. The detection of unfused powder in EBM and SLM additive manufactured components. International Journal of Automation Technology 25 February 2021, Osaka Japan [11].

There is other publication in biology research, but it is not discussed in this work.

Acknowledgements

“If I have seen further it is by standing on the shoulders of Giants”

Isaac Newton (1643-1727)

Many thanks to exceptional people who supported me throughout my research.

Thanks to Paul Bills for making this journey a pleasure from the beginning.

Thanks to Liam Blunt for his advice and support throughout my studies.

Thanks to Radu Racasan for his support and advice.

Thanks to my friends Aaron, Paul Kaye and Chris Dawson for the support and the good times.

All my love and deep gratitude to my family Kristina, Yasin, Gabi and Maria, Mum and Dad.

Sincere thank you for the University of Huddersfield for funding my PhD.

Chapter 1 Introduction

1.1 Background and motivation

There has been limited research in the use of XCT for porosity detection and characterisation, the wide utilization of AM in various industries had driven the demand for robust method of inspection. This is mainly due to the existence of internal defects and the ability of the AM process in creating complex structures that is not possible to inspect with any other device.

An earlier NDT study carried out by the author, which involves scanning square titanium bars using XCT shown in figure 1-1 a). The defect analysis failed to detect the presence of any unfused powder. In order to confirm the XCT results the component was sectioned and it was evident the presence of unfused powder. Also, while inspecting the sectioned part under microscope the author found semi-fused powder shown in figure 1-1 b).

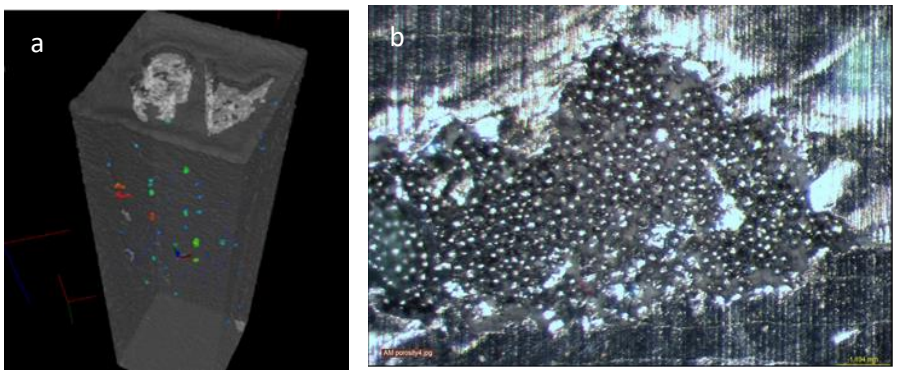

Figure 1-1 a) Defects analysis for titanium AM part b) Semi fused powder

From this study, it was clear that the overall process of porosity detection using XCT is quite complicated and there is no clear standard method, this is mainly due to the complicity of using XCT and imaging analysis software. Thus, there seemed a potential for the porosity detection using XCT especially for the PBF AM applications due to the presence of hollow and powder filled pores. Principally the problem is defect characterisation which is covers in chapter 2, the tool used is XCT which is covered in chapter 3, and finally the selected application is the AM “which is covered in chapter 4” due to the cost of the components and they usually require 100% inspection.

1.2 Thesis Layout

The thesis consists of ten chapters excluding the introduction, plus references and appendices. This section is an outline for chapter 2 to chapter 9. These chapters contain a research rational, experimental work and brief outline of the novelty. The full explanations are being discussed in the specific chapters.

1.3 Chapter 2 Literature review

This chapter is a review of the current state of the art and literature, consisting of three sections. The first section in the literature review is an overview of the porosity detection/analysis methods, which is the research focus. The second section is an overview of the XCT, which is the main tool used in the research. The third section is an overview of additive manufacturing, which is the problem that the research is aiming to resolve.

1.4 Chapter 3 Literature review XCT

In this research, the XCT is the main tool used throughout the research. The author used Nikon XT H 225 industrial CT and XT H 225 Metrology CT, also in one of the studies samples were scanned with Yxlon FF35 CT system. Chapter 3 is reviewing the history of XCT and how it was developed from detection to measurement tool. In this chapter, the author is highlighting how the XCT works. Also, in this chapter, the different XCT imaging algorithms are highlighted.

1.5 Chapter 4 Literature review 3D printing technologies

Chapter 4 is a review of the current literature and state of the art for different additive manufacturing technologies. In this research the author used AM in various case studies mainly components made by PBF technology. AM is used as part of problem definition due to the presence of internal pores/defect and ability in creating complex geometry that can only be inspected with XCT. The presences of semi and unfused powder in PBF components that can only be detected with XCT makes AM components the best candidate for exploring XCT capabilities.

In the end of chapter four (section 6) there are an overall summary and study rational, which highlights the artefact developed by other researchers for assessing the XCT defects characterisation capability, and the early experiments that took place in an early stage of the authors' research. This section presents the XCT scanning of the EBM built bars and the porosity analysis took place afterwards, also the destructive testing has taken place to verify the XCT results. In this section, the author presents some of the powder analysis studies and techniques to highlight why it is not possible to delineate individual powder particles.

1.6 Chapter 5 XCT Porosity Development method

Prior to the reported work, there has been no published porosity/defects analysis from XCT reconstructions for AM components. Most of the published work has been machined artefact and those studies lacked high resolutions scans to visualise individual powder particles. This chapter discusses the development of artefacts to validate and verify porosity characterisation method. In this chapter, the repeatability of the obtained results is being discussed. In addition, the results of the XCT for several artefacts are compared to the results obtained from a focus variation instrument. The results were presented at several conferences [2, 10] and a journal paper. [9]

1.7 Chapter 6 XCT Porosity method imaging optimization

The porosity analysis method, shown in chapter 5, had shown big potential but the overall process requires optimisation. Things related to XCT machine, X-ray beam filtration, best angle for the scanned object and the impact of all of this on scanning resolution. This chapter discusses the impact of voxel size on resolution and porosity analysis; additionally, in this chapter, the X-ray beam filtration techniques and beam scatter has been explored. Another factor affecting XCT scan, is X-ray beam penetration, in many cases the scanned object needs to be tilted to reduce the beam penetrating passage. In this chapter, the object tilt is being discussed. In the end of the chapter 6, some case studies for scanning large and dense components has been shown. The results were presented at a conference [3] and journal papers. [6]

1.8 Chapter 7 Challenges in porosity analysis (XCT porosity method image analysis optimisation)

For porosity analysis, it is important to understand that the object is being scanned, then results are analysed using sophisticated visualisation software. The image analysis has been proven quite challenging; most of the challenges are in the process of differentiating between back ground (air) and actual material. In this chapter the challenges in porosity imaging is being discussed and the best

practice is being identified. The results of the studies discussed in this chapter were presented at a conference [4] and published as a journal paper [10].

1.9 Chapter 8 Porosity analysis case study

Several collaborations with industrial partners have shown the requirement for a precise high-resolution porosity detection method. In some critical components i.e. medical and aerospace applications the resolution needs to be as small as 15µm (powder particle size). In the chapter 8, several case studies have been shown. The first study is a virgin and recycled AM powders analysis, some of this powder had shown traces of contaminations. In this chapter, XCT powder characterisation is being discussed, and the effect of build location on internal features printability in SLM AM technology is being investigated.

1.10 Chapter 9 Discussion and conclusions

In chapter 9 the overall conclusions are being highlighted and the contribution to knowledge is being presented. In the end of the chapter, there is an overview of the ongoing and future work.

1.12 Research Scope

1.12.1 Aim

- The primary aim of this work is to characterise internal defects and associated features of additively manufactured components, presenting a defect analysis method that is verified and robust, in order to provide industry with high confidence in using XCT as a defect characterisation tool.

1.12.2 Objectives

In order to meet the aforementioned, aim the following objectives were set.

- Identify the optimal technique for characterising the internal defects and features in metallic AM components.
- Develop novel AM porosity-specific artefacts for XCT result verification and use such artefacts to understand the effect build location has on internal feature printability in SLM AM technology.
- Investigate the impact of different XCT scans parameters on the accuracy of XCT defect analysis.
- Identify the process limitations and challenges.
- Develop and optimise a technique for detecting and characterising semi-fused and un-fused powder.
- Validate the repeatability and reproducibility of the defect characterisation technique developed in the previous objective.

Chapter 2 Literature review part one: Porosity analysis

This chapter is an overall review of the background literature and current state of the art research in defects/porosity detection methods, and its impact on the expected service life of a component. This chapter is divided into four sections: section 2.1 is an overview of the current available NDT inspection methods, their advantages and drawbacks. Section 2.2 is highlighting the impact of porosity on structural integrity of mechanical components. Specifically, defects influence on crack propagation, Thremo - mechanical fatigue with some fatigue failure examples. Finally, the impact of defects size and location on the fatigue life of a component.

2.1 Current NDT inspection methods

The history of porosity measurement goes back to 287 BC, when king Hieron ll of Syracuse in Sicily tasked the Greek mathematician Archimedes (figure 2-1) to verify the authenticity of a gold crown. The king was suspicious that the goldsmith had cheated and mixed some of the gold with silver. The king asked Archimedes to find out if the crown was made of pure gold, without damaging it. One day while he was getting into his bath and noticed the water spilling over the bath sides. The Greek inventor was trying to establish the relation between the quantity of expelled water and density of the submerged body, causing him to exclaim 'Eureka'; 'I found it'' in Greek. Archimedes then put the crown in water and measured the volume of the displaced water, then he placed a bar of pure gold in water and found that the volume of the crown is larger than bar of pure gold, confirming the king suspicious [12].

Figure 2-1 Archimedes 287-212 BC [12]

Interestingly there is a similarity between what Archimedes had done and what the author is trying to establish in this thesis. Archimedes was validating the golden crown metal composition and the author is validating the XCT internal defects volume and dimension using different measurement method (Alicona).

2.1.1 Archimedes

Archimedes' buoyancy technique is generally utilised in porosity and density measurement. In this method, immersed, soaked and dry weights are used with test specimen weights in water or other fluids like mercury, if the materials are sensitive to water. This method is well established with many standard test procedures (BS EN 993-1:2018, ISO 5017:2013 and ASTM C20). The Archimedes density-based testing method is relatively inexpensive and considerably quick. An example of an Archimedes test device is shown in figure 2-2. This classic Archimedes porosity determination method is used for quantifying the density of components made with additive manufacturing technologies. [13]

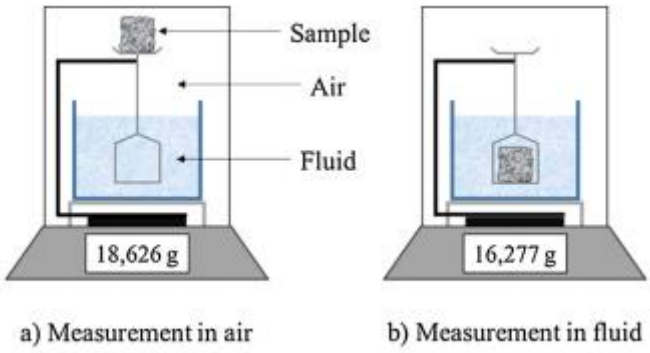

Figure 2-2 Archimedes density measurement method [13]

This test method is quite sensitive to temperature; temperature variation can lead to inaccurate results. In addition, AM samples usually contains cracks or surface porosity that allow water impregnation causing imprecise results. Additionally, Archimedes' method can only be used to obtain a global density value in relation to utilised fluid. [14,15]

2.1.2 Gas Pycnometer

The gas pycnometer is another density based non-destructive test method; the device computes the sample density by measuring the mass and volume separately in an absolute sense. Then the gas displacement is used to determine the sample volume. A gas pycnometer (Sartorius mettle balance type AE200) is shown in figure 2-3. Measuring density with a gas pycnometer is similar to using Archimedes methodology in terms of speed and accuracy but the down side is it is more expensive. Furthermore, the device can only measure small parts i.e. parts that fit in the device and like the Archimedes method, gas pycnometer can only measure overall part global density without the possibility of analysing local individual defects [16,17].

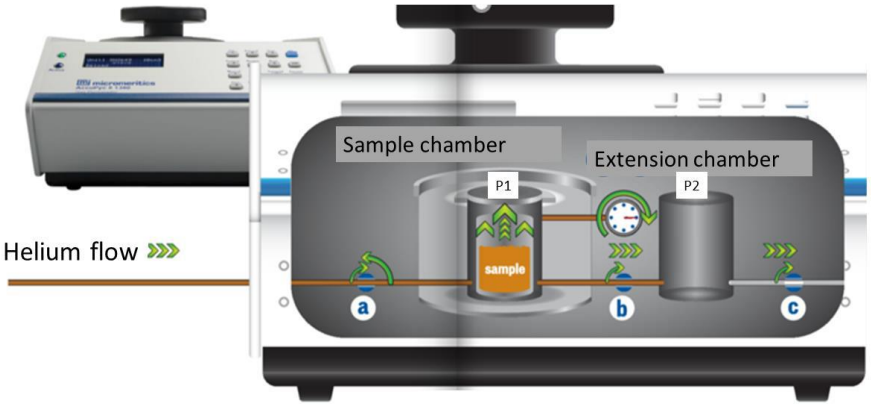

Figure 2-3 Mettler balance (type AE200) [17]

2.1.3 Electromagnetic testing

Electromagnetic testing (ET) is one of the commonly used NDT methods; a magnetic field and electric current is induced inside the test piece whilst observing the electromagnetic response. The presence of any defect or crack within the test object will result in a measurable response contrasting from normal background noise. [18]

Historically electromagnetic induction was discovered by Michael Faraday in 1831, David Edward Hughes noted the impact of connecting a coil to metals with different conductivity in 1889 [19]. During the Second World War ET testing (eddy current) was used for the first time for materials testing. [20]

Electromagnetic testing includes three different categories, eddy current testing (ECT) [21], alternative current field measurement (ACFM) and remote field-testing [22]. All these systems operate with the same principle of examining conductivity through utilisation of electromagnetism [23]. Aerospace, Nuclear power and oil and gas industries are utilising ET in detecting small surface or sub surface cracks and for material and coating thickness measurement. The use in these industries is mainly due to the ability to obtain immediate results, with minimal part preparation needed. Test devices are small and portable so they can be used in the field as shown in figure 2-4, where the instrument is used in inspecting a tube.

Figure 2-4 Eddyfi lyft (EC) Device used in the field [23]

In addition, ET can be used to measure conductivity to help identify the material or detect thermomechanical fatigue. NASA reported the ability of detecting cracks as small as 80µm using ET in laboratory conditions [24]. This test method can also be used for testing complex shapes and because it is a non-contact method, it can be used for inspection of underwater or high temperature surfaces.

There are limitations to the ET method; the depth of penetration is limited, and it can only be used on conductive materials, furthermore, the results can be affected by surface finish and the whole process relies on operator skill in analysing the results [25]. Furthermore, the process is sensitive to magnetic permeability; resulting in difficulties in testing welds in ferromagnetic materials. One other limitation is the detection of defects that are parallel to the surface [26].

2.1.4 Ultrasonic testing pictures

One other NDT method that is widely used in several industries like manufacturing, automotive and aerospace is ultrasonic testing. In this method, a transducer is used to generate ultrasonic waves as high as 10MHz into an object and the resultant returning waves are analysed by a device to produce an image; allowing detection of subsurface defects. The ultrasonic waves are generated by applying electric current to a thin crystal disc inside the transducer. In order to avoid result distortion, sound absorbing materials are utilised to stop any waves from returning to the device [27].

The soviet scientist Sergei Y. Sokolov initially utilised ultrasonic testing in defect detection in metals in 1928. His research and experimentation were the foundation for future developments of ultrasonic in NDT. After Sokolov in 1942, the British scientist Donald Sproule managed to adapt the theory of eco sounding to detect porosity in steel. Sproule's new device used two different transducers for receiving

and transmitting the ultrasonic sound waves. In 1945 the first commercial ultrasonic defect detection device became available; the American scientist Floyd Firestone developed the device and it was commercially known as the 'Supersonic Reflectoscope'. In 1949, Mitsubishi Electric Corporation developed a Japanese system and with help of Tokyo Ultrasonic, industrial company the system began to be commercially produced [28].

The early generations of ultrasonic testing devices were quite bulky and needed a significant amount of energy to operate. Only after solid-state circuitry invention in the early 1960s and with the use of batteries did ultrasonic devices became relatively small, enabling easy transportation for field use. The early devices used anloge signals for data processing, in 1984 Panametrics non-destructive testing company introduced the first digital defect detection ultrasonic device. The introduction of digital signals improved the overall measurement precision and data maintenance [28].

Recently phased array ultrasonic testing (PAUT) has been widely used. PAUT utilises several probes creating steered beams. This system can generate cross sectional images similar to those obtained from medical ultrasounds. Ultrasonic testing produces high-resolution images and provides instant results. Other advantages are high result accuracy and the ability to detect surface and subsurface defects. Furthermore, ultrasonic testing requires access to only one side of the test part and very little preparation to the test sample, as shown in figure 2-5; the inspection of an aeroplane landing gear takes seconds with no surface preparation required.

Figure 2-5 landing gear ultrasonic inspection [29]

No other portable NDT methods have higher penetration power than that of ultrasonic testing. On the other hand, there are several limitations; the presence of high signal noise in some materials like cast iron, the process does not allow defect detection in irregular shaped or thin walled components like trabecular structures. If the test piece has a pore parallel to the sound beam, the transducer might fail to detect it. Furthermore, this method always requires access to the surface to enable the transmission of ultrasonic waves and extensive training and experience is required to operate the device [30].

2.1.5 Radiographic testing

One other method widely used in NDT is radiographic testing (RT); this method can inspect the test specimen volume and detect internal defects. RT uses X-ray or Gamma ray to produce a radiographic

image of the test specimen. RT has the ability to inspect and detect changes in thickness, the presence of defects and the relationship of assembled components to guarantee optimum build quality [31, 32]. Historically there are two beginnings for the use of RT; the first scientist that discovered X-ray was Wilhelm Röntgen in 1895, he said, "I did not think; I investigated" when he was asked his thoughts about his discovery. After Wilhelm in 1898 Marie Curie announced the discovery of a new radioactive material called "Radium". Marie developed a method to separate radium from radioactive deposits [33-35].

Radiographic testing works with the same concept as medical radiography. The test specimen is placed between a radiation source and a radiographic film/detector, radiation is emitted from the source, penetrating the specimen before it is finally absorbed by the radiographic film. The film produces various degrees of black and white from the different degrees of absorbed radiation. Material density and thickness variation will result in radiation attenuation: for example, the presence of defects/cracks in the specimen will result in darker areas on the film and contamination in the material of denser materials like Inconel or tungsten will appear as light areas. In industrial radiography, there are several methods to display the results like Digital Radiography (DR), Real Time Radiography (RTR), Computed Radiography (CR) and Computed Tomography (CT). One of the CT advantages over any other NDT method is the ability of characterising internal defects by providing cross sectional and 3D volume models of the scanned object. CT will be discussed in detail in chapter three.

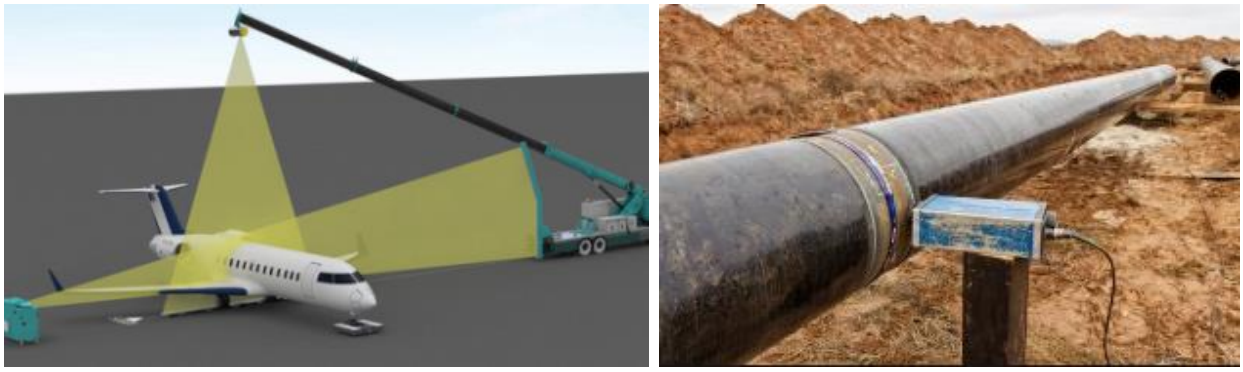

Figure 2-6 a) Aeroplane X-ray scanner [36] b) pipeline joints X-ray scanner [37]

In the process of NDT, there are advantages and limitations. The advantages are the ability to detect surface and subsurface defects, it can be used for reverse engineering as the film contains the outer and inner geometry of the imaged component and it is a good method for quality control due to the ability to inspect the full component volume [38]. The limitations are the presence of radiation hazards, in some components, access is required for both sides, the test equipment is expensive and the inspection process is time consuming. The equipment is bulky and quite often the results can only be interpreted by experienced individuals [39].

RT is well established and several standards are covering it, for example ASTM E 2104 [40], ISO 10675-1 [41] and EN444 [42]. This process is widely used in various industries including transport, aerospace and automotive. Figure 2-6 a) shows and example where an X-ray scanner is used to detect explosive substances in aeroplanes. Figure 2-6 b) shows an example where an RT scanner is used to detect defects in oil and gas pipeline welded joints.

2.2 Impact of porosity of structural integrity

NDT can be used to assess the mechanical properties of a component; it offers several benefits over conventional destructive methods, by definition, destructive testing usually results in a non-functional component and often requires long testing times [43].

The mechanical properties of a 100% dense component will outperform those with internal porosity. The acceptable size and quantity of internal pores are solely dependent on the design intent, for example in some applications like an aero chocolate bar the pores are designed to be there. On the other hand, a micro defect located subsurface in a component, which operates in extreme conditions, can result in catastrophic failure. Generally, there are two conditions of stress loading failures; the first condition are static loads that do not change over time, the second condition is where loads change overtime in this condition the stress force at the crack initiation point will vary.

A crack will propagate when the static or dynamic load exceeds the component stress threshold. Defects in materials act as stress raiser, increasing stress in the component at the edge of the defect.

The stress at the edge of a defect; like that shown in figure 2-7 can be calculated using the Inglis equation shown in equation 1, where $\boldsymbol{\sigma}$ is the nominal stress, $\boldsymbol{\rho}$ is the defect radius of curvature and **a** is half the length of the defect.

$$\sigma \max = \sigma\left(1 + 2\sqrt{\frac{a}{\rho}}\right) \quad \text{Equation 1}$$

When a component is under load, stress is distributed over the area surrounding the defect causing plastic deformation; the plastic region. The occurrence of plastic deformation in the area surrounding the defects causes the defect edge to diminish thus increasing the radius of curvature leading to component fracture [44, 45]. Another main cause of fracture failures is the crack/defect loading. There are three main modes; the first is when a tensile stress pulls the defect apart; the opening mode. The second mode is when shear stresses force the defect faces in opposing parallel directions to the primary defect dimension; the sliding mode. The third mode is when shear stresses force the defect faces in opposing perpendicular directions to the primary defect dimension; the tearing mode. The worst case from the aforementioned modes is the opening mode and it is the most common failure. Furthermore, if the crack initiation-loading mode was not the opening mode it will turn itself to be the opening mode, because of this most engineering analysis assumes the opening mode to be the crack loading mode [46, 47].

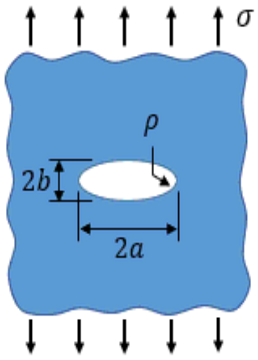

Figure 2-7 crack initiation process

In aerospace applications, the cyclic forces from the pressure variation on an aeroplanes outer aluminium skin clad leads to fatigue failures. One of the extreme examples is the catastrophic failure of Boeing 737 Aliha airline flight, the Fatigue cyclic load caused cracks in the lap riveted joints on the flight 243 leading to an opening in the fuselage shown in figure 2-8 [48]. In applications with low factor of safety, it is always recommended to include NDT in the preventive maintenance plan to reduce the possibility of catastrophic failure occurrence.

Figure 2-8 Boeing 737 flight 243 Aloha Airline [48]

Higher levees of porosity result in shorter fatigue life for the same magnitude of applied stress. It had been shown that there is a direct relation between defect size distribution and failure initiation defects. Shrinkage porosity and micro-porosity found in castings usually result in stress concentration points leading to crack initiation, meanwhile the successful quantification of porosity distribution proved to enhance the prediction accuracy of the components life [49]. Two main aspects to create a relationship between pore size distribution and fatigue life (i) crack propagation model based on fracture mechanics (ii) crack initiation defect size distribution [50].

Any fatigue model based on microstructure uses defect size distribution as an input. Researchers in literature have taken two approaches to link the effect of porosity on the fatigue life of metals: the first approach utilises the distribution of the largest pores; the second approach takes the complete defect size distribution into consideration [51, 52]. For example, Yi et al. assumed that the defect size is a best fit of lognormal distribution, which conforms to the statistical analysis of defect sizes for magnesium alloy castings [53]. Las et al. adopted the lognormal distribution for pore size in aluminium 2024-T3 alloy and discovered that the main crack initiation defect was one of the largest pores [54]. Furthermore Gruenberg et al. confirmed that in Aluminium 7075-T6 alloy, utilising lognormal distribution could enhance the accuracy of fatigue variability modelling [55]. Alternatively, Zamber et al. created a model that predicts fatigue life of Aluminium 2024-T3 alloy parts with oxidized pits. After examining the crack initiating pits the author found that the Gumbel distribution was almost identical fit to the measured pits that caused crack initiation [56, 57]. Przystupa et al. investigated defects causing fatigue crack initiation in Aluminium 7050-T7451 alloy and suggested that the defects follow the log-Gumbel distribution and estimated the largest defects in this distribution [58].

Murakami et al. suggested that if the Root cause for crack initiation are the largest defects then their size must follow an extreme value distribution [59]. In order to successfully predict fatigue life of a

given component a probability plot is used for the defects causing crack initiation, these plots are utilised to confirm whether the defects follow Weibull, Gumbel or lognormal distributions.

Tiryakioğlu et al. investigated the size of fatigue-initiating pores on several aluminium and magnesium alloys by using the equivalent pore diameter equation [60]:

$$\mathbf{d_{eq}} = \sqrt{\frac{4Ai}{\pi}} \qquad \text{equation 2}$$

In equation 2 A_i is the area of the fatigue-initiating pore. The author found that 80% of the datasets followed the Gumbel distribution. Furthermore, the author used the cumulative probability equation:

$$\mathbf{P} = exp\left(-exp\left(\frac{deq-\lambda}{\delta}\right)\right) \quad \text{equation 3}$$

δ and λ are scale and location parameters respectively. The results are conforming to the sizes of the pores measured from the retrieved fractured surfaces of steel castings.

Another form of fatigue that is directly affected by defect presence is thermal fatigue. Thermal fatigue is the continuous weakening and cracking of a component after several cooling and heating cycles due to thermal expansion and contraction. There are two categories of thermal fatigue: thermal shock fatigue (TSF) and thermomechanical fatigue (TMF). Thermal shock fatigue is when the component is exposed to internal thermal load combined with rapid heating or cooling, while thermomechanical fatigue is when the component is subjected to external thermal expansion [60]. Thermal fatigue is a common failure mode in several automotive and aerospace components; figure 1- 10 (a) shows a TMF crack in a turbine-housing flange [61], and figure 2-10 (b) shows a TMF crack in a cylinder head due to alternate expansion and contraction [62].

Usually, the areas, which contain high content of porosity, are prone to crack initiation and propagation. Arami et al. investigated the relationship between porosity and TMF in aluminium A319 alloy, this experiment confirmed that the quantity of defects is inversely proportional to the resistance to thermal fatigue; if the porosity content increases the thermal fatigue life decreases. The authors suggested that the pores presence in front of a crack leads to a reduction in matrix resistance against crack propagation, increasing the thermal fatigue crack propagation rate. When thermal fatigue cracks are passing through defects the propagation will be accelerated due to weakness of the voids, this can be seen in figure 2-9 a), that shows several TMF cracks in a turbo charger turbine-housing inlet. Furthermore, this kind of failure is commonly found in aluminium internal combustion engine cylinder heads as shown in figure 2-9 b) [63].

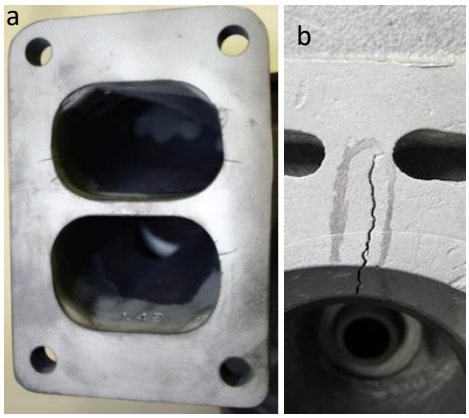

Figure 2-9 a) TMF crack in a turbine housing B) TMF crack in cylinder head

Porosity presence affects mechanical properties significantly, which directly compromise thermal fatigue life expectancy. The defects presence reduces ductility and impact energy. The crack propagation direction is determined by the pores location in the crack zone; pores are hollow space with no strength. Several studies investigated the manner of crack propagation and found that the initial main crack is divided into numerous smaller cracks expanding towards nearby defects/pores as shown in figure 2-10.

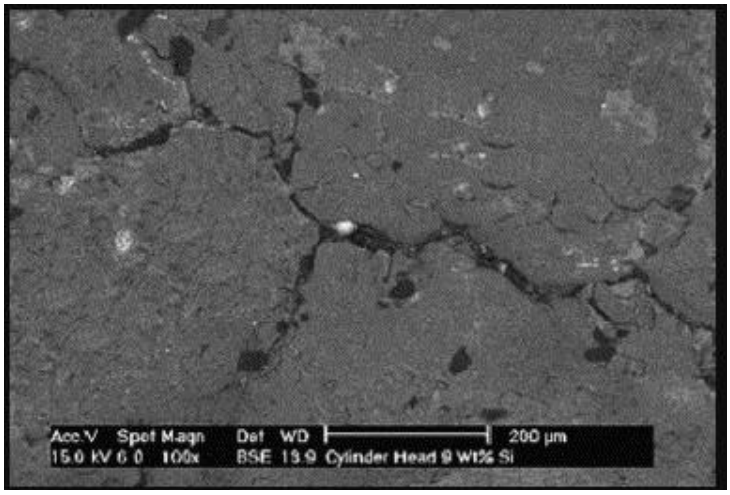

Figure 2-10 SEM image of crack propagation

Several studies confirmed that the presence of defects on the surface or subsurface of a component accelerates crack initiation and growth [64]. Dabayeh et al. confirmed that surface and subsurface porosity presence resulted in earlier crack initiation than pores located deeper in the material [65]. Buffière et al. investigated the impact of defects on aluminium alloy fatigue life. The author created artificial pores in the test specimens; this experiment confirmed that the presence of defects reduced the average number of cycles to failure at high stress levels [66]. Generally, when the defect quantity increases in a component the yield strength drops dramatically; furthermore, the increase of defects will cause a drop in the matrix strength against indenter pressure, leading to a decrease in hardness.

Elsner et al. looked into the impact of micro defect density and size in aluminium 7050 alloy on fatigue life prediction. The author created three plates with different micro defects, this experiment confirmed that when the density and size of defects increase the fatigue life decreases significantly [67]. Seniw et al. investigated the impact of defect size and location on fatigue failure in aluminium A356 alloy, this study confirmed that the fatigue life is not only affected by defect size but also their distance from surface. The author used X-ray techniques to identify defect size and location and measured fatigue life by cycles to failure at constant load amplitude. The author plotted a graph (figure 2- 11) of defect size against distance from surface and fatigue lifetimes (cycles to failure). The results from this experiment highlighted an accept/reject line (shown in figure 2-11) that takes in consideration defect location and size.

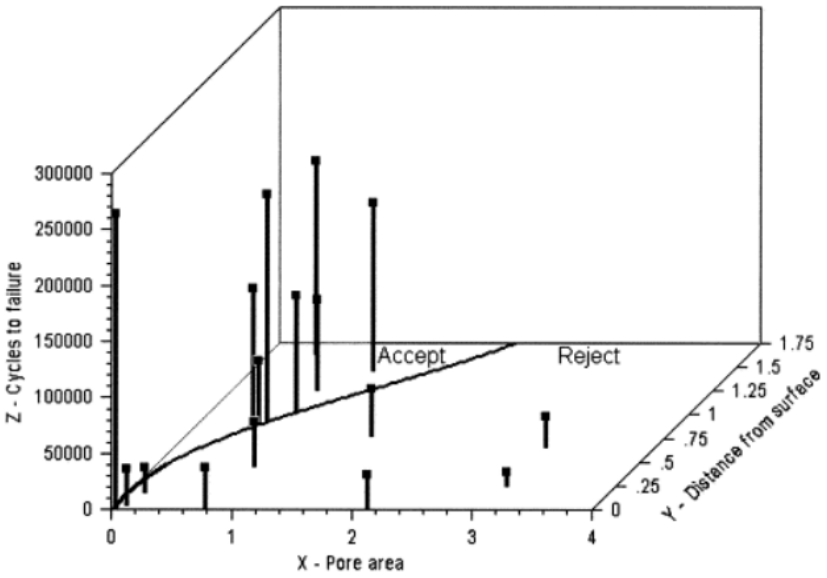

Figure 2-11 Cycles to failure VS defect area (mm2) VS distance from surface (mm) Cycles to failure VS defect area (mm^2) VS distance from surface (mm) [67]

This experiment confirmed that large defects located far away from the surface had much less effect on the fatigue life, on the contrary a small pore located close to the surface had a large effect on the reduction in fatigue life. Furthermore, on several occasions, the defects which were expected to cause fatigue failure were not the root cause, but smaller defects closer to surface initiated the crack. The results of this experiment suggested for the tested materials that: in case of small defects with $0.1mm^2$ the minimum accepted defect depth is 0.25mm from surface, for large defects with $2mm^2$ the minimum accepted defect depth is 1.75mm from surface [68,69]. It was proven that in aluminium alloys the presence of a 1% defect volume could compromise fatigue life up to 50% and endurance life up to 20% [70, 71]. Buffière et al. classified the defects found in Al-Si7-Mg0.3 to two populations, the first is the defects with size lower than 50µm and second population is defects with size larger than 50µm. It was found that the larger the defect size, the lower the sphericity, furthermore it was evident from the results of this experiment that defects which are less than 50µm equivalent size did not cause any crack initiation.

2.3 Summary

The defect presence can cause unpredicted early failure in any component, the defects shape, size and location must be identified before utilising a component in critical applications. X-ray computed tomography is one of the most promising devices that can be used to detect porosity presence. XCT can be used as a measuring device with up to nanometre accuracy in some micro CT devices “depending on beam spot size”, but the use of XCT in industrial markets is well known for it is high cost and complicity. Chapter 3 will look more into the XCT adaptation for metrology and defect detection in various applications.

Chapter 3 Literature review part two: XCT

This chapter is an overview of background literature and current research in industrial X-ray computed tomography (XCT), it advantages, challenges and accuracy compared to other methods of NDT. This chapter is divided to three sections: Section 3.1 How industrial XCT works, 3.2 Advantages and applications, 3.3 Challenges and accuracy.

As previously mentioned in chapter two, XCT is a radiographic testing (RT) method where X-rays are used to create a radiographic image of the scanned component. This method can used to identify any changes in wall thickness defects; external and internal. When comparing XCT to Archimedes or ultrasonic testing, XCT got the advantage of providing information about pore size, shape and distribution.

3.1 Industrial XCT

RT is old technology that has been around since the early 1920's. Apparatus for back projection CT was first patented by Gabriel Frank in 1940, in 1972 Sir Godfrey Hounsfield and Allan Coemack developed the first commercial CT scanner [72]. Seven years later, they won Nobel Prize in medicine for the development of computed assisted tomography [73]. XCT was available commercially in late 1970's for medical applications; it proved to be extremely helpful in several medical diagnoses like broken bone examination and the identification of tooth decay. XCT is a powerful device that can be utilised in testing those elements with high atomic number. On the other hand, magnetic resonance imaging (MRI) can be used for testing elements with very low atomic numbers like natural soft tissues. XCT and MRI are similar systems; both use electromagnetic radiation, MRI produces images by measuring the magnetic resonance of hydrogen molecules but XCT relies on the amount of absorbed X-ray beams. In addition, MRI operates with non-ionizing radiation, but XCT uses ionized radiation. Non-ionized radiation is similar to FM radio frequency radiation. CT is the computational reconstruction of several 2D X-ray images of a component that had been taken at several angles; then the obtained reconstructed data can be processed to generate a 3D image. Tomography is driven from 2 Greek words: "tomos" that means slice and "graphia" which means drawing [74].

In medical application, XCT is currently used in full body scanners with quite high resolution that can be used to investigate specific organs like lungs or skull. The problem is X-ray exposure may cause cancers and it was reported that 2% of cancer patients had been exposed to X-ray radiation in the past [75]. On the contrary, MRI is safer and provides better resolution for scanning soft issues. XCT machines started to become popular for industrial application only from the beginning of the 1990's. There are two different XCT machines, the first machine utilises a fixed X-ray source and a fixed or horizontally moving detector; in this type of machines the inspected component is placed on a rotating stage. The second type of machine is the spiral/helical machine where the x-ray source and detector rotate around the inspected component; the spiral machines are very popular in medical applications.

The XCT market development in industrial applications was driven by the urgent need for a more informative NDT method. X-ray found is used in security applications like preventing terrorist activities by carrying out full body scans or inspecting luggage in airports. The food market is utilising XCT for contamination detection; foreign bodies like those that glass or plastic can easily be detected by XCT. Other industries like military applications and electronic industries are relaying on XCT for NDT and quality assurance.

Most of the experiments in this thesis are carried out with Nikon XTH or XTM 225 which is cone-beam CT scanner" the specifications are attached in the appendix", both of those machines are available on site and the author had unlimited access to the machines, which enabled the author to carry out

several experiments. This section will expand on cone-beam CT with a planar detector configuration as shown in figure 2-1. The cone beam machine usually operates in a monoplane to create a 2-D image of the scanned volume; the CT takes several 2-D images at several planes by rotating the component 360° around a single axis like the one shown in figure 3-1. The detector in the cone beam XCT machines are either fixed or moving horizontally, in the Nikon machine the detector is fixed and to adjust the magnification the rotary stage moves; the closer to the x-ray source the higher the magnification. The scans are made up of 2-D pixels (x,y), post processing of this data generates a 3-D pixel (x,y,z) called a Voxel. In section 5 of this chapter, voxels will be discussed in more detail.

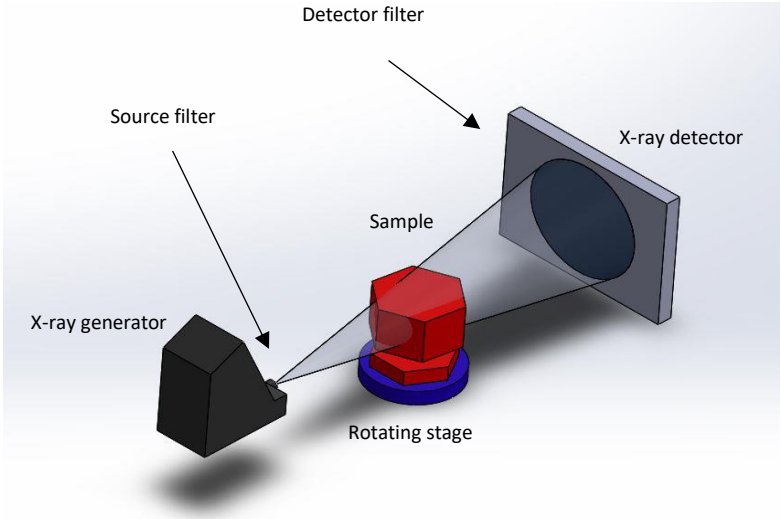

Figure 3-1 Schematic illustration of XCT [4]

When scanning starts, the X-ray generator will radiate/emit an x-ray beam, the scanned component material will absorb some of the X-ray beams as it penetrates through it. The absorption rate differs through air and material, also, the material thickness and density will also absorb different amounts of x-ray. The absorption rate can be calculated using the Beer-Lambert law [76] shown in the absorption equation:

$$I = I_{0e^{-\mu t}} \qquad \textit{Equation 3.1}$$

I Is X-ray intensity, μ and t are attenuation coefficient and material thickness respectively. The data of each voxel is obtained by calculating the exponential deterioration of the X-ray beam when it penetrates the scanned material. In order to linearise the X-ray beam deterioration each ray attenuation can be calculated using equation 2:

$$\ln(\frac{I_0}{I}) \qquad \textit{Equation 3.2}$$

The values of each pixel in the images are calculated by the total density values of X-ray beam paths from the source to the detector. The X-ray images are combined to generate the 3-D grey-scale volume; utilising filtered back projection. Each pixel is assigned a single grey value to it, with no *depth* information [76]. In order to visualise the projected images, a combination process considers the scanned object is stationary and each projection is rotating around it, each projection is adding more information to the previous one. A convolution matrix (filter Kernel) is used to correct the blurring that occurs from back projection [77]. The XCT image reconstruction process is shown in figure 3-2.

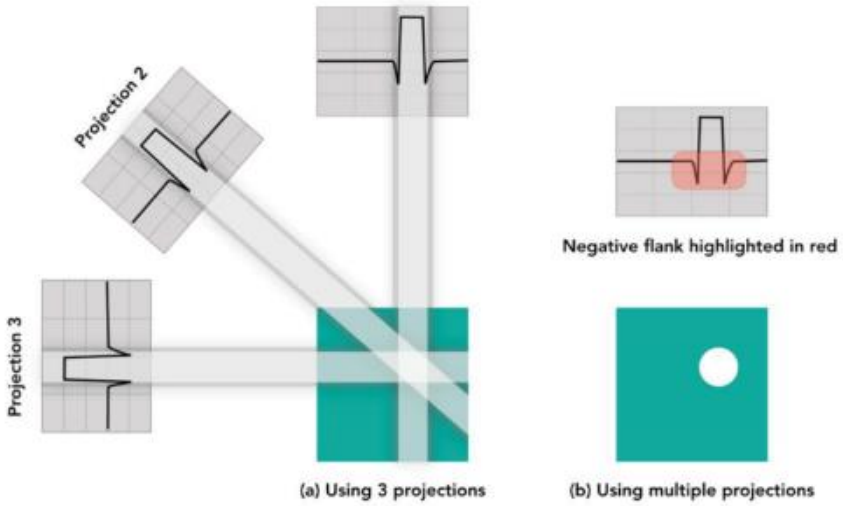

Figure 3-2 XCT reconstruction from several projections [78]

The acquired images are then digitally reconstructed to generate a 3-D model of the scanned component; this model contains all the defects and internal geometry. After data collection and model reconstruction, a sophisticated proprietary software is used for data analysis and model visualisation. The software is used to differentiate between air/material background. The differentiation process is called grey value threshold (X-ray absorbency) of the scanned component and its background. To understand the XCT scanning process the role of the components shown in figure 3-2 must be understood. In the next secion the X-ray source, detector and x-ray filters will be discussed.

3.1.1 X-ray source

The X-ray source produces the X-ray beam that penetrates the scanned component; it is a crucial part of the XCT machine, any instability or wrong setting-up for the X-ray source can cause errors like noise or scatter. These errors will be discussed in more detail later in this chapter. Figure 3-3 shows the XCT water cooled tube where K is the electron source (cathode), A is the target electrons (anode), C is the water coolant, U_h is the heating voltage, U_a is the accelerating voltage and X is the emitted X-rays.

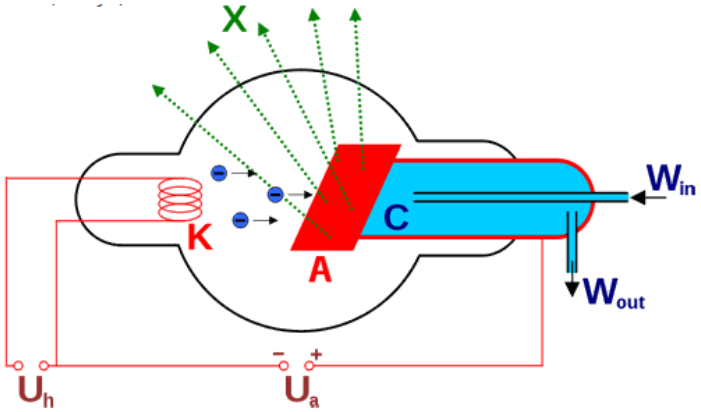

Figure 3-3 XCT water-cooled X-ray tube [79]

The X-ray beams are generated by electron acceleration from the cathode interaction with the target anode atoms. The target anode is often made from molybdenum or tungsten, this is mainly due to this material orbital arrangement, which induces more X-ray than any other material. The Nikon XTH and XTM machines are using tungsten as a target anode material to allow the generation of high intensity X-rays. The electron acceleration from the cathode to the anode takes place by electrostatic

attraction, this is achieved by the large potential difference that affects the anode and cathode making them positively and negatively charged respectively [74].

When the electrons strike the anode only 1% of the energy generated are X-rays. A large amount of the remainder is heat therefore, coolant use is crucial during machine operation [79]. The process is carried out in a vacuum environment to eliminate the possibility of collision between foreign atoms and the electrons as this would reduce the process efficiency. The interaction of electrons with tungsten generates two types of X-ray; the first type are characteristic X-rays, which are a resultant of the collision between accelerated electrons and the tungsten inner shell electron. The collision causes the accelerated electron to be ejected from the atom, the missing electron from the inner shell causes instability to the tungsten atom. To stabilise the atom an outer shell electron drops in energy level to replace the inner shell electron. During this process, the excess energy is emitted from the electron as an X-ray photon [80]. The greater the differential between inner and outer shell releases more energy and produces higher energy X-rays. Bremsstrahlung (Braking radiation) is the second type of generated X-ray, it occurs when any accelerated electron passes close to the tungsten atom nucleus. When this takes place, the electron slows down and deflects its path. The X-ray photons are emitted from speed reduction and energy loss. Approximately 20% of the X-rays are characteristic, of these only 20% have higher energy levels than Bremsstrahlung [81].

The direction the X-rays are generated determines whether the tube is panoramic or directional. The tubes can be divided into unipolar and bipolar based on the electrical earth arrangement in relation to cathode and anode [74]. The unipolar tube voltage functional range is 300kV and bipolar tubes are designed to operate in the range of 450kV.

X-ray cone beams pass through a diaphragm creating a focal spot, the spot is crucial for image quality. Micro focus XCT systems have a spot size between 1µ and 1000µm, conventional systems have a spot size usually greater than 1000µm [82].

X-ray generation from the tube is mainly controlled by the amount of voltage and current supplied. Voltage (kilovolts) controls the beam spectrum; voltage and wavelength are inversely proportional so increasing the voltage will result in a wavelength reduction in the emitted X-ray. On the other hand, current increase while maintaining the same voltage increases emitted beams intensity within the same X-ray spectrum [83, 84]; this can helpful in beam penetration of denser materials.

3.1.2 Filtration

Low energy X-ray needs to be absorbed/removed to introduce beam hardening, this increases effective energy and improves material penetration; this can be done by means of a high pass beam filter. Beam filter material and thickness are application dependant, common materials are aluminium, copper and tin. The materials are selected based on their K-edge, which is the atom's inner shell electron binding energy. For low energy medical CT aluminium is the most common material used due to its lower K-edge (1.6 keV). Other applications like industrial CT that requires a higher K-edge material, copper (8 keV) is used. Figure 3-5 shows a cone beam 0.5mm copper filter.

Filter thickness and voltage are directly proportional; higher X-ray voltages are required for the penetration of denser materials or large cross-sectional objects. The amount of low energy X-ray increases as voltage increases, so a thicker filter is required.

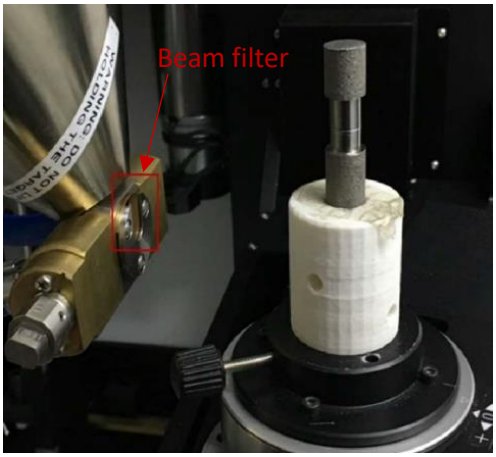

Figure 3-4 XCT 0.5mm Copper beam filter

3.1.3 Detector

Initially X-ray evidence was discovered on photographic plate, Röntgen recorded that exposing a screen coated with barium cyanide glows when it is exposed to X-ray beams. There are several types of X-ray detectors and ISO standard (15708) divides X-ray detectors into two groups: scintillation detectors and ionization detectors [85, 86]. In recent decades radiography scanner performance has improved due to the advance in computing technology. In the beginning, industrial film-based detectors and non-dedicated detectors were used, resulting in low image contrast. In the section below three different detectors are discussed, scintillation detectors, direct detection of X-ray photos and direct semiconductor detectors.

3.1.3.1 Scintillation detectors

Scintillation is the ionisation of transparent material; this process can be thought of as a flashlight. This type of detectors converts high-energy photons to low energy photons in the visible range of wavelength. The low energy photons are detected by photodiode or photomultiplier tube, one of the advantages of scintillation detectors is the high sensitivity to low doses of X-rays [87]. The indirect detectors (shown in figure 3-5) are a combination of flat panel detector (FPD) and a scintillator; those detectors are made of amorphous silicon substrate covered with sodium-activated caesium iodide.

Materials commonly used in scintillator detectors are Thallium-activated structured Caesium iodide crystals (CSI: TI) combined with Gadolinium Oxysulfide (Gadox or GOS). These detectors are known as ceramic screens. Amorphous silicon (α-Si) detectors are an example of scintillator detectors; they are indirect detectors, so the X-ray beams are converted to light photons. A thin film transistor (TFT) made from (α-Si) material combined with a scintillator plate and an array of photodiodes converts the photons to electronic charges, converting from analogue to digital [88]. These detectors are also known as integrated area detectors, they have high spatial resolution and fast images requisition [89]. One of the disadvantages of these detectors is the difficulty in pixel size reduction [90].

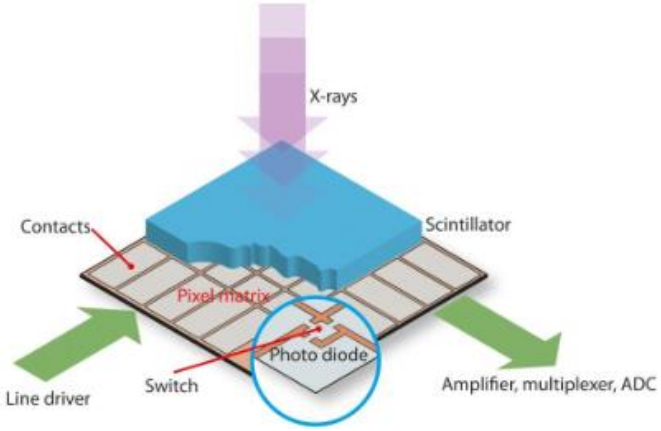

Figure 3-5 indirect detectors [88]

3.1.3.2 Direct semiconductor detectors

Semiconductor detectors have been used since the early 1970s, they use lithium doped in germanium or silicon. Direct detectors, also known as solid-state detectors (shown in figure 3-5) generate electric current when exposed to X-ray beams. The use of these detectors in radiation detection has evolved in both X-ray and optical frequency range, Most of the modern solid-state detectors utilise photoconductors, like multi-pixel microelectronic plates coated with cadmium telluride or amorphous selenium (α-Se). In these detectors, thin film transistors (TFTs) are used to collect output current.

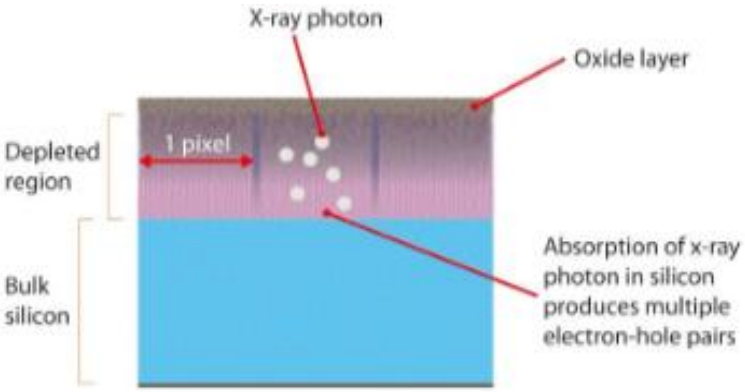

Figure 3-6 direct semiconductor detector configuration [88]

Amorphous selenium (α-Se) detector technology uses a thin layer of photoconductive material placed on an imaging plate; the surface is constantly under uniform positive charge. The advantage of this technology is the direct X-ray conversion to electric charge, this prevents scintillation noise minimises sharpness and avoids the conversion losses of indirect X-ray detectors. Generally, direct detectors have lower noise and produce a sharper image. The main disadvantages are ghosting and long image lag [89].

The thin-film transistor-based detectors are known for their high performance, ability to cover large scan area and radiation hardness. On the other hand, the disadvantages of these detectors are baseline drifting caused by the amorphous structure, high noise presence and the large pixel size (100-130µm). These characteristics make this type of detector a good choice for several industrial XCT applications [91].

ASTM E2597-07 is the standard practice for the manufacturing characterisation of digital detector array (DDA). It can be used to compare the performance of different detectors [92], and it allows selection of the right detector for the application. The charts shown in figure 3-6 are characterising basic spatial resolution, material thickness range, efficiency, image lag and contrast sensitivity [93].

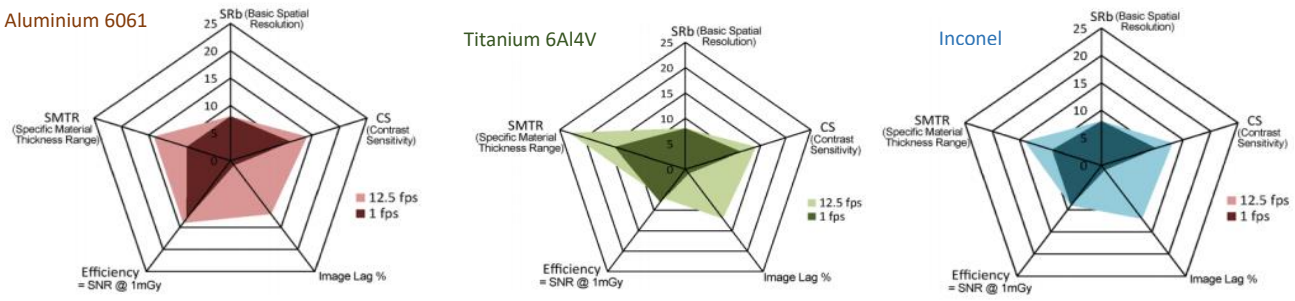

Figure 3-7 PaxScan 2520DX-I industrial detector characterization charts [93]

The charts shown in figure 3-6 show the performance of a Varex 2520 industrial detector, the charts are comparing the detector performance at 1 and 12.5 frames per seconds (fps) for aluminium 6061, titanium 6Al4V and Inconel 718. The charts show that the material density and thickness affect the spatial resolution and efficiency.

Nikon XTH225ST and MTC225 comes with Varex 1611 and Varex 1620 respectively [94], Varex 1611 is a FPD amorphous silicon X-ray detector with 100 µm pixel size and 41X41 cm panel size [95]. The MTC detector panel (Varex 1620) is a single substrate amorphous silicon active TFT diode array with direct deposition scintillator (Scl:tI or Gd_2O_2S:Tb), with 200µm pixel size and 67X67 cm panel size [96].

3.2 Spatial resolution

Resolution is the ability of the measurement/imaging system to accurately measure the distance between two points. Similarly, the spatial resolution can be defined as the capability of imaging fine detailed structure in an object; this can be quantified by measuring the smallest distance at which two points can be distinguished as different units [97].

X-ray beams emitted from an X-ray tube penetrate the scanned component located on the rotating stage, the centre of rotation from the source to object distance known as (SOD) (shown in figure 3-7. After the beam passes through the component it is detected by the flat panel detector, the source detector distance (SDD) is then recorded (shown in figure 3-7) [98]. The magnification (*M*) of the scanned object is given by:

$$M = \frac{SDD}{SOD} \qquad \textit{Equation 3.3}$$

The spatial resolution $\boldsymbol{\Delta}X_{Obj}$ is given by:

$$\Delta X_{Obj} = \frac{\Delta X det}{M} \qquad \textit{Equation 3.4}$$

Where ΔX_{Det} is the detector pixel resolution, equation 4 can be used to determine the minimum resolution of the CT volume, however the X-ray focal spot size must be considered. Focal spot is a function of power; at low power (3W), the focal spot is 3 microns, at 225 kV (225W) the focal spot is 225 microns; the resolution will be proportionate 3 to 100 microns. When a CT operator is setting up a machine to scan, the energy per unit area must be considered. In a 225kV machine, the beam is defocused above 10W to prevent target/detector damage.

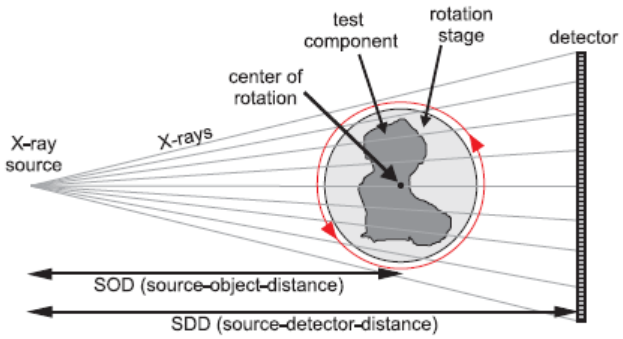

Figure 3-8 CT scanner illustration [99]

In order to obtain high-resolution scans a small X-ray focal spot size has to be maintained, this is mainly due to the effect of penumbra blurring. As mentioned before resolution is the capability of the CT system to resolve features that are close to each other. The amount of blur controls the resolving ability of the imaging system. The impact of blur can be seen in figure 3-9, if blur is present, the individual features begin to run together until it is not possible to resolve them or distinguish between them anymore. To be able to resolve individual features, the space between them has been proportionally more than the present blur [100] .

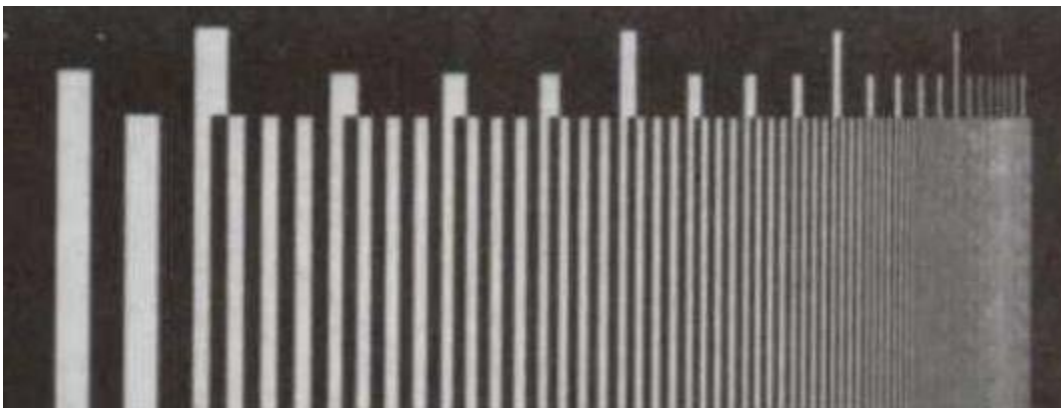

Figure 3-9 Test pattern for XCT system resolution measurement. [100]

Resolution characteristics can be assessed by the contrast transfer function (CTF) and modulation transfer function (MTF). The CTF assesses the capability of the imaging system to solve different size features in the scanned object in the presence of blur [100]. The blur graphical description can be defined by the modulation transfer function (MTF). CTF and MTF are similar; the difference is that CTF describes the capability of the CT system to image line sets, whereas MTF describes the capability of the CT system to image sine-wave figures/spatial frequency. The MTF tests the object peaks and troughs per millimetre of length, one cycle equals to a peak and a trough and CTF is testing certain number of lines per millimetre. There is a strong relationship between the system's ability to image different spatial frequencies and the amount of blur present in the image.

In fact, detectability and resolution are two different terms; ISO15708 defined detectability as the reliable detection of a feature presence by using a tomographic inspection image [85, 87]. Detectability is mainly dependant on the CT system resolution, noise presence and feature size. In some occasions, unresolved small features can be detected given that sufficient contrast is present. Generally smaller objects than pixel size could be detected if there is enough signal amplitude to affect pixel scale of the grey value.

3.3 Contrast

Contrast is defined as the ability of XCT system in detecting and measuring sensitive variations in the grey scale values. For example, features within the object that create small variation in the signal intensity to the background, causing a difficulty in edge detection and separating background from the scanned object. The contrast resolution parameter is the signal to noise ratio (SNR); it evaluates the integrated signal of the scanned area containing object and background, divided by the noise. The SNR can be calculated using the following equation:

$$\text{SNR} = \sum_i \frac{(x_i - x_{bg})}{\sigma_{bg}} \qquad \textit{Equation 3.5}$$

In equation 5 x_i is the region of interest (ROI) pixel signal amplitude, x_{bg} is the background ROI pixel signal amplitude and σ_{bg} is the background noise [100]. Figure 3-10 a) shows SNR equation

parameters, x_i is an example of a noise bright spot, but in figure 3-10 b). The bright spots are AM powder contamination. To the un-educated eye both of the spots are very similar, but with a closer look at the noise spot (figure 3-10 a)) the brightness intensity is higher in the middle and fades gradually towards the edges.

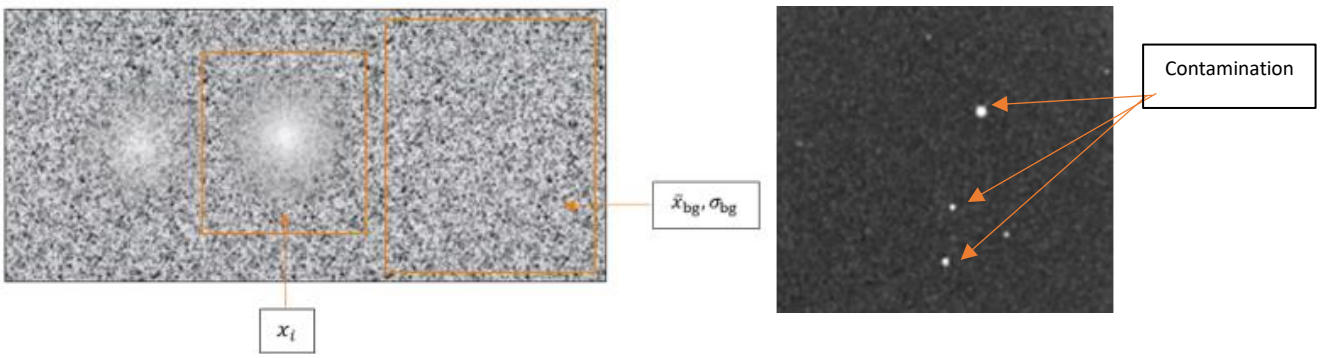

Figure 3-10 a) Irregular bright spots with SNR parameters [101] b) XCT image of Aluminium AM powder contamination

On the other hand for the powder contamination (figure 1-10 b)), the brightness intensity is consistent. Contrast is very important for defect analysis, contamination detection and edge detection, furthermore contrast can enhance sub-micron detection [101].

3.4 Grey Scale

Generally, the image could be black, white or several shades in between them. Those shades in-between are grey that can be in varying light or dark shades. Grey scale images can be used to determine light intensity, the shade variation can be used to obtain useful information that can used in measuring dimensions and comparing geometries.

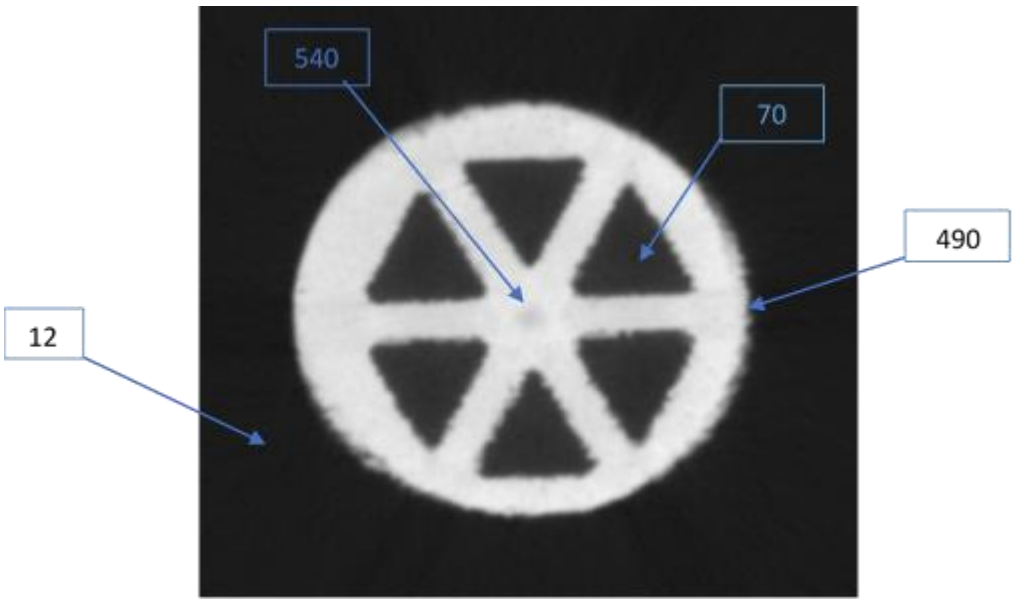

Figure 3-11 XCT image with different grey values

The grey scale values vary depending on the material thickness, the background/air is always lower value than the centre of the scanned object. Denser materials will always have greater grey value. The grey value variation can be seen clearly in figure 3-11; the scanned object is titanium with internal hollow features. The background/air grey value is 12 whilst the air inside the internal hollow feature is 70. The outer edge of the object is 490 and the centre of the component is 540.

3.5 Voxel

A voxel is defined as a 3-D analogue of a pixel; Voxel size is a 2-D pixel size combined with slice thickness. The scanned area imaged by the CT is called the field of view (FOV). The matrix is the number of pixels rows multiplied by columns. Pixel size can be calculated from the field of view (FOV) and image matrix; Pixel size equals to FOV divided by matrix size. The pixel size is strongly related to spatial resolution. Generally low pixel size will result in high spatial resolution. Figure 3-12 shows voxel size explanation whereby the length matrix and high matrix creates the overall FOV. Voxel size is the pixel area multiplied by the slice thickness and the voxel depth equals the slice thickness.

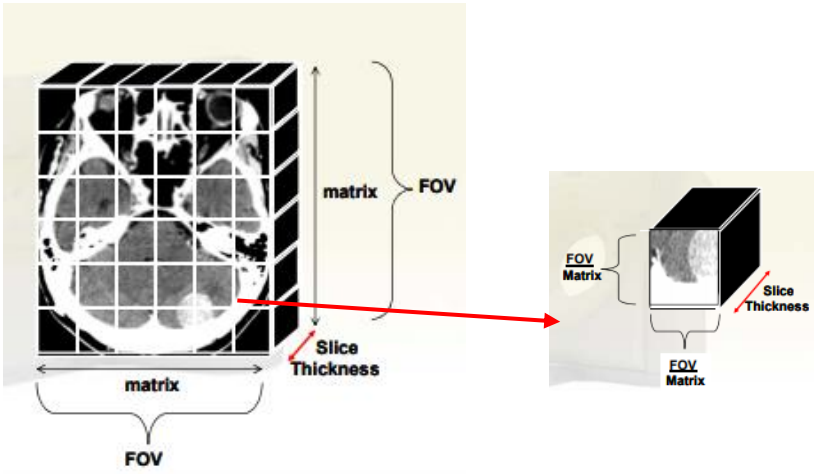

Figure 3-12 Voxel size demonstration [102]

Voxel size in cone beam computed tomography is isotropic, so all the dimensions are equal and the resolution is constant in all the directions. Since it is isotropic any measurement will be consistent in all three orthogonal planes. In order to calculate the voxel face dimensions the FOV must be divided by the number of voxels across the slice. So, for example, a 20mm FOV with a 512 matrix equates to a voxel dimension of 0.040mm. The voxel size has an impact on the noise presence, blurring and overall scan resolution. Mulder et.al investigated the impact of voxel size on resolution; the author scanned 100 ellipsoids, with radii length 2.7mm, width 2.7mm and height 5.4mm with different Voxel size. Figure 3-13 shows a sample of the results of geometry detrition.

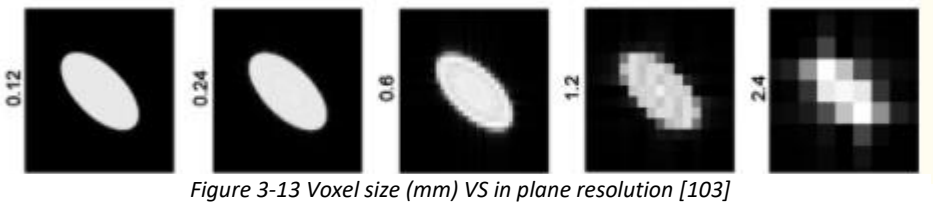

Figure 3-13 Voxel size (mm) VS in plane resolution [103]

It can be noted from the image that at low voxel size 0.12mm the ellipsoid geometry is clear with no blur, from 0.6mm the blurring is protruding make it very difficult to identify the edge of the material. Finally, at 2.4mm voxel size the ellipsoid geometry cannot be identified.

3.6 Reconstruction

The reconstruction process is accomplishing the CT operator requirements through image processing algorithms to adapt and manipulate the raw data. The algorithms optimise the data output to reduce overall image quality degradation by preventing artefacts and noise that might lead to wrong or inaccurate results. There are several types of reconstruction algorithms; each machine manufacturer has developed their own interface, for example Nikon's CT Pro reconstruction interface. The reconstruction interface usually focuses on resolving any imperfections found in the raw data for the specific application.

Reconstruction algorithms can be classified to statistical [104], algebraic [105] or Fourier-transform based [106]. The statistical and algebraic reconstruction methods are capable of reducing beam hardening, improving overall results presentation and reducing errors, but the Fourier-transform based filtered back-projection (FBP) reconstruction method is more popular due to low computational power requirements [99]. When comparing different types of reconstruction algorithms several aspects must be considered, the first aspect to consider is if the reconstruction algorithm is exact or approximate. The exact algorithm is considered mathematically right if the data do not contain any noise and has been captured with enough density alongside the x-ray source trajectory, with the detector array consuming sufficient detector part density. The approximate method must be chosen when the CT scan is preformed using stationary x-ray source and detector, while the sample is rotating 360 on the rotational stage. This is mainly due to the phenomena of data sampling in Radon space; this phenomenon is defined as the presence of a torus shaped zone in the 3D radon space, these shadow zones usually develop along the rotational axis, preventing the exact reconstruction of the 3D model. Cone beam artefacts are developed from the scanned object points that are off–centred axial planes; deviation angle ≠ Zero.

Approximate method is the most common used 3D reconstruction method for con beam x-ray systems with planar detectors, the algorithm was developed by Feldkamp et al. and it is known as FDK method. The author developed this method from algorithm used in fan beam where it is assumed that the beam source vertex geometry is circular. The only problem with this method is the development of a cone artefact [107].

3.7 Visualisation software

After the 3D volume reconstruction, the volume can be viewed by proprietary software, e.g. VG studio max, Avizo and Simpleware. This software's provide advanced functions for visualisation and segmentation of the scanned object. The CT volume is presented/visualized as a 3D cuboid with individual voxels demonstrating the attenuation coefficient for each voxel. Consequently, the scanned object can be viewed in three cross sectional views known as XCT slices [108]. The visualisation software permits several tasks depending on end user needs and software capability. Tasks like converting models to STL file format, defect evaluation and checking wall thickness can be carried out easily. Those tasks can be divided to quantitative and qualitative visual assessment, quantitative tools like geometrical dimensional measurement, defects/porosity analysis and foam structural analysis. To do this the scanned object surface has to be distinguished from the background/air, this can be done by grey value thresholding known as surface determination (SD). The dimensional measurement accuracy is mainly dependant on the resolution; VG Studio max recommends that 1-10% of the voxel size accuracy could be achieved [108].

3.8 Surface determination

When the object is visualised in the software a threshold for the grey value must be identified, this process is required prior to any dimensional or defects analysis. This plays an essential rule in the accuracy of the generated scanned object. The XCT machine dimensional calibration is accomplished by measuring centre-to-centre length of spheres to prevent erroneousness created by SD selection [109]. After applying SD, cross-sectional slices and a 3D model can produced similar to what is presented in figure 3-14 , an M6 Allen bolt with internal features was scanned and figure 3-14 (a) shows top view, (b) front view and (c) is a right view, while (d) is the complete 3D model.

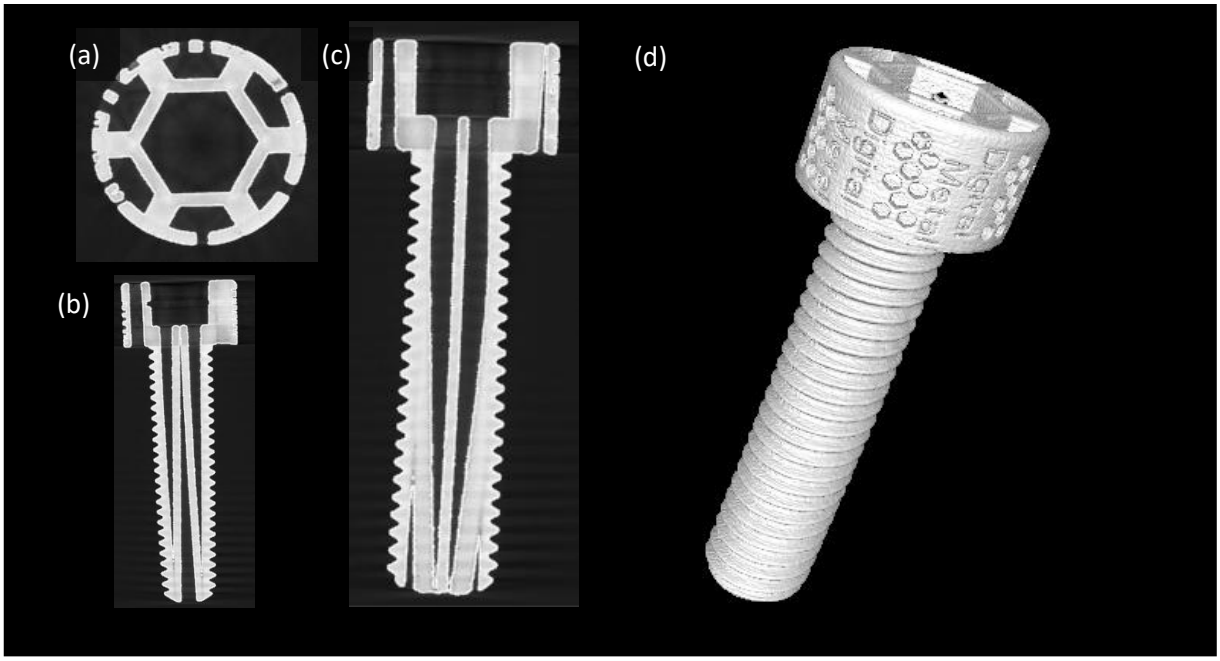

Figure 3-15 (a) top view (b) front view (c) right view (d) 3D model of reconstructed 3D volume of M6 Titanium Allen bolt made by AM technology

The methods used in SD can generally be divided to two categories: local and global. The local SD is the process where a target grey value is chosen, for example (ISO 50%) threshold, then the grey level values around the edge of the object are analysed, for example within 3 voxels around the initial surface, finally the surface is located where the maximum grey value voxel is situated. The ISO 50% is shown in figure 3-17; the threshold is located at 50% between the peak of the material and the peak of the background/air in the histogram [6].

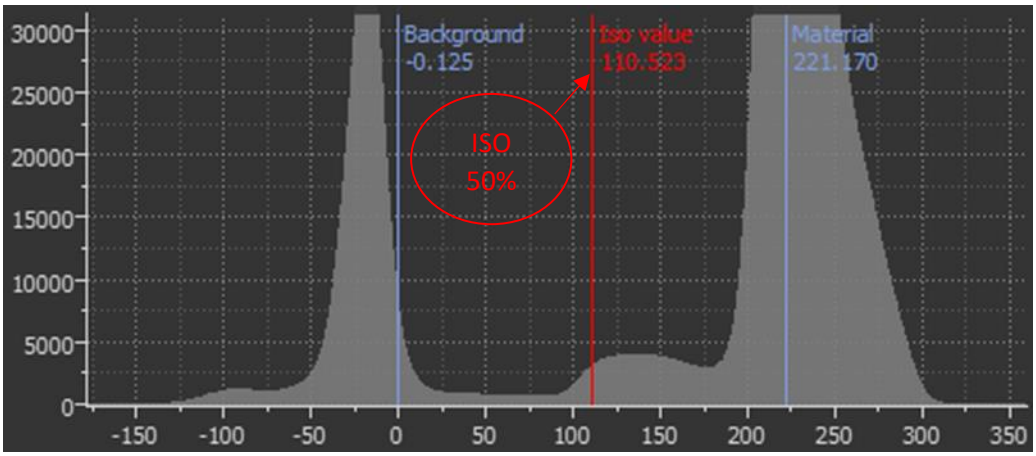

Figure 3-17 Surface determination histogram [6]

Global SD identifies the edge/surface at a particular single grey value; the grey value threshold selection is based on grey scale value histogram (shown in figure 3-17) analysis or by identifying a volume in the background/air and a volume in the object material. Considering both methods, the local SD requires more computing power and takes more time for analysis but it can enhance the scanned data quality, promoting sub-voxel detection. Alternatively, the global method requires less time and combined with high resolution; scan sub-voxel detection can be achieved.

3.9 XCT Errors

There are several sources of error in the XCT process. The errors can be split into physical beam characteristics, x-ray tube, detector and setup/operator errors. Several researchers investigated these errors and their impact on obtained data quality [83, 110-112].

3.9.1 Noise

The random variation in the image pixels grey value without the presence of features causing this variation. There are several types of noise, but they are mainly statistical and detector noise. The statistical noise occurs when a finite number of photons interact with the detector and it is amplified by instrumentation and data processing after the scan [87]. In order to achieve noise reduction the voltage must be reduced, however in certain situation such as when scanning a high-density material, it is difficult to reduce the voltage without increasing the scan time. It is always recommended to increase scan time and reduce voltage to avoid statistical noise. Several researchers have investigated the influence of statistical noise and methods of reduction [113,114]. Figure 3-18 shows an example of the statistical noise in a scan object.

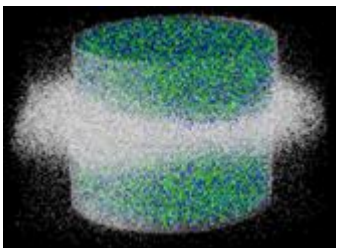

Figure 3-18 scanned object with noise [6]

The noise presence in x-ray detectors can be divided into electronic temporal noise, input signal noise and fixed pattern noise (FPN). Electron flow that carries output signals can create electronic temporal noise in the electronic detectors; this type of noise can cause poor image quality at low signal level. The input signal noise, also called quantum noise/photon shot noise is the variability in the detection of x-ray photons. The input signal noise can be reduced by increasing the number of detected photons. The FPN also known as structured noise is created by read out channels in the detector pixels; dust in the sensor can cause it. This type of noise is constant in time so the image can be corrected by characterizing offset and gain factors for each pixel in the reconstruction process [89].

3.9.2 Beam Spot Drift

The x-ray focal spot spatial stability affects the XCT system accuracy; focal spot instability can cause beam drift, due to x-ray tube thermal expansion. The presence of heat load will randomly expand the x-ray tube; this dimensional variation causes the focal spot to drift. The cooling system used in the XCT machine cools the x-ray tube to control beam spot drift [115-117].

3.9.3 Ring artefact

Ring artefact is one of the most common errors of XCT systems. This error is mainly related to the detector or x-ray source to detector misalignment. Defect presence and incorrect calibration of the detector can cause ring artefact. Detector sensitivity is another factor that can cause ring artefact, the

detector sensitivity must be consistent, any presence of faulty pixels in the detector will cause ring artefact in the reconstructed data. Figure 3-19 shows a XCT image top view of a cylindrical object with ring artefact.

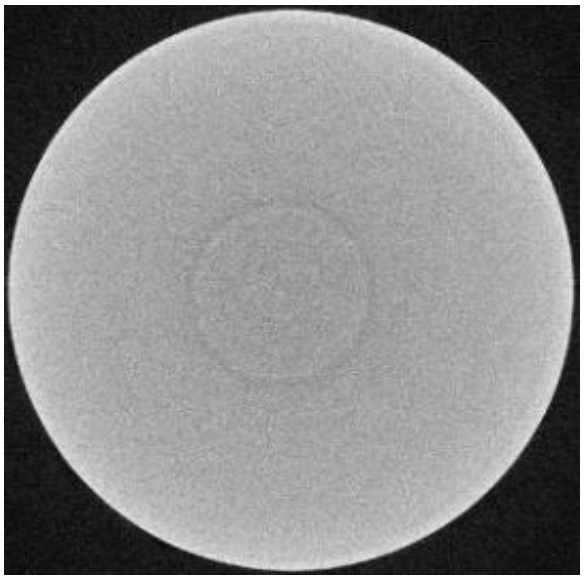

Figure 3-19 ring artefact in a scanned cylinder

The errors resulting from ring artefact can be reduced by XCT detector calibration; this can only be done if there is no permeant damage to the detector pixels. Alternatively, converting XCT images to a polar coordinate system is a numerical method of ring artefact correction [118].

3.9.4 Beam Hardening

Industrial and medical XCT tubes are generating x-ray from electron impact sources, with the emitted beam a continuous spectrum of characteristic and bremsstrahlung emission lines are generated.

X-ray polychromic beam spectrum is one of causes of the beam hardening (BHD), it mainly occurs when the beam is penetrating the material polychromatic spectrum causing nonlinear attenuation. The low energy photons in the path get absorbed or scatter due to their low attenuation characteristics compared to high energy photons. While the beam is penetrating, the material lower energy photons are lost from the x-ray photon flux than high energy photos. The x-ray photon flux with high energy photon intensity creates a different spectrum with higher mean energy and the beam spectrum gets hardened. The increase in the beam mean energy reduces the probability of the photons interacting with the scanned object, but this is depending on the object length. The beam-hardening phenomenon is directly affected by penetration length, if the penetration length is long the nonlinearity increases. When it increases the individual projects starts to be inconsistent, causing beam hardening artefacts. This can make the material look falsely non-homogeneous.

There are several methods to correct or reduce beam-hardening effects, these methods can be categorised into three different categories: pre-processing, post processing and dual energy [119]. Pre-processing is done via beam filter; the filter is placed between the x-ray source and the object. It filters out low energy photons and narrows down the beam before it reaches the object. A balance between the filter thickness and current voltage needs to be considered; if the filter is too thick it will filter low and high-energy photons creating lack of penetration, on the other hand if it is too thin it won't filter the lower energy photons and this will result in BHD artefacts. The only drawback of using beam filter is signal to noise ratio reduction.

The post processing method use for correcting BHD is water correction or the linearisation approach; this method is applied in the XCT machine pre the reconstruction stage [120,121]. In this method, the measured signal is mapped to the signal from a monoenergetic signal with the same path length. The mapping function can be developed by simulating a polychromatic beam spectrum [122]. The only problem with the water correction approach is that it can only be used if the scanned object is made from a single material. In the presence of multi materials, the measured projection integrals will produce an unknown mixture of attenuation when the beam passes through the different materials. For multi- material scans a post processing forward projection iterative method can be used [123]. A final method called the dual-energy approach is used to correct BHD, this approach is the most effective method, but it requires two scans with different voltage x-ray tubes [99, 124]. The two x-ray beams are used in the calculation of energy dependency required for BHD correction [125]. The utilisation of dual energy XCT is expensive and time consuming.

3.9.5 Scattering

Scattering is one of the other sources of error that causes severe artefacts in the XCT image. In industrial CT scattering occurs when the x-ray beam collides with the object, a small proportion of the x-ray beam is absorbed by the object but most of that beam's photons scatter by Compton or Rayleigh scattering. The Scattered photons are diverged from the cone beam path and starts traveling in random directions as shown in figure 3-20, some of these photons reach the detector and increase the signal randomly.

This signal does not correlate with the signal created from the straight cone beam that penetrated the object, causing nonlinearity to the signal and generating scatter artefacts in the reconstructed image. Beam scatter artefacts appears like as streaks or BHD. In cone beam, computed tomography scattering artefacts are still considered unsolved [126,127].

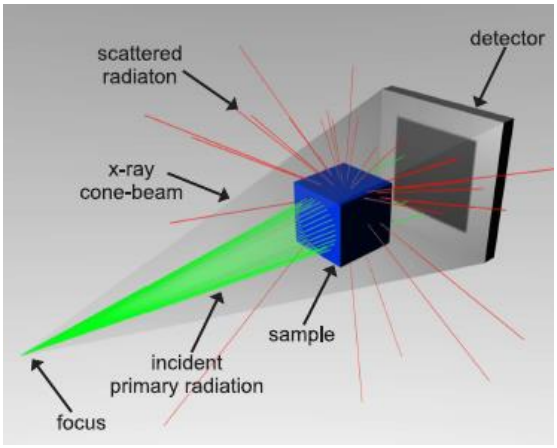

Figure 3-20 beam scattering radiation [99]

3.9.6 Partial Volume Artefacts

It is not recommended to limit the field of view to a section of the scanned object, it is always recommended to maintain background/air around the object. XCT reconstruction algorithm assumes that the scanned object is visible from all angles; shading artefacts are produced when the object is not fully imaged by the detector. The partial volume artefacts cannot be fully eliminated but its affect can be reduced by numerical estimation [87].

3.10 XCT Standards and traceability

Any measurement system can be assessed by verification and calibration. The verification is the assessment of the instrument operation within a defined specification supplied by the manufacturer. Calibration is defined as the process of comparing the obtained results against those obtained from a known well-established national or international standard [128]. The XCT system is a non-contact system and the only similar non-contact system is the optical CMM. The ISO 10360 part 7 standard states that it is recommended to compare the values of different traceable five calibrated test lengths to the calibrated values. The acceptable length error including uncertainty should meet what the manufacturer had previously specified [87]. There is no standard with complete guidelines for XCT result verification. XCT system is imaging the scanned object by measuring the difference in intensity between emitted and detected beam. Therefore, the accuracy of those two values is critical [129]. The detector can be calibrated by analysis of the signal with and beam illumination. Each individual pixel is observed by checking the reaction from the radiation dose; defective pixels are assigned with the average values of the neighbouring properly operating pixels [130]. In the recent years, XCT systems are gaining large interest due to the system ability in the inspection of internal and external geometries. Similar to any dimensional measurement device the traceability of the system is essential for the data analysis. Traceability is the classification of the measurement results by linking it to a well-documented continuous chain of calibrations. Each of them back up the uncertainty of the measurement [131]. For XCT systems the traceability can be done by calibrating the scanned object with CMM. If the measurement model has more than one input, every individual input value must be metrologically traceable and contributes to the network of the calibration. At the moment there is no single object that can be used for XCT calibration, this is mainly due to parameters like grey value threshold and scaling which cannot be easily calibrated.

3.11 Summary

XCT is the tool used in this thesis, from chapter 3 it was concluded that XCT process is quit complex with several variables. In order to establish the best practice for using XCT a suitable application must be selected. The author selected AM as the application for testing and understanding XCT capabilities. The next chapter will highlight the AM technologies.

Chapter 4 Literature review part three: 3D printing technologies

This chapter is a review of the current state of the art and literature in additive manufacturing (AM) consisting of 6 sections. Section 4.1 is an overview of AM, section 4.2 is a review of the AM applications. Section 4.3 is the AM classification. Section 4.4 is an overview of the defects found in PBF process, Section 4.5 is an overview of PBF powder morphology, and section 4.6 is a summary, which highlights the artefacts developed by other research, and the early experiments that took place in an early stage of the authors' research.

4.1 Additive manufacturing

AM is the process of producing a component/part layer-by-layer from a 3D model, usually in STL format. AM technology is relatively new it was first patented by Chuck Hull in the USA in 1986 [132]. More recently, AM technologies have received large industrial interest. This interest has driven rapid evolution of the technology. Various industries including aerospace, medical and automotive are investigating AM methods, mainly due to the substantial advantages in producing geometries and internal features that are not possible with conventional subtractive machining. At present AM, technology is only used for low volume components and prototype testing, mainly due to the manufacturing cost per unit and lack of confidence in the structural integrity of AM components. On the contrary, subtractive machining processes are well understood and the mechanical properties can be accurately predicted. For high volume, low-cost components, like a mass-produced passenger car cylinder head; casting and machining will always be the first choice. Furthermore, safety critical applications like aerospace or medical will always approach subtractive machining for non-complex geometries or components that can be made with conventional methods. Although some additive manufacturing methods like Binder Jet are relatively cheap and produce large volumes, the structural integrity of AM components needs be improved through post processing to be useable. AM is not a replacement for conventional machining, it can enhance the abilities of conventional machining but it cannot replace it as most AM components still require machining.

4.2 AM applications

Design Engineers are considering AM for components with internal features or complex geometries; components with geometries/features that are not accessible with subtractive machining tools [133-136] can be made with AM techniques. In medical applications, AM technologies are utilised to emulate bone functional and structural properties to promote bone ingrowth and support anisotropic stiffness to enhance load transfer and help the adaptation of bone density to the different practical forces. Figure 4-1 a) shows an actual bone structure and 4-1 b) shows a titanium alloy AM lattice structure with internal trabecular cavities made by an implant manufacturer, this structure replicates the bone cancellous; to permit blood flow within the implant [137]. Bones are living material that can heal, regenerate and alter when under stress; this is part of the human skeleton efficiency, which distributes the bone density based on body requirement. When an implant is placed in a patient's body, if the implant is stiffer than the bone the implant will stress shield the bone when it is under load. This means that most of the forces will be distributed onto the implant, causing the bone to recedes/remodel and become weaker, this phenomenon is known as osteopenia and it causes implant loosening, leading to implant wear and eventual failure [138].

The body of a human being differs from one to another; similarly, bones are different in shape and structure. Bone density adapts to load so bone structure will vary depending on human age, weight and physical activity. Therefore, each patient requires bespoke implants; doing so with conventional subtractive machining is very difficult, time consuming and not cost effective. AM technologies enable the manufacturing of patient specific implants, figure 4-1 c) shows and example of titanium

customised trabecular hip cup made by EBM technology [139]. Titanium implants made by electron beam melting (EBM) technology have also been shown to aid cell-ingrowth.

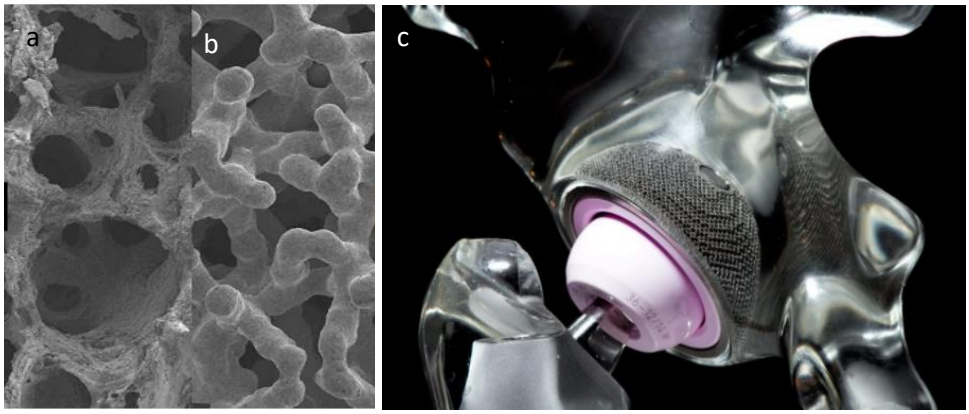

Figure 4-1 a) bone structure b) AM trabecular structure c) AM Titanium hip cup [138]

Medical implants are not the only application that has benefited from the adaptation of AM technologies, the global aerospace industry is considering AM technologies to produce topology optimised components to help with weight reduction and fuel saving. The aerospace and defence industry represent a 16.8% of the $10 billion AM market, mainly through contributions to research and development (R&D) efforts [140]. The aerospace industry is utilising AM in the manufacturing of lightweight components, functional prototypes and aeroplane building tools. Structural and highly loaded components are usually made with either EBM or SLM technologies due to their good structural integrity, figure 4-2 a) shows a jet engine fuel injector made EBM technology, this injector contains internal micro features for fuel atomisation that is not possible to manufacture with subtractive machining [141]. On the other hand, non-structural components like air conditioning air ducts are made with selective laser sintering (SLS) or fused deposition modelling (FDM) technology; figure 4-2 b) shows an air duct made by FDM that received an FAA airworthiness approval tag [142].

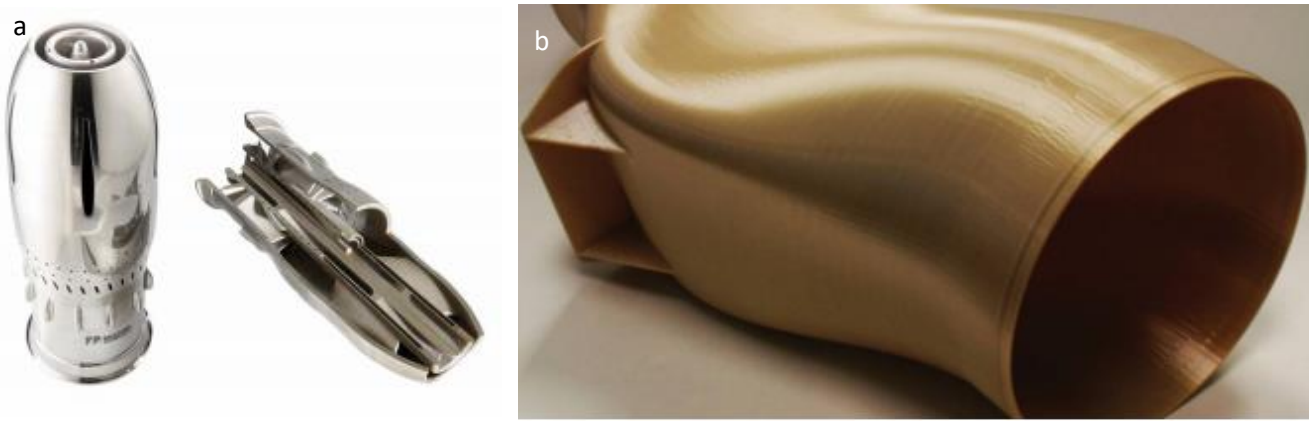

Figure 4-2 a) aerospace fuel injector [141] b) Aerospace cooling duct [142]

The aerospace industry requires complex components with relatively low volumes; this fits well with AM abilities, cutting the costs of investing in machining tools makes the components more cost effective. One of the most important elements to consider in the early design phase of an aircraft is weight reduction; this aids the reduction in fuel consumption and carbon emissions. AM components are made layer by layer which is more efficient than conventional subtractive machining; building layer-by-layer uses raw material only when required, this combined with powder recyclability reduces wasted material. The adaptation of AM technologies have enabled design assembly simplification by combining several parts into a single functional component. Assembly simplification leads to

maintenance cost reduction and saves time in the assembly process. Figure 4-3 a) and b) show an example of aircraft duct component consolidation [143], 4-3 a) shows the original assembly which consists of 16 components and 4-3 b) shows the redesigned assembly made by SLS AM technology [143].

The service life of an aircraft ranges between 20 to30 years, any time lost in maintenance or repairs leads to financial loss for the airline. The aerospace industry is utilising direct energy deposition (DED) AM technologies in the repair process by fusing metal alloys to the damaged/worn component surface. Figure 4-3 c) shows an example of DED used in helical shaft repair [144].

Another fast-growing AM application is the automotive industry, global revenues for AM technologies in the automotive industry was $1.4 million in 2019. Demand on AM technologies are increasing rapidly and are expected to reach $5.8 million by 2025 [139]. They are mainly used for prototyping; however, high-end sport cars and racing applications are utilising AM for functional components due to the low volumes requirements and no cost constraints in the high end and supercar automotive industry.

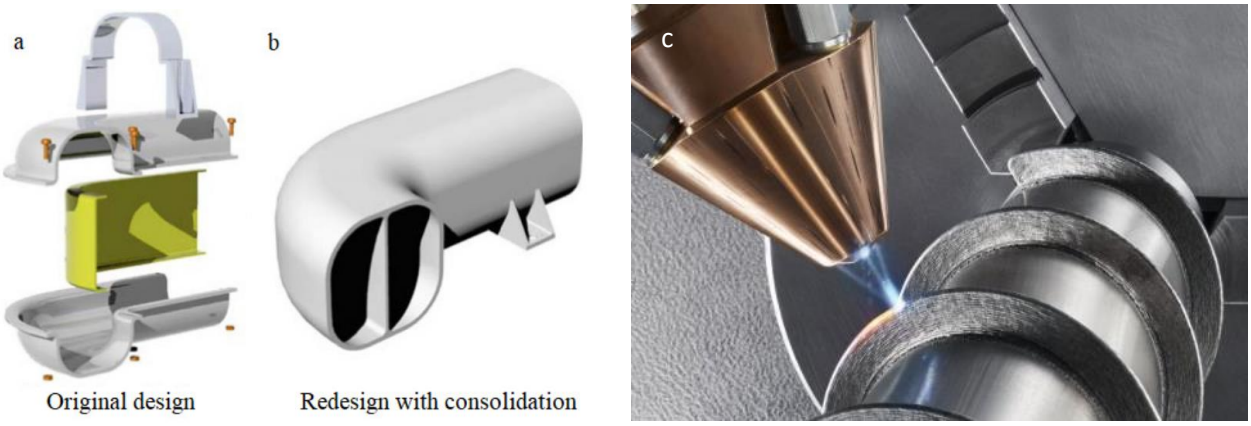

Figure 4-3 a) aircraft duct assembly b) Aircraft air duct made by AM technology [143] c) DED AM technology used for component repair [144]

Several automotive manufacturers are expending in AM adaptation, this is mainly to overcome manufacturing and design limitations, and achieve weight reduction. For example, in 2018, Bugatti launched the new Chiron hyper car, the new model got an AM state of the art brake calliper and titanium exhaust tips. The eight-piston calliper shown in figure 4-4 a) is 40% stronger than regular alternative, it is made from titanium and takes 25 hours to build. It is the world biggest calliper, it measures 21cm wide and 13.6cm high and 41cm long but only weighs 2.9kg. In addition to weight reduction, the calliper benefits from several cooling vents for heat dissipation [145].

BMW is another automotive manufacturer that is using AM technologies; the top of the range i8 roadster has folding roof brackets made using AM technology [146]. The brackets shown in figure 4-4 b) are designed with specific structures that are not possible to produce using conventional machining.

BMW used AM technology to manufacture the new M850i Coupe Night Sky edition [147], the car features a 6-piston calliper shown in figure 4-4 c). Similar to the Bugatti calliper the M850i calliper has various cooling cavities and is made as one piece. Similar multi piston callipers made by conventional machining methods usually consist of six components.

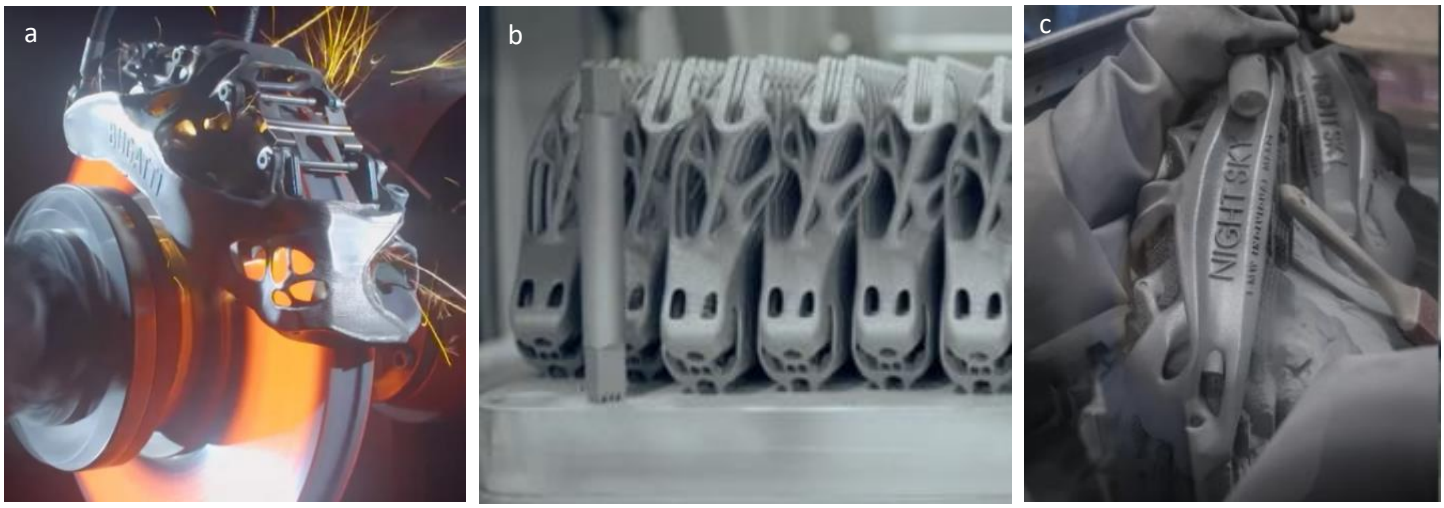

Figure 4-4 a) Bugatti titanium 8 piston AM calliper [145] b) BMW i8 roadster folding roof brackets [146] c) BMW M850i Coupe Night Sky Edition [147]

Another AM user in the automotive industry is Porsche, Porsche offer more than 20 reproduced AM plastic, titanium and aluminium parts for classic cars. AM technology has enabled reproduction in small patches. For new models, Porsche offers a body form bucket seat made by AM technology and they are using AM to manufacture engine pistons for 911 GT2 RS, the pistons are 10% lighter than their counter forged pistons. The AM pistons also benefit from integrated cooling ducts within the piston crown.

The Swedish supercar manufacturer Koenigsegg is one of first manufacturers to adopt AM technology; Koenigsegg designed and produced the first AM variable geometry turbine housing featuring internal moving vanes and a dual volute system. The vanes are used to adjust the volume of the turbine housing inner volute by switching gas flow between the volutes, reducing lag at low engine RPM and delivers a much smoother torque curve [145].

Koenigsegg produced only 14 of those patented turbine housings, this low volume production makes a perfect case for the use of AM techniques, saving tooling development, manufacturing costs and time. It also guarantees exclusivity to the designed parts [145].

One of the smart AM technique adaptations is the airless tyre prototype developed by the French manufacturer Michelin and General Motors (GM), the tire shown in figure 4-5 is known as Unique Puncture-proof Tire System (Uptis); worldwide there are 200 million tyres scrapped prematurely every year due to punctures [148].

The new design incorporates middle treads with no sidewalls and are completely airless, increases the tire life span significantly and adds protection from hazards like inadequate air pressure. This tyre is made from 100% recyclable micronized rubber powder, which contributes to the future vision of sustainable mobility [148].

Figure 4-5 AM manufacture tyre [148]

The examples highlight some of the different applications that see AM as a game changer, and are considering using AM for component production. Furthermore, in the research, there are some impressive adaptations of AM methods; researchers in the medical field are exploring the possibility of bio fabricating vitro tissues and organs of the human organism using AM tools [149].

4.3 AM Classification

AM is a relatively new technology that can be classified various ways depending on material or method used for bonding the material/layer, the most common classification is one used by American Society for Testing of materials (ASTM) committee F42, and it classifies the AM technologies into seven methods [150]. Those methods are discussed below; general information like materials used, process resolution is highlighted in table 1. The main discussion will focus on high-resolution applications that are mainly involving powder sintering or melting.

Sheet lamination

In this process the bonder; usually glue or ultrasonic welding is used to bond sheet layers, the bonded layers are then trimmed to the designed shape. The process advantages and disadvantages are shown in table 1.

Material Jetting

Material jetting is the process in which the material is jetted layer by layer on a build plate; the process is relatively similar to single layer two-dimensional ink jet. The process resolution is shown in table 1.

Material Extrusion

Material Extrusion is the process in which the material is deposited layer by layer and extruded from a nozzle, this process is also known as fused deposition modelling (FDM) [151]. Common applications that utilise this process are shown in table 1.

Vat Photo Polymerisation

In this process ultraviolet light (UV) is utilised to selectively cure a vat of photopolymer resin, the component is built on a platform which is lowered after each layer. The process advantages, disadvantages and resolution are shown in table 1.

Binder Jetting

Binder jetting is the process in which liquid adhesive is used to glue powder material layer by layer. The excess glue is burned off and then the powder is sintered in a separate oven.

Directed energy deposition

Directed energy deposition (DED) is the process where wire or powder is feed into the heat source usually laser beam, a melt pool is created on the material surface.

AM Technology	principle	Materials	advantage	Disadvantage	Application	Approximate Accuracy	Resolution (elements mm−3)
Binder jetting	A layer of binding solution is jetted on a layer powdered material. This process is repeated until the product is fully formed .	Metals [153] Polymers [154] Ceramics [155] Composites	No support required Inexpensive High speed Large build volume	Poor surface finish Delicate parts produced	Medical models, injection-moulded like prototypes, and full-colour products.	23-30 µm	1900
Material extrusion	Material is heated to a semi-solid state and extruded onto the defined path.	Polymers [156] Composites [157]	Multi-Material printing Multi-colour printing Fully functional parts Inexpensive	Step structured surface Vertical Anisotropy	Biomedical (scaffolds, stents), automotive, aerospace	35-40 µm	46
Direct energy deposition	Principle same as ME but the nozzle has multiple degrees of freedom	Metals [158] Hybrids	Multiple degree of freedom of nozzle Used for repair Higher quality parts	Balance need to be maintained between speed and finish	Automotive, aerospace.	45-50 µm	17
Material jetting	The dispenser drops droplets of the material which solidifies under UV light	Polymers [159] Ceramics [160] Composite [161] Hybrid	Multi-Material printing Smooth surface finish High dimensional accuracy	Support required Limited range of material used	Medical models, injection-moulded like prototypes, and full-colour products.	20-85 µm	15.200
Powder Bed fusion	Here an electron beam or a laser is used to melt and join together the material powder	Metals [162] Ceramics [163] Polymers [164] Composite Hybrid [165,166]	High Speed No support required High Accuracy Relatively inexpensive	Small build size High power consumption Poor surface finish	Biomedical (tissue engineering scaffolds, cartilage repairs) automotive, aerospace	20-35 µm	211

Table 1

4.3.1 Powder bed fusion

In the metal powder bed, fusion (PBF) process the utilised source of energy could be laser or electron beam. Both technologies are similar in the way they operate. The first step is powder spreading and levelling on the platform bed. Thermal energy is used to selectively fuse regions of the powder layer; the energy source traces the geometry on the powder layer on the top surface of the powder bed. The exposed powder absorbs the energy from the beam spot creating a melt pool. The powder particles are fused together after the melt pool solidifies. The platform is then lowered and the cycle is repeated [167, 168]. There are several devices (shown in figure 4-6) enabling the process, including a roller for powder levelling spreading and a hopper (reservoir) supplying fresh powder [169]

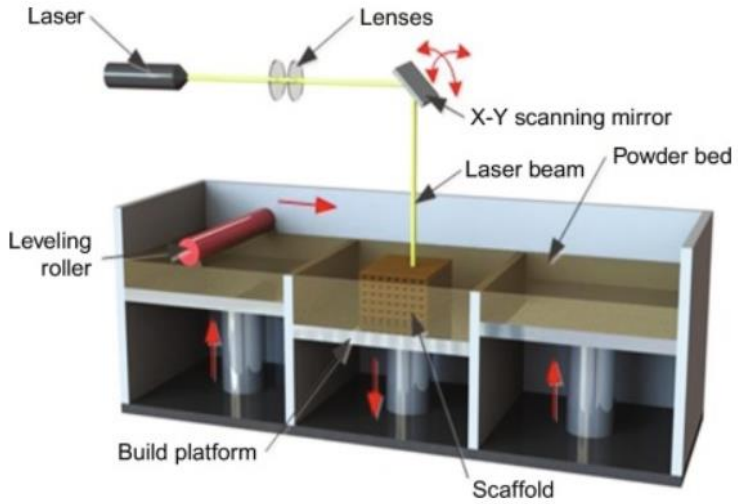

Figure 4-6 SLM PBF process [167]

There are several methods using a PBF process; Selective laser melting (SLM), Electron beam melting (EBM), selective laser sintering (SLS) and direct metal laser sintering (DMLS). Most of these methods fuse the powder by full melting of the material, the only exception are SLS and DMLS in which the powder is heated just below its melting point. The next section will focus on SLM, EBM, DED and binder jetting processes, those methods are the most widely used and all the components tested in this thesis were built using PBF.

Laser PBF

The laser PBF shown in figure 4-6 can be divided into two different processes: laser sintering and laser melting, the sintering process was the first commercially available PBF process for metals, in this process the powder is not melted to the point of liquefaction [168]. On the other hand, the laser melting process heats the powder particles to a temperature above the melting point, this is done in a chamber filled with an inert gas (Argon). The inert gas is used to reduce oxygen content and minimise the possibility of hydrogen pick up [169]. Some of the SLM machines are equipped with 1kW laser modules [170,171]; a galvanometer is used for controlling the beam focus and a lens is utilised for beam movement on the build plate. In the SLM process layer thickness can range from 20-100µm and the powder bed is pre heated to 200°C, each layer is built in two steps, the outer edge of the component and then the internal features.

In the laser PBF process there are several parameters that affect the build quality; like the hatch spacing, energy density, traverse speed and powder morphology are directly linked to build quality and material discontinuity. During the AM process material discontinuity (pores) takes place between layers (elongated pores) [172] or within the layers (gas pores) [173] and are the most difficult to detect.

The optimization of laser power has had a massive impact on pore formation; too higher power will lead to turbulence in the melt pool and excessive evaporation creating gas pores within the bulk material. On the other hand, low laser power will not melt the powder sufficiently creating gas pores as well [170,171]. The Presence of oxygen will lead directly to oxidisation, the oxidisation will lead to a phenomenon called ‘Balling up’ in a high laser power environment, where the powder material forms spheres that exceed the layer thickness [174]. Research carried out by Li et al has shown that

increasing oxygen content in laser-PBF up to 10% resulted in the oxidization of the powder upon solidification [175]. The defects and discontinues found in PBF are highlighted in table 2 [176,177].

Electron beam PBF

Electron Beam behaves completely different from laser, electron beam is faster and much more powerful than the laser beam. Figure 4-7 shows a schematic of an EBM system. The system consists of an electron gun assembly, a lens for beam focusing and deflection coils for beam control. Powder delivery and spreading is done by means of a mechanical system.

Arcam AB in Sweden initially patented the EBM process. The use of electrons as an energy source made the use of vacuum a necessity to provide an oxygen free environment, decreasing the possibility of hydrogen pick up. In EBM, the build volume temperature is kept at 700°C, aiding residual stress reduction; controlling warpage and distortion. The electron beam source operates at 60W, producing energy density beyond 100KW/cm^2. The electromagnetic lens controls the beam focus and deflection coils are used for beam movement. The layer thickness in EBM is 100µm [168], the powder is stored in two hoppers inside the build chamber, the powder is collected and spread from both sides as shown in figure 4-7. Just before the powder melting process the electron beam is used to preheat the powder, this preheating process is done at a high scan speed.

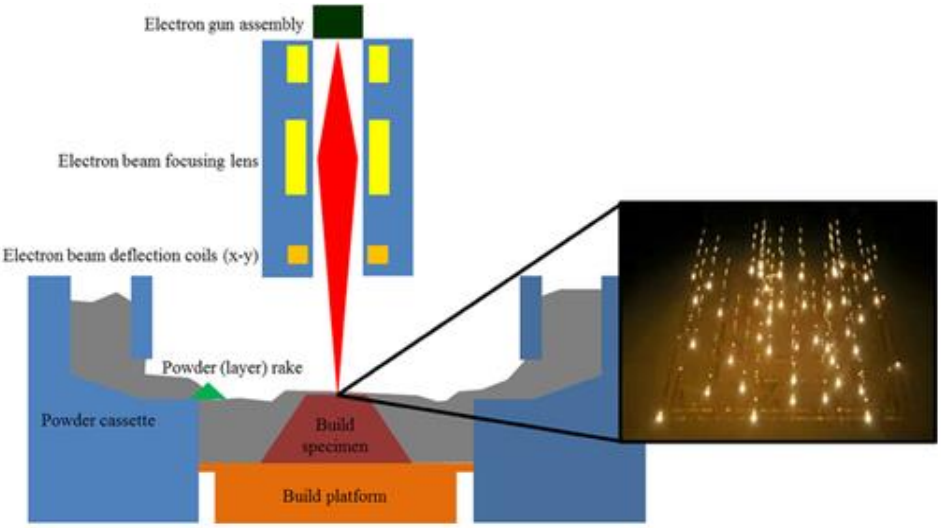

Figure 4-7 EBM PBF system [169]

During the melting phase, the electron beam melts each layer in two steps, the first step melts the part outer edge then the inner features, these two-steps are done for each layer until the designed component is built. In the EBM process, there are mainly three types of defects: Shrinkage pores, spherical pores and lack of fusion defects [177]. Defects examples are shown in table 1. When comparing SLM to EBM, EBM benefits from high temperature and ultra-low oxygen content which contributes to the reduction in residual stress, defect size and quantity. EBM's disadvantages include poor surface finish, material limitation and process complexity.

4.3.2 Direct energy Deposition

The Direct energy deposition (DED) process is not melting powder on a bed, in this process the powder is deposited onto the surface through nozzles fitted to the energy source, figure 4-8 shows a DED system layout, using this method, no separation of the part from the bed is needed. This method is

used widely in polymer 3d printers utilising powder or wires and it has proved to be very effective. Metal DED can produce complex 3D shapes and is used in service repair applications producing components with high strength and ductility [178]. The DED energy source can be an electron beam, laser beam or plasma arc. This process is commonly used in novel hybrid manufacturing processes; in hybrid, manufacturing machines AM and subtractive machining are used to produce finished components. This technology is widely used for adding material and repairing failed or worn components such as worn gears or turbine blade repairs.

Metallic oxidisation in DED systems is reduced by utilising an inert gas (Argon) for laser and arc energy sources, vacuum is used in electron beam systems. DED technology was original developed in 1995 by Sandia National Labs and became commercially available through Optomec Design Company [179]. Defects found in powder DED are very similar to those found in PBF but in the case of wire deposition, the defects are mainly keyhole or shrinkage defects, lack of fusion defects are not found in wire deposition due to powder absence.

There are several advantages of DED, the process can produce large parts, has a fast build rate due to low resolution, the ability of alloy customisation by using multi-materials, materials refill and swap are quite easy keeping wasted material to a minimum. The process disadvantages are the technology is quite expensive compared to other AM methods, components made with DED have lower resolution and poor surface finish, therefore most components require post manufacture surface machining/ processing. DED does not utilise a support structure, the lack of support structures eliminates the possibility of producing overhanging features.

Figure 4-8 DED system [180]

4.3.3 Binder Jetting

Binder jetting (BJ) is one of the fastest developing AM process; mainly due to the process capability in producing big quantities of relatively large components, at low costs compared to PBF. These benefits have attracted the attention of the automotive industry and enhanced the competition in the BJ machine development market.

The technology was initially invented in 1993 during a Massachusetts Institute of Technology (MIT) project, and then later the technology was acquired by Z Corporation before finally bought by the AM giant 3D systems. ExOne developed the first commercial machine in 1996 [181].

The metallic BJ process is illustrated in figure 4-9, the first step in building a component is powder spreading, a blade spreads the first powder layer then a nozzle with binding agent (glue) selectively bonds the powder particles, after each layer is completed the platform moves down and then another layer of powder is spread by the blade.

The process is repeated until the whole component is built. In the next stage the glued component, also known as the green part is left to cure. The part is then removed from the platform and any excess powder is cleaned using pressurised air. The components usually require further post processing, metallic BJ parts are sintered or insinuated with bronze or similar low melting temperature metal. Alternatively, moulds and casting cores can be used in green state. BJ layer height can vary from 50µm for metallic components to 400µm for casting moulds [181].

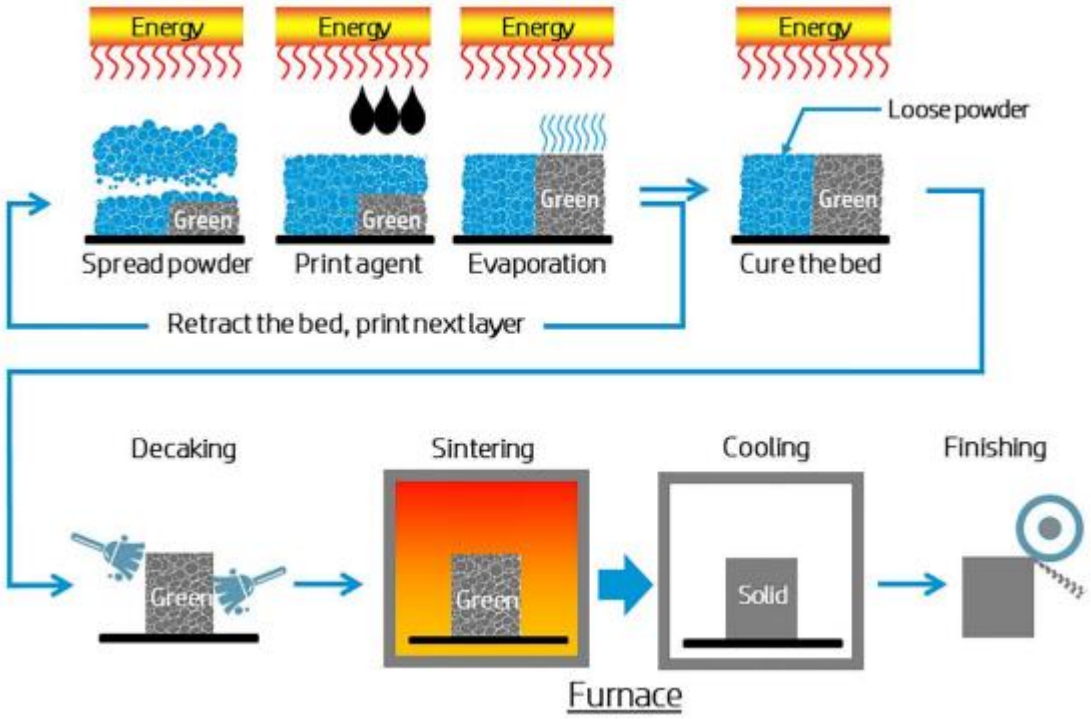

Figure 4-9 Metal jet printing process [182]

The advantages of BJ: that the process is relatively quick, has less material waste compared to other AM methods, the use of binder and infiltrator enables mechanical property optimisation by combining different powder and binder. There are a big variety of materials available for BJ process, the build volume in BJ machines is one of biggest available in any AM process, so the machine can accommodate more components per build, but it is recommended to keep each part within 50mm length to prevent damage during the post processing step. The process is also up to 10X cheaper than SLM/EBM processes [183].

Like any other AM method there are several disadvantages, shrinkage is one of the biggest issues, this is mainly due to the complexity in predicting it as shrinkage can vary greatly across the geometry of a part. There are two stages of shrinkage; the first stage happens in the infiltration process where the components with 25 to 75 mm length shrink between 0.8 to 2%, the second stage of shrinkage takes place in the sintering process where the component can shrink up to 20%. The slicing software

compensates for the shrinkage but components with complex structures are subjected to non-uniform shrinkage.

Figure 4-10 shows a cross sectional view of metal particles with cured binder (green state) highlighted with red arrows, at the green state the printed component is 60% dense, while infiltrated component density is around 90% and sintered is 96% dense [183]. The relatively high percentage of defects affect the mechanical properties, the voids act as stress concentration points, which lead to crack initiation. The components made by BJ technology are weaker than those made by PBF, but it is possible to improve the structural integrity by hot isostatic pressing (HIP) or similar processes. However, this will increase the cost per component and production time. Figure 4-10 shows an example of an M5 screw made by BJ technology, this screw has several internal features; some of these features are as small as 75µm and it is 35% lighter than its solid equivalent.

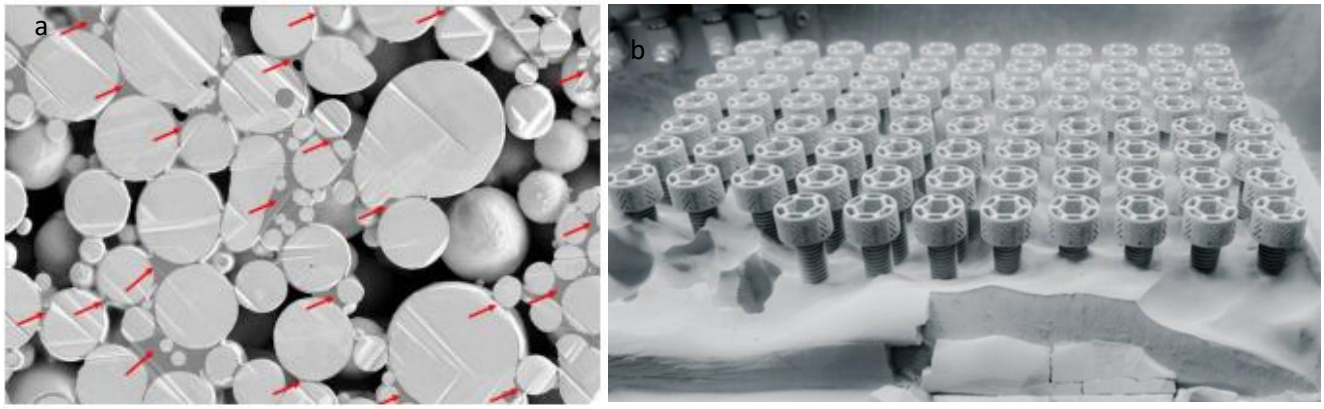

Figure 4-10 a) cross sectional view of powder with cured binder [184] b) M5 screws build with binding jet technology [185]

As it shown in figure 4-10, the bolts are built with no supports, with quite high resolution. In addition, one of the other points to note is powder recyclability and degradation rate. BJ offers 100% powder recyclability, this is mainly due to the lack of melting or sintering in the first stage so the particles shape and structure remains the same. Powder degradation will be discussed later in this chapter.

4.4 AM defects

In AM, there are several types of defects caused by different reasons such as powder morphology, incorrect process parameters/variability and the direction of gas follow in the SLM process [186-188]. Defects include cracking, balling, and lack of fusion, gas pores, shrinkage and elongated pores [189,190].

There is always a concern about the susceptibility of cracking in any molten made metallic alloy; especially in the SLM process, cracking can occur during the process or afterwards in the post processing process. Figure 4-11 shows different type of crack.

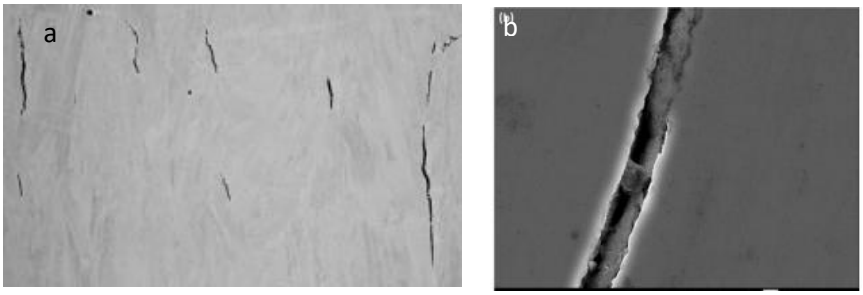

Figure 4-12 (a) Cracking defect in the build direction (b) High magnification image of grain boundary crack [191]

There is a relationship between crack generation and material hardening that occurs when the alloy is heated up to its aging temperature. The repeated heating within the aging region causes material hardening accompanied with ductility reduction and increases crack probability [191]. Hot developed cracks in the building process also known as ductility-dip cracking or liquation cracking. Solidification cracking or 'hot tearing' takes place while the melt pool solidifies in partial solid state [192,193]. In the solidification process, the developed dendrite blocks the melt pool flow in the interdentritic regions [194]. The cracks are then initiated in the liquid region due to the stress caused by solidification. The liquation cracks occurs in the areas distant from the melt pool, which is subjected to a heat shock at a temperature lower than the melt pool temperature. This heat shock creates a thin liquid film on certain grain-boundaries; this thin film could be a potential crack initiation point at the grain-boundary [195,196]. Finally, strain-age cracking occurs at the post processing stage or after the solidification stage, the aging process increases the material strength but reduces ductility and causes strain on the material that exceeds the ductility limits creating crack initiation points, those cracks size can be as small as 20µm up to several millimetres [197,199].

4.4.1 Balling

Balling is another phenomenon that can occur in Laser PBF; it exists on the surface of the part as small blubs or continuous lines. Figure 4- 13 shows the balling phenomenon, figure 4-13 a) shows the balling due to a slight increase in oxygen content. Figure 4-13 b) shows the balling created by a large increase in oxygen content. While figure 4-13 c) shows the balling caused by layer thickness increases and finally figure 4-13 d) and E) show balling caused by laser speed and power.

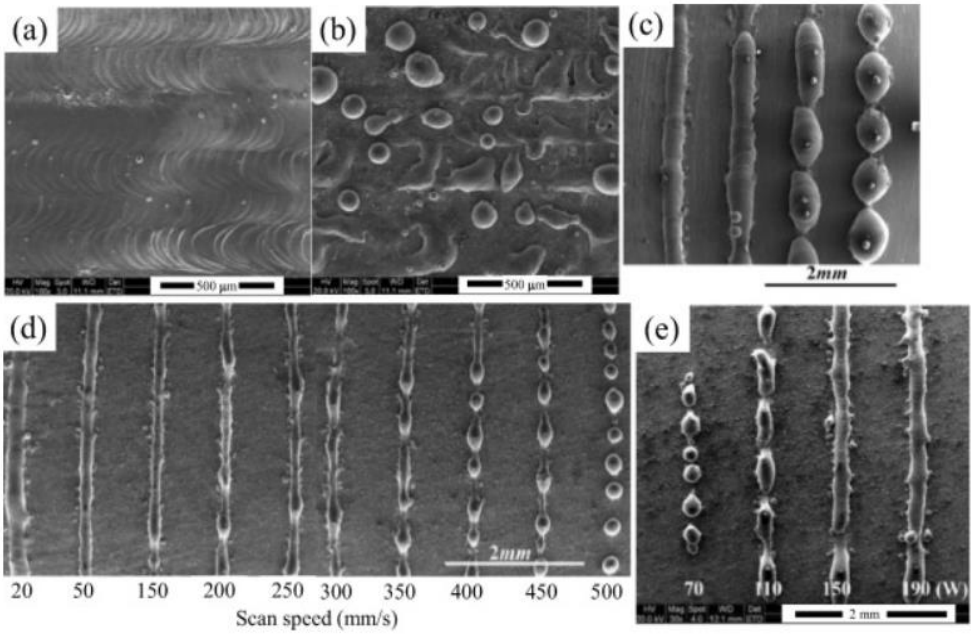

Figure 4-13 balling defect [200]

Increasing laser speed or the quick movement of the energy source leads to insufficient energy supply for melting the powder creating continues metal blubs; similarly, low power will cause the same issue. The Balling phenomenon is often related to poor process parameters [200].

4.4.2 Lack of fusion

Lack of fusion (shown in figure 4-14) is one of the common defects found in the AM process and is mainly caused by incorrectly selected process parameters, leading to insufficient melt pool

penetration to the lower layers or the substrate [201,202]. Lack of fusion defects can be hollow with unfused powder or semi-fused powder. The lack of fusion compromises the structural integrity of AM components causing unexpected premature failure.

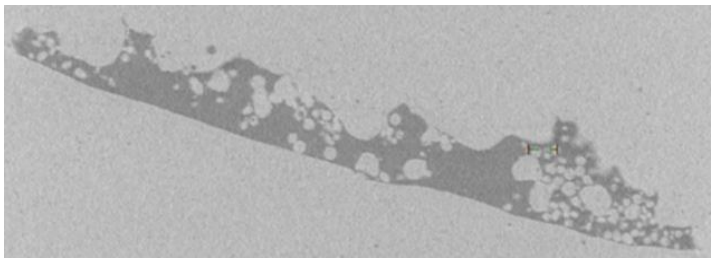

Figure 4-14 Lack of fusion defect [10]

The ratio of the melt pool depth to the layer thickness is known as lack of fusion index (LF), to ensure minimum presence of lack of fusion defects the melt pool must adequately penetrate the preceding layers [203]. Moreover, the ratio of laser power to laser scanning speed is directly related to the melt pool depth, where rapid beam scanning decreases the melt pool depth and increases the probability of lack of fusion defect development. On the contrary, porosity can be reduced by increasing the melt pool size pool depth penetration [204].

4.4.3 Gas pores

Using high power in AM processes can potentially change from the conventional conduction mode to a keyhole mode [205]. In the keyhole mode, the laser beam is powerful enough to cause metal powder evaporation and plasma creation. The evaporation develops vapour cavities and increases laser absorption causing the laser beam to penetrate deeper than the conducting mode. The laser beam collapses the vapour cavity, creating voids [206,207]. Those pores are spherical in shape like those shown in figure 4-15 (a).

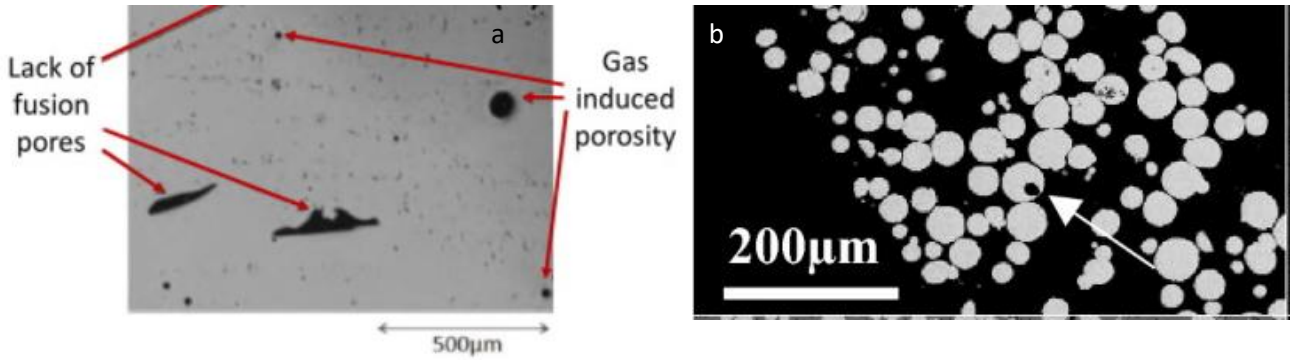

Figure 4-16 a) Gas induced defects [208] b) Gas pore on the metal powder [209]

Another cause of the gas pores is the gas trapped in the powder particles during the atomisation process [209,210], the trapped gas in the powder produces microscopic spherical gas defects similar to those shown on figure 4-16 (a). Finally, gas pores can be formed due to trapped shielding gas in the melt pool.

4.4.4 Shrinkage pores

Shrinkage pores are typical type of elongated pores that are often situated in the interlayer area. Those micro structural pores are created by the thermal residual stress [211], after the material is melted the top layer shrinks due to thermal contraction and any defects present on the previous layer will produce an elongated pore [212].

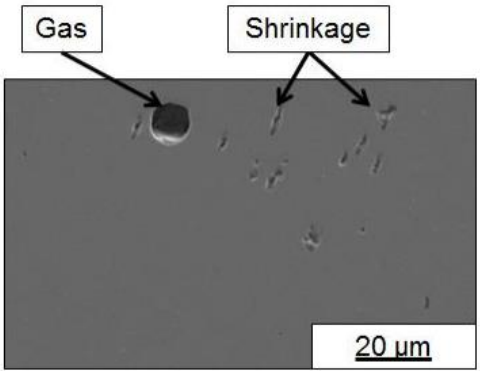

Figure 4-17 Shrinkage and gas pores in Inconel 718 made by EBM [213]

In EBM, shrinkage pores align in the centre of the melt pool, as this is the final solidification region; this type of defect is usually found just before or after the beam turning point. The beam speed increases when it comes out of the edge resulting in melt pool instability due to inconsistent power – speed mixture [213].

4.5 PBF Powder morphology

Powder specifications can affect the AM process in many different aspects like process costs, component requirement and overall performance. Lack of understanding of powder mechanics and the AM system can produce non-cost-effective components with undesirable characteristics. The powder characteristics include material and surface composition, flow and spreadability, shape (sphericity) and powder size distribution (PSD) [213]. ASTM F3049-14 "Standard guide for characterising properties of metal powders used for additive manufacturing "is standardising the process of powder characterisation for metal AM. The guidelines state that powder material composition specifies the thermodynamic behaviour of liquidus and solidus curves, and traces specific elements like carbon, sulphur, boron and oxygen [214,215].

Powder is commonly produced through the atomisation process [216-218], the process affects the powder shape, size, mean particle size and surface features. Atomisation produces the powder particles by melting the material then droplets disintegrates and freeze to produce the final particles [219]. There are three powder atomisation techniques; plasma atomization (PA), gas atomization (GA) and water atomisation (WA). The PA and GA techniques produces spherical morphology particles, alternatively the WA produces particles with irregular morphology. Powder particle morphology is directly affecting the apparent component density, figure 4-18 a) shows the different particle shapes and different surface features.

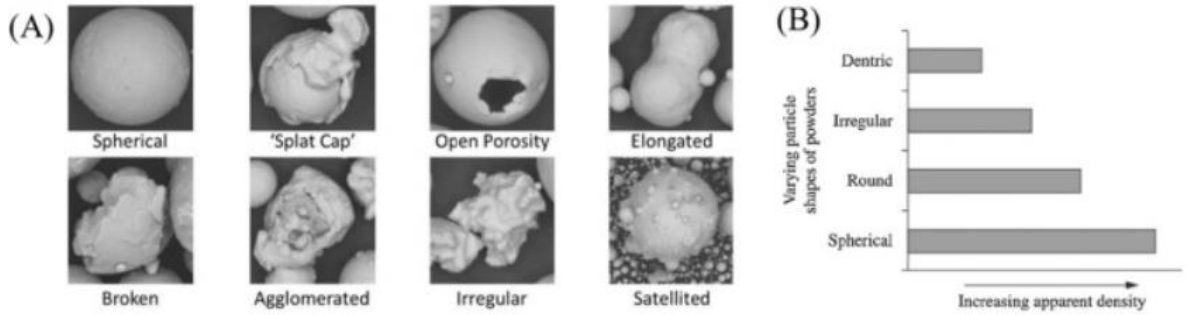

Figure 4-18 a) powder particles with different shapes and surface features relation between the apparent density and powder shape [219]

Figure 4-18 b) shows the relation between the apparent density and powder shape, the spherical shaped particles produce the densest materials, and irregular shaped particles result in a dramatic decline in component density, mainly when particle size ranges between 15 to 45 µm [219]. Spherical powder particles are preferred in PBF applications due their higher density packing. Powder size distribution affects the packaging, flowability and layer thickness, it can be measured by electron microscope or XCT [220].

It is always recommended, in both PBF and DED processes to use powder particles with good surface finish and uniform size distribution, which is usually inspected by SEM analysis focus. The powder shape and size distribution play an essential rule in attaining competitive structural integrity [221]. The atomisation process could result in the development of internal powder particle porosity, like what is shown in figure 4-19 (a). These internal particles can create gas pores in the final component. Plasma rotating electrode process (PREP) is another powder producing method; a plasma arc that melts the material in a rod form rotates rapidly inside a chamber. The centrifugal force discharges the molten metal that solidifies to spherical shaped particles.

Powder produced with PREP tends to have the highest sphericity and least amount of satellite particles [222,223]. Sames et.al compared powder produced from GA and PREP; and it was found that PREP powder produced final components with no gas pores 213. Powder internal porosity is dependent on the production method; Powder manufactured with PREP (shown figure 4-19 (b)) has no trapped gas, compared to those produced with GA technology

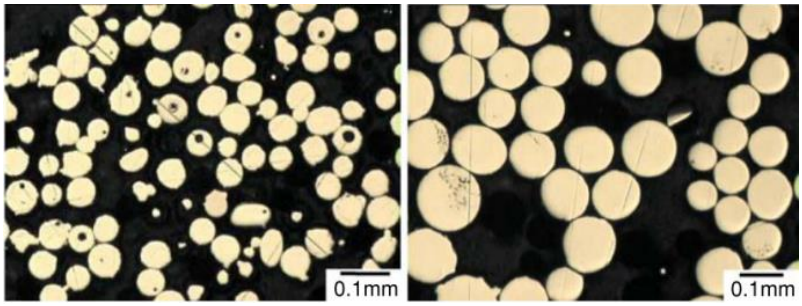

Figure 4-19 a) GA powder (b) PREP powder [223]

Moreover, components made with PREP powder proved to have superior fatigue life when compared to similar components made with GA powder [213]. However, powder made with PREP are expensive compared to GA; due to cost constraints GA powder is the most used powder in PBF technology [224].

PBF powder can be recycled for cost reduction but after each build the powder degrades, this degradation and irregular shape formation (See figure 4-19 (e)) causes internal defects and poor surface finish. The recycled powder can have irregular shape compared to virgin powder and the particles are larger, the increase in size affects powder flowability [225,226], and causes incomplete melting [227]. Gunther et al. investigated the impact of spatter developed in the material melting process, the author confirmed that the spatter particles contain high oxygen content and introduce coarse size distribution, also the particle presence accelerates powder degradation [226].

Ahmed et.al studied the powder recycling impact on 17-4 SS tensile specimens made by an EOS M290 SLM machine; the author compared virgin powder to six- and ten-times recycled powder [228]. The results from this experiment (figure 4-20) confirmed the increase in the irregular powder particles presence after each build. Figure 4-20 shows the SEM image of the powder, where figure 4-20 (a) shows virgin powder with a perfectly spherical shape, figure (b) shows the powder after 1 print; the presence of some satellite particles can be noted. Figure 4-20 (c) shows the powder after 6 prints; the irregular particles are clearly visible, 4-(d) shows the powder after 10 prints with large irregular

particles highlighted in the red box. SLM powder particle sizes range between 15-45µm, the particles highlighted in figure 4-20 (d) has a calculated length of 80µm. The presence of those large irregular particles causes irregular powder compaction, decreasing flowability and increasing defects in the component [228,229]. When comparing virgin powder particles to the particles obtained after 10 prints, it was noted that particle size distribution increased by 3%, this change in size distribution would cause uneven heat distribution during energy deposition; this will introduce lack fusion in the printed components [230, 231].

Powder particle sphericity is another aspect that is affected by recyclability, the presence of irregular shapes reduces flowability; a crucial parameter for maintaining the printed components quality. The results obtain from the experiment found that after print 10 the sphericity is reduced by 34% compared to virgin powder. The reduced sphericity combined with an increase of the irregular particles compromises the powder flow properties and introduces porosity leading to early mechanical failure [228].

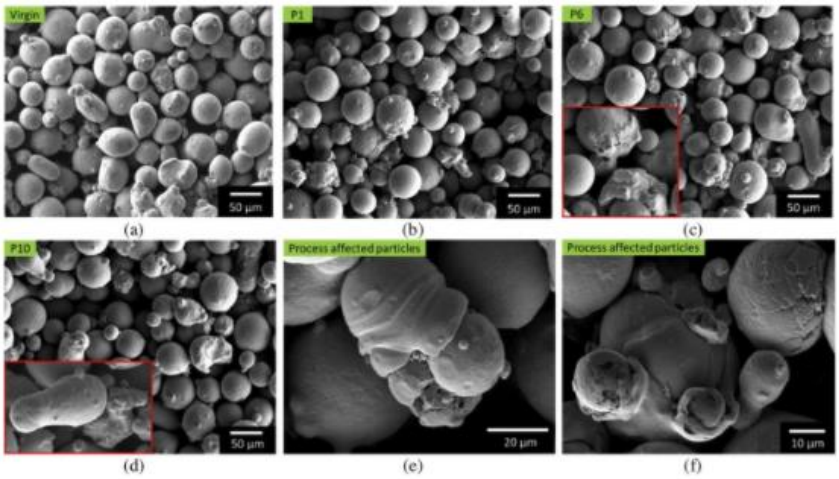

Figure 4-20 SEM images (a) Virgin powder (B) After 1 print (c) after print 6 (d) after print 10 (e & f) [228]

The results also confirmed that the largest pore size increased by 50% after print 10, when comparing virgin powder to print six the largest pore size increased by 4%. Excessive powder recycling increases large particle presence and changes the overall powder size distribution and increase defects in the component [230]. In order to fully melt large particles high energy is required; on the other hand, smaller particles require lower energy levels. In the SLM process, virgin powder ranges from 15-45µm, the size distribution is consistent but after recycling some particles can be as large as 80µm, so it is important to detect these changes and tune the process parameters accordingly to reduce defect development.

Powder in the PBF process is prone to contamination, this can be external or process related. External contamination also known as cross contamination is the presence of different materials that are not present in the specified chemical composition. This is mainly due to either powder manufacturer error or machine operator error in the powder changeover process. Powder contamination is one of the defects formations causes in 3D printed components, which result in mechanical failure. Powder contamination can be categorised into three broad types: carbon rich, metallic and ceramic [231]. Carbon rich contamination is usually caused by environmental causes, metallic contamination (shown in figure 4-21 (a)) can be cross contamination of individual particles from other metallic powder alloys picked up during the atomisation process. The generation of ceramic contamination usually takes place by micro spalling of refractory insulation of the atomisation device [232]. Powder contamination

can compromise the mechanical properties of the AM printed component [232-234]. The contamination will create a lack of fusion due to the difference in thermal expansion characteristics compared to surrounding matrix.

Figure 4-21 (b) shows an SEM image of a fatigue failure due to contamination defects, the image highlights the contamination inclusion in the failure zone. The contaminating particle was not fully melted; the component is made of cobalt chrome which melts at 1395°C whereas the contaminating powder is titanium which melts at 1660 °C, since the printing parameters were optimised for printing a lower melting point material the titanium did not melt [235]. When the contaminating particles have a higher melting point than the matrix material it will cause brittle un-melted defects, this phenomenon has been observed in many studies [232,235].

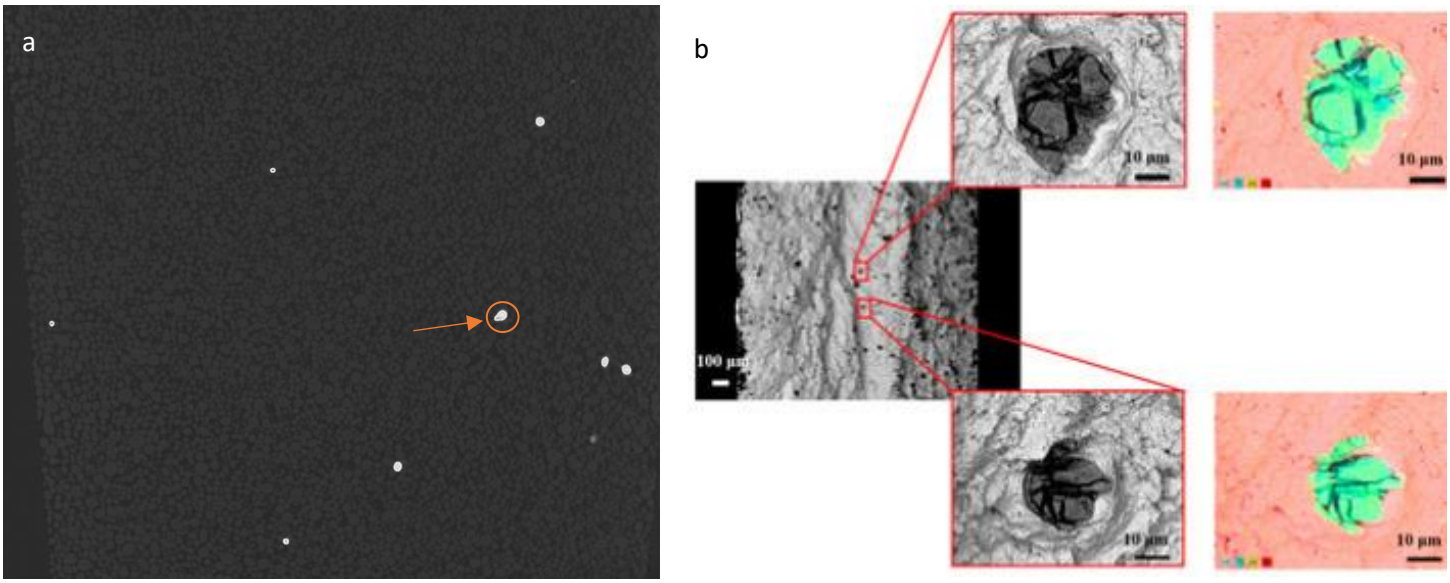

Figure 4-21 (a) XCT Image of aluminium powder with titanium particles contamination (b) SEM image of fracture area[235]

In high-end applications such as medicine or aerospace, it is a crucial requirement for the AM powder to be contamination free. This requirement is often underrated and has proved to be quite difficult to detect. The presence of a small quantity of contamination (less than 1%) most likely will not change the macroscopic and rheological of the powder. The techniques that are capable to characterise the AM powders morphology of the metal powders includes XCT and scanning electron microscopy (SEM) [236-238]. The XCT demonstrated to be a powerful technique in defect detection and powder cross- contamination characterisation [239-242].

4.6 Summary

As mentioned previously in chapter 3, because of the effect of material density on x-ray attenuation, different material will have different grey values. The contrast of low-density materials will be closer to background contrast; for example, in figure 4-21 (a) the background/air is black but the light grey aluminium powder particles are much darker than the titanium particle bright spots; difference of contrast can be used in contamination detection and characterisation.

Industrial needs supported the competition in the technological development of AM techniques with the ability to produce complex structures with no tool path constraints. Repeatability and quality assurance are some of the challenges that high-end applications face in the process of adopting AM. Defect characterisation is one of the essential steps in the qualification of an AM component.

Usually, the qualification process requires quantitative criteria that accept or reject the drawing regardless of the manufacturing technique. PBF technology is commonly used in aerospace and medical applications but currently they require 100% inspection. XCT proved to provide internal and external details about the component because of its ability in imaging the internal features of the scanned object. In the early stage of this research, there has been no published information about using XCT to measure internal micro defects similar to those found in AM components. There is limited information about using artefacts with internal machined features for precise measurement using XCT. As previously mentioned in chapter three the use of XCT is not simple and not fully documented, this is mainly due to the complexity of the scanning process and data analysis techniques. In order to obtain high quality scans, the operator must understand the relationship between the data requirements, machine capabilities and data handling. Another problem with XCT is lack of traceability, so usually the results must be verified with a conventional metrology system. Focus variation is one of the surface metrology systems that can be used for verification.

4.6.1 XCT Artefacts

In this section, the development of porosity characterisation artefact methodology is explained. In this research, artefacts are used to investigate the capability of XCT systems at detecting AM micro defects. As discussed previously XCT has the potential to characterise internal defects without sectioning or destroying the component, however there are several limitations (discussed in chapter three) in the process ranging from sufficient X-ray beam power to achieve material penetration to data processing. XCT Systems require regular calibration; for metrology measurements it is essential to verify the results. Calibration and verification are usually done by the means of a reference object, which is also known as an artefact. The reference object is helpful in assessing the traceability and uncertainty of the XCT system. Researchers and scientists have designed several artefacts with different materials and dimensions for XCT system assessment. Most of the developed artefacts are for dimensional measurements [243]., utilising spherical shaped objects that are measured by CMM before being scanned with XCT [244]. Carmignato et al. developed an artefact for identifying the errors in length measurement using XCT, A fibre gauge artefact (shown in figure 4- 21 (a)) was used in this experiment, it contains 12 inner and 12 outer cylindrical features; the smallest diameter is 125 µm with cylinders length ranging from 350µm to 700µ [245]. Schmitt et al. developed an aluminium artefact (shown in figure 4-21 (b)) with different sized holes [246], all those artefacts were calibrated with CMM, and mainly used for assessing the impact of different process parameters on results accuracy and uncertainty [247].

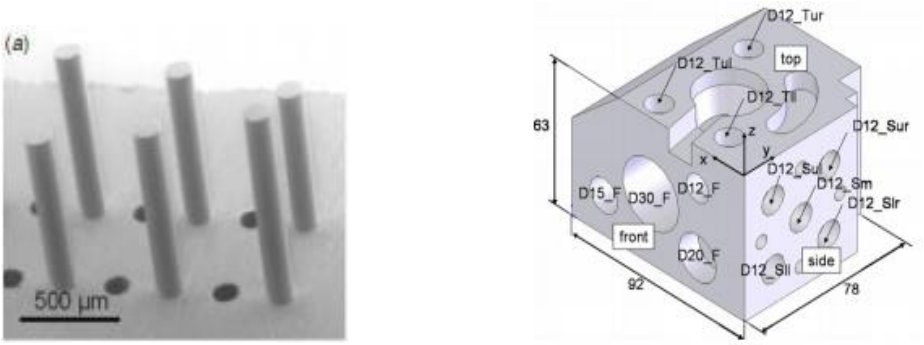

Figure 4-22 a) fibre gauge artefact [245] (b) Aluminium cube artefact [246]

There are a number of artefacts that have been developed for evaluating geometries and surface texture using XCT. However, artefacts that evaluate internal/fully enclosed features are quite limited. When comparing internal to external features there are some differences in terms of scanning

parameters and surface determination, this is mainly due to the background differences between air and scanned material.

4.6.2 XCT Porosity artefacts

Nikishkov et al. designed an artefact (shown in figure 4-22 (a)) with twenty 100µm diameter-drilled holes for quantifying defect dimensions in composite materials; the artefact was made from a carbon/epoxy composite with a 6.95mm long square cross-section. A North Star X5000 XCT machine was used in this experiment and the results were verified by a digital microscope at 50X magnification with 70µm resolution. Four different voxel sizes were compared and the impact of grey value threshold was compared [248].

Hermanek et al. developed an artefact to evaluate the accuracy of defects measurement using XCT. The cylindrical artefact shown in figure 4-22 (b) was made of aluminium with four cylindrical inserts; each insert has eighteen micro milled hemispherical features, the machined calottes range in size from 100µm to 500µm [249].

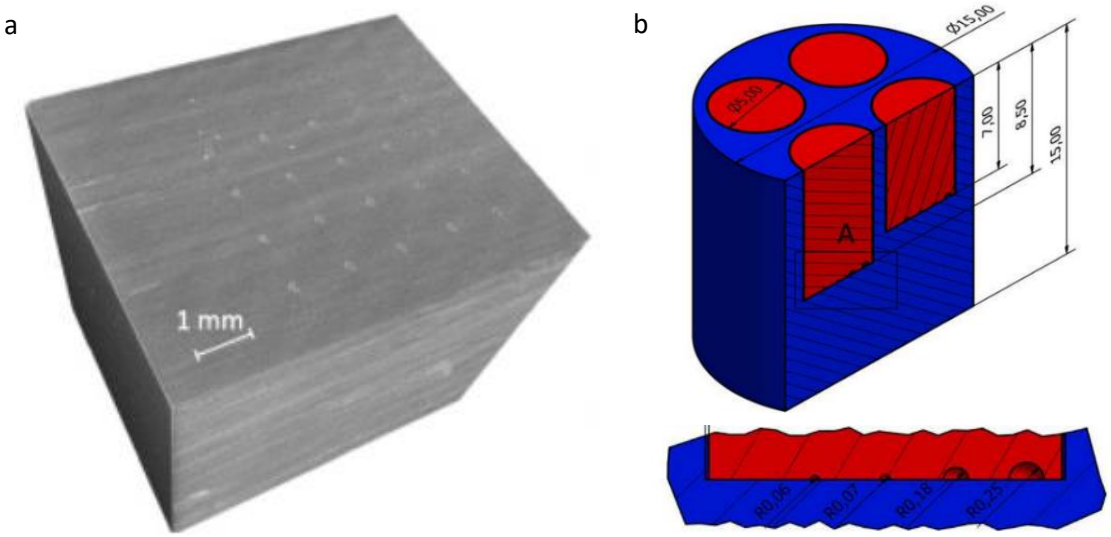

Figure 4-23 (a) Composite artefact with 20 drilled holed [248] Aluminium artefact with 72 micro drilled features [249]

Prior to XCT, defects were characterised using two different optical measurement systems, CMM and a 3D optical profiler [249]. This was limited to hollow defects that were filled with air. In AM PBF components LOF can result in defects with un-fused or semi-fused powder.

Currently XCT is being used as an inspection and quantitative measuring tool for internal and external geometries, but the lack of process traceability requires the use of the reference object/artefact for XCT calibration and result verification.

4.6.3 Early experimentation

An early NDT experiment conducted by the author, scanned 16 X 16mm square shaped titanium bars (shown in figure 4-23 (a)) manufactured using an EBM machine. The square bars were scanned with a 38µm voxel size. The defect analysis carried out after the scan failed to detect the presence of any un-fused powder in the components. In order to confirm the defect analysis results the bar was sectioned, by a ZCC Solid carbide end mills were procured to 3um ground tolerance (AlTiN HM Range). Tools were then held within Haimer Heat Shrink tool holders, balanced to 20k rpm and pressed on a tool setter (calibrated to 3um) to verify runout was within 4-5um and verify overall length. Several iterations of heating and cooling the holder and cleaning of the tool was required to

obtain runout low enough for the machining trials. The tooling hardware (BT40) was then assembled within a Doosan DNM 450II with glass slides. The machine undertook a 30min warming cycle and cut a test block at varying heights. These test cuts were then checked with in process probing with a Renishaw OMP40. No issues found and depths correlated to measurements within 3-4um. The specimen was clocked flat against a machined datum face, and then probed on the top face without removing either the probe or the tooling from the carousel. Material on the surface of the specimen was then machined. It was evident that the process did not detect the presence of some defects. Furthermore, un-fused powder was identified and evidence of semi-fused powder was found while examining the bar under the microscope as shown in figure 4-23 (b).

The detecting of such defects proved to be quite challenging, mainly due to defect size. Figure 4-23 (c) shows an SEM image of virgin Ti6aL4V ELI powder that was used in the EBM process, the powder particles are spherical in shape and uniform with size ranging from 45µm-100µm. The powder particle size variation causes the smaller powder particles to fill the gaps between bigger particles, which makes the cavities smaller than other pores found though the PBF process. The above reasons have driven the need for a reference object/artefact with calibrated internal cavities that can be filled with powder [3]. The defects within the artefact needs to be accessible for verification with conventional non-contact metrology instruments, the reference object can then be used for XCT process optimisation in defect detection [4,5]. There are several points that need to be considered while designing a reference object for XCT result verification; the artefact needs to be representative of the actual component; this will allow understanding of the influence of scanning parameters on the results.

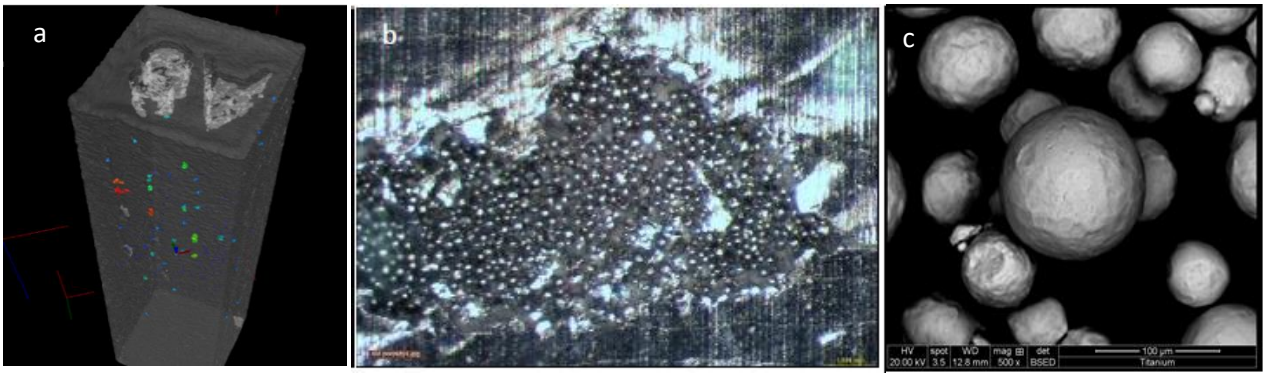

Figure 4-24 a) Defects analysis for titanium AM part (b) Semi fused powder (c) SEM image of virgin Ti6aL4V powder [3]

Prior to the reported work, there had been limited published studies about porosity/defect analysis from XCT reconstructions for AM components. Most of the published work were for machined artefacts and those studies lacked high-resolution scans to visualise individual powder particles.

In order to understand the challenges in detecting un-fused powder, An experiment was carried out by scanning a plastic test tube filled with powder shown in figure 4-24 (a), the powder used was Ti6AL4V with a particle size of 45-100µm; typically employed with Arcam electron beam melting (EBM) machines. A Nikon XTH 225 industrial CT was used to measure the samples and to detect the pores/defect locations and volumes [1]. The main aim of this experiment is to understand the challenges in scanning unfused powder, specially the resolution required to image the air gaps between the powder particles.

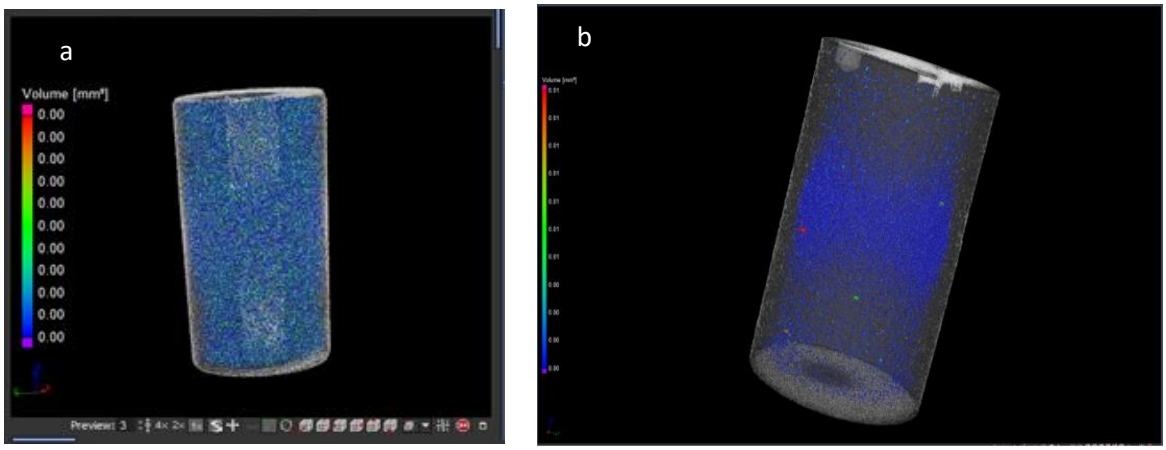

Figure 4-25 a) Mag 15.75 Voxel size 13µ [1] (b) 3D view of the pores with Mag. 10 Voxel size 0.020 [1].

The plastic test tube was scanned with a 13µm voxel size. The acquired data was processed using a surface determination and defect analysis was carried out using VG Studio Max 3.0 (Volume Graphics, Germany) software package. The results of defect analysis show significant noise presence. The next experiment carried out, evaluated defect presence in a Titanium bar made by EBM technology, the results of defect presence; shown in figure 4-24 (b) had excessive noise. The results from both experiments proved that the XCT process is challenging, this is mainly due the presence of several variables in the process, and therefore a reference object is required to optimise the process parameters and to explore XCT limits in defect characterisation.

Chapter 5 XCT Porosity Development method

Statement of Publications Arising from This chapter

The first artefact results were presented at conference Euspen October 2017 “Method for characterizing defects/porosity in additive manufactured components using computed tomography” [2]. The second artefact was presented in ICT 2018 Austria Wels “Development of an artefact to detect unfused powder in additive manufactured components using X-ray CT” [3]. The third artefact was presented at conference EUSPEN 2019 in Spain “The challenges in edge detection and porosity analysis for dissimilar material additive manufactured components” [9]. Finally, the fourth artefact results were published in the International Journal of Automation Technology “The Detection of Unfused Powder in EBM and SLM Additive Manufactured Components” [11]. The author performed all the research and wrote the entire manuscript with guidance and editorial changes from the co-author. It is indicated where text from this publication has been reproduced in this thesis. In order to assess XCT measurement results, a method for result verification is required; usually CMM or focus variation devices are used. While designing internal defect artefacts for XCT capability evaluation, defect size needs to be representative to defects found in the PBF process, the internal defects must be accessible for result verification and the materials must be similar to those used in the actual process.

5.1 Artefacts designs

Two main designs were considered to address defect accessibility for XCT result verification. The main design considerations were, the internal defects must be enclosed, and must be measurable with other device, so the artefact must be easily assembled and dis-assembled. The Artefact must be made with AM process, and it must be made of a common AM printable alloys for example (Ti6AL4V, AlSi10Mg). Another point taken in consideration is duplicating lack of fusion defects, by either filling artificial defects with powder or designing internal features in 3D printed artefact that will be naturally filled with semi-fused and un-fused powder. The PBF AM machines printing tolerance is between 100 – 150 µm, and since the resolution of all the measurement devices used in this research are capable of achieving sub 10µm resolution, the author did not specify tolerance in printed artefacts designs.

Several artefacts were designed to assess the XCT process capability, limitation and the impact of different process parameters in defect analysis results. The artefacts used in the research evolved from a basic AM small titanium rod with random uncontrolled internal defects, to fully 3D printed artefacts with internal geometries. Figure 5-3 shows the artefact design iteration flow chart the first artefact; a simple AM artefact with uncontrolled internal defects was used for establishing the relationship between voxel size and resolution of internal defect analysis in detecting internal defects.

5.1.1 Slip gauge concept

The first concept is a duplication of the slip gauge effect, by designing a component that consists of two halves with both mating surfaces machined to a diamond cut finish when the two surface are rung together there will be no gap between them, similar to that employed for slip gauges. In order to assess this concept two-slip gauges rung together were scanned using XCT with a 15µm voxel size. Figure 5-1 (a) shows a top view of the slip gauges and figure 5-1 (b) shows a 3D model of the slip gauges. The results of this scan were then analysed using Volume Graphics VG studio Max 3.0; the initial inspection for the grey value confirmed that there is no gap between both surfaces. The defect analysis algorithm in VG studio confirmed the initial inspection results and no gap between both halves was detected. This first experiment confirms that the diamond cut finish design will minimise the gap and can be used for simulating internal enclosed defects. The artefact is highlighted in figure 5-3 and it is number 2 in the diagram.

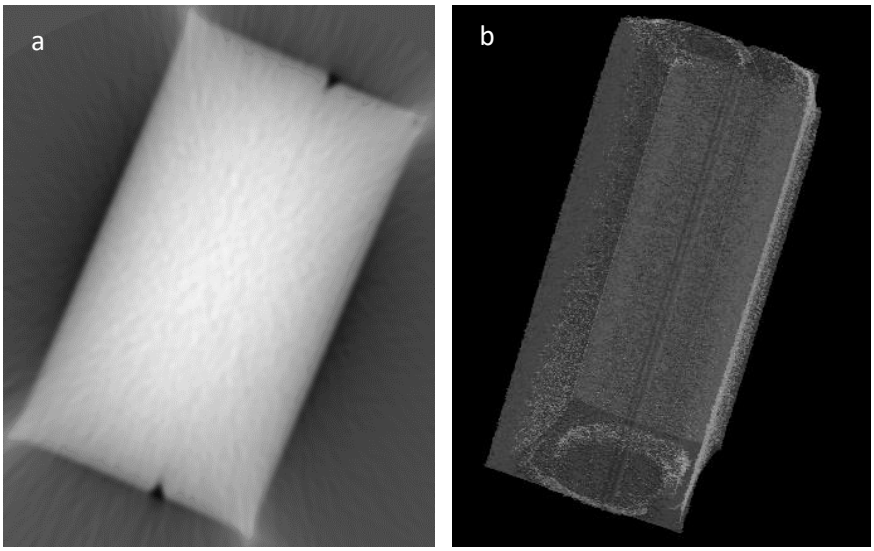

Figure 5-1 (a) XCT image of slip gauges top view (b) XCT 3D image of slip gauge

5.1.2 Interference fit concept

The second design principle is the interference fit, also known as shrink or press fit. This is a type of assembly of mating parts to create a solid joint; usually in a situation where a shaft outer diameter is larger than a mating hole diameter. The amount of interference governs the fitting process; when the interference is small it will usually require pressing with a hydraulic press or tapping with a hammer. In some critical components the interference fit is usually done by freezing to shrink the larger diameter shaft, this type of joint is usually tough and in such cases it has been shown that this approach can improve fatigue life of the assembly.

The author designed an artefact to assess the use of interference fit for defect characterisation in reference objects. This design simulates internal enclosed defects. The artefact was made using SLM PBF technology with Ti6AL4V material, that is commonly used in medical devices, with a 10.5mm outer diameter to achieve high-resolution scans. The artefact 3D model is shown on figure 5-2(a), the artefact was sectioned to two halves and the upper half was machined to have a protruded cylindrical section with 6.020mm outer diameter. The lower half contained a 6mm diameter machined hole.

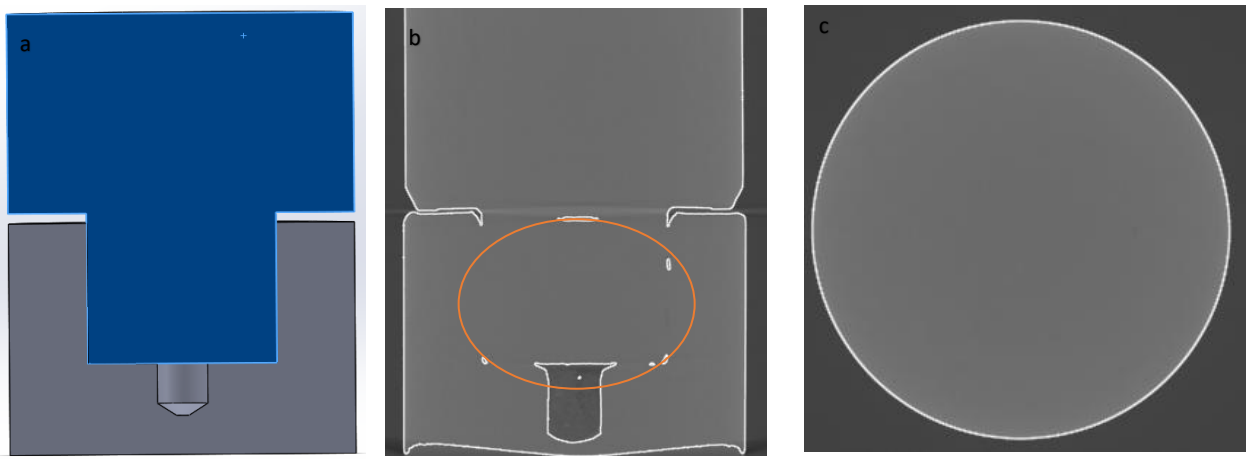

Figure 5-2 (a) interference fit artefact 3D model (b) interference fit artefact front view (c) interference fit artefact top view

Figure 5-2 (b) shows a front view of the interference fit artefact and it is clear there no gap between the two sections at 4µm voxel size, this was also confirmed by the artefact top view in figure 5-2 c). It

was noted that the grey value is uniform across the reference object, which also confirms that the interference fit design could be used for simulating internal enclosed defects.

The second artefact (drilled micro defects artefact) was made of two halves from titanium material using EBM with micro internal drilled holes/defects, shown in number 3 in 5-3 diagram. Both halves surfaces were diamond finished and rung together to enclose the drilled holes, thus creating internal defects/pores. The specific dimensions for the (drilled/holes) defects were selected based on actual pores identified earlier within the AM produced bar described in section 4.6. The principle of ringing the two surfaces together is like that employed for slip gauges. This artefact (discussed in section 5.5) was used in several experiments including a powder characterisation experiment that was published in the NDT journal and is currently used by Volume Graphics as an application example on their website.

5.1.3 Dissimilar material interference fit artefact

The third artefact was made by two different AM processes; SLM and EBM, the artefact design is shown in figure 5-2 a) and it uses the interference fit principle to enclose the drilled holes thus creating internal defects/pores. The artefact discussed in 5.5, was used in several experiments and publication, including identification of the challenges in edge detection and porosity analysis for dissimilar materials in AM components made by 2 different PBF process.

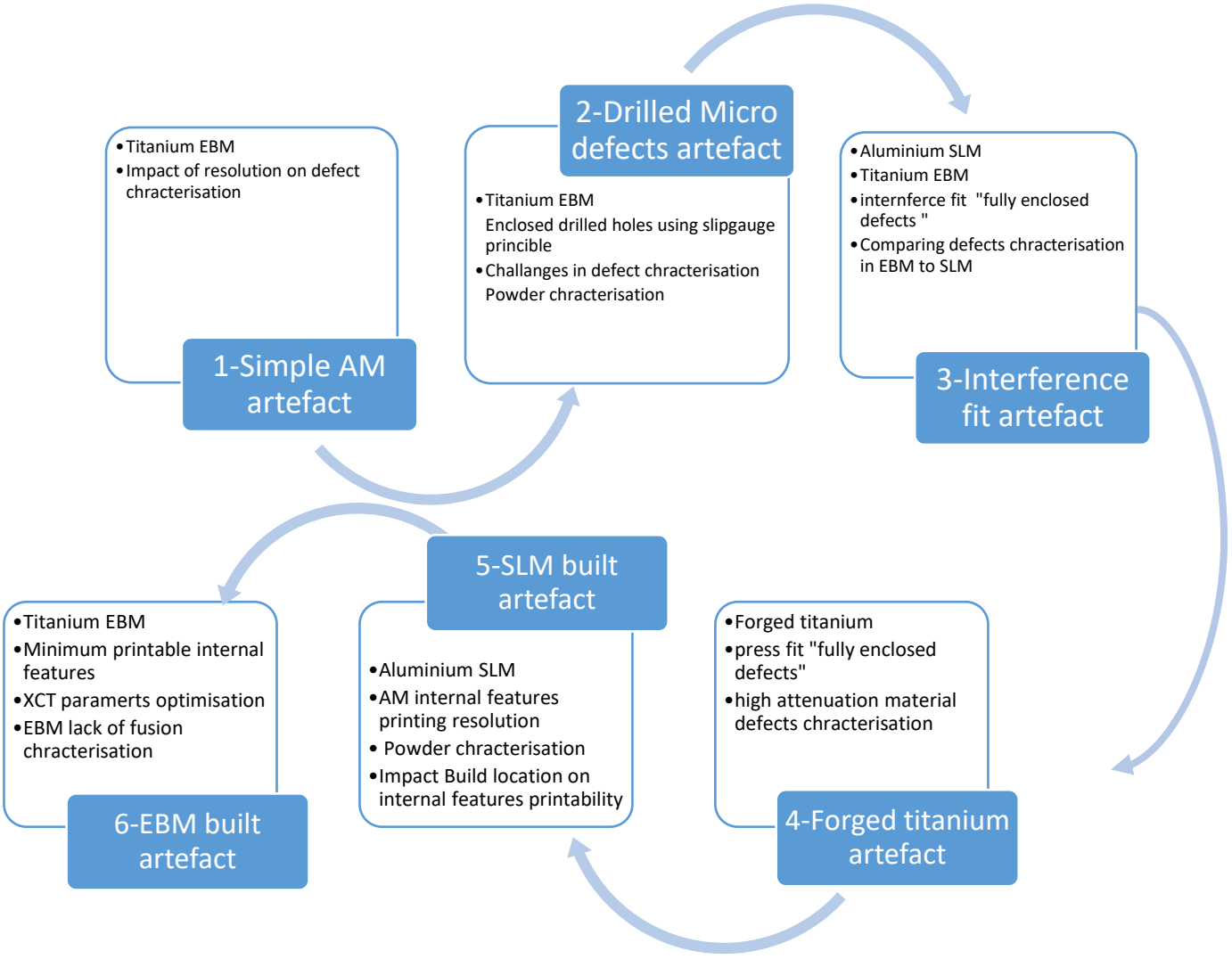

Figure 5-3 Artefact development chart

5.1.4 Forged titanium artefact

The fourth (forged titanium artefact) artefact was a relatively large artefact, 36mm diameter, this was forged titanium, and it contained several internal drilled holes/defects. It used the interference fit principle to enclose the drilled holes thus creating internal defects/pores. The artefact (discussed in section 5.8) was designed to be used for high attenuation material defect characterisation. It is highlighted in figure 5-3 as number 4 in the diagram.

5.1.5 SLM built artefact

The fifth artefact (SLM built artefact) was made using SLM AM technology, with 10.5mm outer diameter, and made from aluminium material; it contained several designed internal features. The artefact was used in several studies including SLM AM internal feature printing resolution and the characterisation of semi-fused powder. This specific material and dimensions was selected to enable a high-resolution scan with the smallest spot size possible. It is highlighted in figure 5-3 as number 5 in the diagram.

5.1.6 EBM built artefact

Finally, the last artefact (EBM built artefact) was made using EBM AM technology with titanium material; it contained several designed internal features. I was 8 mm cube, and it was used in assessing the minimum printable internal features in the EBM process and the lack of fusion characterisation in components made by EBM technology. This artefact is highlighted in figure 5-3 as number 6 in the diagram. The Titanium was selected due to its usage in medical and aerospace application, and author selected this cube dimensions to enable high magnification scan.

5.2 Reference measurement device

There are several devices used for reference measurement, in this work a focus variation system is used to verify the results obtain from the XCT scans. The system used is an Alicona G4 system (shown in figure 5-4 a), which is an optical areal measurement system. The focus variation has been used previously as an AM surface measurement tool [250-252]. The focus variation microscope (Alicona G4) used in the study was implemented due to its ability to characterise small surface defects below the resolution of conventional CMM machines available to the author.

a

b

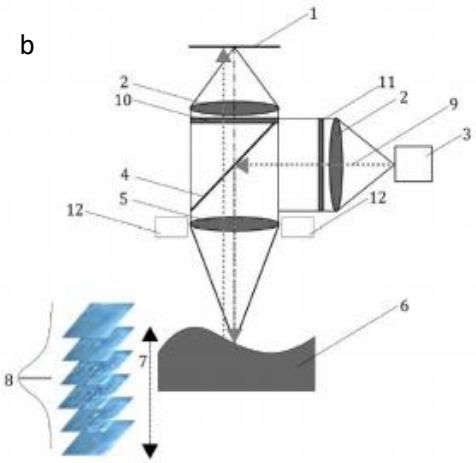

1. array detector
2. lenses
3. white light source
4. beam splitter
5. objective
6. specimen
7. vertical scan
8. focus curve
9. light beam
10. analyser
11. polarizer
12. ring light

Figure 5-4 a) Alicona G4 Focus variation measurement device b) focus variation principle diagram [253]

Figure 5-4 b) shows a schematic illustration of a focus variation system, this system combines the narrow depth of the field optical elements with vertical scanning of the optics. The method obtains the surface features dimensional information and can also be used to measure hole diameter and

depth. The magnification of the focus variation system ranges from X2.5 and X100 [253], the magnification selection is governed by the resolution required for the specific sample. The focus variation system lens has a field of view with narrow depth, so a specific area in the measured component is in focus with sharp image. The Z-axis stage is motorised to enable focusing and defocusing of the image, the focus plane is situated just underneath the component. In the focus variation, process the image is obtained then the stage is lowered by a known distance, which is controlled by the system resolution and lens, then another image is obtained. The procedure is repeated until the highest point of the component is in focus. This guarantees a precise linkage between Z-axis and every surface lateral measurement. Throughout this research, the Alicona G4 focus variation system is used for result verification and to compare the XCT measurements to a conventional metrology measurement system. The focus variation microscope was used by the author in his research, due to its ability to characterise small surface defects below the resolution of conventional CMM machines available to the author. The lateral resolution of the FV approach is 1um, while the metrology XCT lowest achievable resolution is 2µm, so the Alicona can be used to reference the XCT measurements. Consequently verifying XCT results using the focus variation system is an essential step in confirming XCT results, leading to XCT method standardisation for industrial adaptation.

5.3 Simple resolution artefact

The first artefact for defects characterisation was titanium, made by an Arcam Q10 EBM PBF machine. The artefact was simple with uncontrolled AM process generated internal defects. This artefact was mainly used for identifying the impact of voxel size on internal defect detectability. The artefact shown in figure 5-4 (a) was a round bar with 11.8mm diameter and 25mm length, for accurate defect location identification, three holes with different depths were drilled in the top and bottom of the artefact. The artefact was scanned using a Nikon XTH225 industrial CT and to reduce the process variability all scanning parameters such as X-ray filter thickness, material, filament current and acceleration voltage are kept constant.

Data processing and defect analysis was carried out using VG studio Max 3.0 (Volume Graphics, Germany) software package. The only varied parameter was the magnification; the magnifications used were 2.5, 5, 10 and 15. The largest pore location within the artefact was used as a marker and this pore diameter and volume was compared for each magnification; the defect volume ratio was also compared between the different levels of magnification. The results were verified by sectioning the component and measuring the largest pore dimensions. The scanning parameters are shown in table 5-1.

Filter	**2mm Copper**
Exposure	**500 ms**
Filament current	**180 kV**
Acceleration voltage	**150 uA**

Table 1 XCT scanning parameters

The parameters and data processing were kept constant throughout the experiment. The Grey value threshold used was ISO 50% for all the scans. This study was focusing on identifying the best practice for choosing the inspection parameters and the impact of magnification on defect characterisation [3].

5.3.1Defect characterisation

Figure 5-5(a) shows a 3D view of the defect analysis results for magnification 2.5, by using the spatial resolution (equation 4 in section 3.2 of the literature review) this equates to a 80µm voxel size. The image is clear and the defect analysis results show only six defects, the largest defect is highlighted in figure 5-5(a).;at this low resolution the defect diameter was found to be 0.59mm. Figure 5-5(b) shows a 3D view of the defect analysis results for magnification 5, which equates s to a 38µm voxel size.

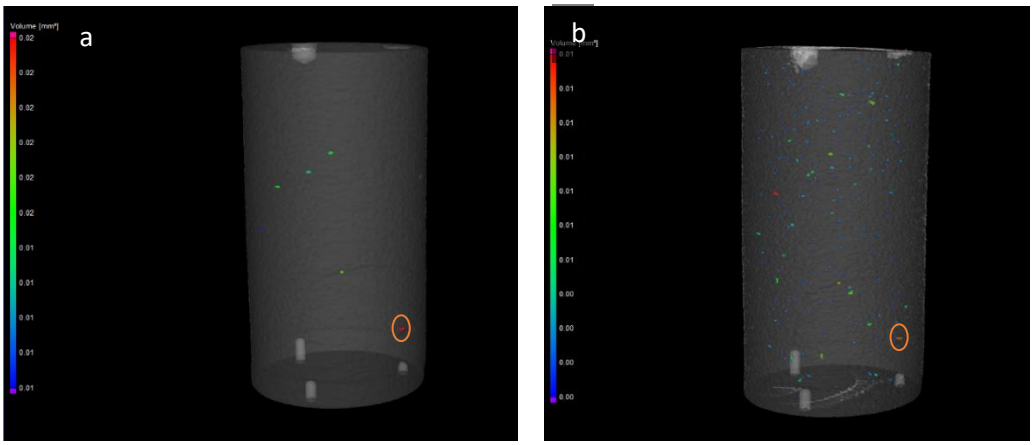

Figure 5-5(a) 3D view of the pores detected at 80µm voxel size (b) 3D view of the pores found at 38µm voxel size

The image is still clear but the results show 221 defects and largest defect identified at magnification 2.5 is no longer the largest defect; there are two defects larger than this defect. Furthermore, the defect diameter was found to be 0.50mm, this is 90µm less than that found in the lower resolution scan. Figure 5-6 (a) shows the defect analysis results for magnification 10 that equates to a 20µm voxel size. Figure 5-6(b) shows the results for magnification 15, which equates to a 13µm voxel size.

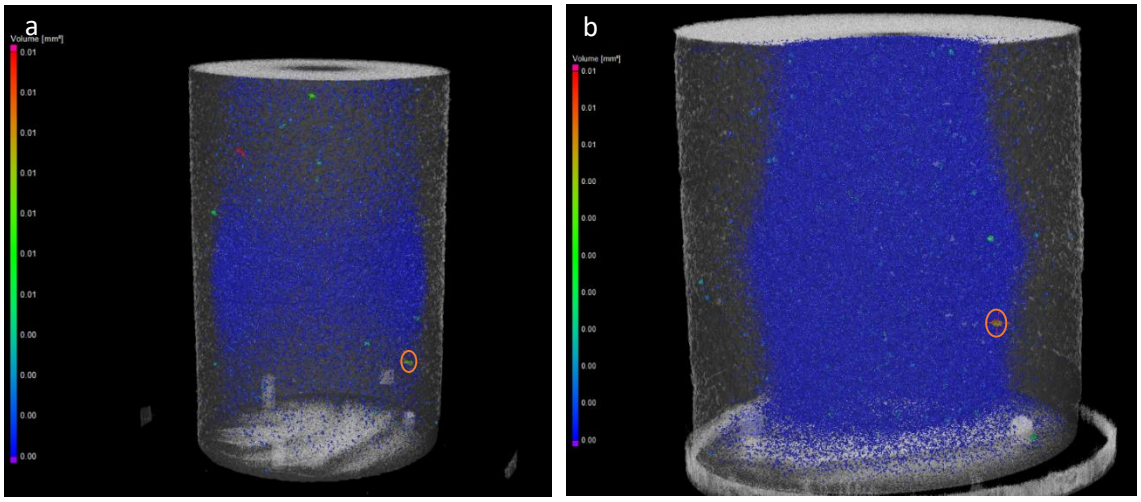

Figure 5-6(a) 3D view of the pores detected at 20µm voxel size (b) 3D view of the pores found at 13µm voxel size

It is clear from figure 5-6 that in the higher magnification scans there is excessive noise present, the same defects highlighted in the lower magnifications are still present in the high magnification scans, however the diameter of these defects at a 20µm voxel size were 0.59mm, and 0.45mm for the 13µm voxel size scan. These results had driven the need in understanding the impact of scan parameters on

high-resolution scans, whether the same scan parameters can be used for the object in high and low magnification scans.

5.3.2Defect volume

Data analysis provides information about defect volume, position and probability. The probability will be discussed in detail later in this chapter in section 5.9. The largest defect detected in the 80µm voxel size scan is used for the volume comparison. Figure 5-7 shows the different magnification volume comparison; figure 5-7(a) is for 80µm voxel size, (b) is for 39µm voxel size, (c) for 20µm voxel size and (d) for 13µm voxel size.

The results suggest that the volume of the highlighted defect is decreasing as the resolution increases. The volume of this defect at 80µm voxel size is 0.024mm^3, at 38µm voxel size it is 0.011mm^3, while at the high-resolution scans (20µm and 13µm) the defect volume is 0.009mm^3 and 0.005mm^3 respectively.

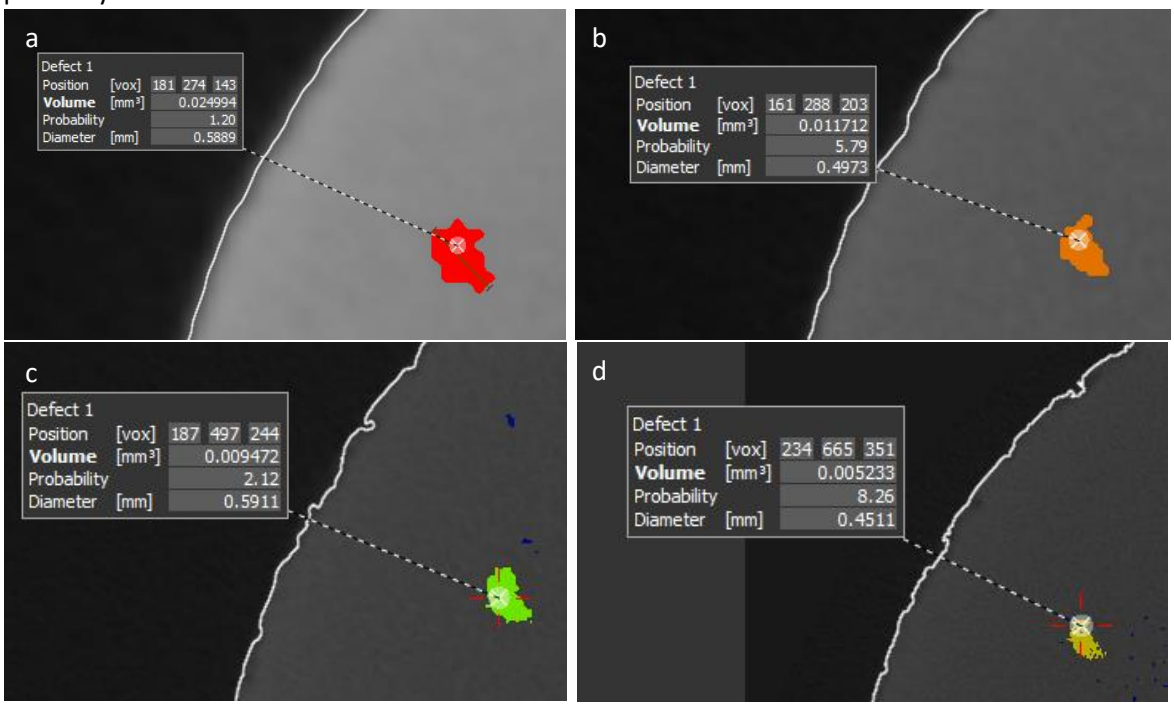

Figure 5-7 Defect 1 volume (a) at 80µm voxel size (b) 39µm voxel size (c) 20µm voxel size (d) 13µm voxel size

5.3.3Defect percentage (component density)

Components built by AM technologies are usually assessed by overall density, for example, components built with binding jet technology are expected to be between 93 to 96 % dense. While those built with SLM or EBM technologies are expected to be over 98% dense. Data obtained from the XCT scans was processed to produce overall defect volume within the scanned object. The results of the overall defects volume ratio are shown in figure 5-8, the graph shows that at low magnification (80µm Voxel size) the defect's volume ratio is zero (see figure 5-5(a)), thus the sample is fully dense. While the 39µm scan defect volume percentage is 0.03% (see figure 5-5(b)) and for the high magnification scans (20µm and 13µm voxel size) the defect volume ratio is 0.78% and 1.78% respectively.

The graph in figure 5-8 suggests that the defect volume ratio is inversely proportional to the scan voxel size/resolution. It was also noted that when the voxel size is reduced from 20µm to 13µm; the percentage of the defect volume ratio significantly increased mainly due to noise presence.

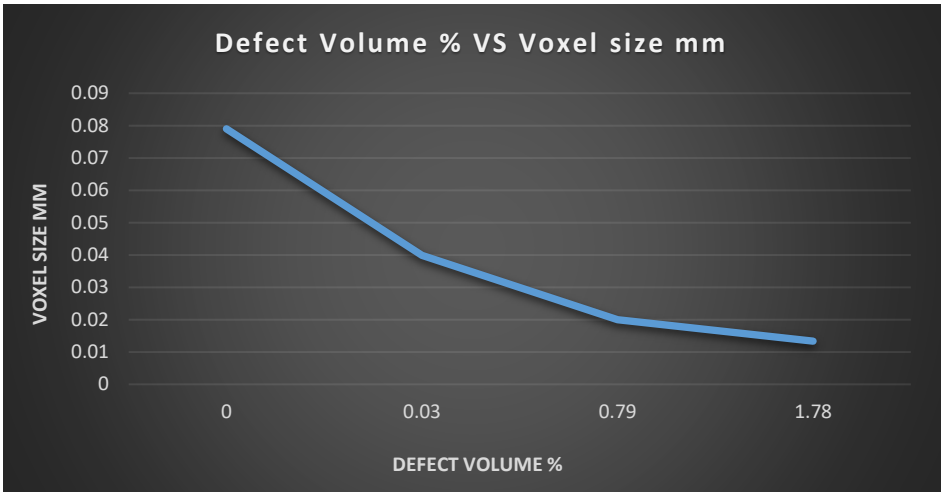

Figure 5-8 Defect volume % VS Voxel size mm

5.3.4 Results verification

To confirm the defect analysis results the artefact was sectioned to verify the largest defect location and dimensions. Sectioning was done using a Doosan DNM 450II with glass slides CNC machine, the sample was not measured after each cut to avoid any misalignment in fixing the sample in the machine. The location of the defect was identified by the analysis software instrument length measurement. The distance from the lower edge of the artefact to the bottom edge of the defect was compared at different magnifications. The results of the location identification are shown in figure 5-9, where Figure 5-9(a) and (b) show the largest defect location for the low magnification scans and Figure 5-9(c) and (d) for the high-resolution scans.

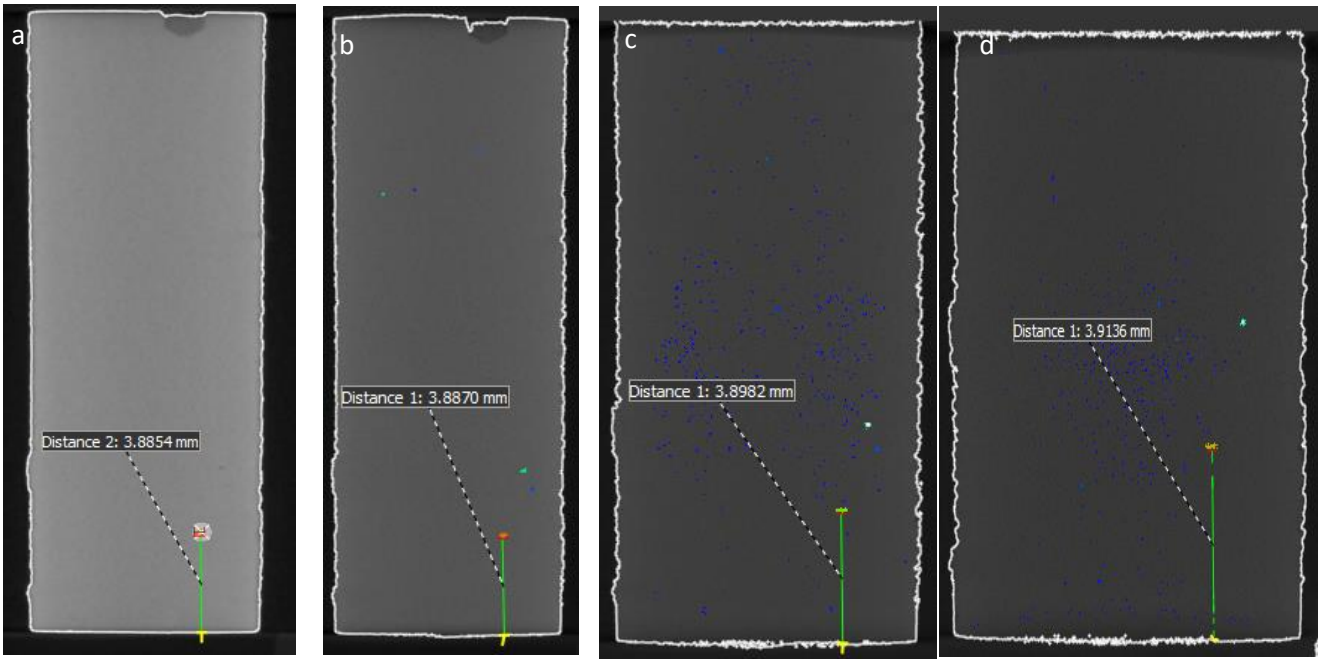

Figure 5-9 defect location (a) at 80µm voxel size (b) 39µm voxel size (c) 20µm voxel size (d) 13µm voxel size

The artefact was then sectioned by a CNC machine; the machine was programmed to detach the bottom 3.5mm of the artefact, then a milling tool was used to machine the artefact in 50µm increments. The defect was exposed after machining 3.96mm from the bottom edge of the component. Figure 5-10 shows a microscopic image of the defect, the device used was a Keyence digital microscope VHX-500F.

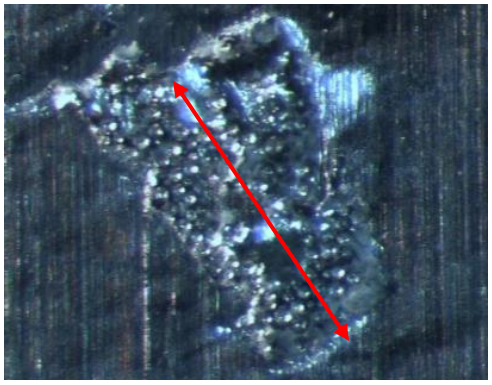

Figure 5-10 lack of fusion defect found in the artefact.

It is clear that the defect is a lack of fusion defect, which is filled with partially fused powder. The defect length (highlighted in figure 5-10) was measured with a digital microscope and it was found to be 0.41mm

The results of this experiment show that as magnification increases so does the number of the detected defects. The highest resolution in this experiment was 13µm voxel size; this is mainly due to the limitation of reference object size, for sub 10µm voxel size resolution the artefact should to be 8mm or less.

The largest measured defect length is 10% smaller than the highest resolution scan. The actual defect location was found differ by 1.2% from the one identified using XCT. The noise presence in the high-resolution scans had a negative impact on the acquired results; also, the high-resolution scans produced large files that required a long time for analysis.

The defect dimension needs to be accessible to enable reference measurement with different measurement devices; depth measurement in lack of fusion defects that are filled with semi-fused powder are not possible. The impact of parallel and perpendicular geometrical measurements in relation to x-ray beam need to be investigated. In this experiment, it was found that there is a relationship between the defect analysis probability threshold and the selected scanning parameters. While scanning the same object, the scanning parameters used for high-resolution scans are not the same to the ones that used for low magnification scans; this was highlighted by the difference in grey value contrast between the different magnifications.

5.4 Drilled defects artefacts

The second artefact was designed to investigate the capability of the XCT methods in detecting gas micro defects and larger powder filled defects, like those found in AM PBF components. The detection of powder-filled defects can be quite challenging due to the difficulty in characterising these types of defect, this is because small powder particles can fill the gap between the larger particles.

The artefact was made from Ti6AL4V material, built by an Arcam Q10 EBM machine with default settings. The artefact shown in figure 5-11 (a) is 6mm diameter and consists of two halves; 9.6mm each. The lower half top face had 50, 100, 500 and 1400µm drilled holes, the lower half top face and upper half bottom face were then polished using a CNC machine.

The designed holes/defects are representative of those found in AM components. In this experiment, the 1400µm hole is defect 1, 500µm hole is defect 2, 100µm hole is defect 3 and 50µm hole is defect 4. The largest defects (1.4mm and 500µm diameter) were filled with EBM Ti6AL4V virgin powder while the 50µm and 100µm defects were left hollow to represent gas pores.

Figure 5-11(b) shows the top face of the lower half with 1.4 mm and 500µm powder filled holes, the 100µm and 50µm drilled holes are highlighted with red circles. Figure 5-11(c) shows the 1.4mm defects filled with powder [3].

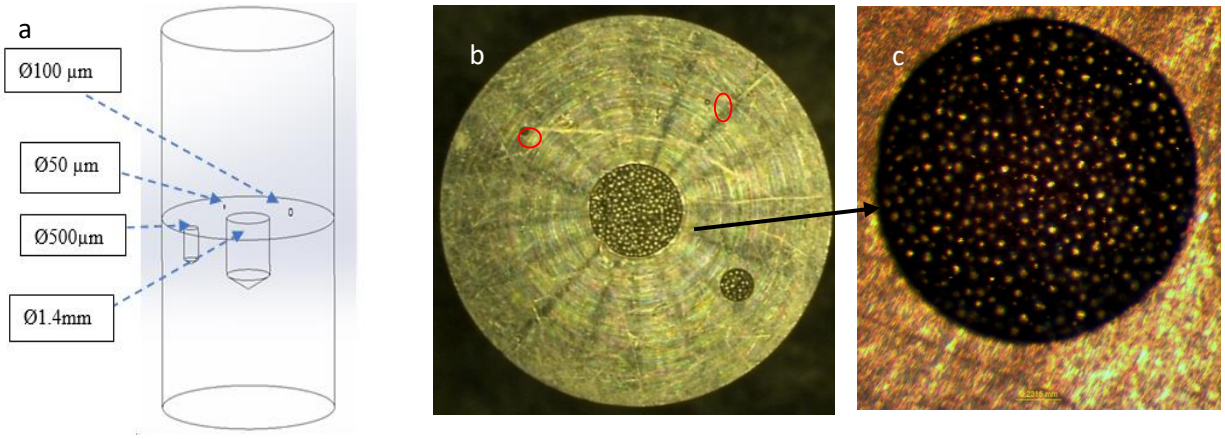

Figure 5-10 5a) artefact 3D model (b) Artefact lower half with holes filled with powder, (c) 1.4mm defect filled with powder [3]

In PBF applications the layer thickness is approximately 40µm, so the 50µm drilled hole will replicate a single layer defect. The 100µm-drilled hole will reproduce a two-layer disruption. The two mating considered as one single part.

The results obtained from the Alicona and XCT results are compared to designed defects dimensions and calculated volume. Table 2 below shows the drilled holes diameter, depth and calculated volume:

Defect	1	2	3	4
Diameter	1.4mm	500µm	100µm	50µm
Depth	2mm	1mm	210µm	100µm
Volume	2.870mm^3	0.193mm^3	0.001mm^3	0.000 mm^3

Table 2 Designed Defects values and calculated volume [3]

5.4.1Alicona defect measurement

The drilled holes in the artefact lower halves were characterised by a focus variation microscope (Alicona G4), each hole diameter and depth were measured 5 times and average values were used. The Alicona was calibrated per the manufacturers' recommendations.

The diameter (shown in figure 5-12(a)) was measured using 6 point best-fit circle. The depth measurement (shown in figure 5-12 (b)) was completed by selecting two points on the top face on both sides of the hole and joining them with a line, the the lowest point of the drilled hole is then selected and linked to the upper line via a horizontal line to obtain the hole depth.

Figure 146 (a) shows the alicona diameter measurement for the largest hole, it was found to be 717.30µm, figure 15-12 (b) shows the depth measurement for the largest hole and it was found it be 2.158mm [3].

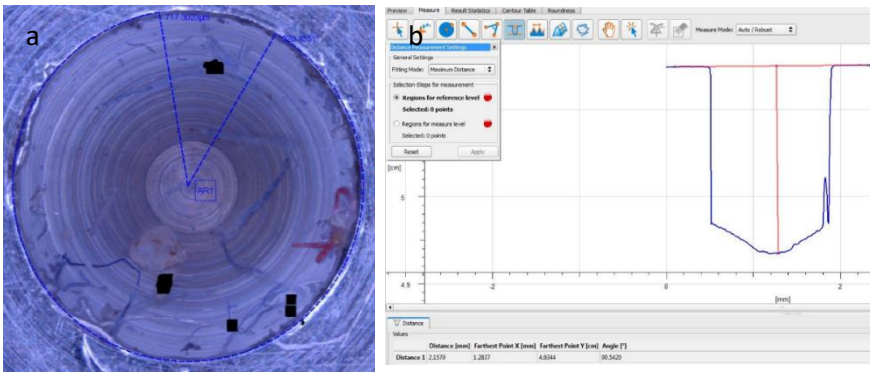

Figure 5-12(a) Alicona value for defect 1 radius (b) Alicona value for defect 1 depth [3]

Table 3 shows the alicona measurement results for diameter, depth and calculated volume. The depth of the 50µm hole was not correctly measured, as the obtained result was 12µm, it was predicted to be 100µm. The result for this hole does not correlate to the values displayed on the CNC machine and the XCT inspection results. The Alicona failure in detecting the depth of the smallest hole is mainly due to the inability of the device in imaging the bottom of the hole for the selected magnification. The alicona measurement results show that the machined holes are larger than the designed dimensions. This difference is due to the machining tolerances during manufacture.

Defect	1	2	3	4
Diameter	1.434mm	526µm	142µm	*86µm*
Depth	2.157mm	1.090mm	280µm	*12µm*
Volume	3.000mm^3	0.215mm^3	0.004mm^3	*NA*

Table 3 Alicona Defects dimensions and calculated volume [3]

5.4.2XCT measurements

The acquired XCT results for the drilled hollow holes are presented in this section. A Nikon 225 XTH XCT was used, the artefact was scanned with a 7.4µm voxel size. CT pro reconstruction software was used for XCT image reconstruction and the data analysis was carried out using Volume Graphics VG Studio Max 3.0.3. The hole depths were measured via a distance measurement tool; identifying the lowest and highest point in the drilled hole. Figure 5-13(b) and 5-13 (b) show the depth measurements for defect 1 and 2, which were 2.120mm and 1.082 respectively. The best-fit circle (shown in figure 5-13 (c) and 5-13(d)) in geometry measurement tools was used for the measurement of the drilled hole, the circle is generated by selecting 6 points on the diameter. Figure 17 (a) and (b) show defect 1 and 2's diameter measurements, defect 1's diameter was 1.426mm and defect 2's diameter was 533µm.

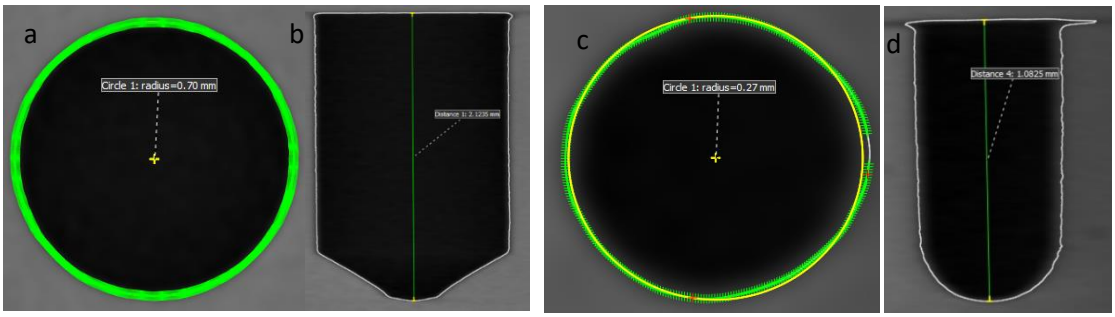

Figure 5-13 a) XCT image for defect 1 with measured radius, b) XCT value for defect 1 depth c) Figure 7 XCT image for defect 2 with measured radius, d) XCT value for defect 2 depth

The geometry measurement tools in the data analysis software are directly influenced by the surface determination accuracy. The XCT scan quality and surface determination accuracy can be assessed by comparing the obtained results to the focus variation results. The XCT diameter measurements have shown that the holes are not perfectly circular; this also was confirmed by the Alicona measurement results. Table 4 shows the results obtained from the XCT scans; the volume of each drilled hole was compared to the volume results obtained from the Alicona.

Defect	1	2	3	4
Diameter	1.426mm	533µm	149µm	82µm
Depth	2.120mm	1.082mm	306µm	71µm
Volume	3.046mm^3	0.220mm^3	0.0052mm^3	0.0008 mm^3
Volume (Alicona)	3.000mm^3	0.215mm^3	0.004mm^3	*0.000 mm^3*

Table 4 Alicona Defects dimensions and calculated volume [3]

The XCT volume results correlates to the Alicona volume results, the only exception is defect 4, which is due to the previously mentioned error in Alicona depth measurement. The XCT results confirmed the capability of the process in measuring internal defect dimensions. The defect diameters are compared in figure 5-14, the designed drilled hole diameters are different than those measured using the Alicona, the largest variation was in the smallest defects (3&4), where the Alicona diameter measurements were 42% and 58% larger than designed for defects 3 and 4 respectively. The slight warpage in the AM part combined by misalignment in the part clamping in the CNC machine could contribute to the defect diameter difference.

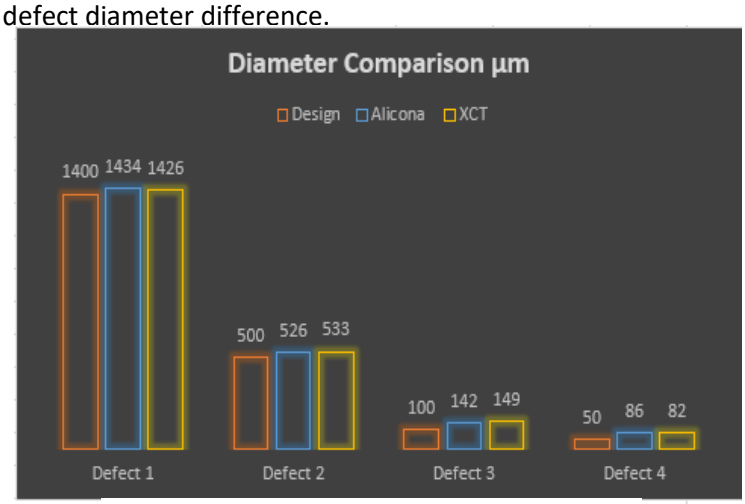

Figure 5-14 Defects Depth comparison µm

The difference between the Alicona and XCT diameter measurement results is noticeably small. The Alicona diameter results for defect 1 is 0.5% larger than XCT measurement and for defect 2 the Alicona

measurement is 1.3% less than the XCT result. The XCT diameter measurement for defect 3 is 4.7% larger the Alicona result and defect 4 XCT result is 4.6% less than the Alicona diameter measurement. Figure 5-15 shows depth measurement comparison, the XCT results for defect 1 were 1.7% less than the Alicona result and XCT diameter measurement for defect 2 diameter were 0.7% less than the Alicona results.

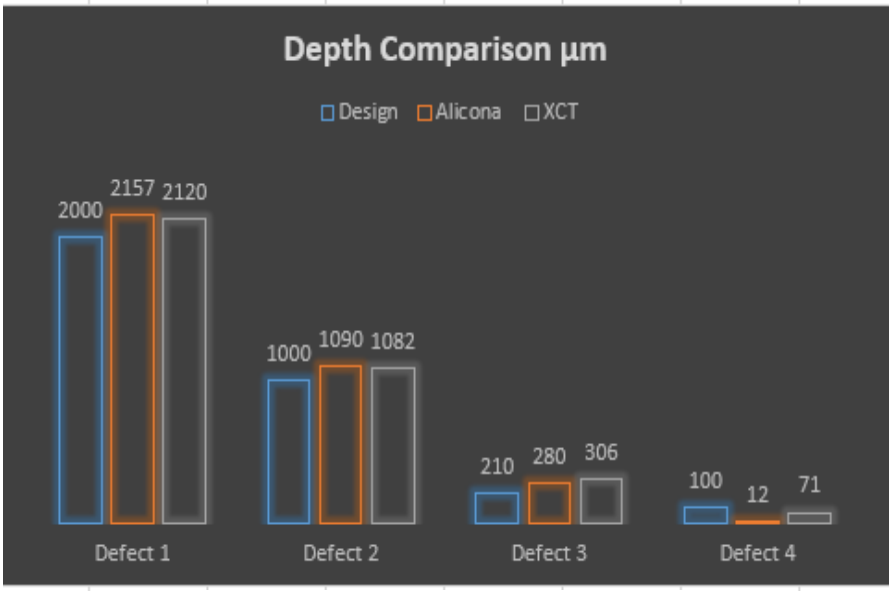

Figure 5-15 Defects Depth comparison µm

The XCT diameter measurement for defect 3 was 8.5% larger than the Alicona result, the defect 4 Alicona measurement result should be disregarded due to the inability of the Alicona in measuring the defect depth. The dimension measurement comparison proved the ability of XCT in correctly measuring internal defect dimensions.

5.5 Interference Fit artefact

The variability in size and shape of the defects/pores found in AM parts results in wide range of grey values, the artefact must contain defects similar to those found in AM components. As previously mentioned in chapter 4, EBM powder particles are larger than SLM particles. The powder particles used in SLM process range from 15 to 45µm, so the defect size and shape will differ from those found in components made by the EBM process. The artefacts used in the previous experiments were made of Titanium, as mentioned in chapter 3 section 3.4 the grey value is dependent on the material density. Consequently, an artefact made of lighter material needed to be investigated.

The artefact (shown in figure 5-17 a)) consists of two cylindrical halves with 10.9 mm diameter. The lower half comprises a 6mm machined hole followed by subsequent a 1.7mm drilled hole. The upper half has a 6.020mm protruding boss that encloses a 1.7mm drilled hole in the lower half by means of interference fit [11]. The interference fit tolerances were calculated to ensure a press fit to fully enclose the 1.7mm drilled hole in the lower half.

The artefact was built using a Renishaw AM250 SLM and the material used was AlSi10Mg powder, the aluminum was used due it low attenuation, prior to the build, a powder sample was analyzed through SEM to evaluate the powder particle shape and size distribution. Figure 5-16 b) shows the SEM image of the aluminum powder used in building the artefact. The morphology of the aluminium powder shown in figure 5-16 b) is non-uniform and the particles are small.

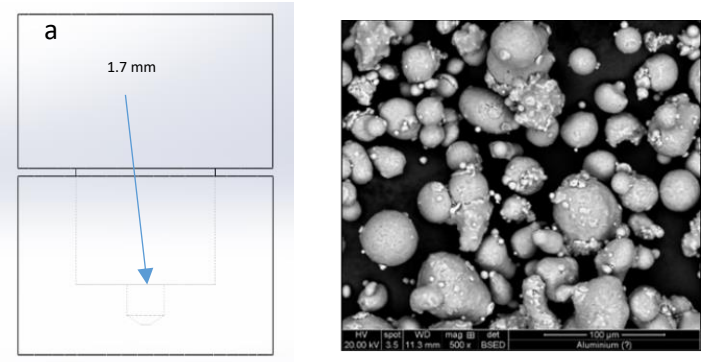

Figure 5-17 Artefact 3D model b) SEM image of aluminium powder

5.5.1 Alicona Characterisation

Prior to assembling the artefact, the drilled holes were measured by a focus variation microscope (Alicona G4) to identify diameter and depth values. The obtained results were then compared to those measured by XCT.

Figure 5-18 a) shows the drilled hole diameter measurement by alicona, the diameter was measured using a best fit circle. The drilled hole depth measurement (shown in figure 5-18 b)) was measured by joining the two highest point on the top surface, and selecting the lowest point, the depth is the horizontal line from the highest points line to the lowest point.

The inner hole was machined with a CNC machine, so the dimensions are expected to vary slightly from the initial design. The designed diameter was 1.7mm and the alicona result for the diameter was 1.740mm. The designed depth was 2.4mm and the depth measured by the alicona was 2.368mm. The drilled hole dimensions were considered acceptable as they are within the 50µm tolerance

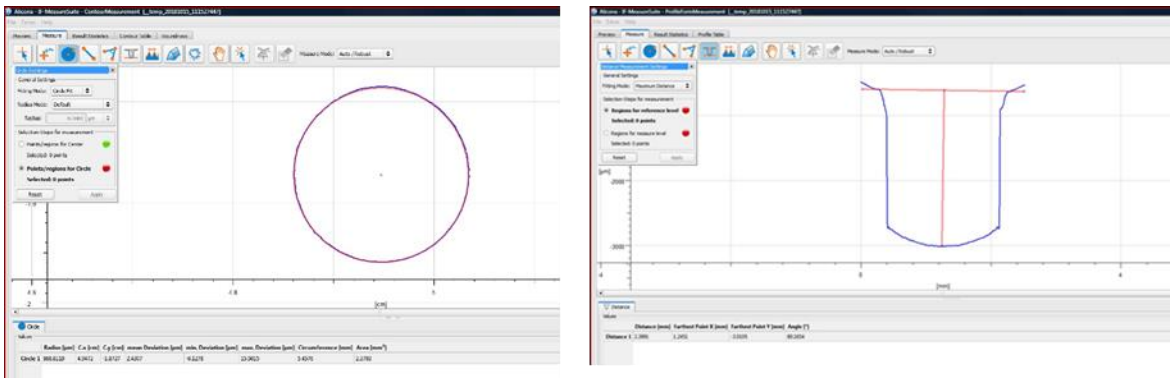

Figure 5-18 a) Alicona defect diameter measurement b) Alicona defect depth measurement

5.5.2 XCT measurement

The artefact was scanned with a Nikon XTH225 industrial XCT, the lessons learned from the scans helped in optimising the scanning parameters to minimise noise presence. In this scan no data and noise filters were used. This way no useful data was omitted in the measuring process, ensuring that the full dataset was analysed. Table 5 shows the parameters used for the artefact scan.

Filter	100 µm
Exposure	2000 ms
Filament current	8.7 W
Acceleration Voltage	150 Kv
Voxel size	9.7 µm
Gain	12

Table 5 XCT scanning parameters used for press fit artefact

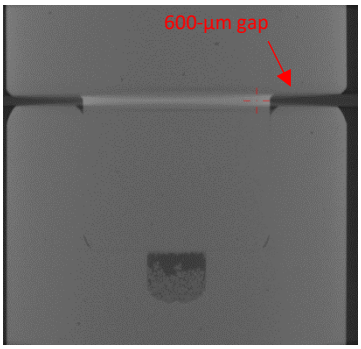

Figure 5-19 XCT image of the artefact

The artefact contained a 600µm gap between the two halves; this gap was later used for contrast enhancement in a surface determination grey value study in section 8.4. The XCT results were analysed by the standard ISO 50% surface determination threshold, the artefact was scanned with a 9.7µm voxel size. The Filament current was kept under 10W to avoid auto defocus usage.

Figure 5-20 (a) shows the diameter measurement of the drilled hole, using a multi-point best-fit circle. The depth measurement (shown in figure 5-20 (b)) was evaluated by measuring the horizontal line between the line joining the highest two points on the top of the lowest point in the drilled hole.

Prior to pressing the upper half, the drill hole was filled with AlSi10Mg powder, the unfused powder is shown in figure 5-20 (b), it is clear that the magnification is sufficient for imaging unfused powder particles and the air gaps in-between [11]. Semi fused and unfused powder will be discussed in more detail in chapter 8. The measured defect diameter was 1.694mm and the depth was 2.347mm.

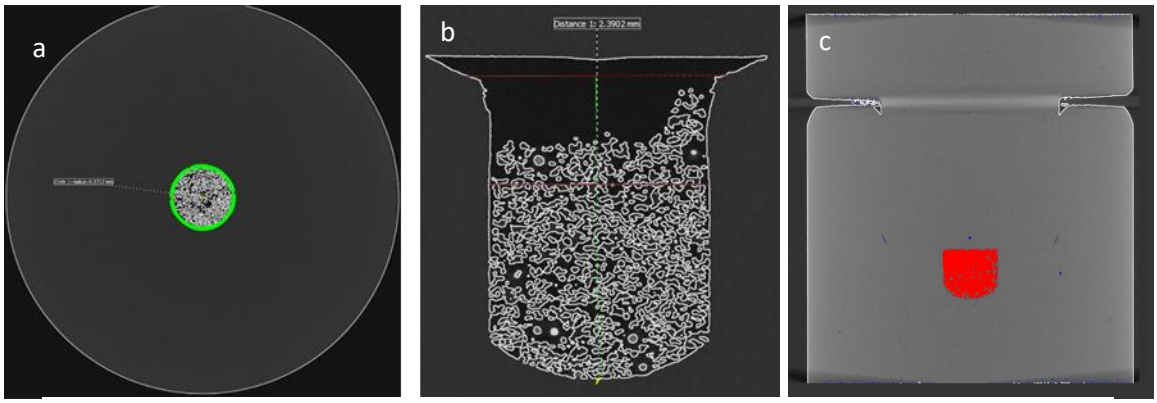

Figure 5-20 XCT defect diameter measurement (b) defect depth measurement (c) defect depth measurement

Figure 5-21 a) shows the diameter comparison, and 5-21 b) shows the depth comparison, the difference between the XCT measurement and the Alicona is 2.7% for the diameter and 2.1% for the depth. This difference in such high magnification could be mainly due to the threshold used for surface determination.

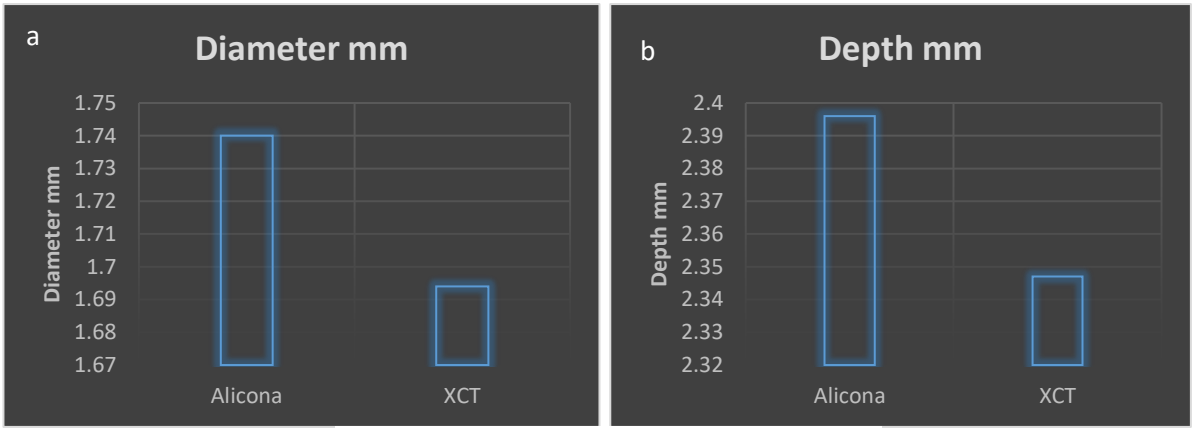

Figure 5-21 (a) diameter comparison (b) depth comparison

The XCT dimensional measurements are based on surface determination and edge detection, it was noted that the edge detection is directly affected by grey value variability therefore the large difference between the background degree of darkness and material degree of brightness will result in accurate edge detection. On the other hand, small differences between background and material grey values will usually result in false edge detection. This could be for several reasons predominantly related to scanning parameters and error in the surface determination threshold.

5.6 EBM built artefact

One of the main barriers in the wide adaptation of AM technologies in several critical application such as medical devices and aerospace components is the limited understanding of the structural integrity and fatigue performance of those components. As previously mentioned in chapter four, the energy source in PBF and direct energy deposition technologies are used to melt/sinter powder particles to create the component.

This artefact was designed for the investigation of EBM machine printing resolution, specifically to test the size of the minimum printable internal feature. This artefact could also be used for XCT parameters optimisation and lack of fusion characterisation. In the EBM process, the minimum possible layer thickness is 50µm and the smallest printable feature size is 100µm. The layer thickness and smallest feature size is directly affected by powder morphology and printing parameters.

It is critical in the PBF process to identify the melt pool dimensions; those dimensions affect geometrical feature printability. Furthermore, the contour chevron patterning directly affects the final surface finish. Melt pool dimensions can be used for the prediction of the metallurgical grain and microstructure [254- 255]. This study focuses on highlighting the challenges in using XCT as a metrology tool and establishing a rationality of the build parameters for a given material in producing internal features.

The designed artefact shown in figure 5-22 contains 37 internal features ranging from 10µm to 500µm. The features smaller than the machine resolution were designed to investigate the slicing software feedback. The geometrical features include spheres, cylinders, truncated prisms and rhomboids. The artefact was a 5.8 X 5.8mm cube, and it was built using an Arcam Q10 EBM machine, the powder used was titanium Ti6Al4V recycled 5 times. Prior to printing, a sample of the used powder was analysed using a SEM. Figure 5-22 (b) shows a section view of the artefact.

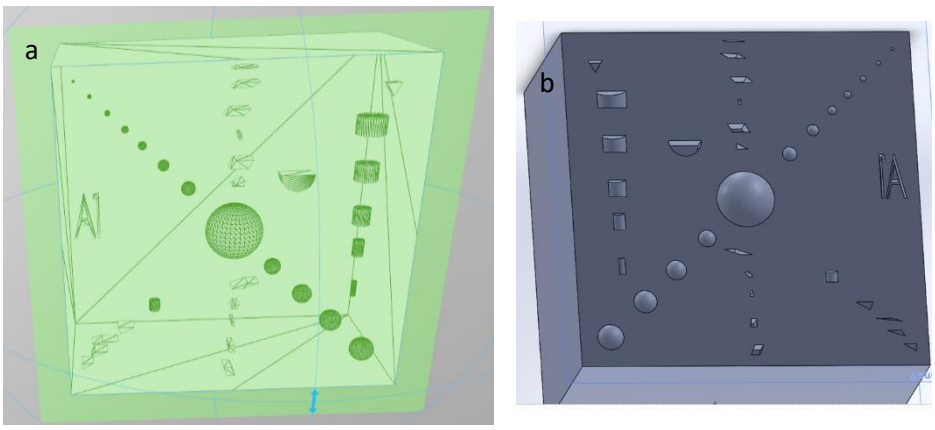

Figure 5-22 3D model of the cube artefact (b) section view of the internal features

The electron beam was used to heat the stainless steel build plate to 700 °C, in a vacuum atmosphere. The scanning strategy used was raster parallel hatching with final orthogonal alternation at the end of each layer. The EBM processing parameters were as follows: Cathode current (i_{Beam}) 0.5 mA, Power 1200 W and 800 mm/s scanning speed (v_{Beam}).

A Nikon XTH225 industrial CT was used for scanning the artefact, the scanning parameters are shown in table 6.

Filter	Exposure	Filament Current	Acceleration Voltage	Voxel Size
1mm	2000ms	46µA	135 kV	15 µm

Table 6 XCT scan parameters for EBM cube artefact

5.6.1 XCT results

The surface determination threshold used was ISO 50%, as mentioned before in chapter 3 section 3.8, this threshold is the common standard method used in most XCT applications. Defect analysis can be carried out using the subjectively determined surface determination threshold (ISO 50%), or the user can identify a component dependent threshold. Figure 5-23 (a) shows the 3D view of the scanned artefact and figure 5-23(b) shows a top view of the artefact with defect analysis results.

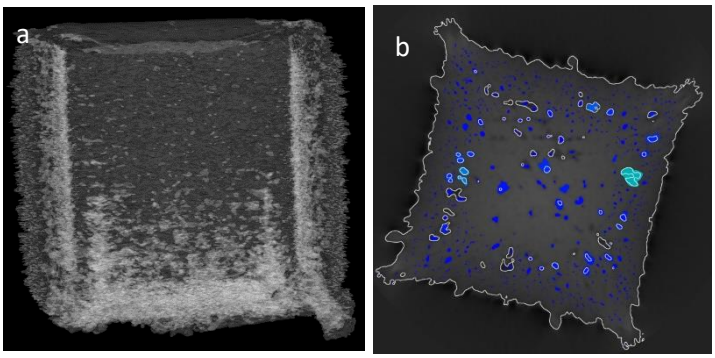

Figure 5-23 (a) 3D view of the artefact (b) Top view of the internal defects

The results show that the designed internal features are not present and there are excessive lack of fusion defects. The failure in the internal feature printing process is mainly due to EBM melt pool

dimensions. The largest designed internal feature is 500µm, in the EBM PBF process the melt pool minimum width is 400µm and minimum depth is 100µm, however the maximum melt pool width and depth can reach up to 1400µm [256]. The parameters used in this experiment should have created a melt pool with 450µm width and 350µm, due to the power and low scanning speed. This combination of power and speed creates a melt pool with a larger width and smaller depth.

The results show that some of the defects are hollow and others have semi fused and unfused powder. Figure 5-24(a) shows a top view of the artefact and figure 5-24(b) shows a front view of the artefact. The hollow defects are highlighted with yellow circles and defects containing semi-fused or un-fused powder are highlighted with orange circles. In figure, 5-24 (a&b) there are some large defects that contain both powder and hollow pores. An interesting point to note is the failure of surface determination in detecting the semi fused and the un-fused powder.

In this experiment, the surface determination threshold used was ISO 50%, in figure 5-24 (a) and (b) the edge detection is highlighted with white contours for the artefact outer edge and inner pores. This threshold failed in detecting and highlighting powder filled defects.

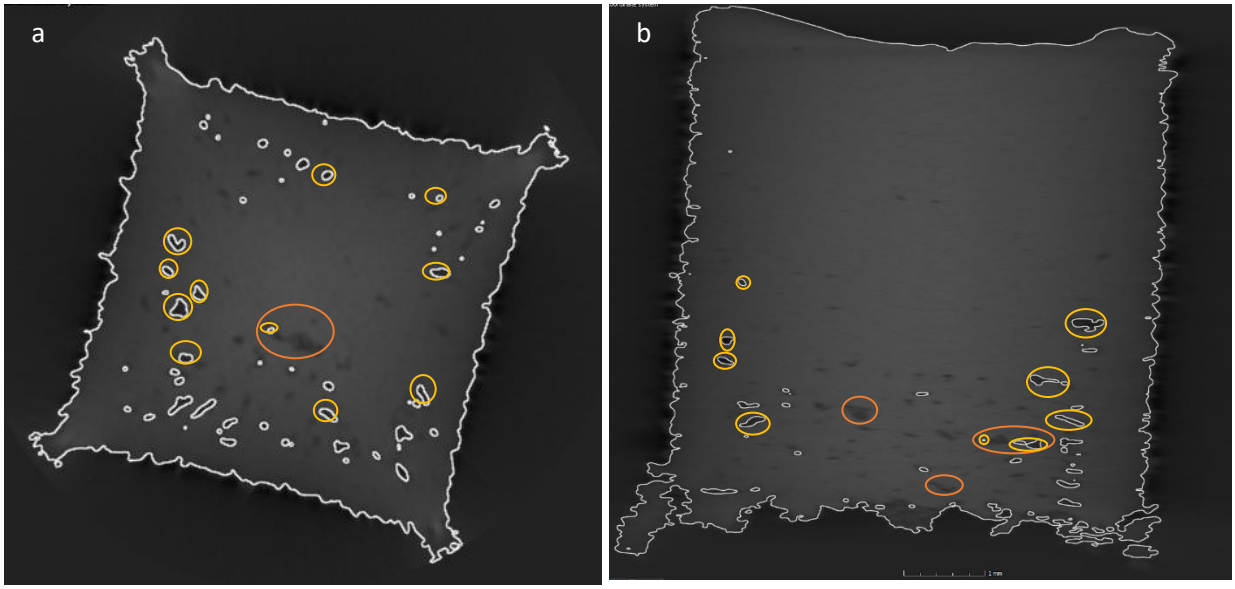

Figure 5-24 (a) top view of the artefact internal defects (b) front view of the internal defects

5.6.2 XCT results assessment

This experiment highlighted several issues in the defect analysis process; several visible defects were not picked up through analysis, furthermore, the analysis showed some defects that do not exist. This failure in the defect analysis process could be caused by unappropriated XCT scan parameters, by wrong defect analysis settings or a combination of both.

In order to understand the causes of these issues the defect analysis results obtained for specific slices were compared to the mean grey value of this slice. The mean grey value analysis can be used for accessing overall XCT scan quality and identifying the causes of the defect analysis failure. As

previously mentioned in chapter 3 section 3.4, the grey value depends on the material thickness; the lowest grey value is the background/air and the grey value should gradually increase to the middle of the object where the highest grey value is found. The grey value is directly affected by the scanning parameters; if the X-ray power is too low causing insufficient beam penetration, the scanned object outer edge grey value will be very low. The insufficient difference in grey value between the outer edge of the scanned object and the background causes difficulty in identifying the outer edge. On the contrary, excessive x-ray beam power will cause scatter and other unwanted x-ray artefacts in the x-ray data, compromising the scan results. Furthermore, increasing the x-ray spot size lowers the resolution.

Figure 5-25(a) shows a top view slice of the artefact, (b) shows the same slice with defect analysis results highlighted and (c) shows the same slice grey value analysis top view. In the first image it was noted that the surface determination ISO 50% threshold did not highlight several defects and the artefact outer section is darker than the inner core of the artefact. Furthermore, there are bright spikes in each corner and the pores are darker closer to the artefact outer edge and are gradually getting brighter towards the middle of the artefact.

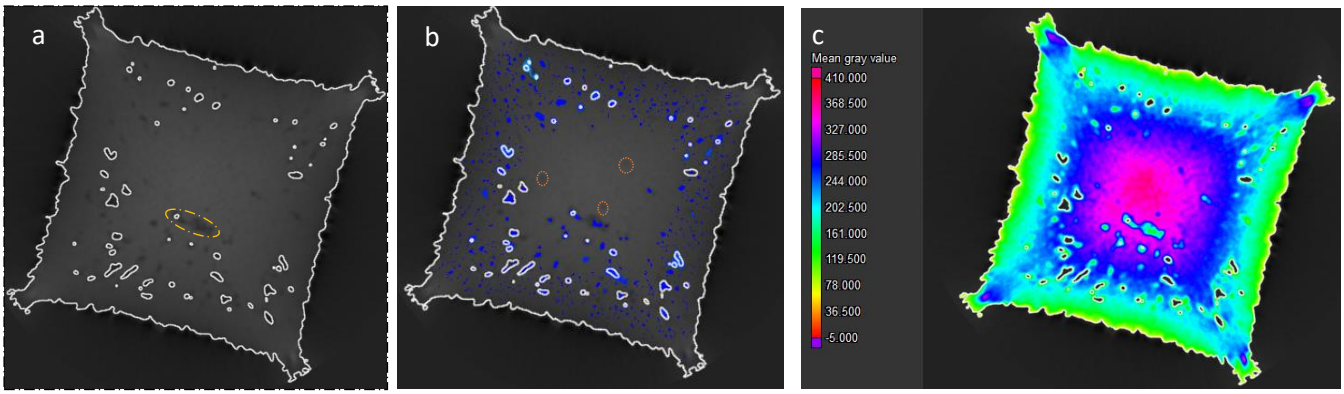

Figure 5-25(a) top view of the artefact (b) top view of the artefact with defect analysis (c) Top view of the artefact with grey value analysis

In figure 5-25 (b), the defect analysis results are not matching the surface determination contours shown in figure 5-25 (a), several small artificial defects are highlighted on the artefact outer edge, and those defects are not visible in figure 5-25 (a). The grey value analysis shown in figure 5-25 (c) supports the conclusions, the artefact outer edge mean grey value (bright green) is 120 apart from the corners which are an exception and there are bright spots (dark blue) present in each corner with 250 mean grey value. In figure, 5-25(c) the largest mean grey value (deep pink) is 410 and it is in the core of the artefact. The grey value analysis highlighted all the dark spots in the image apart from those situated on the bright green outer edge of the artefact, also the grey value analysis highlighted the defect outer contours that both surface determination and defect analysis failed to detect. The defect highlighted with a yellow ellipsoid in figure 5-25 (a), was detected by surface determination as a small dot, but the defect analysis in figure 5-25 (b) detected this defect as two separate dots larger than the one highlighted in the surface determination in figure 5-25(a) and the grey value analysis highlighted the full defect. Another example are the three defects highlighted with orange circles in figure 5-25 (b), those defect are not detected by surface determination or defect analysis but were recognised by the grey value analysis as three small blue dots in the centre (deep pink) section of the artefact. Figure 5-

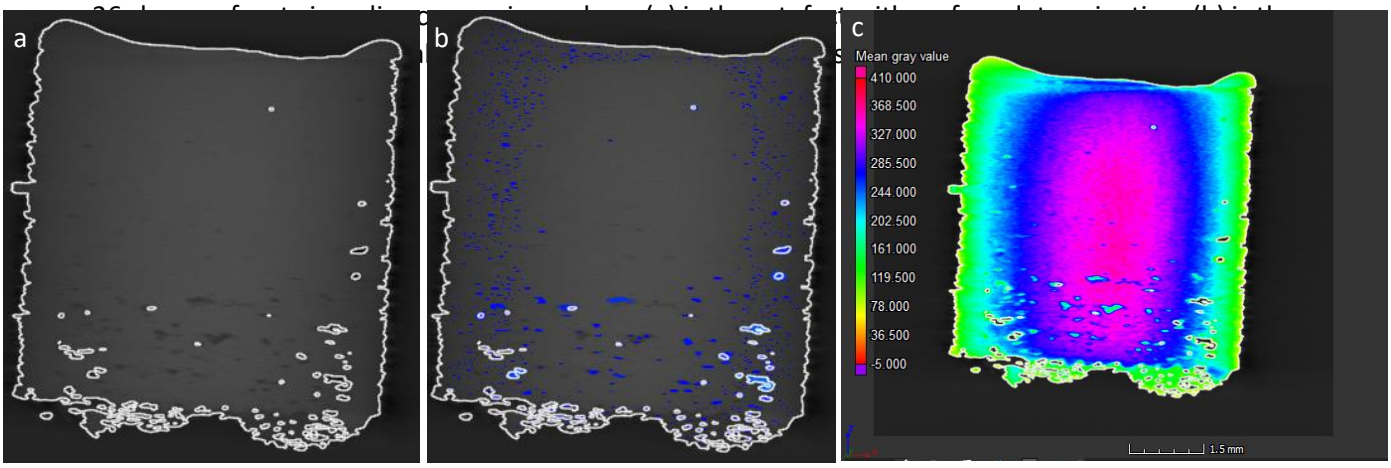

Figure 5-26 a) front view b) front view with defect analysis c) front view with grey value analysis

When comparing the three images it can be noted that in the front view the false defects situated close to the outer edge of the artefact are significantly less than those found in the top view (figure 5-26 (b). In figure 5-25 (b), the false defects are mainly present on the left and right sides of the artefact and the false defect's presence is limited in the top section of the artefact and not present on the lower section of the artefact. When comparing figure 5-25(b) and (c) it was noted that the false defects are following the bright green coloured contours in the grey value analysis (figure 5-26 (c)). Furthermore, the surface determination defects outer contour identification in figure 5-26 (a) is not matching the defect analysis in figure 5-26(b) and is not matching the grey value analysis in figure 5-26 (c), but the grey value analysis highlighted all visible defects in figure 5-26 (a). In this experiment, most of the defects should contain un-fused or semi-fused powder, none-of the defect analysis or the grey analysis succeeded in detecting and identifying powder filled defects. This could be due to in-sufficient resolution for powder detection or the scanned artefact was out focus. This experiment highlighted the presence of a relationship between the x-ray beam being perpendicular or parallel to the pore, which will be investigated at a later stage. The X-ray scanning parameters used in this experiment are not appropriate, the surface determination threshold is not correct causing inconsistency in the mean grey value and finally the defect analysis process failed in detecting several defects, this indicates that the process needs further optimisation.

5.7 SLM built artefact

In order to evaluate XCT capabilities several studies focused on characterising simulated internal defects and features. One of the drawbacks of such simulated defects is their poor representation of the different defects found in the real AM components, such as lack of fusion defects similar to the defect shown in figure 5-27. One of the key drivers in developing this SLM artefact is understanding the effects of semi fused and unfused powder on part metrology by identifying the appropriate XCT settings for precisely detecting semi-fused and un-fused powder and understanding the impact of on lack fusion [10].

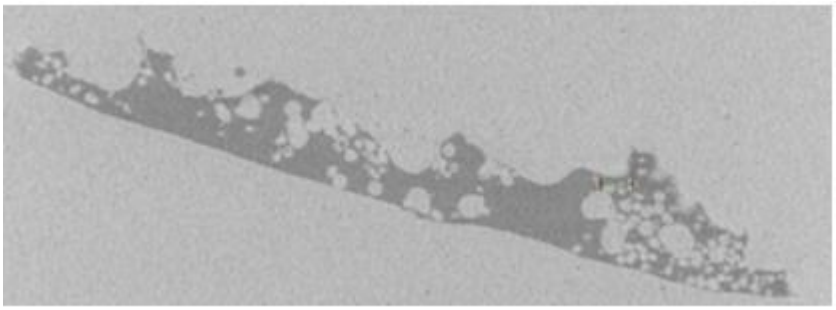

Figure 5-27 High-resolution (4µm Voxel size) XCT image of unfused and semi fused powder in an enclosed internal feature

Selective laser melting (SLM) technology is widely adapted in many industries; several industrial applications are using SLM technology in manufacturing prototypes and low volume high value components. As previously mentioned in chapter 4 section 3.1, SLM is one of the PBF processes that uses 15-45µm powder particles. The small powder particles combined with the high ability of laser control enables the production of smaller melt pools and smaller inner features than the EBM process.

It is commonly recognised in the SLM AM community that the printing resolution is directly related to laser spot size and it is not possible to print smaller than the laser spot. However, this is not entirely correct; several layers underneath the surface can be re-melted from the melt pool. The secondary driver for developing this artefact is identifying the limitation in manufacturing capability of geometrical and internal features as they approach the laser spot size or powder particle size [10].

As previously mentioned in chapter 2, AM component service life can be significantly compromised due to subsurface porosity. Furthermore, subsurface defects are one of the main root causes of fatigue crack initiation. A further design objective of this artefact is assessing if proximity to the surface affects internal feature manufacturability.

In this artefact, various geometries with different sizes were designed as close as 50µm from the surface to duplicate subsurface pores. The final design objective of this artefact was to assist in understanding the correlation of AM slicing software images with final built samples using XCT; verifying the results by physical sectioning [10].

5.7.1 Artefact design

The designed test artefact shown in figure 5-28 (a) contains 64 internal features ranging from 50µm up to 1mm. The geometrical figures include centre located cylinders, prisms, spheres, surface cylinders, edge truncated prisms, two truncated prism helix/spirals and two 350µm internal cylindrical channels. The artefact length was 24mm and outer diameter was 11mm.In the lower half each feature is mirrored in the upper half, by this way the influence of melt pool stabilization in the base of the built can be identified, by quantifying the geometrical dimensional deviation in the lower and upper halves within the same artefact. Furthermore, the 64 features were designed to assess AM machine

printing capability, specifically when the dimensions are approaching laser spot size. finally, there are two circumferential marks on the outer middle section of the artefact that will be used as physical sectioning marks for location verification.

Figure 5-28 (b) shows the artefact location on the build plate, the top face of the artefact was marked with H/H, which stands for the University of Huddersfield and Hieta (the company printed those artefacts). Four artefacts in total were built, one in each corner. These four artefacts will be used later for understanding the reproducibility in printing internal features within the build chamber volume of the same machine, and identifying the relationship between the artefact printing location within the build volume and internal feature printability.

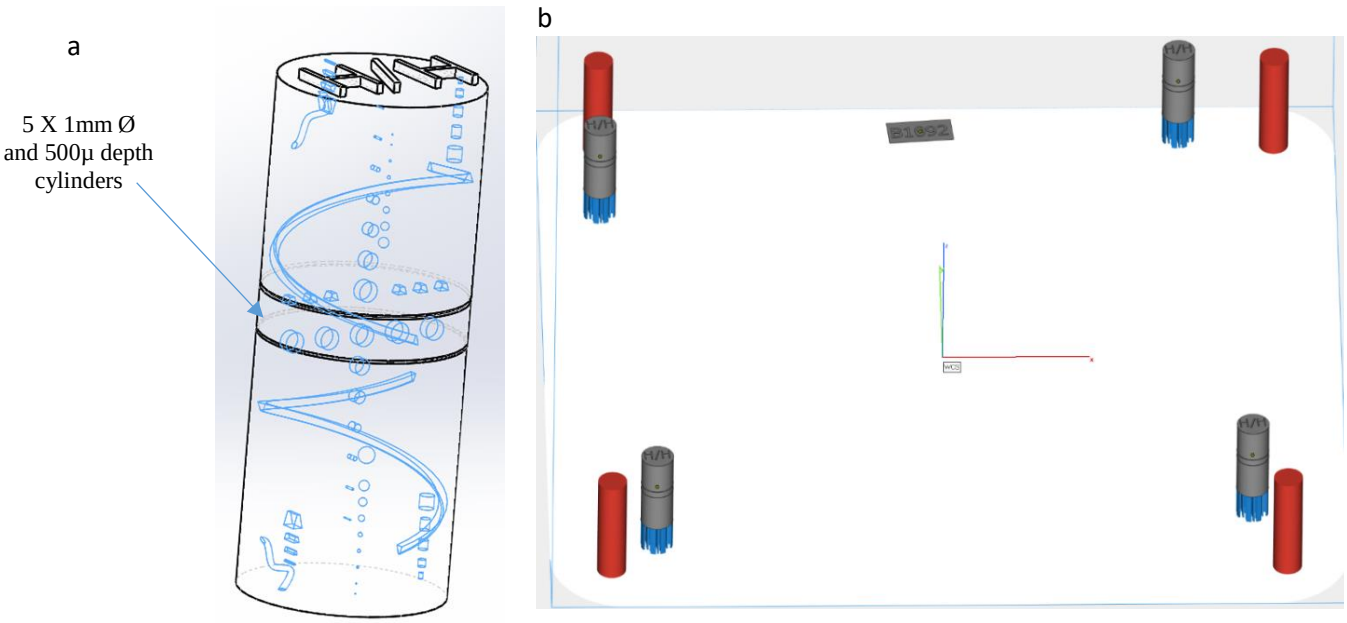

Figure 5-28 a) Artefact 3D model b) Artefact location on the build plate

The AM machine used for manufacturing this artefact was a Renishaw AM 250, using Aluminium AlSi10Mg powder, which had been recycled 8 times. Prior to artefact build, a sample of the used powder was analysed by SEM. As previously mentioned in chapter 4, virgin SLM powder is 20-45µm in diameter. The build parameters used on the AM250 are shown in table 7.

Laser Power	Laser Focus	Laser Speed	Point Distance	Exposure Time	Point Jump Delay	Jump Speed	Jump Delay
200 W	0 mm	0.55 m/s	80 µm	140 µs	NULL	NULL	NULL

Table 7 AM250 build parameters

The laser beam-scanning pattern (shown in figure 5-28 (a)) used in this build was outer contour with hatches with arrays in parallel stripes [10]. Figure 5-28(a) shows the middle slice obtained from Quantum software; the middle slice shows the four cylinders' top view. Figure 5-28 (b) shows an XCT image of the artefact scanned with a 26µm voxel size.

As previously mentioned, this artefact was used in several studies and it was initially scanned with a Nikon XTH225 industrial CT with 26µm for the low magnification scan. Then for a high magnification

scan (4µm voxel size), the artefact was scanned with a YXLON FF20 CT scanner (YXLON international GMBH) equipped with a YXLON FXE 190.61 x-ray tube and Varex Imaging detector model 4343CT.

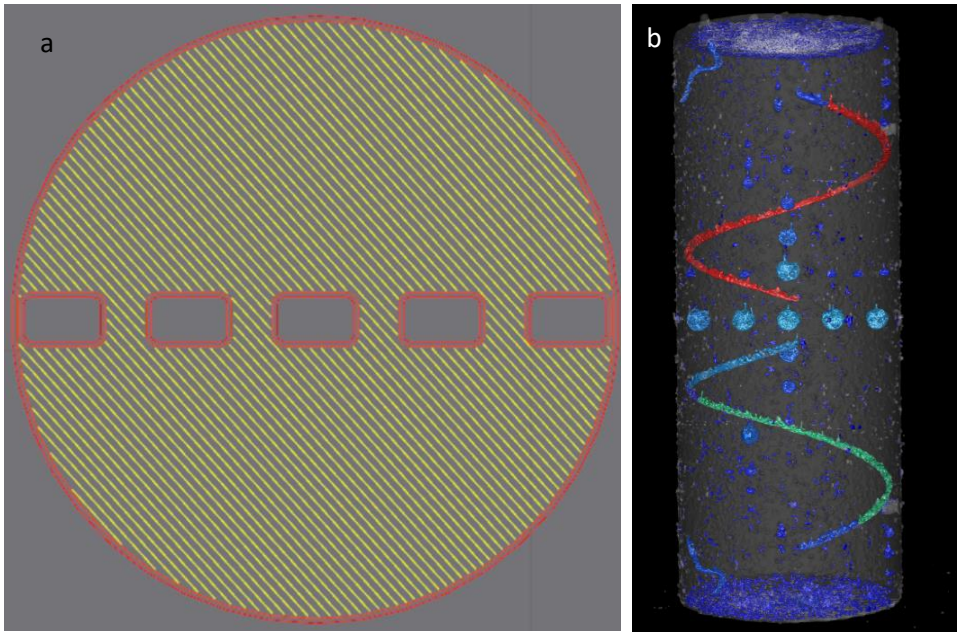

Figure 5-29 a) Quantum software middle slice b) XCT image of the artefact with internal features highlighted

The XCT settings used for the low magnification scan are shown in table 8 below, the scan results were reconstructed by CT-PRO software. The data processing, surface determination process and defect analysis was carried out using VG Studio Max 3.1 (Volume Graphics, Heidelberg). The surface determination threshold used in this experiment was ISO 50%.

Filter	**Exposure**	**Filament Current**	**Acceleration Voltage**	**Voxel Size**
0.25mm	4000ms	58µA	135 kV	26 µm

Table 8 SLM artefact XCT low magnification scan parameters [10]

In the high magnification scan, the artefact did not fit the frame so it was divided into two sections: upper and lower. Each section was scanned and analysed separately. The high magnification scanning parameters are shown in table 9.

Filter	**Exposure**	**Filament Current**	**Acceleration Voltage**	**Voxel Size**
0.10mm	2000ms	30µA	120 kV	4.2 µm

Table 9 SLM artefact XCT low magnification scan parameters [10]

5.7.2XCT Results

In this section, the XCT results will be used in the identification of the minimum build resolution and the effect of internal feature geometry on SLM manufacturability. In addition, the dimensions of the internal features obtained from the XCT scan will be compared to the designed dimensions. The low-resolution scan is used for complete artefact visualisation and the high magnification scan is used for internal feature dimensional measurement.

The first point the XCT results will investigate is the effect of the internal feature proximity to the surface on the SLM artefact manufacturability. Figure 5-30(a) shows the upper section of the artefact design, the largest edge cylinder (1mm diameter X 1mm length) is highlighted. In the design this cylinder was located 50µm from the outer edge. In the slicing software the cylinder was open to surface and not enclosed as shown in figure 5-30 (b). The XCT scan results confirmed that this specific cylinder is not enclosed, the XCT image is shown in figure 5-30 (c).

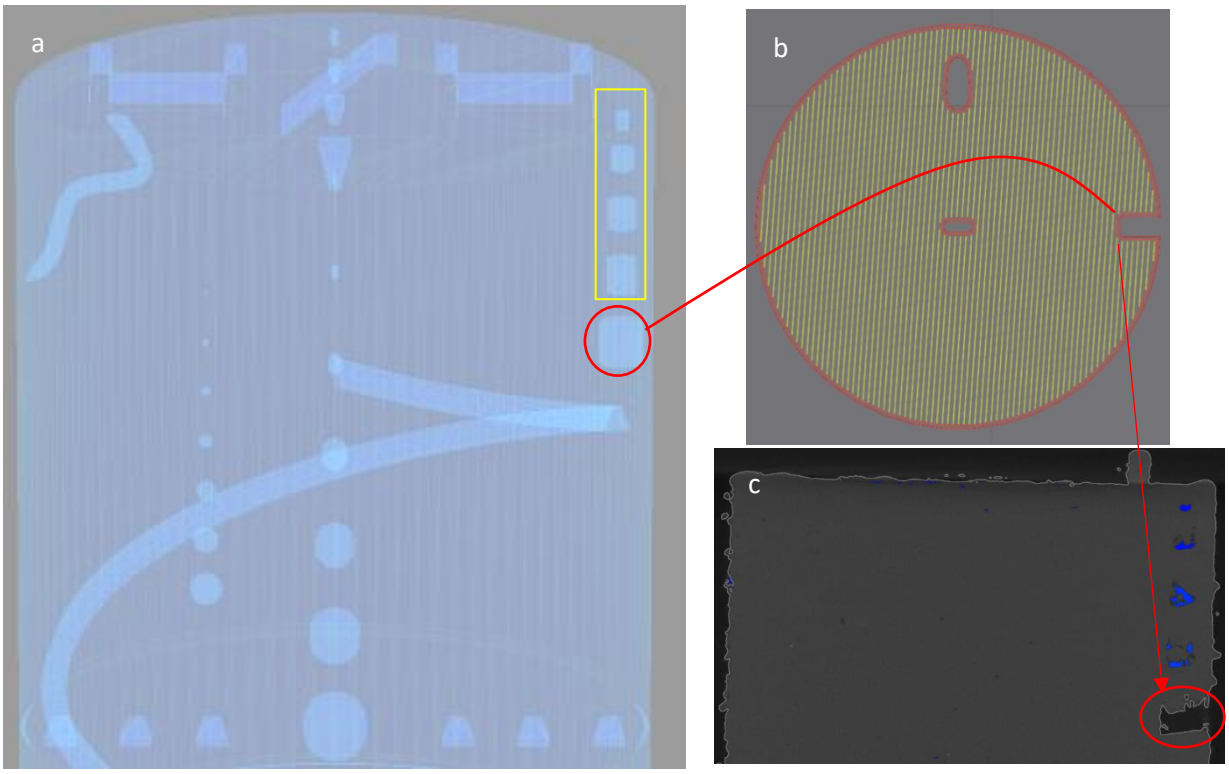

Figure 5-30 a) Artefact 3D model top section b) Quantum software middle slice c) XCT front view image of the artefact

results have shown that any feature closer than 100µm from the surface was not enclosed. This can be seen in figure 5-30 (c) where the four smaller cylinders on the top of the opened cylinder are fully enclosed. The closest to surface was the first cylinder on the top on the open cylinder; this cylinder was designed 100µm from surface.

The XCT results were used in investigating the impact of internal features geometry on SLM manufacturability and the minimum build resolution. The spheres designed size ranged from 50µm to 1mm, figure 5-31 a) shows a part of the model with a series of vertical spheres and figure 5-31 b) shows an XCT image of the actual printed spheres. It was noted that the spheres' minimum printing resolution was 100µm and the 50µm spheres were not present.

The design contained vertical and horizontal cylinders, the vertical cylinders are shown in the top left corner in figure 5-31(c); the vertical cylinders' minimum printing resolution was 150µm diameter. The actual printed vertical cylinders can be seen in the top left corner of figure 5-31 (d).

The horizontal cylinders are shown in figure 5-31 (c) in the middle of the model, the minimum printing resolution for the horizontal cylinder was 100µm diameter. It was also noted in figure 5-31 (d) that the horizontal cylinders roundness was more consistent than the vertical cylinders.

The artefact design included four features passing through several layers, two 350µm internal channels and two spiral / helix prisms. The designed internal channels are shown on the top and bottom right corners of figure 5-31 (c), the actual printed channels can be seen in the top and bottom right corners in figure 5-31 (d).

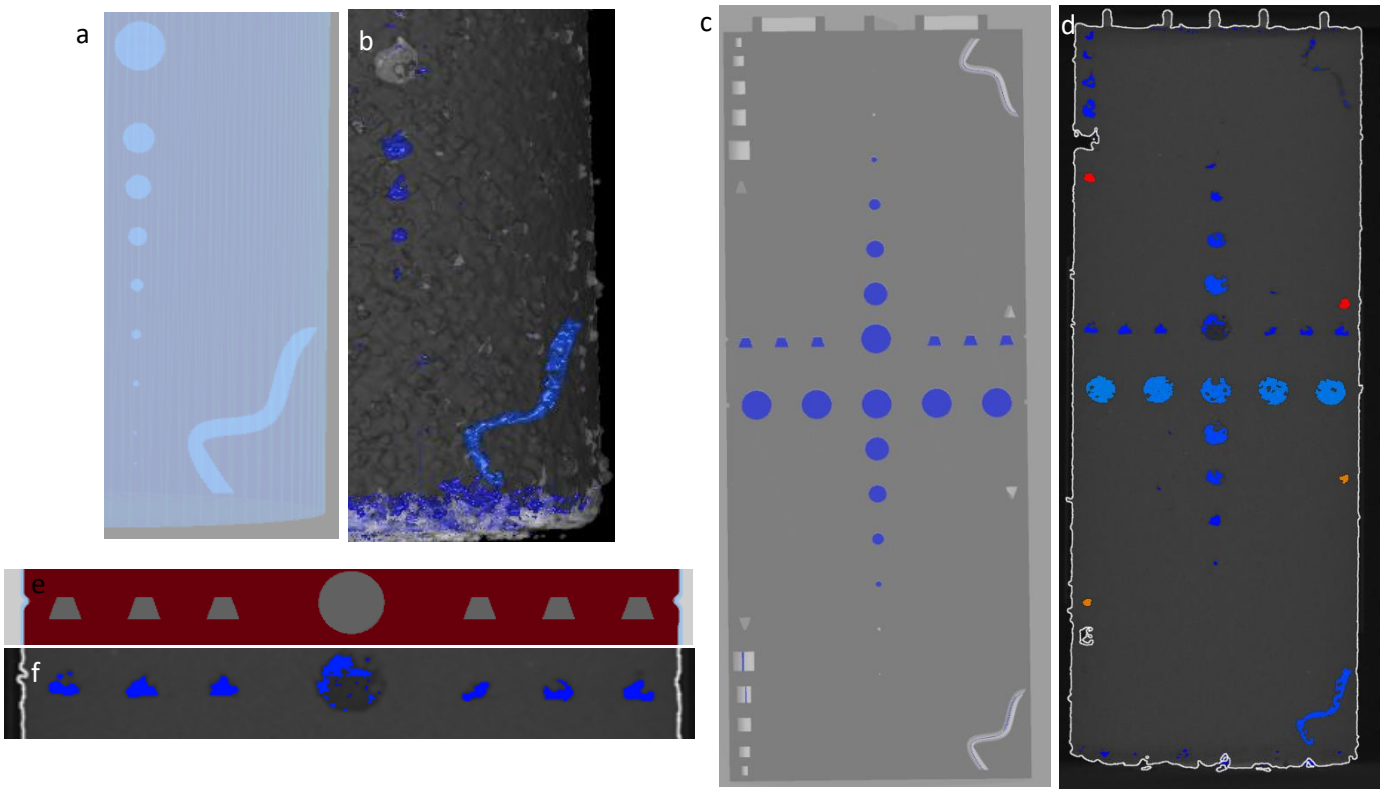

Figure 5-31 a) spheres in the artefact 3D model b) spheres in the XCT image c) model middle section slice d)XCT middle section e) model middle Truncated prims f) XCT image of the truncated prims

The next features are the truncated prisms that were designed with a 100µm base and 50µm top face; these prisms were not present in the build, but the second smallest truncated prism designed with a 150µm base and 100µm top face were present. Figure 5-31 (e) shows the designed centre truncated prisms and figure 5-31 (f) shows the printed truncated prisms, when comparing both figures it is noted that the actual printed prism locations and spacing are similar to the initial model.

Finally, the spiral prisms base was 350µm and the top face was 100µm, those prims printed well and the base and top face were in average 50µm less than the designed dimensions. Overall the spiral and helix features starting angular positions were very accurate and matched the designed location, the spiral prims start and end points can be seen in figure 5-31 (d) as red and orange dots. The results for each feature are shown in table 10.

Feature	Designed size	Build resolution limit
Truncated Prism	Base size 100µm -500µm Top face 50µm- 250µm	Base size 150µm Top face 100µm
Vertical Cylinders	50µm-1000µm dia. X500-1000µm length	150µm dia X 500µm length
Horizontal Cylinders	50µm-1000µm dia. X1000µm length	100µm dia X 500µm length
Spheres	50µm-1000µm dia.	100µm dia
Helix/spiral	Base size 350um - Top face 100µm	Not applicable

Table 10 minimum printed feature resolution

5.7.3XCT results verification

The artefact used in this study were designed for metrology testing by the means of two circumferential location marks situated on the middle of the artefact, just above and below the five centre cylinders. Figure 5-32 shows the location indication marks and illustrates the XCT result verification process, which uses the centre five cylinders. The first step of the process was to confirm the location of the cylinders by XCT (see figure 5-31), and then through sectioning the artefact using a CNC machine in the middle of the indication marks. Where the centre of the cylinder is located, due to the nature of machining, which could produce burrs that affects the geometry, prior to Alicona measurement the artefact face was inspected under microscope and cleaned from burrs. The section slice is shown in figure 5-32; the length and width of the cylinders were verified using an Alicona G4 focus variation microscope. The uncertainty evaluation for XCT and Alicona is discussed in section 7.3.

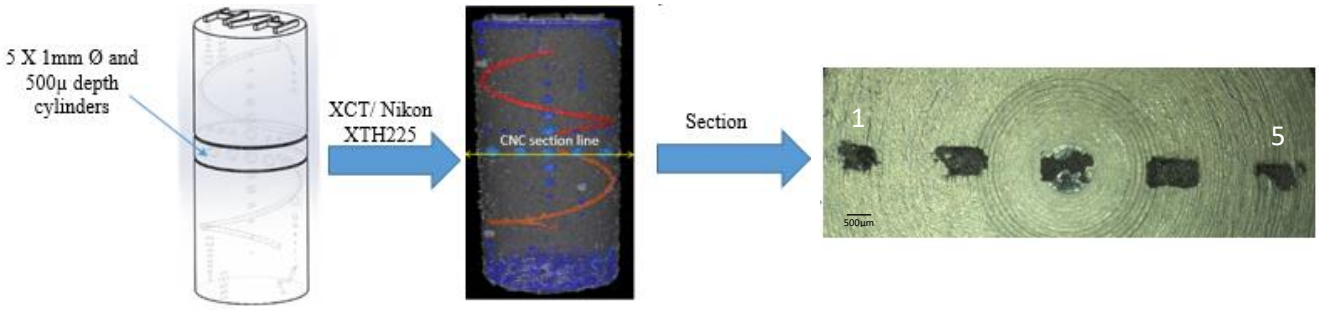

Figure 5-32 *Figure 37 Location verification and physical sectioned slice*

In the designed model the centre of the of the 5 centre cylinders was located 14.40 mm from the base of the artefact, the high resolution XCT scan confirmed that the actual location was 14.38 mm from

the artefact base. The actual location was 18µm lower than the designed location. This value is within the CNC machine tolerance, and half the AM machine layer thickness.

Another method used for location verification was is the space between the mirrored helix spiral truncated prims. The space between the red and orange spiral features shown in figure 5-32 is identical to the designed model. The five cylinders shown in figure 5-32 are numbered 1 to 5 from left to right; the cylinder length is named as “major” axis and width as “minor” axis. Figure 5-33 shows the cylinders major and minor axes used for XCT results verification

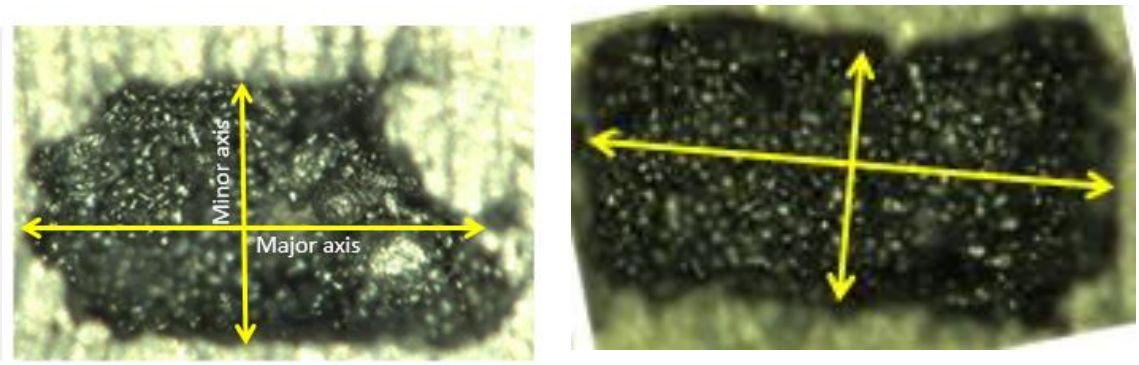

Figure 5-33 Minor and major axis of printed cylinders

The designed five-cylinder results obtained from the Alicona were compared to the XCT results; the surface determination threshold used was ISO 50%. The middle five-cylinder dimensional comparison is shown in figure 5-34, the major is the length and the width is the minor. The length comparison shows that the differences between the XCT and Alicona results for cylinder 1 is 9%, cylinder 2 is 7% and for cylinder 4 and 5 the difference is 7.85 and 5.1 respectively. The length for cylinder 5 was not compared due to the presence of a large semi-fused particle.

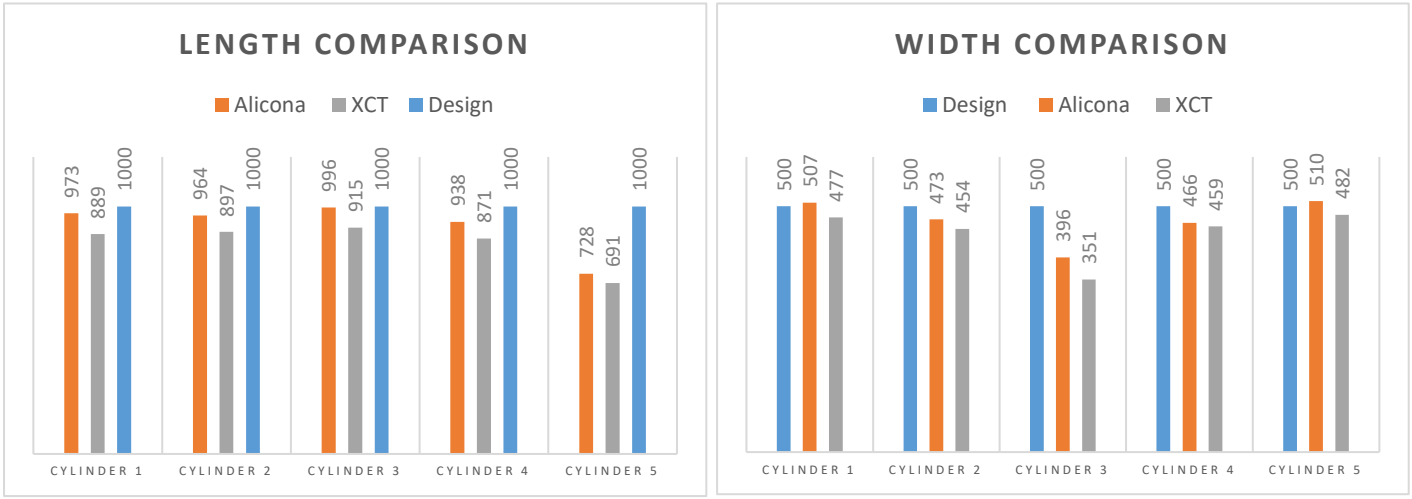

Figure 5-34 Minor and major axis comparison

In the case of the minor (width) comparison, the difference between the XCT measurement and Alicona for cylinder 1 is 6%, cylinder 2 is 4.8%, cylinder 3 is 11.4% and cylinder 4 and 5 are 1.6% and 5.4% respectively [10]. The cylinder length and width dimensions were less than designed. It clear that the slicing software does not consider powder particle size and degradation from powder recycling.

This experiment proved that the melt pool dimensions directly affect AM internal feature printability; any feature less than 150µm did not conform the designed shape and any feature closer than 100µm from surface was not enclosed. One of the main reasons for this was the melt pool dimensions were larger than the spot size. The printing parameters used produced a melt pool with 150µm length, 90µm width and 180µm depth [256,257]

One of the interesting points found in this study are the slicing software's internal features boundary contouring, as the software used did not consider the melt pool or solidification process. Figure 5-35 shows a comparison between the slicing software (a), CT Image (b) and sectioned part (c) at the exact same location. It can be concluded from figure 5-35 a) that the slicing software image shows the distance from the cylinder end face and the outer surface of the part is less than actual build. Furthermore, the cylinder lengths and widths are less that the designed dimensions. Consequently, the spacing of the end faces was larger than designed, which is highlighted by green circles in figure 5-35 b).

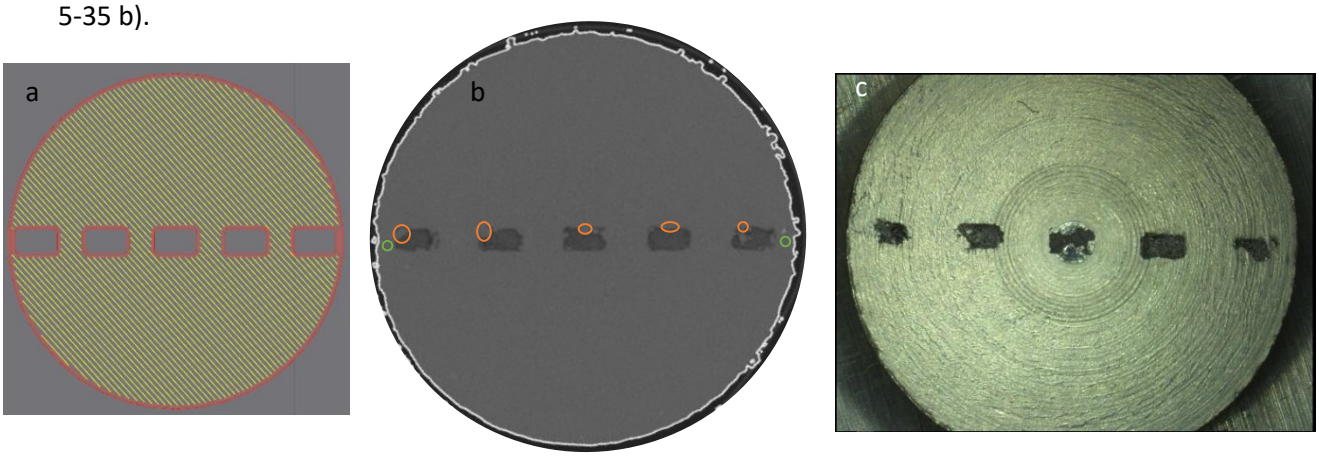

Figure 5-35 a) Slicing software image b) CT Image C) sectioned part image [10]

It is clear that slicing software also does not take in consideration the powder particles size and degradation from recycling, which in this case shows as internal feature geometry errors. These errors are highlighted by orange marks on figure 5-35 b), in the form of large satellite particles and deviation in feature dimensions. For the presently used slicing software there appears to be shortcomings in determining the manufacturability of the parts containing small intricate features near the surface. In this instance, care/experience is needed to realise such features.

This experiment highlighted the challenges in the detecting semi fused and unfused powder in AM components. Generally, powder particle size plays a very important role in the additive manufacturing process; the presence of large powder particles had a negative impact on feature resolution, this is mainly because higher energy is required for melting larger powder particles. If un-sufficient energy is supplied the smaller melted powder particles will be fused to the bigger un-melted particles, creating semi or unfused powder zones within the build [10]

The surface determination threshold used was not adequate in differentiating between semi-fused powder and solid material. Furthermore, the grey value of the unfused powder and semi-fused powder will always be closer to the full dense material [10], consequently a more bespoke approach is required to accurately detect unfused powder, and differentiate between solid material and un-fused/semi-fused powder.

5.8 Forged titanium artefact

All the previously designed artefacts were relatively small to enable high magnification scans and achieve high resolution. Generally, when scanning small objects low power and thin filters are used. In this experiment, a cylindrical forged titanium artefact was designed with 35mm diameter, consisting of two halves; both contain a set of three 500µm diameter drilled holes with 500µm depth. The lower half shown in figure 5-36 (b) had a 10.23mm slot, on the bottom of the slot there are three 500µm drilled holes with 500µm depth. The middle hole is located in the centre of the artefact and the other two are 22mm on the left and right of it. The upper half shown in figure 5-36 (a) is the same diameter as the lower half with 10.25mm cuboid protruding boss section, there are three 500 µm +/- 20 µm drilled holes on the right face and the depth ranges from 250µm to 650µm. The lower contained nominal identical holes drilled on the bottom of the slot. The middle hole is located in the centre of the cuboid and the other two are 12mm on the left and right of the centre hole. All the six drilled holes were enclosed once the two halves were assembled by interference shrink fit. Figure 5-36 (c) shows the artefact assembled 3D model. The artefact size only allowed a low magnification scan, which is representative of an actual component.

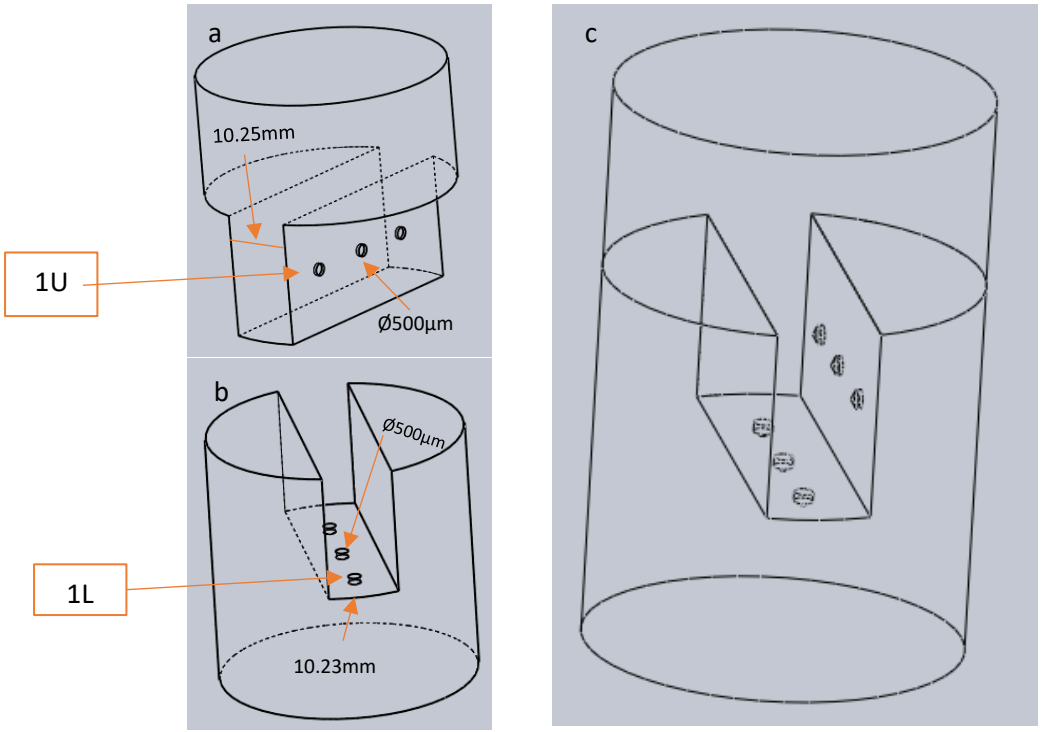

Figure 5-36 a) artefact top half b) artefact lower half C) artefact 3D model

This artefact was be used in several studies: 1- Identifying the influence of X-ray beam defocus on internal defects characterisation, 2- Confirming the impact of the defect being parallel or perpendicular to the X-ray cone beam on dimensional measurement. 3- Identifying the impact of different XCT scanning parameters on the defects characterisation.

5.8.1Alicona results

In this chapter, only the initial XCT scan will be discussed. Prior to artefact assembly, for XCT result verification the drilled hole depths and diameters were measured with an Alicona G4 non-contact instrument. The artefact was then scanned with a Nikon XTH225 Industrial XCT. The drilled hole diameters were measured using best-fit circle from 6 points on the drilled face, the drilled hole depths

were measured by selecting the two highest points on the upper surface and selecting the lowest point in the drilled hole, creating a horizontal line.

The Alicona results are shown in table 11, the three drilled holes in the upper halve are numbered as 1U to 3U from front to back and the three drilled holes on the lower halve are number as 1L to 3L from front to back. The drilled hole numbering is labelled in figure 40(a) and (b), the deviation in diameter and depth values are mainly due to CNC machining process tolerance, which in this experiment is slightly higher than the 20 µm tolerance.

Defect	1L (µm)	2L (µm)	3L (µm)	1U (µm)	2U (µm)	3U (µm)
Diameter	522	516	519	513	517	524
Depth	675	423	272	701	451	245

Table 11 Alicona drilled holes measured dimensions

The holes were machined with a Doosan DNNM 450ll CNC machine in manual mode, not preprogramed which is reflected in the results of the actual hole dimension. The diameters were designed to be 500µm, and the depth of holes were designed to be 250µm, 500µm and 650µm from the first hole to the third hole respectively, therefore the actual dimensions vary slightly due to machining tolerances, and the lack of tool runout verification.

5.8.2 XCT scan results

The scanning parameters are shown in table 12, throughout the experiment no data or noise filtration was applied. This approach guaranteed that no useful data was omitted or discarded during the measurement process, ensuring that the operator had an unfiltered dataset for use in the analysis.

Filter	**1mm**
Exposure	4000 ms
Filament current	9.8 W
Acceleration Voltage	195 kV
Voxel size	48 µm
Gain	12

Table 12 XCT scan parameters

For initial scan the filament current was kept under 10W to images in focus, minimizing blur in the images. The XCT result analysis was carried out with the grey value threshold ISO 50% surface determination and the data analysis was carried out using Volume graphics (VG studio max 3.1). After applying the surface determination threshold, the hole diameters were evaluated using best-fit circle and the hole depths was measured by using the highest 2 points of the drilled hole creating a horizontal line to the lowest point in the hole.

Figure 5-37 (a) shows a top view XCT image of the artefact upper section with the three drilled holes highlighted, figure 5-37 (b) shows a top view XCT image of the artefact lower section with the three drilled holes highlighted.

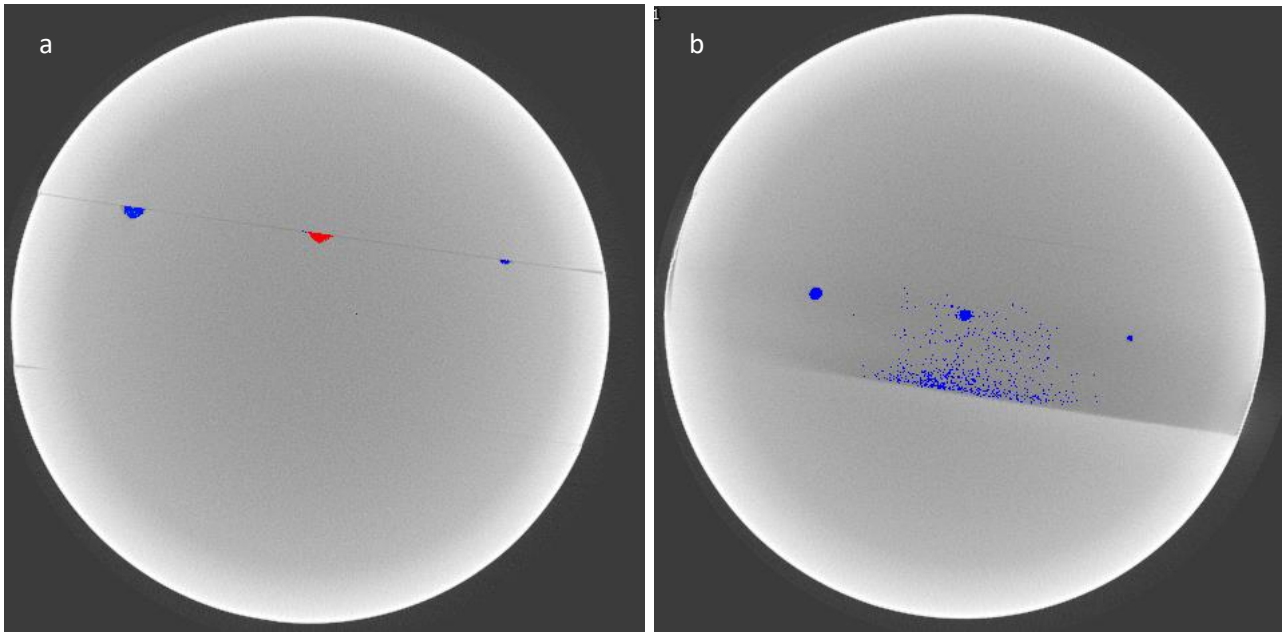

Figure 5-37a) XCT top view image of the upper section with 3 holes b) XCT top view image of the lower section with 3 holes

It was noted in figure 5-37 (a and b) the presence of a large dim circle in the middle of the artefact and the outer edge is bright. Figure 5-37 (b) has noise present in the center of the artefact. These images prove the presence of beam hardening artefacts.

The XCT results are shown in figure 5-38, where figure 5-38 (a) shows the drilled holes diameter comparison between XCT and Alicona, and figure 5-38 (b) shows the drilled holes depth comparison between XCT and Alicona.

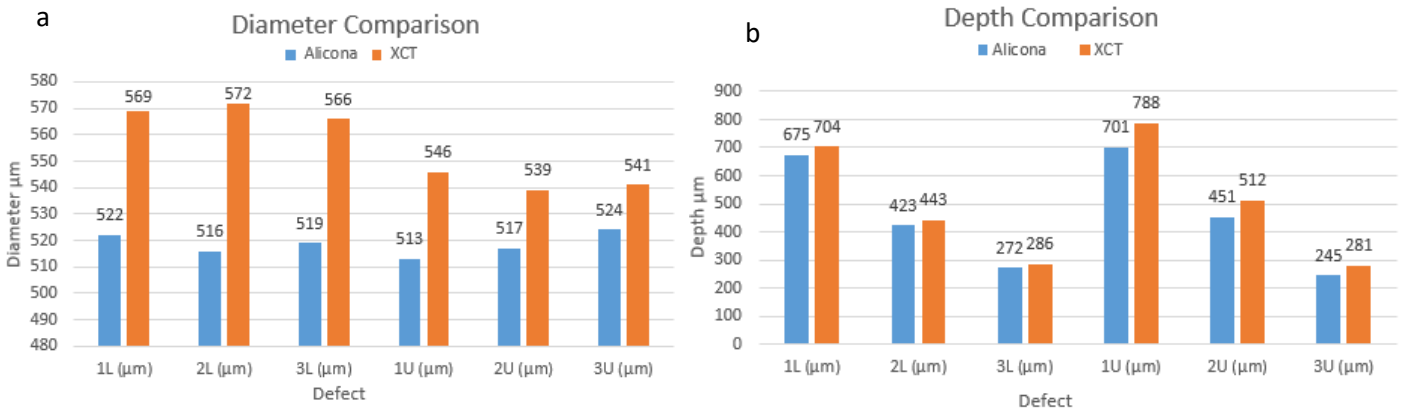

Figure 5-38 a) diameter comparison b) depth comparison

Comparing the diameter results from the Alicona measurement and XCT scan, the difference between the Alicona and XCT for the first lower hole was 8.9%, the second lower hole was 10% and the third was 8.8%. While the first upper hole difference was 6%, the second upper hole was 4.1%, and the third was 3.1%.

The depth comparison is shown in figure 5-38(b), the difference between the Alicona and XCT for first lower hole was 4.1%, the second lower hole was 4.5%, and the third lower hole was 4.9%. For the first upper hole the difference was 11%, the second upper hole difference was 11.9%, and the third was 12.8%.

The results from this experiment highlighted that the error percentage in the lower hole diameters was higher than the upper hole diameters and the error percentage in the depth measurements was higher in the upper holes than the lower ones. The differences between the Alicona and XCT measurements show that in the low magnification scan the error percentage is higher when the feature is parallel to the X-ray beam and lower when the feature is perpendicular to X-ray beam. This conclusion needs further investigation.

5.9 Chapter Summary & Conclusion

Several artefacts were designed to help in understanding the ability of XCT in characterising internal defects and features and identifying error source and percentage by comparing the XCT measurements to reference measurement values obtained from alicona focus variation system. The XCT scanning process is directly affected by scanning parameters and scanned object size.

The XCT results have shown that the percentage of error in the internal defect dimensions are significantly reduced at higher resolution but the noise presence compromised the defect analysis process by showing false non-present defects. The noise presence needs further investigation to identify the root cause, specifically the impact of beam filtration and scan parameters on noise generation, which will be investigated in the next chapter.

The experiments confirmed that the scanning parameters used for high resolution scans cannot be used for low magnification scans, this was highlighted by the difference in grey value contrast between the different magnifications. Furthermore, the relationship between scanning parameters, grey values and surface determination used requires further investigation.

The EBM artefact highlighted the possibility of detecting false non-existing defects in the defect characterisation process; those defects were situated close to the outer edge of the artefact. Upon the inspection of grey value analysis results, the none- existent defects on the artefact outer edge grey values were close the background/ air, this low contrast affected the surface determination threshold, compromising precise edge detection and defect characterisation. Furthermore, for AM artefacts most of the internal features/defects should contain un-fused or semi-fused powder as shown in figure 5-39 (a), none of the defect analyses or the grey analyses succeeded in identifying and quantifying powder filled defects. This requires further investigation to identify the most appropriate combination of scanning parameters and surface determination strategy for un-fused and semi fused defect characterisation. The surface determination threshold used was not adequate in differentiating between semi-fused powder and solid material, furthermore, the grey value of the unfused powder and semi-fused powder will always be closer to that of the full dense material. Therefore, a more bespoke approach is required to accurately detect unfused powder and differentiate between solid material and un-fused/semi-fused powder.

The designed artefacts scans had shown several imaging deficiencies/artefacts, an example of those artefacts are shown in figure 5-39(b,c) and 43. If those artefacts are not acknowledged and accounted for, they will vastly compromise x-ray process results. Figure 5-39(b) shows an example of a beam hardening artefact that usually appears as cupping between the edge and centre of high atomic number materials [258]. Figure 5-39 (c) shows a low contrast artefact, which is opposite to the beam-hardening artefact. It usually occurs due to incorrect X-ray scanning parameters; excessive tube voltage causes high penetration to the scanned object, resulting in the scanned object outer edge grey value similar to the background/air.

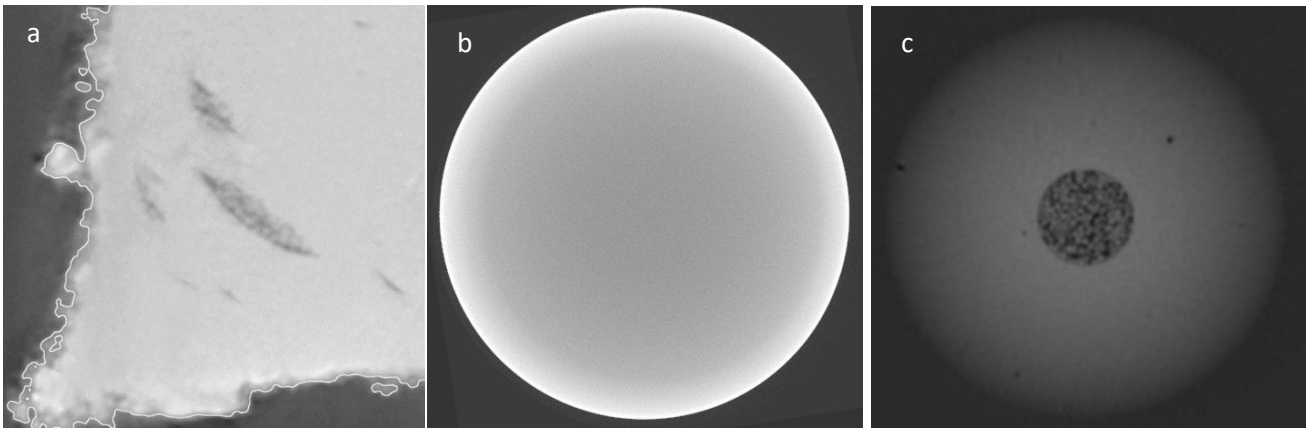

Figure 5-39 a) Unfused and semi fused defects b) beam hardening artifact c) high power artifact

Figure 5-40 (a) shows an out of focus XCT image, where the powder in the upper drilled hole is not clearly visible. Figure 5-40 (b) shows a motion artefact, which was caused by scanned object movement during acquisition. If the sample is placed off-centre resulting in image artefacts, this could be corrected by projection realignment during the reconstruction process. On some occasions, the cone beam artefacts could introduce internal feature/defect geometrical distortion; like those shown in figure 5-40 (b). The distortion increases in distance from the central slice, this is mainly because the reconstruction back projection process relies on the centre slice.

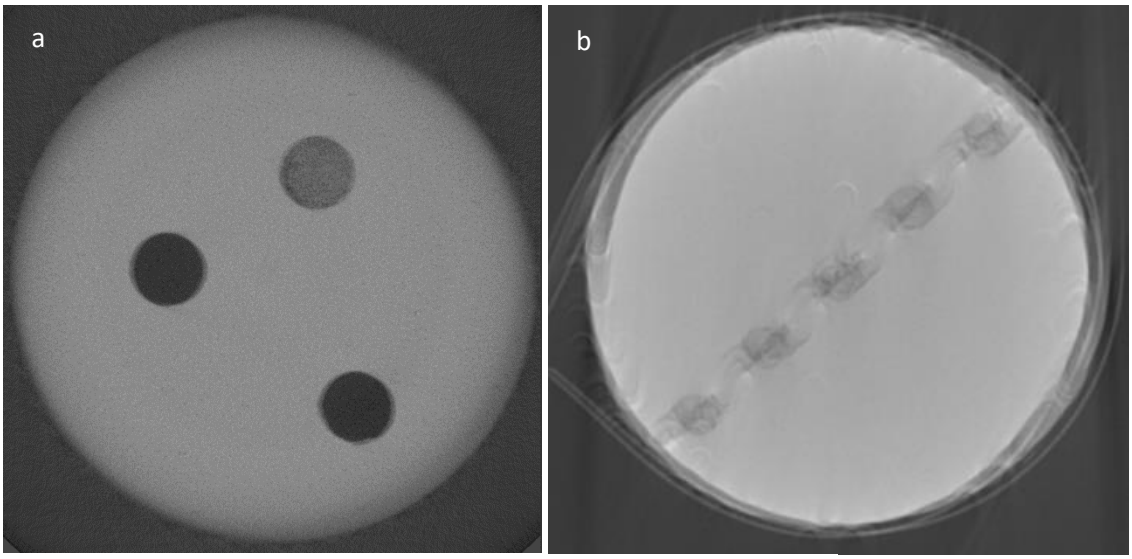

Figure 5-40 a) out of focus artifact b) motion artefact

The first resolution artefact highlighted the presence of a relationship between x-ray beam orientation perpendicular or parallel to the pore. The forged titanium proved that the error percentage in the internal dimension measurement is lower when the measured geometry is perpendicular to X-ray beam when compared to those parallel to the X-ray beam. This conclusion will be investigated through a tilt study in the next chapter.

The defect analysis module in the data processing software is classifies the internal defects based on their probability. The probability values can be random and un-reliable as highlighted in figure 5-41. Where Figure 5-41 (a) shows a defect analysis result with pores highlighted in blue and greens, most of those defects were assigned with a probability value more than 1. The two defects highlighted with

orange circles in figure 5-41 (b) were assigned probability values less than 1, although they are clearly visible and the defect highlighted with a blue circle was not detected altogether.

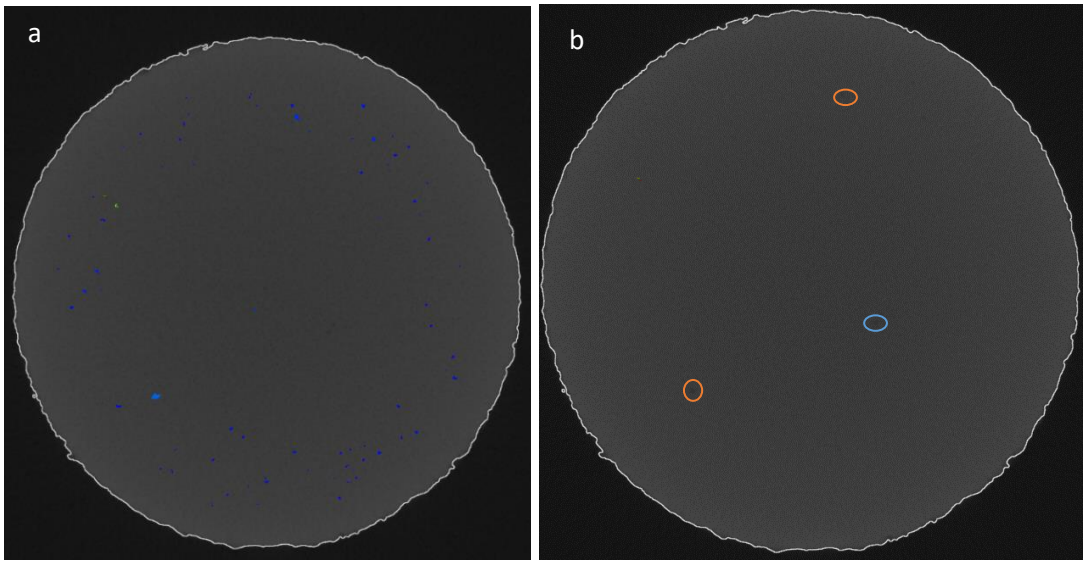

Figure 5-41 a) top slice with highlighted defects b) top slice with low probability defects highlighted

The probability results are often overlooked by most of the software users, the VG studio manual states that the probability threshold can be utilised to differentiate between real internal defects and artefacts by the means of sophisticated image processing algorithms. It was noted that the probability threshold is directly affected by the image contrast; defects with lower probability values tends to have grey values close the material grey value, while defects with higher probability values have grey values closer to the background/air grey values. It is always recommended to start the defect detection analysis on new data sets with a probability threshold of zero to avoid filtering real defects. VG studio max manual states “There is no absolute value for the threshold applicable to all data sets”. Consequently, before using result filtration by probability threshold, the data must be inspected manually to ensure that the contrast is adequate for the defect analysis.

Chapter 6 XCT Porosity method imaging optimization

Statement of Publications Arising from This chapter

The first section is a magnification study where the development work was presented at the 8th Conference on Industrial Computed Tomography, Wels, Austria (iCT 2018), “Development of an artefact to detect unfused powder in additive manufactured components using X-ray CT” [3]. The results were published in the International Journal of Automation Technology, 14, 439-446. Tawfik, A et al. 2020 “Development of an additive manufactured artifact to characterize unfused powder using computed tomography” [259].

In the second section the possibility of reducing noise by using detector filters is investigated, the results were presented at the ASTM conference and published in the ASTM smart and sustainable manufacturing system journal. Tawfik, A et al, no. 1 (2019): 18-30, “Utilizing Detector Filters for Noise Reduction in X-Ray Computed Tomography Scanning for the Inspection of the Structural Integrity of Additive Manufactured Metal Parts [6].

The author performed all the research and wrote the entire manuscript with guidance and editorial changes from his co-author. It is indicated where text from this publication has been reproduced in this thesis.

6.1 Introduction

The developed artefacts for defect characterisation reported in chapter 5 have shown big potential for use in XCT. However, the process needs optimisation. XCT machine settings, X-ray beam filtration, the best angle for scanning the object and the impact of these on scanning resolution requires further investigation. This chapter discusses the impact of voxel size on resolution and porosity analysis. Also in this chapter, X-ray beam filtration techniques and beam scatter are explored. One other factor affecting XCT scan is X-ray beam penetration, in many cases the scanned object needs to be tilted to reduce the beam penetration passage; In this chapter, object tilt is discussed. At the end of chapter 6, case studies for scanning large and dense components are discussed.

This chapter documents several experiments: the first section identifies the impact of increasing the magnification on internal defects characterisation and the overall XCT process. The second investigates the impact of pre and post object beam filtration. The third highlights the impact of beam hardening on grey value and defect analysis and the fourth is a study to identify the effect of the tilting the scanned object on internal defect characterisation. In the final section actual components are used as a case study.

In this section, the impact of voxel size on defect characterisation will be explored using an AM produced artefact shown in figure 6-1 (a). The artefact previously discussed in chapter 5 section 4 was made of Ti6Al4V using an Arcam electron beam melting (EBM) machine. The artefact shown in figure 1 consisted of a 6 mm round bar with designed internal features ranging from 50 µm to 1400 µm [3]. The largest holes (500µm and 1.4mm) contained unfused powder and the remaining holes were left hollow. The diameter and depth of the defects were characterised using a focus variation microscope and the measurements were repeated five times, after which they were scanned using a Nikon XTH225 industrial CT to measure the artefacts and characterise the internal features for defects/pores [3].

The defects were characterised using a focus variation interferometer (Alicona G4) to determine the reference values and ensure the reliability of the results. The defect diameters were measured using a three point best fit circle shown in figure 6-1 (b). The depth was measured by selecting two points

on the upper surface an d creating a horizontal line and a point on the lowest point in the drilled hole shown in figure 6-1 (c). Prior to filling the 1400 µm and 500 µm holes with powder the artefact was scanned using the Nikon XCT.

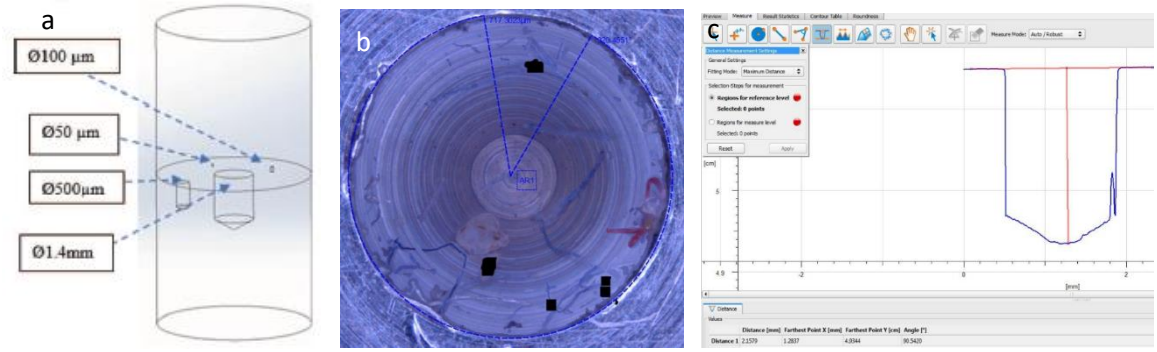

Figure 6-1 a) artefact 3D model) b) Alicona defect diameter measurement c) Alicona depth measurement

To reduce the number of the process variables, the scanning parameters (shown in table 1) such as filament current, acceleration voltage, X-ray filtering material and thickness were kept constant. G Studio Max 3.1 (Volume Graphics, Germany) software package was used for data processing, surface determination and defect/porosity analysis.

After the holes were filled the area of interest was rescanned using 38µm, 20µm, 15µm, 13 µm, and 7µm voxel sizes. The XCT sources of error are multiple and as yet not fully quantified, to minimise uncertainty each scan was repeated 5 times for each magnification [3]. In the reconstruction process no beam hardening or noise filtration was used. The obtained results were analysed using VG Studio Max 3.1. The surface determination and porosity analysis parameters were kept constant for each voxel size scan to ensure that the results were comparable.

Filter	0.5 mm copper
Exposure	4000 ms
Filament current	55 µA
Acceleration voltage	155 KV

Table 1 XCT scanning parameters

The dimensions and volumes for each defect were compared between different voxel sizes, XCT results and the Alicona reference results. The time taken for analysis was compared against the voxel size.

The scanning parameters shown in Table 1 were kept constant throughout the experiment. A 4000 ms exposure time was selected to compensate for the difference in magnification due to the difference in X-ray beam penetration.

Various inputs had an influence on the process of obtaining of a high-definition X-ray image. One of the variables was the accuracy of the turntable's axis. XTH 225 XCT uses a Newport high performance rotation stage with a guaranteed accuracy of +/- 7.5 mdeg .

One other variable is nonhomogeneous shading. Nonhomogeneous shading is a phenomenon whereby the image is corrupted by false intensity variations resulting from the integral imperfections of the image formation process. This phenomenon has a negative impact on the automatic image processing process.

As previously mentioned in chapter 3 section 6there are several methods of shading correction. The one used in XCT is the prospective objection dependent method. In this method a background image is acquired after which the shading is tuned according to the grey value of the background.

The different magnifications were scanned individually and not using patch scans. This way, the shading correction could be refreshed after each scan. As previously discussed in chapter 3 section 8, the results of the XCT scan are presented in the form of a histogram in which the number of voxels is plotted against the grey value. In the case of a single material scan, the histogram contains two peaks, one peak represents the material, while the other peak represents the background (air).

Usually, a single threshold ISO grey value in the greyscale between the two peaks must be selected for material edge detection. In most engineering applications the automatic threshold ISO value is 50% [260,261], which positions the threshold an equal distance between the two peaks of the histogram. In some situations, the use of the ISO 50% threshold can cause an error in the results by selecting some materials as pores or vice versa. However, in the case of this study the ISO 50% threshold was implemented to allow for comparison of results.

6.2.1 Results

To ensure result reliability, the Alicona measurements were carried out 5 times for each defect and the average value was used. The volume of each defect was calculated assuming that each defect consists of a cylinder and a cone.

The XCT data was analysed using Volume Graphics VG Studio Max 3.1. The surface determination and defect analysis settings were kept constant to make the results comparable. The diameter was determined using the best fitting geometry measurements based on the surface determination. Thirteen points were selected on the diameter to generate a circle. The depth was evaluated using the distance measured by selecting the highest and lowest points in the defect. Figure 6-2 shows full part XCT 3D image where 6-2 (a) shows an image of the artefact scanned with a voxel size of 76 µm. Figure 6-2 (b) shows an image of the artefact scanned with a 38µm voxel size and figure 6-2 (c) shows the artefact scanned with a 15µm voxel size.

In figure 6-2 the colour difference highlights the variation in pore volume. The defect analysis has shown that at low magnification (76µm) the defect characterisation process failed to detect the presence of unfused powder. This is evident by the colour of defect 1 that is highlighted as one large pore (red), indicating the volume is larger than 3.31mm$^{3)}$. Whereas the 500 and 100µm holes are blue which is less than 0.82mm^{3}).

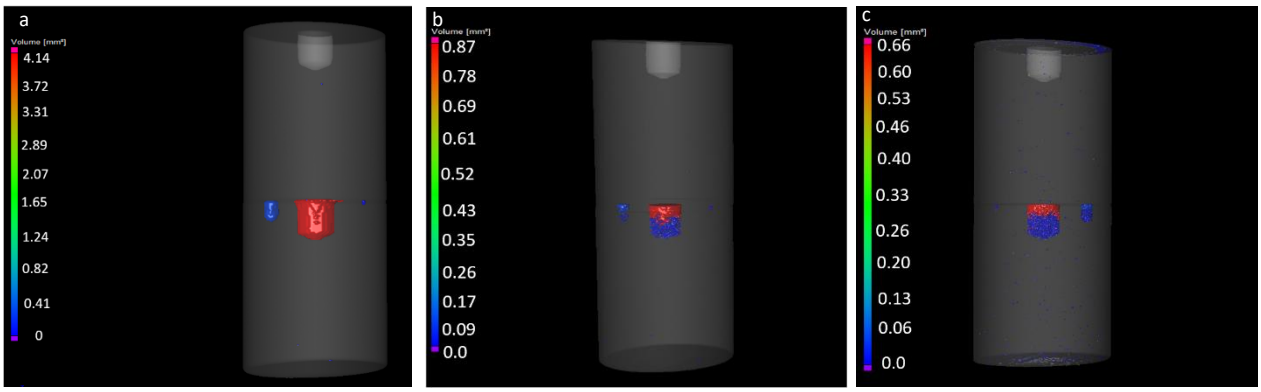

Figure 6-2 defect analysis results (a) 76µm voxel size (b) 38µm voxel size (c) 15µm voxel size [2]

In figure 6-2(b) the 38µm voxel size defect analysis detected the variation in grey value indicating the presence of air gaps between the powder particles. In the case of the 15µm voxel scan, the analysis process detected the presence of the powder particles and correctly identified the air gap between the particles.

Figure 6- 3(a) shows the top view of the defect analysis for the 13µm scan where the powder particles are clearly visible at this voxel size. Figure 5 shows the largest 2 defects filled with unfused powder scanned at 7µm voxel size.

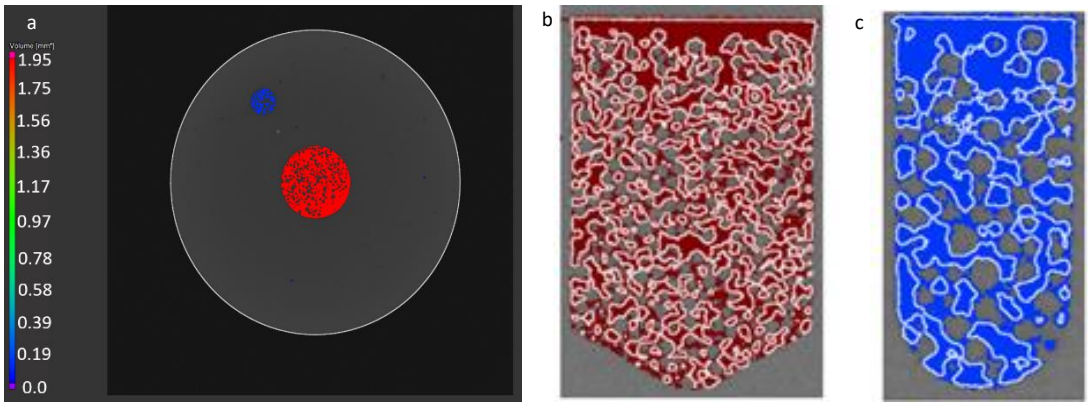

Figure 6-3 (a) 13µm voxel size - 2D image of defect analysis Figure 3 (b) 7µm voxel size - 2D image of defects 1 filled with un-fused powder (c) defect 2 filled with un-fused powder

The air gaps between the powder particles are not uniform owing to the difference in the diameter and shape of the powder particles. It is evident that using the correct XCT settings it is possible to identify the existence of powder and the overall shape of the defect, as well as the size of some of the cavities between the particles.

6.2.2 Discussion

In this section the results at each magnification are compared to the Alicona reference results. The obtained results from this study confirm the ability of XCT to accurately quantify internal defect dimensions and volume.

Figure 6-4 a) shows the diameter comparison, scanning using high magnification at Voxel size 7µm the difference between the Alicona and XCT results is 0.3% for defect 1's diameter and1.4% for defect 2's diameter. In the case of the micro defects 3 and 4 the difference in diameter is 2.9% and 3.7% respectively. Comparing the low magnification results (75µm), the difference between the Alicona and XCT results for defects 1 and 2 are 7.8% and 13.2% respectively. For defect 3, the difference is 26.1% and for defect 4 the magnification was not sufficient to allow for detection. When considering the difference in depth as shown in Fig. 6-4 b), the difference between the reference Alicona results and those for the XCT for defects 1 and 2 at high magnification was 1.9% and 2.4% respectively. For defect 3, the difference is 4.3% and for defect 4 the difference is 83%. For defect 4, the Alicona depth measurement is not correct because of the instrument's inability to image the bottom edge of the drilled defect correctly.

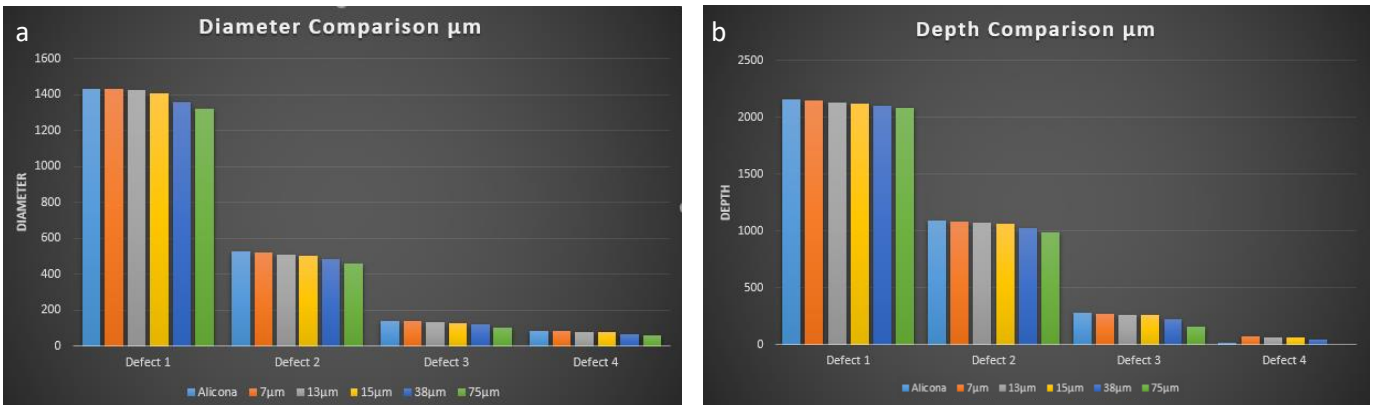

Figure 6-4 a) Diameter comparison b) Depth comparison

The comparison of the low magnification depth results shows that the difference between Alicona and XCT is 6.4% for defect 1 and 10.5% for defect 2. For defect 3, the difference is 45.6%. As with the diameter results, the magnification was not sufficient to allow for the detection of defect 4 [3].

Figure 6-5 a) shows a volume comparison for defects 1 and 2 filled with unfused powder. The XCT results for different magnifications found that there was 25.8% difference between the 7µm and 38µm voxel size for defect 1. In the case of defect 2, the difference between the 7µm and 38µm voxel size volume resulted in a difference of 23.4%. The results of the low magnification cannot be compared due to failure in detecting the presence of unfused powder. The dropping volume values from low to high magnification proved that the process was able to identify the difference in the grey value between the powder particles and air gaps trapped in between.

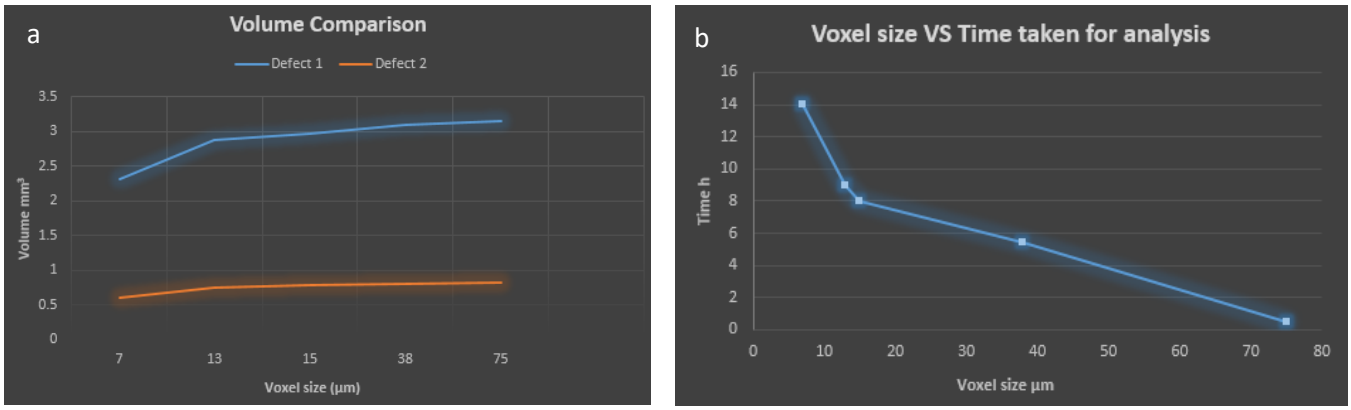

Figure 6-5 a)Defect 1 and 2 volume comparison b) Time taken for analysis VS Voxel size

Figure 6-5 b) shows the voxel size versus the time taken for analysis; the time required for defect analysis for the largest voxel size (75 µm) is reduced by 95% when compared to the analysis time for the smallest voxel size (7 µm).

It was also noted that the number of particles increased, doubling the file size. The impact of magnification on the defect analysis process were investigated. This investigation found that the results of the high magnification scan (7 µm) were within 2% of those for the Alicona. Conversely, for the low magnification (75 µm), the difference was within 15% for the large defects, however, the difference for the micro defects was not detectable. As expected, a higher magnification will provide better image resolution, which will automatically result in a larger difference in the grey value of unfused powder and solid material, enabling the detection of unfused powder.

Whilst scanning the specimen at high magnification improves the accuracy of the obtained results, there are substantial practical limitations in doing so as the small sample volumes and high acquisition time can be a big obstacle in an industrial environment.

This study enables users to generate relevantly sized defects and evaluate the ability of the defect analysis process to identify the magnification threshold for detecting unfused powder in AM parts. The size and quantity of acceptable internal defects depend solely on the intended design. This investigation proved that the detection of micro defects, such as gaps between unfused powders does not require a high magnification. The best strategy is to scan the component using a magnification as low as 38 µm voxel size to identify the location of the defects then rescan the area where the defect is located using a higher magnification. This method allows for the scanning of larger components in a shorter period without compromising the accuracy of the results. The limitation in this case involves scanning relatively large components whereby scanning using a 38 µm voxel is impossible. For these components the component needs to be cut into smaller sections and these sections scanned. This experiment illustrates the need to develop high-resolution scanning capabilities for industrially relevant measurement volumes and component sizes.

6.3 Filtration study

the recent development of industrial CT has enabled inspection of the integrity of mechanical parts without physical sectioning. Using XCT presents many challenges prohibiting industry from widely implementing the technology. The existence of several variables such as filament current, filter material and filter thickness are directly related to the presence of noise and influence the accuracy of the inspection process [6].

Noise in the resultant reconstructed image is the result of low energy X-rays being absorbed by the detector causing large variations of brightness on the computed image, other noise sources such as detector variations and electronic noise are further sources of error. Additionally, the reconstruction method will also have a response to the noise scatter and can contribute to the resulting image noise. The presence of noise can skew the resulting image as shown in figure 6-6 (a) and (b) and create the illusion of pores/defects that are not actually present thus vastly compromising the results of the analysis. Noise reduction is vital in improving the reliability of CT imaging of AM components.

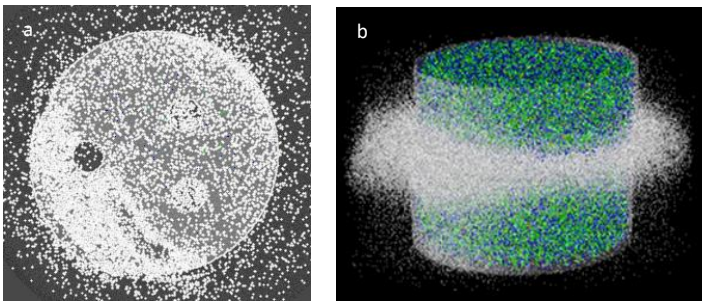

Figure 6-6 a) Top view of titanium artefact with excessive noise b) XCT 3D view of the artefact

This study investigates the possibility of reducing noise by using detector filters, two filter types of 100µm thick aluminium, and100um thick copper filters were compared to a conventional tube filter. The artefact used in this study (see chapter 5 section 4) consisted of a 6mm Ti6Al4V round bar with designed internal features ranging from 50µm to 1400µm containing a mixture of voids; two filled with unfused powder and two unfilled. The diameter and depth of defects were characterised using focus variation microscopy then scanned with a Nikon XTH225 industrial CT to compare the measured internal features. The analysis was carried out using VGStudio Max 3.0(Volume Graphics, Germany) software package to evaluate surface determination and defects/ porosity.

The XTH 225 used in the present study uses tungsten due to its higher atomic number allowing for higher intensity X-rays. As previously mentioned in chapter three section 1.1 electrons are accelerated from the cathode to the anode by electrostatic attraction. This is achieved using a large potential difference causing the cathode and anode to become highly negatively and positively charged respectively.

As the electrons collide with the anode, energy is released in the form of heat with about 1% of the energy released as X-rays [262]. This takes place inside a vacuum to avoid collisions between electrons and foreign atoms as this would compromise the efficiency of the process.

When the electrons interact with the tungsten two types of X-rays are generated. The first are known as characteristic X-rays, which takes place when the accelerated electron collides with an inner shell electron from the tungsten causing it, along with the accelerated electron to be ejected from the atom. This results in the tungsten atom becoming unstable due to the missing electron from the inner shell. This causes an electron from an outer shell to drop in energy level to replace the missing electron

thus stabilising the atom. During the transition, the electron emits its excess energy as an X-ray photon [274]. More energy is released when the energy level difference between the inner shells and outer shells is greater thus producing higher-energy X-rays.

The second type of X-ray generation are known as Bremsstrahlung (or braking radiation in English). This occurs when the accelerated electron passes near the nucleus of a tungsten atom causing the electron to slow and deflect its path. The energy lost from the reduction in speed is emitted as an X-ray photon. Approximately 80% of X-rays are generated in this way and tend to have lower energy levels compared to characteristic X-rays [263].

CT image quality can vary due to several reasons, a major problem is the presence of noise. Image noise is the term used to describe when an X-ray scan produces an image that looks grainy and unclear (see figure 8) due to the large variation in image brightness. This is acknowledged as quantum noise and is a result of X-ray photons interacting with the atoms of the specimen [264].

As previously discussed in chapter 3 section 9.1, the manifestation of projection noise is the result of low energy X-rays being absorbed by the detector causing discrepancies in the brightness; creating cavities or dark spots in the collected images that are not present. This can lead to both a false positive or false negative detection of defects, which is especially evident when real defect is in the order of single voxel size.

One of the sources of noise is the phenomena of Compton scattering, which takes place when the x-ray photons collide with an outer shell electron of the absorbing medium resulting in the loss of energy. The x-ray is deflected from its original path and the loss of the energy results in a scattered longer wavelength x-ray. The deflection angle is directly proportional to the energy loss [265]. Other sources of noise relate to the detector (grain/structure), electronics and/or reconstruction process.

As previously shown in in chapter 5 section 9, beam hardening and scatter results in dark areas with surrounding bright spots mainly between two highly attenuating objects. The resulting image noise can be reduced by implementing iterative reconstruction. Also utilising dual-energy CT can reduce beam hardening [266,267].

Noise reduction plays a crucial role in improving the reliability of CT imaging. The study detailed in this section seeks to investigate how the use of physical filtration can affect the quality of a CT image and whether the resulting images can effectively categorise known defects/artefacts in a component.

As previously mentioned in chapter 3, attenuation is the continuing loss of flux intensity while travelling through a medium. In the X-ray process, the attenuation is the capability of a material to absorb X-rays through the photoelectric effect; reducing the overall beam intensity. In general, materials with higher atomic numbers can attenuate higher X-ray energies, materials like aluminium and copper can attenuate X-rays at varying energy levels and are recommended to use as filters. Aluminium has a relatively high attenuation level for energies below 2000eV suggesting that this would be a good material for a detector filter as this will absorb the low energy X-rays caused by Compton scattering [268].

To evaluate the X-ray beam filter impact on the defect analysis results, the X-ray beam attenuation must be understood. The attenuation equation previously mentioned in chapter 3 section 1 states that the scanned object attenuation rate is determined by the scanned material and the incoming X-ray energy [269] and each material has its own attenuation coefficient. The material mass attenuation coefficient is given by:

$$\frac{\mu}{\rho} = -(\rho x)^{-1} \ln\left(\frac{I}{I_0}\right) \qquad \text{Equation 1}$$

Where ρ is the material density, x is material thickness, I is the beam intensity and material penetration and I_0 is the beam intensity prior to material penetration. The material mass attenuation coefficient unite is ($cm^{-2}g^{-1}$). From equation 1 we can conclude that the required beam filter can be calculated if the pre-penetration beam intensity is known; this conclusion is only correct if the X-ray beam is monochromatic (single energy X-ray). X-ray beams consist of a range of energy spectrums known as polychromatic, which causes inconsistent attenuation of the energy spectrum [270]. The fluctuation in the energy spectrum makes it impossible to precisely calculate X-ray beam intensity and link the image quality to beam attenuation; this can be only done by experimentation.

X-ray beam attenuation for copper and aluminium is presented in figure 6-7, as previously mentioned materials with high atomic values attenuates higher energies of X-ray beam. The photoelectric effect is presented as a spike in the graphs, this spike shows the material absorption. Figure 6-7 (a) shows the copper attenuation coefficient vs absorption coefficient; copper has an attenuation rate of 10000eV; thus, copper is adequate for absorbing low beam energy, minimising the beam hardening effect. Figure 6-7 (b) shows the aluminium mass attenuation coefficient vs mass energy absorption coefficient, the aluminium attenuation rate is sufficient for energies just under 2000eV, therefore aluminium can be used for the absorption of low beam energies produced by Compton scattering. Conversely, the graph does not take the material thickness in consideration, therefor the filter material thickness requires experimental investigation.

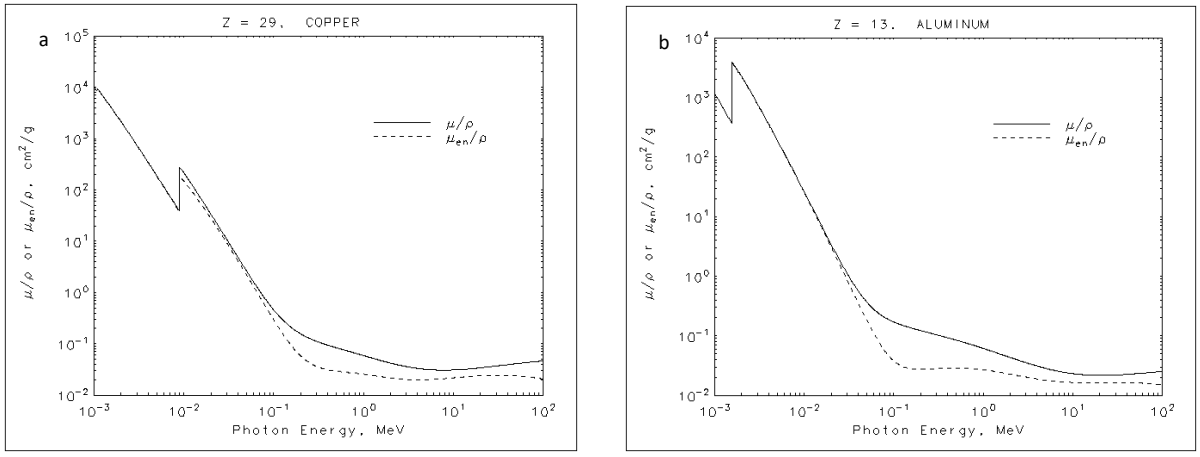

Figure 6-7 a) Copper mass attenuation coefficient VS mass energy absorption coefficient b) Aluminium mass attenuation coefficient VS mass energy absorption coefficient

Salzali et al investigated the impact of using different filter thicknesses on XCT scan results [271]. The author used an automotive engine rear mount; the scanning parameters were 135kV and 2.7mA and kept constant throughout the experiment. The rear engine mount was scanned 4 times and the filtration varied for each scan from (no filter, 5mm Al, 5mm Cu, 2.5mm Cu + 2.5mm Al). The results from this study showed that the unfiltered scan failed to detect defects within the part, whereas all the other filtered scans were able to detect defects. The best contrast was achieved by combining the aluminium and copper filters. The scan which utilised aluminium alone was too bright. The paper presented a clear indication that a correct filtration strategy can improve image quality despite the size of the component and likely consequent voxel size that are not relevant for small AM parts as discussed in this study. Consequently, no information was given regarding accurate voxel size, ergo magnification and results were largely qualitative.

A further study by Nivedita et al [272] investigated the impact of filtration on the image quality of CT, in this experiment the author used low power to scan six different inserts composed of polyethylene, Teflon, Perspex (acrylic), Lexan, nylon (aculon), and water. Different thicknesses of copper and aluminium filters and filter combinations Cu 1 mm, Cu 2 mm, Cu 3 mm each in combination with Al (1 mm, 2 mm, 3 mm, and 4 mm), respectively were used. The results of this study confirmed that for these low-density materials found the aluminium filters produced the best images when compared to images produced with no filter, copper filters or combined (Cu + Al) filters. Kueh et al modelled the penumbra in CT using a Nikon 225 [273]. The author carried this out by deriving Beer's law to quantify blurring in the CT image. The results of this study showed that the source itself produces secondary penumbra due to internal scatter that affects the measurement.

Kourra et al investigated the influence of pre and post x-ray beam filtration threshold dependent and independent dimensional measurement [274]. The author used a CMM calibrated 48mm x 48mm x 8mm machined part, the specimen was scanned without filter once, three times with pre-filtering and once with post filtering. Further scans were performed with different combinations of post filters and pre-filters, in total 11 scans were performed. The results of the study showed that combining pre and post radiation reduces the grey value variation (noise) thus minimising scattering and beam hardening. Also, the combination of pre and post filtration reduced the edge blur and shadowing, and enhanced the effectiveness of threshold selection when using methods like the Otsu [275] threshold method. This experiment is investigating the impact of source and detector filters on image quality of metal additive manufactured components, which are considered specifically in order to identify optimal filtration strategies.

6.3.1 Initial experimentation

An initial experiment was conducted in which a cylindrical 8mm diameter Titanium artefact with designed internal defects was scanned as shown in figure 10, The work piece was scanned using a 1mm Cu source filter, 12µm voxel size and 7.2W and 130kV power and voltage respectively. Defect analysis showed a large number of defects appeared to be present as shown in figure 10 a), it was evident that this was a false result and that there was skew due to noise. The experiment was repeated using a 250µm copper source filter and the obtained data set appeared to have much less noise (see figure 6-8 (b)). The defect analysis detected the presence of the three dissimilar volume defects correctly (blue, green and red) as shown in figure 6-8 b. The low power and 1mm thick filter resulted in lack of X-ray penetration. Furthermore, the noise was exaggerated in the reconstruction process, producing a very noisy image as shown in figure 6-8 (a).

The results from this first experiment enhanced the drive to investigate the possible beneficial impact of filtration on the results of XCT scans of such materials and structures. Post-processing methods such as noise reduction at reconstruction, scatter reduction and noise filtration in visualisation software have been shown by experiment to mask some porosity and internal features, giving a misrepresentative result. It is therefore vital to select an optimised combination of CT parameters and filtration to obtain reliable results when measuring for structural integrity.

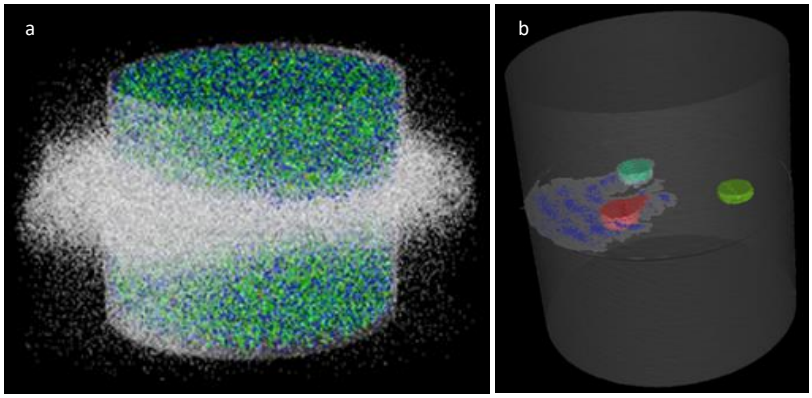

Figure 6-8 a) High magnification scan with excessive noise b) High magnification scan with 250µm Cu filter used.

6.3.2 Methodology

The drilled artefact discussed in chapter 5 section 4 was made of Ti6AL4V material built using an Arcam Q10 electron beam-melting machine (EBM). The artefact shown in figure 6-9 (a) encloses 4 drilled "defects" (sizes; 1400µm, 500µm, 100µm, 50µm) holes of sizes chosen to test the resolution limit of the CT machine. A CNC machine equipped with micro drills and end mills was used to drill the so-called defects into the surface of the artefact as shown in figure 6-9 (a). The 1400µm and 500µm defects shown in figure 6-9 (b) were filled with titanium powder (45-10 µm grain size), whilst the 50 and 100µm diameter holes were left as voids. The complete work piece consists of 2 halves; the lower half contains the drilled defects and both halves were machined using a diamond-cut finish. This meant that the two halves could be rung together using a similar principle to that employed for slip gauges.

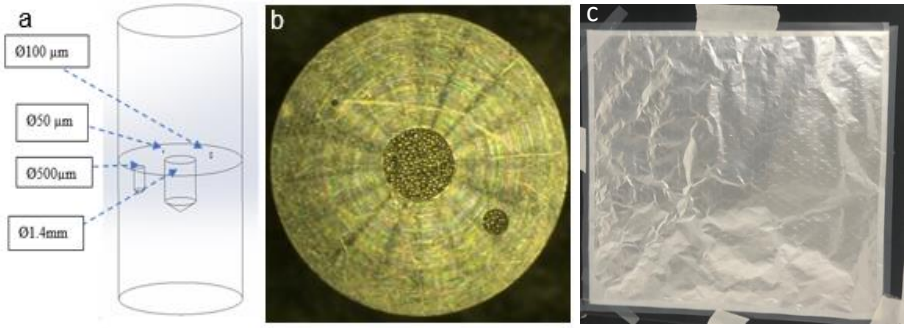

Figure 6-9 a) artefact 3D model, b) top view of the artefact with defect 1 and 2 filled with powder, c) Aluminium detector filter.

Prior to ringing the parts, the defects were characterised using a focus variation (FV) microscope (Alicona G4 – Alicona, Graz, Austria) to determine the reference values for the diameter and defect depth. The Alicona was calibrated per the manufacturers' recommendations. The minimum lateral resolution is 4.4µm with minimum repeatability of 0.44µm and a step height accuracy of 0.05% [276]. In order to determine the best filtering strategy for imaging the artefact discussed previously. several different filter combinations were used, as shown below;

- No Filter
- 125 µm Cu Source filter
- 100 µm Cu Detector Filter
- 100 µm Al Detector Filter

In each case, the pre-measurement CT grey level histogram was used as an iteration loop to ensure that the best image contrast was achieved for each given filter setting. The pre-measurement histogram is directly affected by the x-ray filter and CT settings used, thus using different filter thickness or material will cause changes in the histogram.

For clarity, the 'source' filter denotes a filter that is placed at the Beryllium window of the X-Ray source, whereas the 'detector' filter is a filter that is placed over the detector on the opposite side of the component to the X-Ray source. Two different detector filters were used in this study, the 100 µm aluminium filter is shown in figure 6-9(c). the scan parameters are shown in table 2.

Exposure	2000 ms
Gain	12dB
Voltage	175kV
Power	9.5W
Magnification (voxel size)	7.9µm

Table 2 XCT parameters

To reduce the number of process variables, the CT settings and surface determination were kept constant throughout the experiment. The CT was calibrated to manufacturer recommendations prior to scanning to reduce the influence of geometry error. The selected parameters were optimised by reference to the grey level histogram for the test scanned artefact as explained previously. The acquired data processing, surface determination process and defect analysis were carried out using VGs Studio Max 3.1 (Volume Graphics, Germany).

6.3.3 Results

In this section, the results obtained from the Alicona are compared to those from the XCT. Defect depth and diameter are characterized and reported from the Alicona data. Each XCT dataset is then analysed and compared for the same parameter values.

6.3.3.1 Alicona results

The Alicona was used for the determination of the drilled holes dimensions (depth and diameter) prior to powder filling. The results are shown in table 3.

Defect	1	2	3	4
Diameter	1.438mm	524µm	141µm	83µm
Depth	2.161mm	1.084µm	280µm	16µm

Table 3 Alicona results

As previously mentioned in chapter 5, The defect depth was measured by creating a horizontal planar line on the level top surface of the artefact and a point on the lowest point of the drilled hole, a perpendicular line was then created to calculate the length. The diameter was measured using a multi-point best-fit circle [3].

6.3.3.2 XCT results

In this section the results obtained from the XCT scans are presented, the artefact was scanned using different filters as mentioned before and with a 7.9µm voxel size. Subsequent data analysis was carried out using Volume Graphics VG Studio Max 3.1. As previously mentioned in chapter 5, the defect depth was measured by firstly establishing the upper plane of the surface. The lowest point of the hole was then manually selected and a perpendicular distance was calculated, the defect diameter was calculated by definition of a multi-point best-fit circle. In order to ensure that the same points

were selected between the scans, the location of the measurement was referenced to the base of the artefact in the analysis software.

Using this method for characterising the defect diameter and depth is dependent on the level of optimisation of the scanning parameters and the accuracy of surface determination and contains a level of subjectivity. To ensure that the difference is not just random variation, the analysis was carried out 5 times for each filter and the mean value was used. The XCT results for hole diameters are shown in table 4.

Filter	1/(D.A)	2/(D.A)	3/(D.A)	4/(D.A)
No filter	1.357mm/(81µm)	487µm/(37 µm)	126µm(15 µm)	89µm(6 µm)
125µm Cu source	1.381mm/(57µm)	508 µm/(16µm)	133 µm(8 µm)	87 µm(4 µm)
100µm Cu detector	1.409mm/(29µm)	513µm/(11 µm)	139 µm(2 µm)	87 µm(4µm)
100µm Al detector	1.435mm/(3µm)	529 µm/(5µm)	145 µm(4 µm)	85 µm(2 µm)

Table 4 XCT values for defect diameter and difference from Alicona reference (D.A).

It is evident from the results that the difference in diameter between the different filters and the Alicona results were within 4% for defect 1 while using no filter. For defect 2 the no filter scan was 7% from the Alicona. Figure 6-10 shows the diameter comparison.

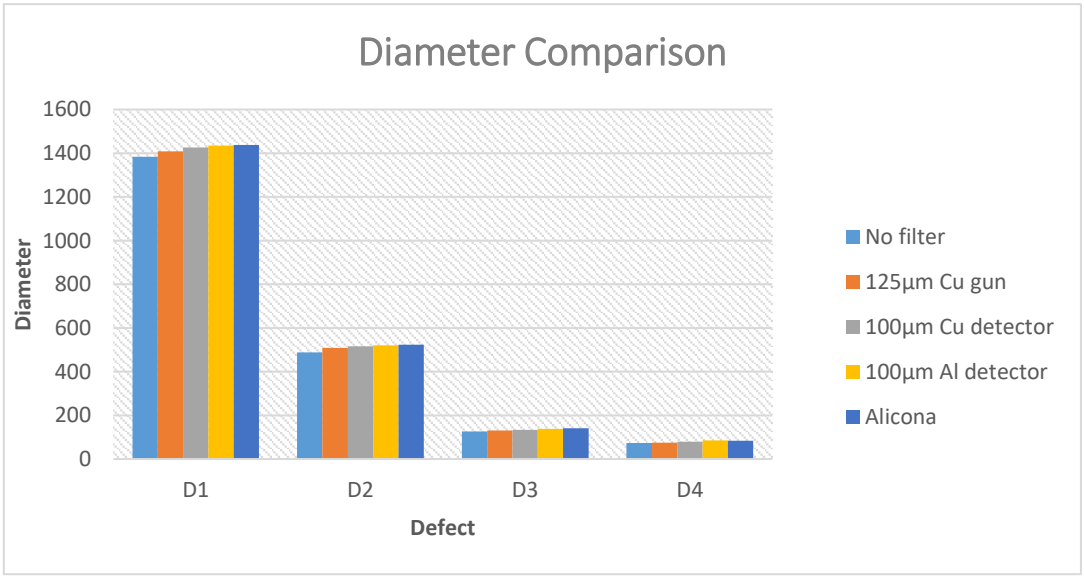

Figure 6-10 Diameter comparison graph.

Generally, the differences in diameter are low but there is a marked difference between the result of the unfiltered scan compared to the Alicona reference measurement (3.9%) and the result between the Al detector filter and the Alicona reference measurement (0.2%) for defect 1. The pattern is similar for the other defects being measured albeit the percentages scale somewhat with size, given the ratio of voxel size to measured feature size. In all cases the Al detector filter gave the best result when compared with that calculated from the Alicona dataset. The XCT results for the hole depth are shown in table 5, and the difference from the Alicona reference value is included in the table and referred to as (D.A).

Filter	1/(D.A)	2/(D.A)	3/(D.A)	4/(D.A)
A	2	1	2	1
No filter	2.182mm(21 µm)	1.112mm(28µm)	298µm(18µm)	87µm (NA)
125µm Cu source	2.174mm(13µm)	1.098mm(14µm)	292 µm(12µm)	81 µm (NA)
100µm Cu detector	2.171mm(10µm)	1.095 mm(11µm)	294 µm(14µm)	84 µm (NA)
100µm Al detector	2.164mm (3 µm)	1.080 mm (4 µm)	283 µm (3 µm)	78 µm (NA)

Table 5 XCT values for defect depth and difference from Alicona reference (D.A).

Figure 6-11 shows the comparative results for defect/drilled hole depth between the filtration methods. As with the results for defect diameter the largest differences in calculated size when compared to the Alicona reference values were those from the unfiltered dataset. The largest scaled difference within this was found in defect 3 with a difference of 6.1% between values.

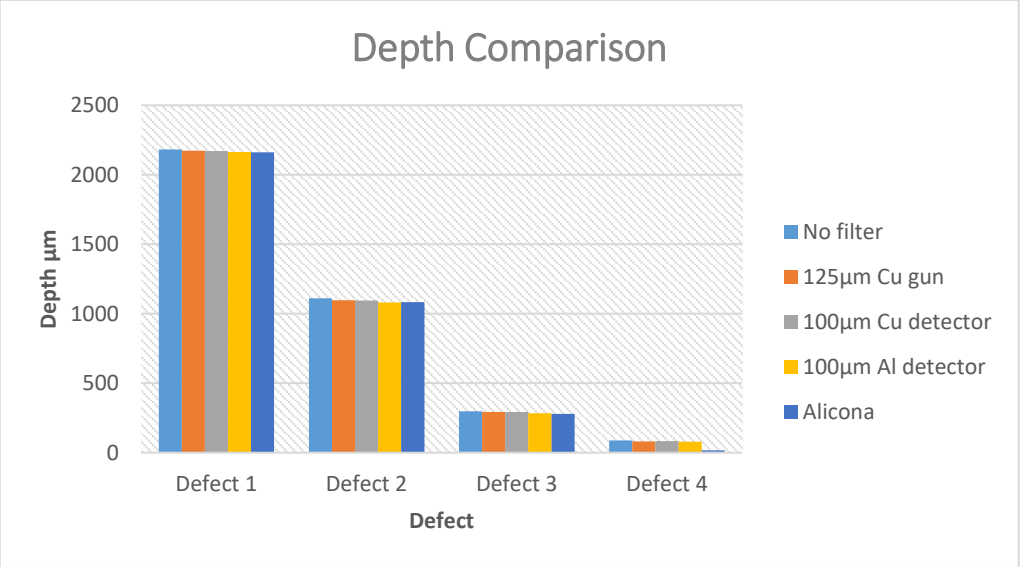

Figure 6-11 Depth comparison graph.

When comparing the Alicona results to the different filtration methods, the largest difference was for the no filter scan then the 125µm source filter, 100µm copper filter, finally the 100µm aluminium filter was the closest to the Alicona results.

6.3.4 Grey value histogram comparison

As previously discussed in chapter 2 section 8, the XCT grey value histogram is a graphic that illustrates the distribution of densities of the X-ray beam through attenuation. High attenuation is presented as high grey values on the spectrum suggesting high-density material while the lower grey values represent low attenuating material.

The area under the histogram peak represents the proportion of the X-ray path that corresponds to any particular attenuation level. Tall peaks represent a large proportion and vice versa. Therefore, increasing the filtration increases the proportion of attenuation resulting in the overall shift of the histogram to a higher level.

The shape of the XCT histogram reflects the image quality [277]; beam hardening, scatter artefacts, image blur and noise amongst other factors influence the scan quality. The grey values in the histogram represent the level of contrast of any particular voxel.

he height of the histogram at any individual grey level is determined by the number of voxels that equals to that grey level. In the case of a single material scan, the histogram will show only two peaks; one for the background (air) and the second for the material.

In the case of fully dense materials, the distance between the two distributions can be identified as the difference in contrast. However, in the case of a material of variable density the histogram will be less defined in shape.

For instance, in the case shown below (figure 6-12) where there are defects containing unfused powder; which is of a slightly lower grey value to the bulk material, the resulting histogram has a characteristic 'bump' or widening of the grey level peak (as highlighted in figure 6-12 (a)). Ideally, to determine unfused powder with the maximum possible clarity the width of this 'bump' and consequent contrast between that and the grey level of the bulk material should be maximised.

Since the same voxel size was used throughout the experiment, any change in the width and height of the peaks in the histogram will be due to a difference in contrast. Consequently, it was also noted that the width and height of the pre-material 'bump' on the histogram is different for each filter. Figure 6-12(a) shows the histogram for the non-filtered scan, which shows the lowest level of contrast of the scans performed. Although the histogram peaks are well spread the pre-material bump width is lowest level of contrast of the scans performed.

Figure 6-12 (b) shows the histogram for the 100µm Cu source filter, the pre-material bump width is larger than that of the no filter histogram. Figure 6-12 (c) shows the 100µm Cu detector filter scan, in this case the image has a higher level of clarity than either of the previous two scans. It is notable that the 'bump' portion of the histogram relating to the unfused powder is higher in intensity than that of the 100µm source copper filter. The scan performed with a 100µm Al detector filter is shown in figure 6-12(d). It can be seen that the unfused powder has the best definition and contrast from the bulk material of all.

Upon comparison of the histograms relating to all four filtration strategies, it is clear that the use of a detector filter has a beneficial effect, such that unfused powder can be differentiated from bulk material of the same composition and that the higher level of contrast that is achieved allows for a more stable analysis to be carried out.

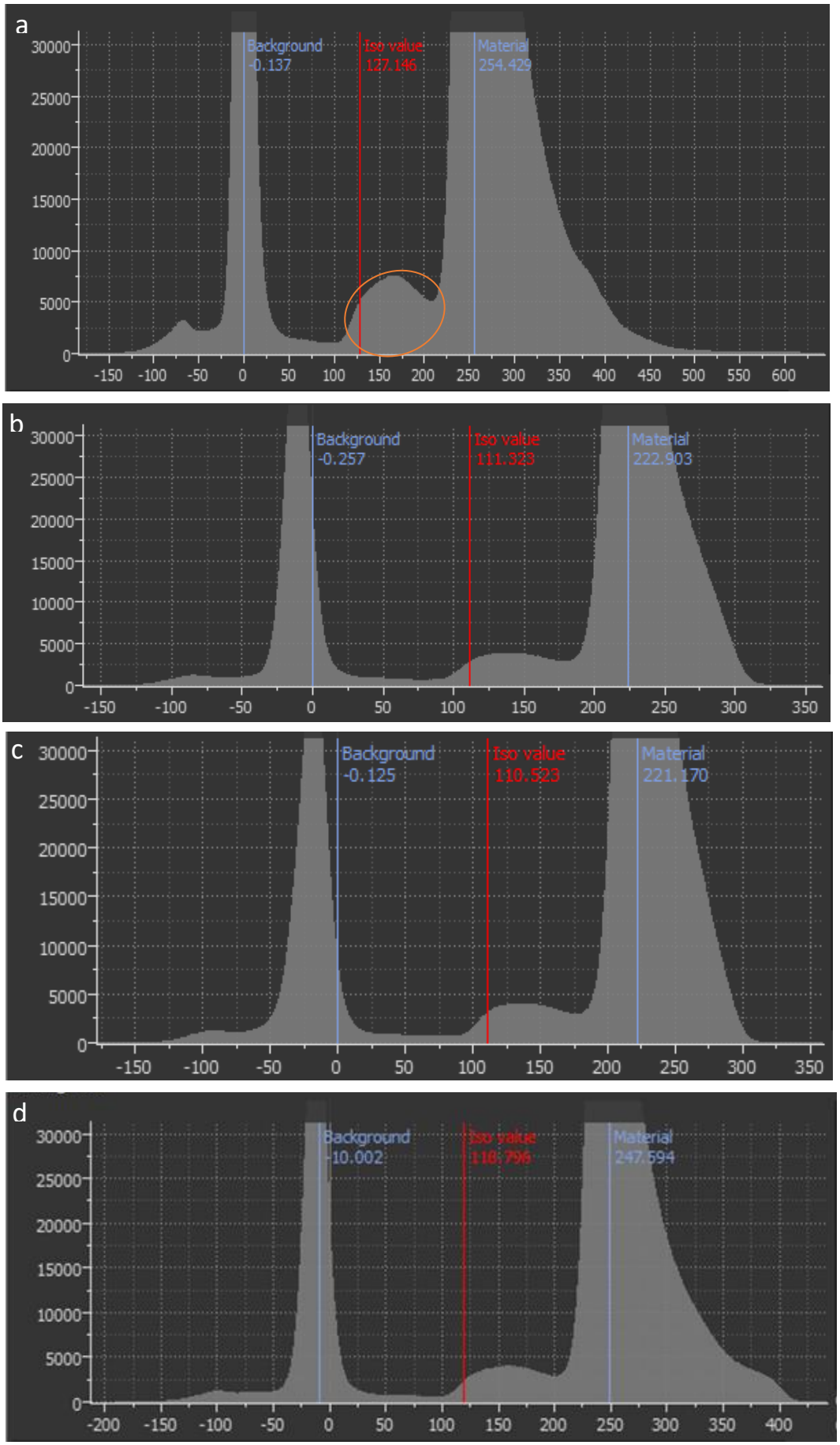

Figure 6-12 a) Histogram - no filter, b) Histogram - source filter, c) Histogram - Cu detector filter, d) Histogram - Al detector filter.

6.3.5 Discussion

In the XCT scan process there are several sources of image noise; two of them are photoelectric effect and Compton scattering. The photoelectric effect takes place when the inner shell electron completely absorbs the X-ray photon, ionising the atom and producing a photoelectron. The photoelectron phenomenon can be avoided by using High X-ray intensity whenever scanning large components. Beam hardening occurs when a high proportion of low intensity X-ray beams are absorbed by low-density materials; creating dark areas. The Compton scattering phenomenon is the change in the direction of the X-ray beam increasing its wave length (resulting in energy loss). This occurs due to the partial interaction between an outer shell electron and the X-ray photon.

The Compton scattering phenomenon is solely dependent on the material density and thickness. This is due to the existence of outer shell electrons in the path of the X-ray increasing the probability of interaction [278,279]. The aforementioned two types of noise and additional reconstruction noise mostly occur due to the operator, as the XCT scanning parameters are optimised by the operator, this optimisation is subjective and based on experience which results in non-useful data especially if quantitative information is required.

The results obtained from this experiment show that quality of the results can be largely affected by the presence of such noise but utilising the correct X-ray filtration strategy can minimise noise. Furthermore, the contrast of the scan can be optimised if the correct strategy is adopted. By optimising contrast in this way, the ability of the defect analysis to detect internal features and defects is increased.

While comparing the diameter results in terms of the scanned voxel size differences, it was noted some of these results are greater than a couple of voxels out whilst some are sub-voxel. For Defect 1 the difference when using no filter is more than 10 voxels, whilst scanning with the detector filter the difference is half a voxel. As defects, 1 and 2 were filled with powder, calculation of the volume of those defects was considered to be important. This was achieved for each filtration method (shown in figure 6-13). The aluminium detector filter returned the lowest volume value in each case then the copper detector filter.

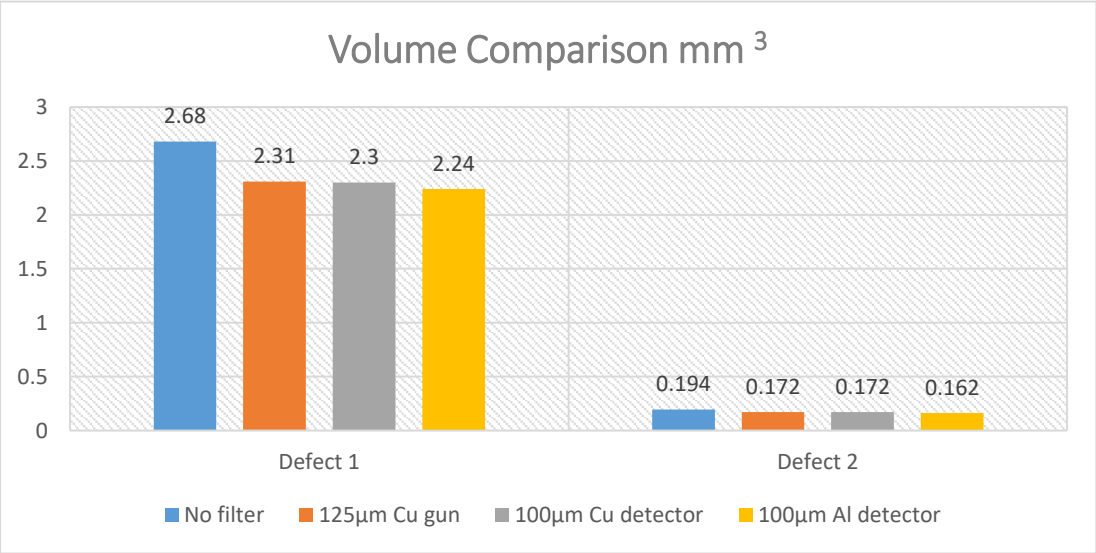

Figure 6-13 Volume comparison graph.

This could be due to the removal of the low energy x-ray radiation [280-282]. As there was no reference data, in this case it is difficult to conclude which value is the most accurate though careful powder extraction and weighing the powder could give an indication.

Given that the defect diameter value calculated with the Al detector filter was the closest to the reference value, it would be reasonable to assume that this would be the more accurate calculated volume. When comparing the 2D images of defect 1 shown in figure 6-14 it is apparent that the no filter scan failed to accurately identify the difference between powder particles and air gaps; hence, the unfiltered scan resulted in the largest defect volume.

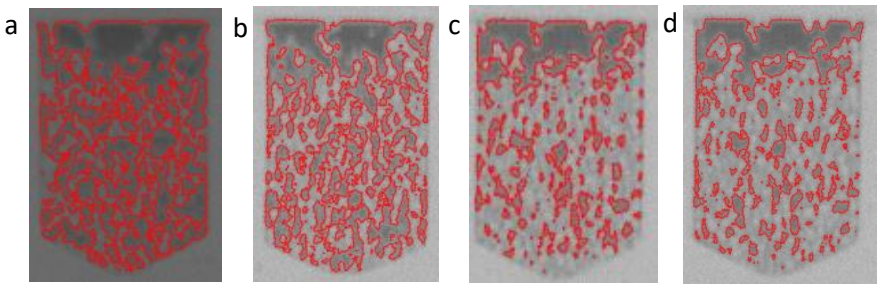

Figure 6-14 Cross sectional X-ray image for defect 1: a) no filter b)100µm source filter c) 100µm Cu detector filter d)100µm Al detector filter.

It was also noted that the contrast is relatively poor when compared to the other datasets, therefore, compromising the effectiveness of the threshold. Overall, the Aluminium and copper detector filters resulted in a generally higher contrast image and more effective threshold determination. In figure 6-14 c and 6-14 d, the gaps between the powder particles are significantly less defined than figure 6-14 a and 6-14 b. In general, the detector filter improved the image quality leading to better air/material threshold that can enhance the overall process of porosity detection.

The filters used in this experiment have shown gradual change in the grey value enhancing the edge detection. When comparing the differences between diameters and depths it was evident that the depth difference is less than the diameter. This specific point was investigated in chapter 5 section 8 with the titanium artefact and requires further investigation as to whether the position of the part and internal geometry being parallel or perpendicular to x-ray beam has an impact on the XCT results.

6.4 Tilt study

The results of the forged titanium artefact discussed in chapter 5 section 8, showed better results for the dimensional measurement of the features perpendicular to the X-ray beam. In the forged titanium artefact experiment, the features were either perpendicular or parallel to the X-ray beam, this experiment investigated different tilt angles. An aluminium artefact (shown in figure 6-15 (a)) made by SLM AM technology was used, the artefact was 12mm diameter and 27.50mm length, it consisted of two halves; the lower halve contained three drilled holes.

The three drilled holes shown in figure 6-15 (b) were 1.2mm diameter and the depths were 0.5mm, 0.74mm and 1.5mm. Both halves surfaces were machined using a diamond cut finish whilst the mating part with the same diameter was designed to enclose the drilled holes thus creating internal defects/pores. The principle of ringing the two surfaces together is like that employed for slip gauges, therefore, the XCT machine will consider the two halves as a single component with internal defects.

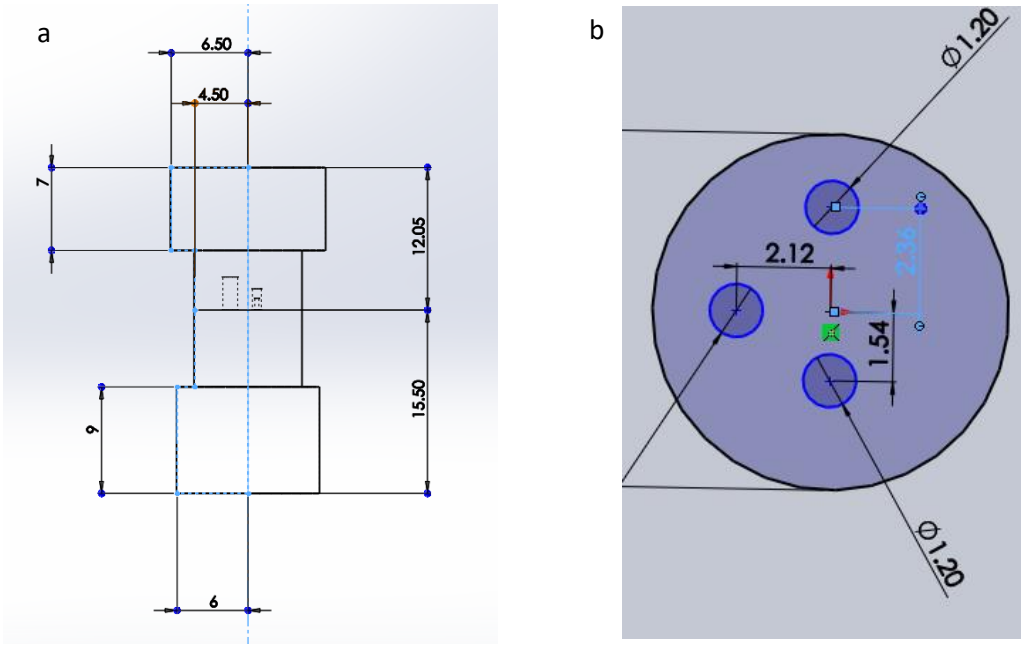

Figure 6-15 a) artefact front view b) artefact top view

The artefact was scanned at four different tilt angles, 0°, 15°, 45° and 60°, using four fixtures. Figure 6-16 a) shows the 45° fixture drawing, and figure 6-16 b) shows the 3D model. The fixture must be made from a material less dense than the artefact; ideally a material that will not affect the grey value histogram. For cost effectiveness and time saving the fixture were made from ABS using FDM 3D printing technology.

The artefact was made of Aluminium (AlSi10Mg) using an AM250 SLM machine, prior to assembly the artefacts containing the drilled defects were characterised using a focus variation microscope (Alicona G4) to determine the reference values for diameter and depth for comparison with the CT results. Each drilled hole was characterised 5 times and the average used for comparison.

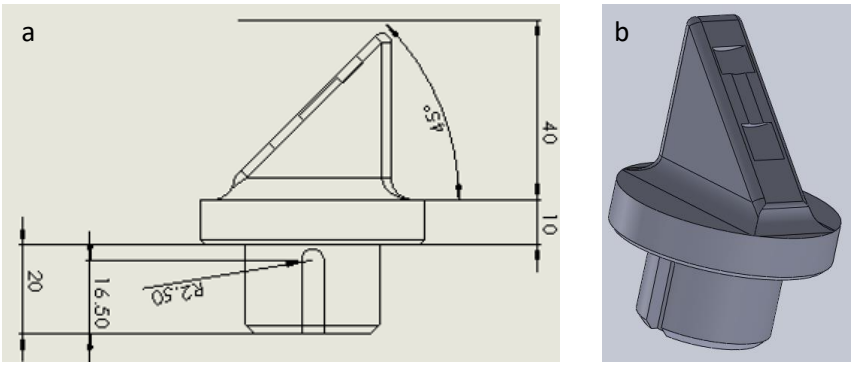

Figure 6-16 a) 45° fixture drawing b) 45° fixture 3D model

6.4.1 Alicona defects measurements

The defects/drilled holes depth and diameter were characterised using the Alicona, the defect diameters were measured using several points best-fit circle. The defects depth was measured by selecting the highest two points on the upper surface and selecting the lowest point in the drilled hole creating a horizontal line.

Table 5 shows the Alicona values for diameter and depth for the titanium and aluminium artefacts, the defects were machined with a CNC machine and this is reflected in the results of the actual hole dimension. The diameter of the three drilled holes were designed to be 1.2mm but the actual diameter found in the artefact was 1.203 mm for defect 1, 1.201mm for defect 2 and 1.216mm for defect 3. The Alicona measurements were also repeated 5 times and the average values used.

Defect	1 (mm)	2 (mm)	3 (mm)
Diameter	1.203	1.201	1.216
Depth	0.746	1.453	0.678

Table 5 Alicona results

The depth of the three drilled holes were designed to be 0.75 mm for defect 1, 1.453mm for defect 2 and 0.65mm for defect 3, but the actual depth found in the artefact was 0.746mm for defect 1, 1.453 mm for defect 2 and 0.678mm for defect 3.

6.5.2 XCT results

A Nikon XTH225 Industrial CT was used in this experiment, all the CT scanning parameters were optimised to ensure the noise was minimised by reducing the Gain to 12db, additionally throughout the experiment no noise or data filtration was utilised. This approach ensured no useful data was omitted or discarded during the measurement process ensuring the operator had an unfiltered dataset to use for the analysis. The XCT scan parameters are shown in table 5.

Exposure	2500 ms
Gain	12dB
Acceleration voltage	150kV
Power	9.5W
Magnification (voxel size)	33.4µm
Filter	250µm

Table 5 XCT scan parameters

The voxel size used was 33.4µm; this was chosen to fit the 60° tilted artefact in the frame. The XCT results were analysed using Volume Graphics VG Studio Max 3.1.

In this experiment, the surface determination used was ISO50% threshold and the defect analysis settings were kept constant to make the results comparable. The diameter was determined by using best fit geometry measurements based on the surface determination. thirteen points were selected on the diameter to generate a circle. The depth was evaluated using the distance measurement by selecting the highest and lowest point in the defect. Figure 6-17 (a) shows a 3D XCT image of the artefact with 0° tilt angle, and figure 6-17 (b) shows a 3D XCT image of the artefact with 15° tilt angle.

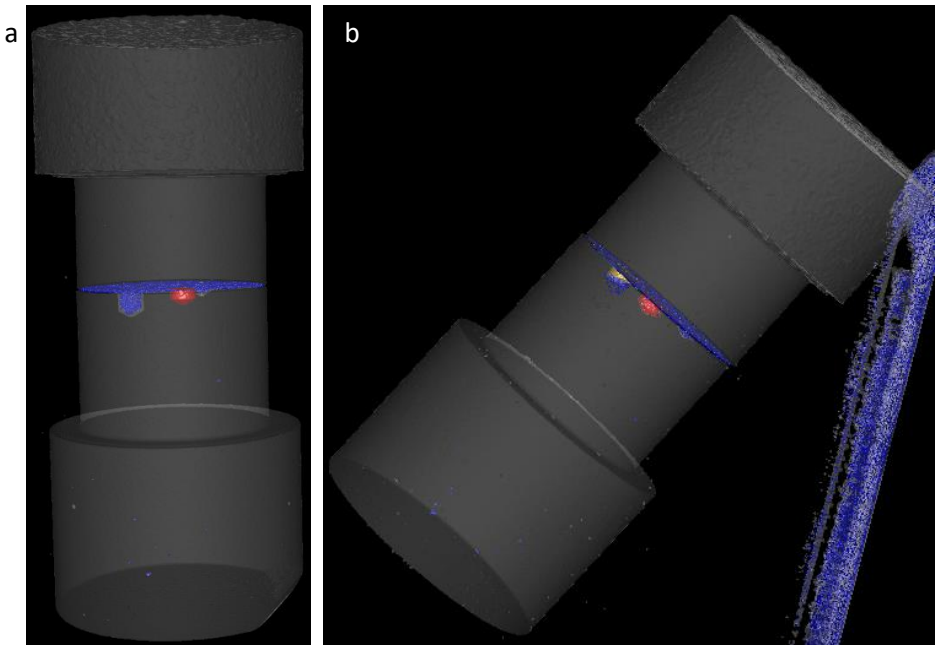

Figure 6-17 a) 0° artefact 3D XCT image b) 15° artefact 3D XCT image

Figure 6-18 (a) shows a 3D XCT image of the artefact with 45° tilt angle, and 6-18 (b) shows a 3D XCT image of the artefact with 60° tilt angle. The visual inspection of the four scans did not show any significant difference in terms of noise or scatter presence.

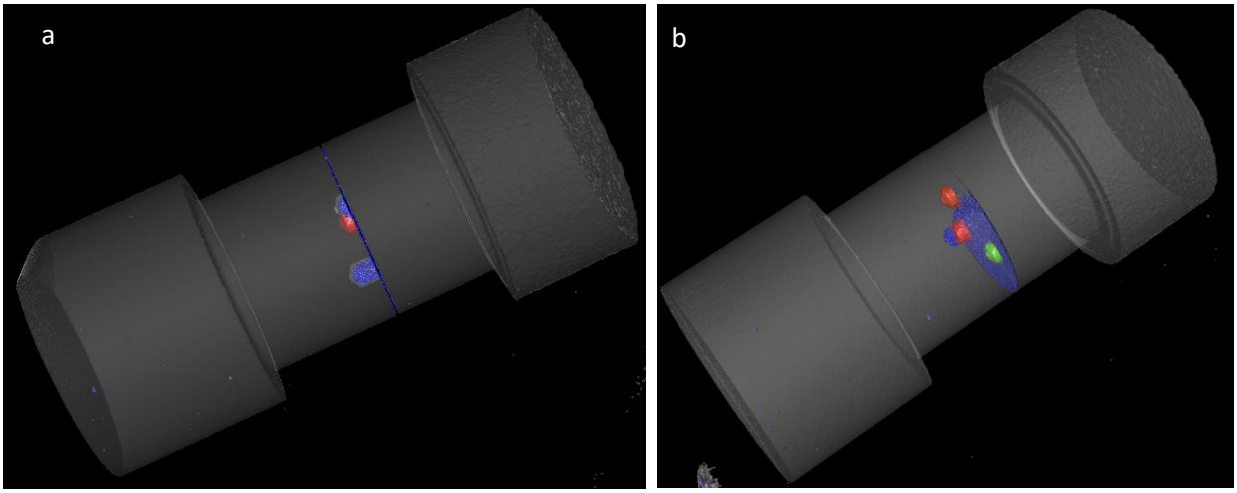

Figure 6-18 a) 45° artefact 3D XCT image b) 60° artefact 3D XCT image

All the images are clear and the defect analysis highlighted the three drilled holes and the gap between the two halves. The section below the obtained XCT results were compared to the results obtained for the Alicona measurements. Figure 6-19 shows the diameter comparison results, for defect 1 the difference between the Alicona and the XCT with no tilt angle is 4.3%, Alicona and XCT with 15° tilt angle is 2%, Alicona and XCT with 45° tilt angle is 2.3% and for the 60° tilt angle is 2.8%. For defect 2, the difference between the Alicona and XCT with no tilt angle is 4.2%, 15° tilt angle is 2.5%, 45° tilt angle is 3.5%, and 60° tilt angle is 4.1%. For defect 3, the difference between the Alicona and XCT with no tilt angle is 2.4%, 15° tilt angle is 1.5%, 45° tilt angle is 2%, and for 60° tilt angle the difference is 3.3%. Since the voxel size was 33 µm most of the diameter results fall within the scan resolution. Therefore, it is not possible to draw a solid conclusion.

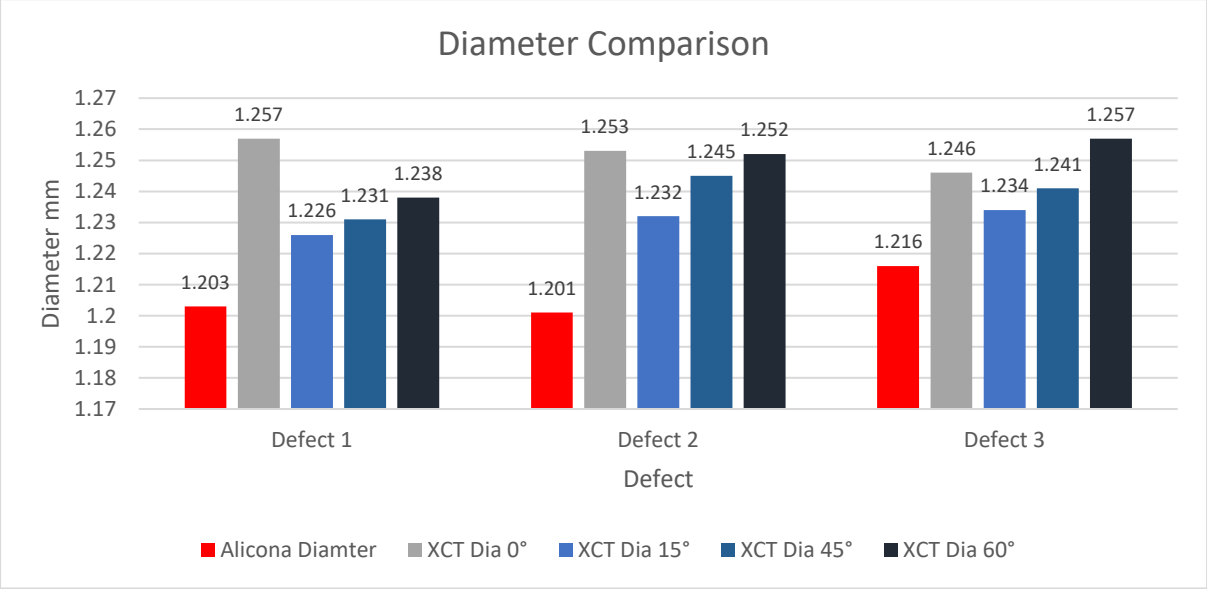

Figure 6-19 Diameter comparison

Figure 6-20 shows the depth comparison results, for defect 1 the deference between the Alicona and the XCT with no tilt angle is 1.1%, Alicona and XCT with 15° tilt angle is 1.5%, Alicona and XCT with 45° tilt angle is 3.6% and for the 60° tilt angle is 3.4%. For defect 2 the difference between the Alicona and XCT with no tilt angle is 1.4%, 15° tilt angle is 1%, 45° tilt angle is 2.4%, and 60° tilt angle is 2%. For defect 3, the difference between the Alicona and XCT with no tilt angle is 2.4%, 15° tilt angle is 2%, 45° tilt angle is 5%, and for 60° tilt angle the difference is 5.7%. When comparing the XCT defect diameter results for the different tilt angles to the Alicona reference measurements, it was noted that the 15° tilt angle results are the closest to the Alicona.

Then after the 15° tilt angle comes the 45° then 60° and finally the biggest difference was found in the straight scan with no tilt angle. When comparing the depth measurement results, defect 1; the no tilt results are closer to the Alicona, followed by the 15° tilt angle. For defect 2 the 15° tilt is the closet to the Alicona results followed by the straight scan with no tilt angle. For defect 3, the 15° tilt angle results are the closest to the Alicona results followed by the straight 0° scan. The depth results fall within XCT scan resolution (33 µm), so in order to draw a solid conclusion, the experiment must be repeated with higher magnification/voxel size.

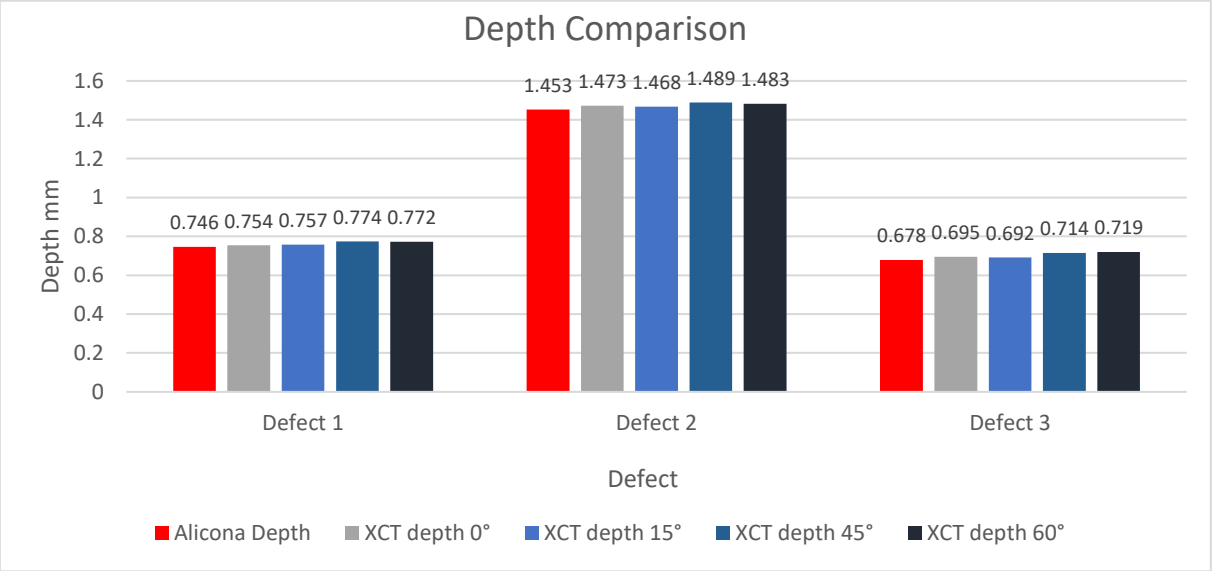

Figure 6-20 Depth comparison

Although the results are within XCT scan resolution, the 15° tilt angle produced the closest results to the Alicona measurements; the only exception is the defect 1 depth measurement. In this experiment each scan grey value histogram was compared to understand the difference in the ISO 50% surface determination threshold. Figure 6-21 shows the grey value histogram for 45° tilt scan. The histogram shows three different materials; air, polymer and metal; the third material is the polymer from the fixture.

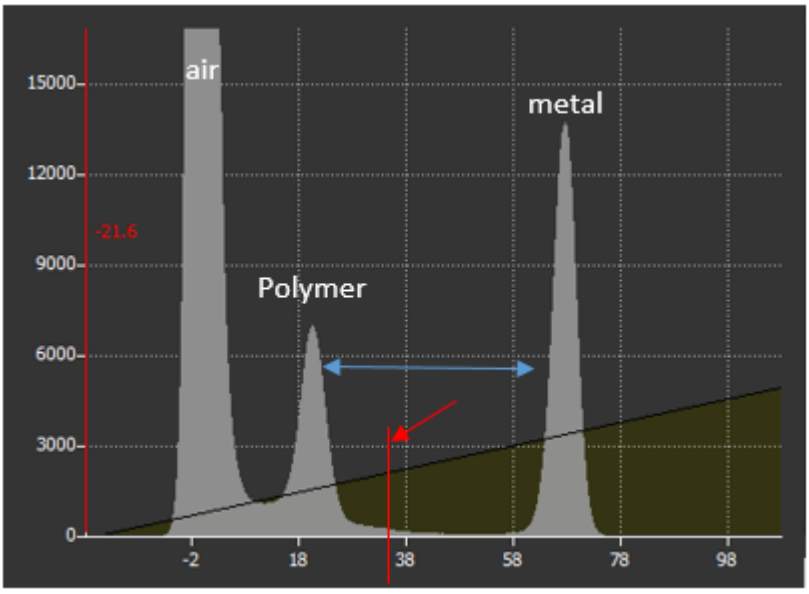

Figure 6-21 45° grey value Histogram

The surface determination threshold value for the no tilt scan was 32, for the 15° tilt scan was 33.54, for the 45° scan the ISO50% value was 33.84 and for the 60° tilt angle scan the ISO50% value was 34.28. In this experiment the scanning parameters were kept constant. The parameters were optimised for the no tilt scan; the x-ray beam was optimised to penetrate the diameter of the artefact and every time the artefact was tilted the beam penetrated larger cross section of the material. At the

60° tilt angle the beam is nearly penetrating the full length of the artefact. The change in thickness could require different parameters and different threshold. To evaluate the scan quality further inspection and grey value analysis was carried out on the 60° tilt scan.

Figure 6-22 shows the top and front view of the 60° tilt scan grey value analysis; it is clear that the scan parameters are sufficient to penetrate the full length of the artefact; figure 26 (a) the grey value analysis of the artefact diameter shows the artefact diameter consistent grey value with no change in colour.

Figure 6-22 (b) shows a front view of the artefact full length, the grey value analysis proves that the scan parameters are sufficient with no noise, scatter or beam hardening presence. The difference in in XCT results in this experiment could be due to difference in the beam angle of penetration, which resulted in changes in the surface determination threshold (different ISO value). Furthermore, the difference in the tilt has an impact on the image focus. In the process of selecting the appropriate XCT scan parameters, if the power is less than 10W the operator has the option to adjust beam focus. This can be done manually by moving the slider or can be done automatically, where the machine compares all the available focuses and selects the most appropriate one.

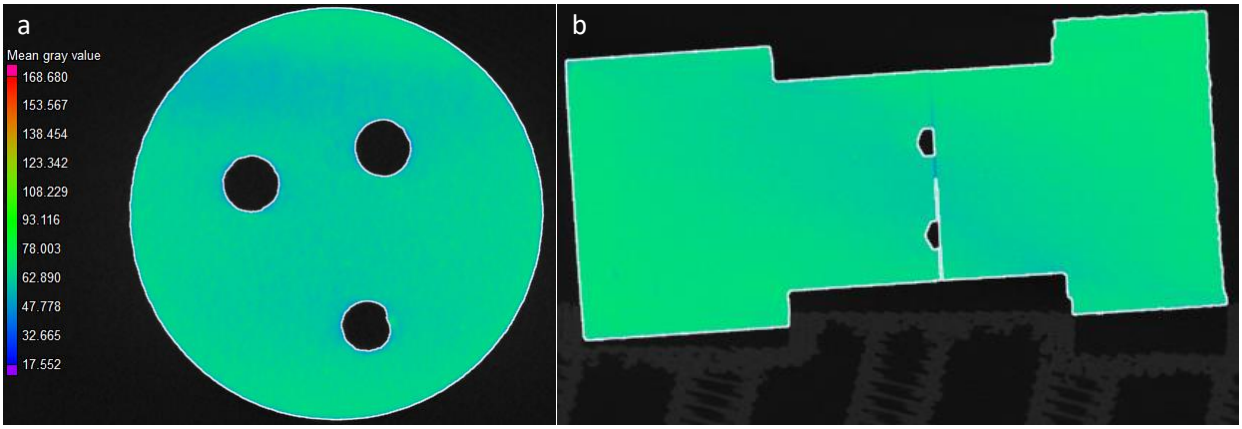

Figure 6-22 a) Grey value analysis top view of the 60° tilt scan b) Grey value analysis front view of the 60° tilt scan

There are two causes of XCT image blur, magnification (voxel size) and the beam focus. High magnification will improve the resolution and reduce the image blur which enhances the defect analysis results. Similarly, if the image is out of focus this will cause image blur. The image blur affects edge detection which subsequently affects the defect analysis results. Image blur could either increase or decrease the internal defect dimension values, depending on the selected surface determination threshold. If the threshold is lower than the surface determination ISO 50% grey value, the internal defect dimensions will be lower than the actual value. Alternatively, if the threshold is higher than surface determination ISO 50% grey value the internal defect dimensions will be higher than the actual dimensions. This is mainly because when the grey value is above the ISO 50% threshold part of the material will be detected as cavity/air and when the lower grey value is below the ISO 50% threshold the detect analysis will detect part of the air as a material. In most engineering applications the automatic threshold ISO value is 50% which positions the threshold equidistant of the two peaks in the histogram. Utilising ISO50% threshold in some situations can cause an error in the results by selecting some material as pores or vice versa. In the next chapter surface determination impact on defect characterisation will be investigated.

6.5 Scan parameters study

Currently the selection of the optimum XCT scan parameters is manual, relying on operator experience. If the appropriate parameters were not selected the produced data could be compromised due to the low image contrast, resulting in high noise levels and measurement errors. In the process of scanning an object there are no exact XCT parameters; there are usually a range of different combination of parameters that produce a high contrast image which result in precise edge detection and defect analysis.

In this experiment the impact of selecting different XCT parameters on internal defect characterisation was investigated, specifically the impact of scan parameters on mean grey value and the influence of beam focus on enclosed internal feature dimensional measurements. In this experiment, three different operators with various levels of experience scanned a titanium artefact (shown in figure 27) which was previously discussed in chapter 5 section 8. The operators selected their own individual scan parameters, the only exceptions were the magnification and surface determination threshold.

The artefact was cylindrical shaped and made of forged titanium with 35mm diameter and consisted of two halves, both containing a set of three 500µm diameter drilled holes with depths ranging from 250µm to 700µm. The artefact model is shown in figure 27(a), more details about the artefact design and assembly are discussed in chapter 5 section 8

The diameter and depth of defects/drilled holes were characterised using a focus variation microscope and then scanned with a Nikon XTH225 industrial CT to measure the artefacts and characterise the internal features for defects/pores. The voxel side was fixed to 40µm, VG Studio Max 3.1 (Volume Graphics, Germany) software package was used for data processing, surface determination, and defect/porosity analysis. The XCT result analysis was carried out with a fixed grey value threshold ISO 50% for all the scans. Figure 27 (b) shows an XCT 3D image of the artefact with all the defects highlighted in blue.

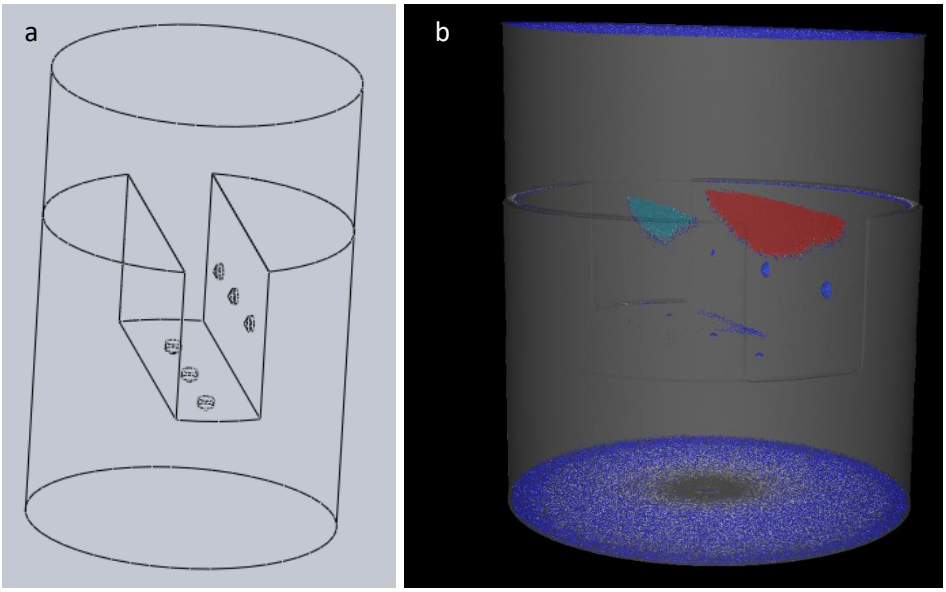

Figure 6-23 a) artefact 3D model b) artefact XCT 3D image

The drilled hole diameters were measured using the best-fit circle, and the depth were measured by selecting the two highest points on the upper surface and selecting the lowest point in the drilled hole, creating a horizontal line

6.5.1 XCT setup

All the XCT operators used 42µm voxel size, also no data or noise filtration was applied throughout the experiment. This approach guaranteed that no useful data was omitted or discarded during the measurement process; ensuring that the operator had an unfiltered dataset to use in the analysis. The scanning parameters are shown in 6 below.

Operator	**1**
Exposure	4000 ms
Filament current	8.1 W
Acceleration Voltage	175 kV
Filter	0 µm/no filter
Gain	12

Operator	**2**
Exposure	1415 ms
Filament current	57.2 W
Acceleration Voltage	200 kV
Filter	2.5mm
Gain	12

Operator	**3**
Exposure	2000 ms
Filament current	35.1 W
Acceleration Voltage	205 kV
filter	2mm
Gain	12

Table 6 XCT scan parameters

It can be noted from table 1 that each operator selected completely different parameters and each operator used a different strategy. The first operator chose a low filament current below 10W, to use the smallest x-ray spot size and benefit from beam focus, they maxed out the projection exposure time and used no beam filter to compensate for the lack of power. Operator two-used high power (57.2W) combined with 200kV acceleration voltage, 2.5mm copper filter with a low projection exposure time (1415mS). Operator three used lower power than the second operator but increased the voltage, combined with a 2mm filter and moderate projection exposure time (2000mS). Beside the difference in the image contrast there is a significant difference in the scanning time across the operators. The first operator scan took 3.5 hours, the second scan took 1 hour and 39 minutes, and the third scan took 2 hours and 24 minutes. Figure 6-24 shows the results of the different operators defect analysis, where figure 6-24 a) is for operator 1, b) is for operator 2 and c) for operator 3.

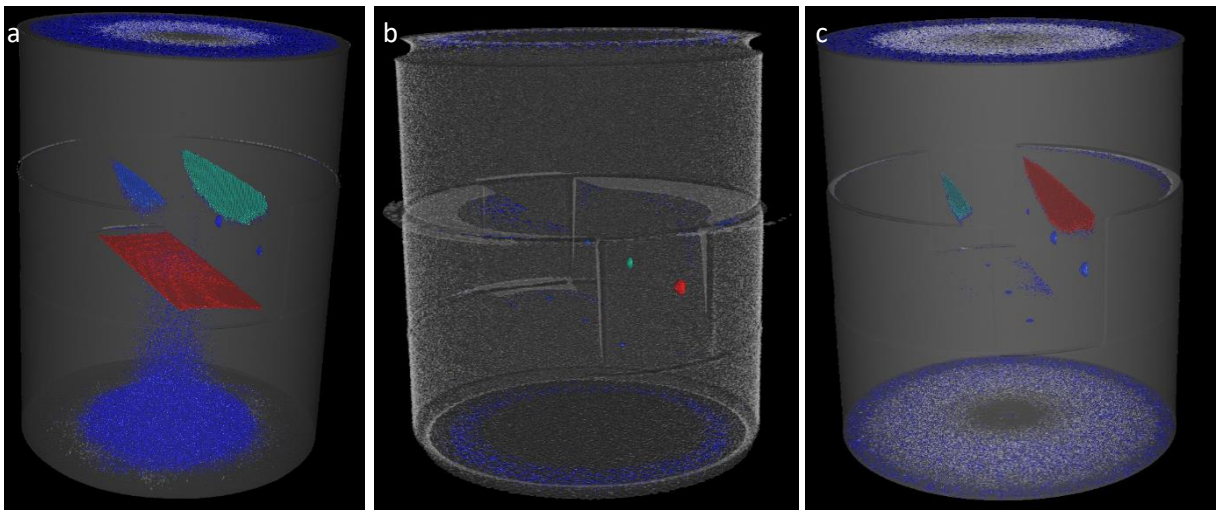

Figure 6-24 a) artefact XCT 3D image operator 1 b) artefact 3D image operator 2 c) artefact 3D image operator 3

The visual inspections of the results show that all the three operators scan parameters detected the presence of the 6 defects/holes. The first operator results (figure 6-24 (a)) confirmed noise presence in the lower half of the artefact.

The second operator scan parameters produced clear image with a small amount of noise in the middle of the artefact, furthermore the XCT results confirmed the presence of an artificial beam artifact in the middle outer section of the scanned object. The third operator scan parameters produced the clearest image with no noise or beam hardening artefact.

6.5.2 XCT results

The drilled holes/defect dimensional comparison are shown in figure 6-25 and 6-26, where figure 6-25 shows the diameter comparison and figure 30 shows the depth comparison. The graphs compare the results obtained from the Alicona measurement to the results obtained from operator one-scan parameters (shown as XCT1), the results obtained from operator two (shown as XCT 2) and the results from operator three (shown as XCT 3).

Comparing the diameter results from the Alicona measurement and XCT scan the difference between the Alicona and XCT for the first lower hole/defect for operator 1 was 9.3%, operator 2 29.3% and operator 3 5.3%. For the second lower defect the difference for operator 1 was 9.8%, operator 2 13.2% and operator 3 9.2%. For third lower defect the difference for operator 1 was 9.9%, operator 2 4.4% and operator 3 5.3%. The first upper hole difference for operator 1 was 20.7%, operator 2 8.6%, and operator 3 10.1%. The second upper hole difference for operator 1 was 5.5%, operator 2 12.6% and operator 3 4.1%. The third defect/hole difference for operator 1 was 47.3%, operator 2 31.1% and operator 3 7.8%.

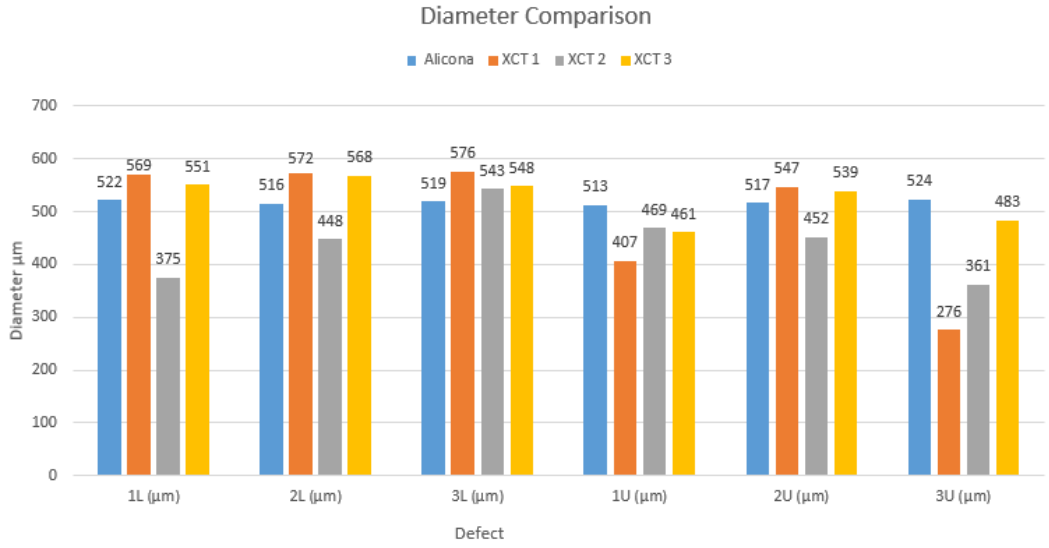

Figure 6-25 Diameter comparison graph.

The depth comparison shown in 6-26, shows the difference between the Alicona and XCT for the first lower hole for operator 1 was 7.1%, operator 2 9.8% and operator 3 3.3%. For the second lower hole the difference for operator 1 was 7.8%, operator 2 11.8% and operator 3 4%. For the third lower defect/hole the difference for operator 1 was 11.7%, operator 2 12.9% and operator 3 6.6%.

For the 1st upper drilled hole the difference between the Alicona and operator 1 was 18.3%, operator 2 3.3% and operator 3 2%. For the second upper hole the difference between the Alicona and operator 1 was 9.4%, operator 2 12.2% and operator 3 6.4%. For the third upper defect/hole the difference between the Alicona and operator 1 was 24.1%, operator 2 16.7% and operator 3 10.6%.

The results from this experiment did not confirm the conclusions from the initial experiment in chapter 5 section 8. This could be due to the difference in voxel size and scanning parameters, therefore it is

not possible to have a solid conclusion about the impact of features being parallel or perpendicular to the x-ray beam on internal feature dimensional measurements.

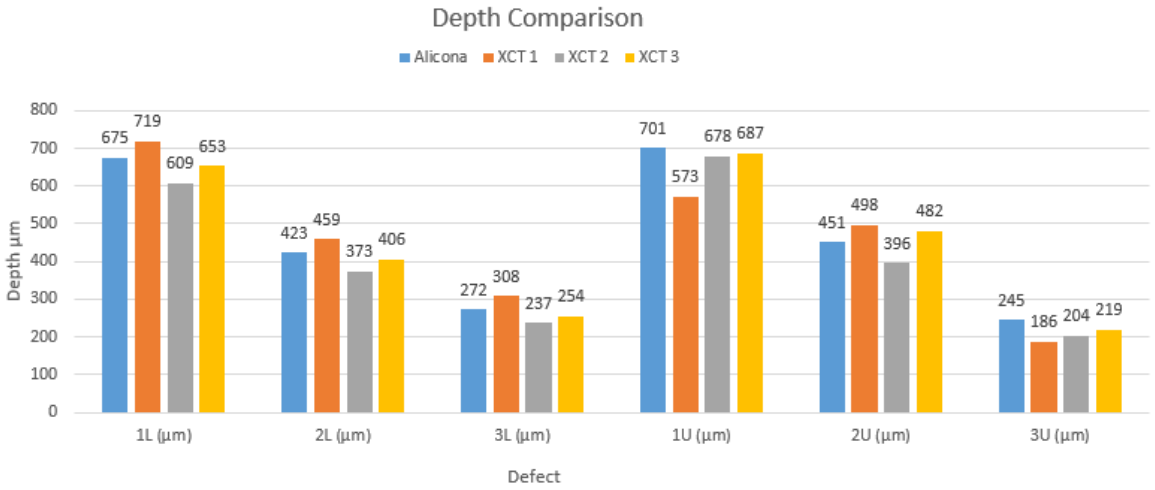

Figure 6-26 Depth comparison graph.

6.5.3 Discussion

The result of this study shows a large difference between the 3 operators scanning parameters; the closest dimensions to the Alicona results were from operator 3. To understand the root cause of the difference in results the XCT image grey value must be evaluated to identify the impact of the scan parameters on image contrast and defect characterisation. Figure 6-27 shows the mean grey value analysis comparison between the 3 different operators.

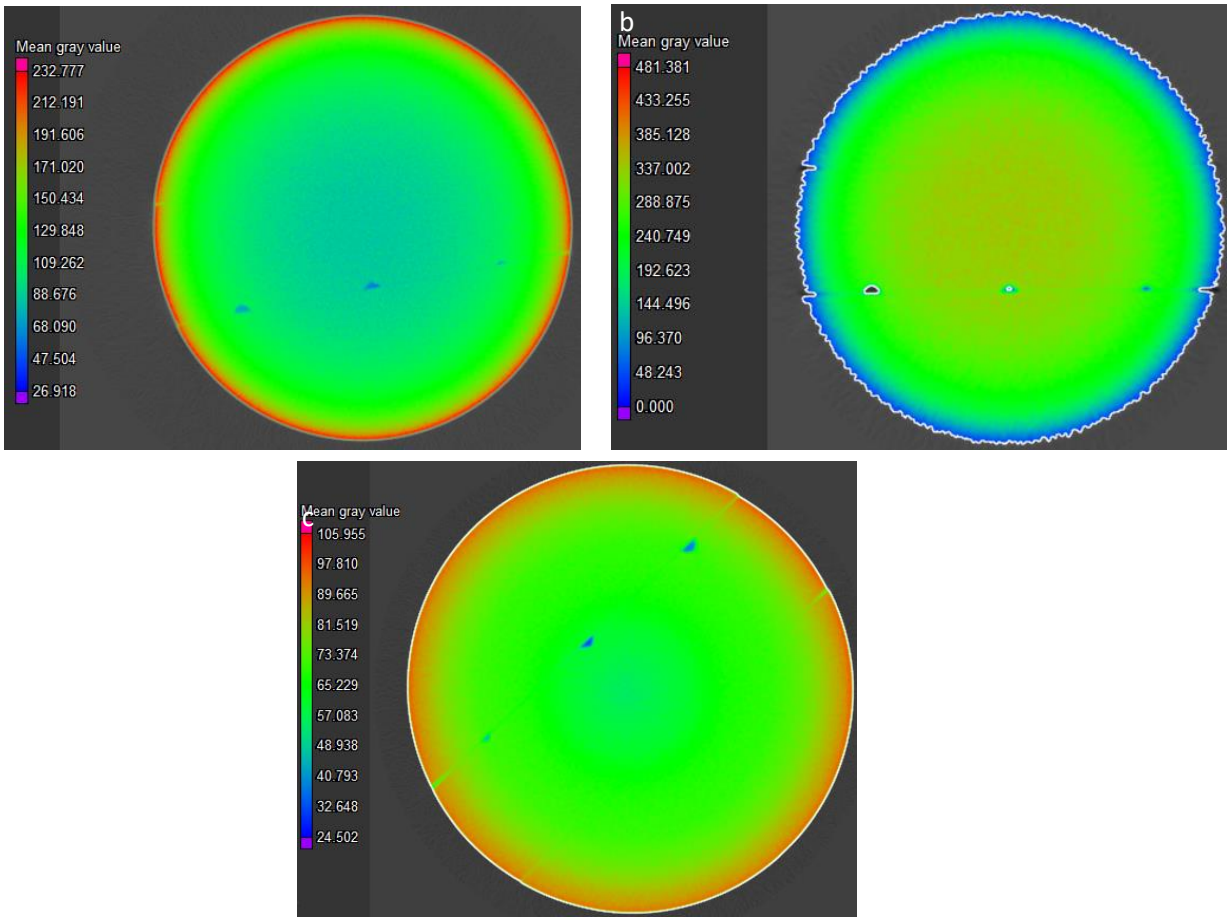

Figure 6-27 grey value analysis a) operator 1 b) operator 2 C) operator 3

Figure 6-27 a) shows the mean grey value analysis for operator 1's scan, 6-27 b) shows the mean grey value analysis for operator 2's scan, and 6-27 c) shows the mean grey value analysis for operator 3. The initial visualisation inspection shows that there are significant differences between the 3 scan parameters; the highest mean grey value (just above 481) is in operator 2's results, followed by operator 1(just above 232) and finally operator 3's results which was 105.955.

The highest difference in grey value was found in operator 2's scan (figure 6-27 (b)), where the minimum mean grey value was 48 and the highest was 481. Next was the first operators scan (figure 6-27 (a)), where the lowest mean grey value was 26 and the highest was 232. The least difference in mean grey value was found in operator 3's scan (figure 6-27 (c)), where the lowest minimum grey value was 24 and the highest value was 105.

Theoretically, the large difference between the minimum and maximum mean grey values should result in a high contrast image which enhances the defect characterisation results. However, in this experiment the excessive power and acceleration voltage combined with the low thickness filter resulted in several errors. The high voltage caused the outer edge of the artefact to retain the lowest mean grey value resulting in wrong outer edge detection; where the outer edge grey value is very close/similar to air/background, so it is impossible to distinguish between the background and material. This error in external edge detection is also found on the defect closest to the outer surface, but the middle of the artefact recorded the highest grey value.

On the contrary, operator 1 utilised low wattage to maintain beam focus and small spot size but the lack of beam penetration resulted in a spike of mean grey value on the outer edge and low mean grey value in the middle of the artefact. The X-ray beam focus reduced the blur but the lack of power resulted in low contrast between the enclosed drilled holes and the material. Furthermore, the defect analysis is compromised due to the noise presence, this specific issue could be solved by the implementation of a result filter.

Operator 3's scan parameters resulted in the closest values to those measured by the Alicona, the third operator used high wattage lower than that of operator 2, the high wattage was combined with a 5 kV higher acceleration voltage than the second operator, and a 2mm filter. This combination of parameters produced the clearest image and best defect analysis results. The highest grey value was found on the outer edge and it fades consistently towards the middle of artefact. Although the difference between the highest and lowest mean grey values were the smallest in the third operator scan, the image contrast is the finest.

Figure 6-28 shows a magnified image of the upper middle drilled hole/ defect mean grey value, where (a) is operator 1, (b) is operator 2, and (c) is operator 3. The first image shows infinite small particles with the same blue shade as the defect, the second image shows an inconsistent orange shade and a halo artifact around the defect, this explains the low values for upper defect 2 in operator 2's scan.

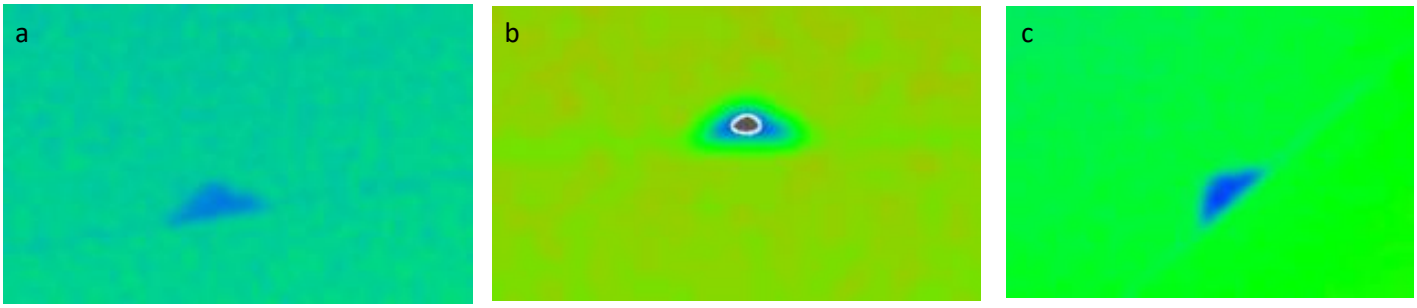

Figure 6-28 mean grey value for the middle upper hole analysis a) operator 1 b) operator 2 C) operator 3

Finally, the third image shows a consistent green shade around the defect and the defect is highlighted with a bright blue colour. This combination enhanced the results of defect characterisation and resulted in the closest dimensional results to the Alicona measurements.

The results of this experiment proved that the XCT scan parameters play a crucial rule in the overall process. An experienced operator that chooses appropriate scanning parameters, contributes to the precision of the XCT process and can minimise the file size and scan time. Furthermore, the results of this experiment have shown the possibility of enhancing defect characterisation by optimising the surface determination threshold. This can help in compensating for the errors resulting from inappropriate XCT scan parameters and potentially could promote sub voxel detection for low magnification scans by manually selecting the grey values of the surrounding voxels that are 50% material and 50% air.

6.6 Chapter summery and conclusion

In this chapter, a set of porosity specific artefacts were used to assess the impact of different scan parameters in defect characterisation. The scan parameters investigated were magnification (voxel size), beam filtration; including pre and post object x-ray beam filtering, tilt angle, power and acceleration voltage.

The magnification experiment was used to identify the most effective strategy for AM defect detection. The most effective strategy was to scan the component using a magnification as low as 38 µm voxel size to identify the location of the defects and then confirm the area where the defect is located using a higher magnification. Using this strategy permits scanning relatively large components in a shorter period without compromising the precision of the results. In some cases where the scanned object is very large, utilising the 38µm voxel size scan strategy is impossible. The commonly used method is to section the component into smaller pieces and scan the sectioned parts individually. The downside to this method is that once sectioned the component will not be functional anymore; this is not considered a non-destructive inspection. The results of the magnification study have driven the need to investigate the possibility of using surface determination in promoting sub-voxel defect detection, this will be discussed in chapter seven.

The results of the high magnification scans highlighted the possibility of developing errors due to the implementation of ISO50% surface determination threshold. The XCT external and internal dimensional measurements are based on surface determination and edge detection. It was also noted that the edge detection is directly affected by grey value variability, therefore the large difference between the background darkness and material brightness will result in accurate edge detection. Small differences between background and material grey value will usually result in false edge detection. There could be for several reasons for this, predominantly related to scanning parameters and surface determination threshold. This specific point was investigated in the scan parameter study in section 5, the results showed that the large differences between background and material does not necessarily improve edge detection and could cause errors in identifying the appropriate surface determination threshold.

The x-ray beam filter experiment investigated the impact of different beam filtration strategies, namely the impact of pre and post component beam filtration on photoelectric effect and Compton scattering.

The experiment showed that dark areas created by beam hardening could be minimised by using the appropriate beam filtration material. The use of an aluminium detector filter gave better contrast than

the beam source filter. Generally, the filters used in this experiment showed a gradual change in the grey value, which enhanced edge detection.

In the scanned object tilt experiment, the influence of the different beam penetration angles was investigated by tilting the scanned object mounted in different fixtures. The artefact was scanned with no tilt, 15°,45°, and 60° tilt angle. Overall, the 15° tilt angle produced the closest results to the Alicona measurements.

In this experiment, the histogram for each scan was compared to identify the changes in the grey values from the scanned object tilt. The surface determination threshold value for the no tilt scan was 32, for the 15° tilt scan was 33.54, for the 45° scan the ISO50% value was 33.84 and the 60° tilt angle scan the ISO50% value was 34.28.

In this experiment, the scanning parameters were kept constant. The scan parameters were optimised for the no tilt scan. Consequently, the x-ray beam was optimised to penetrate the diameter of the artefact and whenever the artefact is tilted the beam is penetrating a larger cross section of the material; at the 60° tilt angle the beam is nearly penetrating the full length of the artefact. The variation in thickness usually requires different parameters and a different surface determination threshold. To evaluate whether the chosen scan parameters were appropriate or not the 60° tilt angle mean grey value was analysed. The analysis showed that the scan parameters were sufficient to penetrate the full length of the artefact, with no noise, scatter or beam hardening present.

There are two reasons for XCT image blur, the magnification (voxel size) and the beam focus. High magnification will improve the resolution and reduce image blur; enhancing the defect analysis results. In the process of selecting the appropriate XCT scan parameters, if the power is less than 10W the operator has the option of adjusting the beam focus. This can be done manually by moving the focus slider or can be done automatically; where the machine compares all the available focuses and selects the most appropriate one. If the image is out of focus this will cause image blur. This affects the edge detection and subsequently causes errors in the defect characterisation process.

Figure 6-29 shows edge blur, where figure a) shows the ISO 50% threshold, b) shows ISO 43% threshold and c) shows ISO 47%. The white line shows the edge identified by the surface determination threshold,. In figure a) the threshold failed to include all material and an example of the material that was acknowledged as air/background is highlighted with an orange ellipsoid.

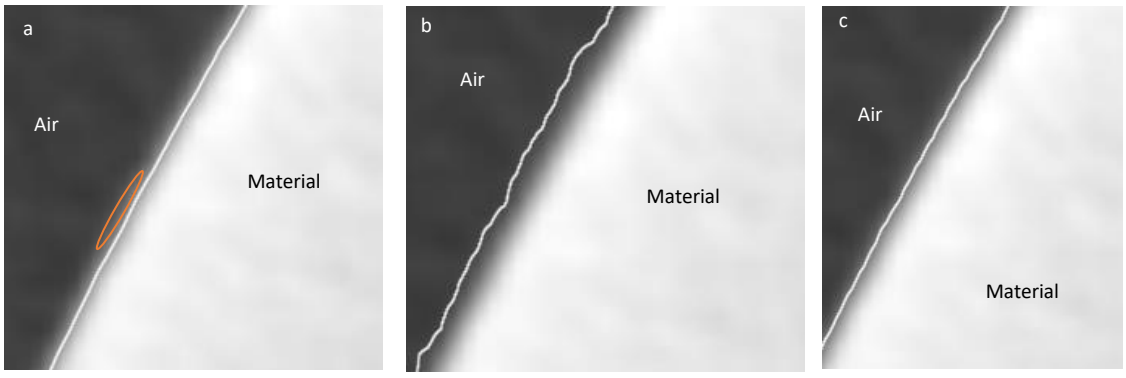

Figure 6-29 surface determination threshold a) ISO50% b) ISO43% c) ISO47%

In figure 6-29 b) the surface determination threshold identified some of the air/background as material. As mentioned previously, the edge blur could either be insufficient magnification or because the scan was out of focus. In both cases the blur will occur on the material voxels adjacent to the air/background, where those voxels are not 100% material or air. A proportion of the voxel will be material and the remaining will be air. If the voxel grey value is closer to the material mean grey value

then a bigger proportion of this voxel is material, on the contrary if the voxel's grey value is closer to the air/background then a bigger proportion of this voxel is air. Figure 6-29 c) shows the surface determination threshold that includes outer edge voxels containing 50% material and 50% air.

The investigations discussed in this chapter demonstrate the impact of different scan parameters on the XCT results. The first parameter; acceleration voltage (kV), enhances the beam penetration of the scanned object as it identifies the maximum beam energy. The second parameter; beam power or current (W/ μA), identifying the number of photons in the x-ray beam, generally higher current will increase the number of photons in the beam, improving the image contrast.

When the acceleration voltage is above 10W this causes the x-ray tube to auto defocus the focal spot, reducing XCT image sharpness and introducing blur. If the power/wattage is too high the XCT image becomes low definition and out of focus. These parameters play a crucial role on XCT image quality.

Chapter 7 Challenges in porosity analysis (XCT porosity method image analysis optimisation)

Statement of Publications Arising from This chapter

In this chapter, a method for enhancing the results of defects characterisation is discussed. The first section discusses the errors that could result from the ISO 50% surface determination threshold. The development work was presented at the 2018 ASPE and Euspen Summer Topical Meeting, United States, California, San Francisco, Advancing Precision in Additive Manufacturing, American Society for Precision Engineering, ASPE "Optimisation of surface determination strategies to enhance detection of unfused powder in metal additive manufactured components"[4].

In the second section the possibility of improving the accuracy of internal defects by the optimization of surface determination is discussed, the results were presented at the 9th Conference on Industrial Computed Tomography, Padova, Italy (iCT 2019). *Tawfik, A et al, (icT2019): pp. 1-7, "Optimisation of surface determination to improve the accuracy of detecting unfused powder in AM Aluminium components" [7].* The paper was published also published on NDT.net. Another section of the study was presented at the *4th ASTM Symposium on Structural Integrity of Additive Manufactured Materials and Parts* (pp. 102-121). ASTM International." Challenges in Inspecting Internal Features for SLM Additive Manufactured Build Artefacts" [10]. The paper was published in the ASTM technical papers in 2020.

The author performed all the experiments and research and wrote the entire manuscript with guidance and editorial changes from the co-author. It is indicated where text from this publication has been reproduced in this thesis.

In the previous chapters, it was noted that the surface determination threshold affects XCT defect characterisation results. The image analysis proved challenging; most challenges were in the differentiation between background (air) and actual material. In this chapter the challenges in porosity imaging are discussed and the best practice identified.

7.1 ISO 50% Surface determination threshold study

In this study an artefact with micro drilled holes (discussed in chapter 5 section 4) was used to identify the impact of surface determination threshold on defect characterisation. The commonly used ISO50% threshold is compared to a threshold that was identified based on grey value analysis combined with visual manual inspection. The focus of the study was to provide best practice guidance regarding the selection of inspection parameters and identifying the capability of ISO 50% surface determination in precisely detecting micro internal pores.

As previously discussed in chapter 3, industrial CT is an NDI method that has the capability to detect porosity whilst analysing the component volume; providing position, location distribution and volume of pores/defects. The data obtained from the scan consists of a volumetric file that contains specific gray values for each three-dimensional pixel (voxel). Data analysis uses proprietary software (e.g. Volume Graphics VG Studio Max, Avizo) to differentiate between gray values of background and object material [4].

The results are presented in the form of histogram, plotting the number of voxels versus gray value. In the case of single materials, the histogram will contain two peaks: one peak will represent the air and the other will represent the material. A single threshold (ISO) grey value in the grayscale between the two peaks represents the edge of the material. The automated algorithm commonly used and cited in the engineering applications is ISO 50% surface determination [283,284]. ISO 50% shown in figure 7-1 automatically positions the threshold within equal distance between the maximum values of the two peaks of the histogram.

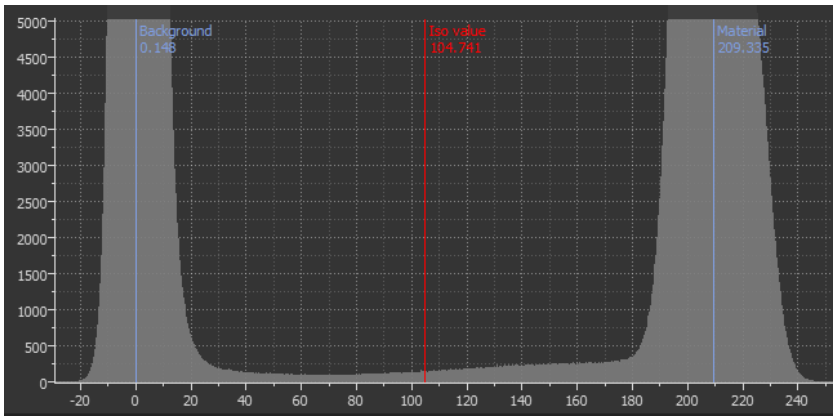

Figure 7-1 XCT histogram image for single material

There is no exact scientific explanation for selecting the ISO 50% surface determination threshold. However defining an inappropriate ISO value could erroneously classify some material as air and vice versa; resulting in failure in edge detection of the component [285].

An earlier study carried out at K.U. Leuven showed that ISO 50% would result in dimensional shrinkage for aluminum and elongation for steel and zirconium dioxide (Zro_2). The study recommended utilising ISO values 35-45% and 80-90% for aluminum and steel respectively [286].

It can be extremely complex to achieve correct edge detection in an XCT image, due to the presence of beam hardening or the use of an inappropriate scan parameters that result in minimal difference in grey value between the outer edge of the material and air/background surrounding the scanned object; similar to figure 7-2 (a). In this case, it is not possible to identify the outer edge of the scanned object, due to the grey value similarity between the background and material.

Inappropriate scan parameters that result through in lack of beam penetration can result in a reduction in grey value in the middle of the scanned object. The reduction in the grey value shown in figure 7-2 (b) will result in errors in the defect analysis process because the areas of low grey values will be detected as defects, compromising the sensitivity of the defect grey value threshold.

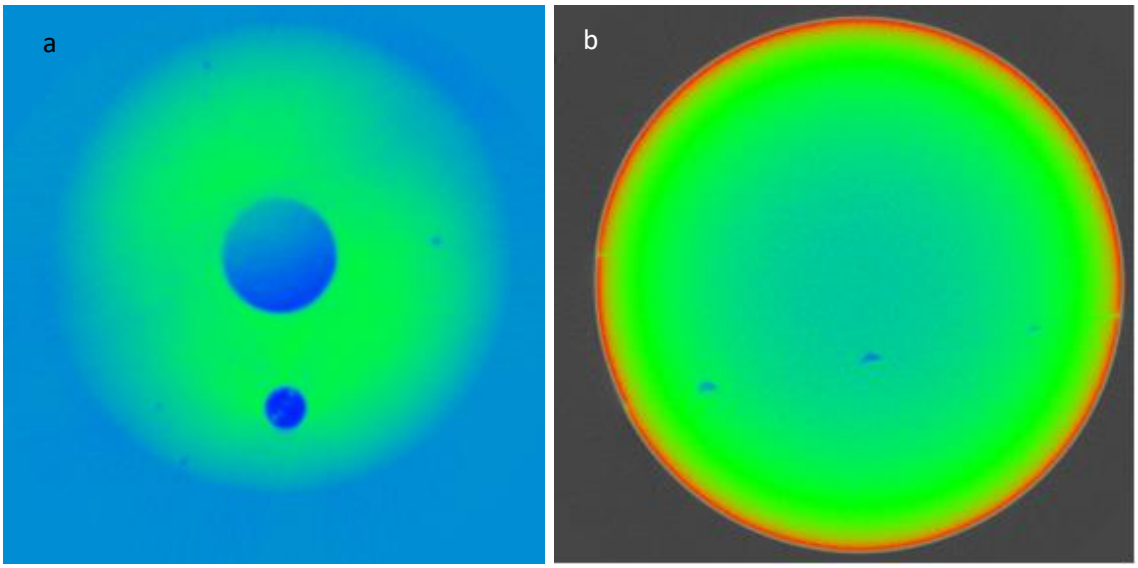

Figure 7-2 XCT images of inappropriate scan parameters a) excessive acceleration voltage b) lack of penetration

In this study the ability of ISO 50% in detecting micro defects in an EBM built artefact was discussed, along with the possibility of improving the results through alternative ISO value threshold selection. Sub-surface micro defects are of great concern for additive manufactured part, therefore an accurate threshold (ISO) value selection is required.

7.1.1 Methodology

In this study a Nikon XTH225 industrial XCT was used to characterise a Ti6AL4V artefact built using an Arcam Q10 electron beam-melting machine (EBM), as discussed in chapter 5 section 4. The artefact shown in figure 7-3, consists of 2 halves; the lower half contains the drilled defects. The surface of both halves was machined to a diamond cut finish, whilst the mating upper half with the same diameter is designed to enclose the drilled holes thus creating internal defects/pores. The principle of ringing two surfaces together is similar to that employed for slip gauges.

The artefact contained 50µm (defect 4), 100µm (defect 3), 500µm (defect 2) and 1400µm (defect 1) holes which were drilled into the polished surface of the artefact using a CNC machine equipped with micro drills and end mills as shown in figure 7-3(a). Figure 7-3 b) shows a top view of the artefact lower section with 50µm drilled hole highlighted with an orange circle, 7-3 c) shows a top view XCT image of the artefact upper face [4].

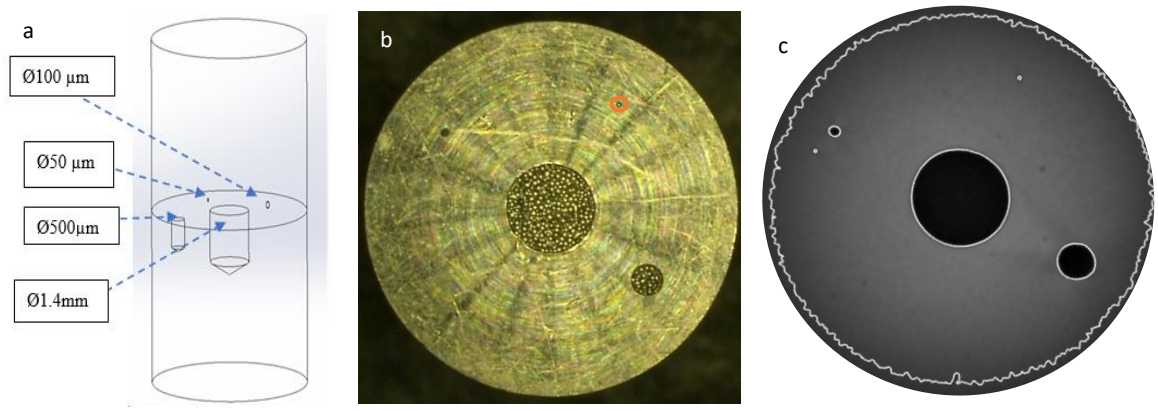

Figure 7-3 a) Artefact 3D model, b) top view of the artefact with defect 1 and filled with powder, c) XCT top view image of the artefact

The drilled defects/pores depth and diameter were measured using AliconaG4 focus variation microscope then each defect volume was calculated assuming that each drilled hole consisted of a combined cylinder and cone. To reduce uncertainty, the alicona measurements were repeated 5 times, and the average value used for comparison.

As previously mentioned in chapter 5 section 4, the defect diameters were measured using a three point best-fit circle. The depth was measured by selecting two points on the upper surface and creating a horizontal line and a point on the lowest point in the drilled hole.

The artefact was scanned with a Nikon XTH 225 to create a volume file of the entire artefact. The XCT scanning parameters (shown in table 1) were optimised to minimise noise presence; gain was reduced, exposure was increased, the acceleration voltage was kept as low as possible low wattage/power was used to minimize spot size without compromising beam penetration.

Filter	0.5mm Cu
Exposure	4000 ms
Filament current	7.8 W
Acceleration voltage	165 KV
Voxel size	15 µm
Gain	12

Table 1 XCT scan parameters

The data obtained was analysed using Volume Graphics VG Studio Max 3.1 to quantify the unfused powder volume and determine the gray value threshold. The diameter and depth of each defect was evaluated five times using geometry measurements tools in the software (see 5.4).

In this experiment, three different surface determination threshold methods were employed to determine the required ISO threshold: manually selecting background and material, selecting automatic ISO 50 and manually identifying grey values of the pores/defects.

7.1.2 Results

The two-surface determination strategies; manually selecting background and material and selecting automatic ISO 50% resulted in the exact same histogram and the ISO value threshold for both strategies was identical. Optimum threshold value was identified by finding the middle-drilled hole outer contour voxels highest grey value; this includes the voxels that contain both air and material.

Figure 4 a) shows the center drilled hole with ISO 50% surface determination selected, the blue arrow shows the outer edge voxel where the diameter contours are identified. On the opposite side of the ISO 50% identified white circle there is a dark shade which is above the grey value surface determination threshold.

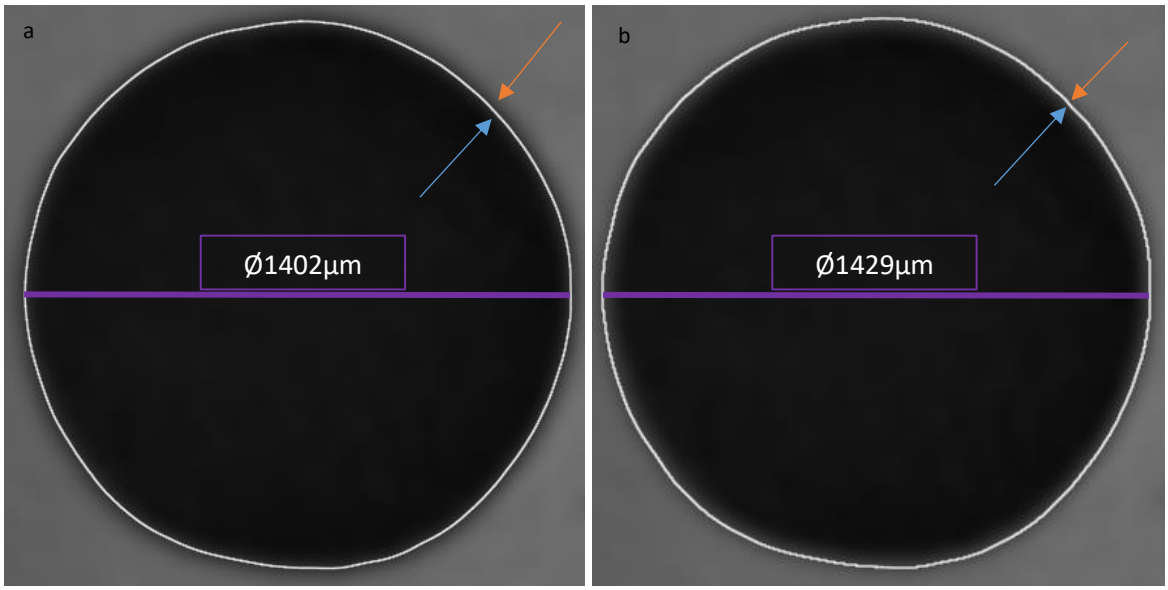

Figure 7-4 XCT image of the middle drilled hole a) ISO50% surface determination, b) Optimised surface determination threshold

The ISO 50% threshold grey value was 38, the area highlighted with the orange arrow had a grey value of 46. Figure 4 b) shows the center drilled hole with optimised surface determination. The results of the defect diameters are presented in table 2, the custom ISO values are closer to the Alicona values than the ISO 50% results.

	Defect1	Defect2	Defect3	Defect4
Alicona	1434	526	142	86
XCT ISO 50%	1402	489	114	48
XCT Custom ISO	1429	521	138	82

Table 2 XCT diameter results

It was also noted from values in the above table that the error is significantly higher in the ISO 50% results for smaller defects. Table 3 presents the results for defect depths, it was noted from the depth results that the custom ISO values are closer to the Alicona values than the ISO 50%.

	Defect1	Defect2	Defect3	Defect4
Alicona	2157	1090	280	96
XCT ISO 50%	2094	1017	244	59
XCT Custom ISO	2149	1081	291	84

Table 3 XCT Depth results

7.1.3 Results discussion

Utilising the ISO 50% approach is widely cited and is the a generally accepted method for XCT surface determination of single material components. This experiment proved that the gray values of pores and powder defects of additive manufactured components are such that they require a different, more bespoke approach. This study presents an approach to determine the threshold level in AM produced components by manually defining the maximum gray value of the pore. Figure 7-5 a) shows a comparison between the results of defect diameters obtained with Alicona, XCT with ISO 50% surface determination and XCT with an optimized ISO value.

The difference in value between Alicona and ISO50% for defect 1 is 2.2%, defect 2 is 7% and defect 3 and 4 are 20% and 56% respectively. Comparing custom ISO to the Alicona results, the difference in defect 1 is 0.4%, defect 2 is 1%, defect 3 is 2.8% and defect 4 is 4.7%.

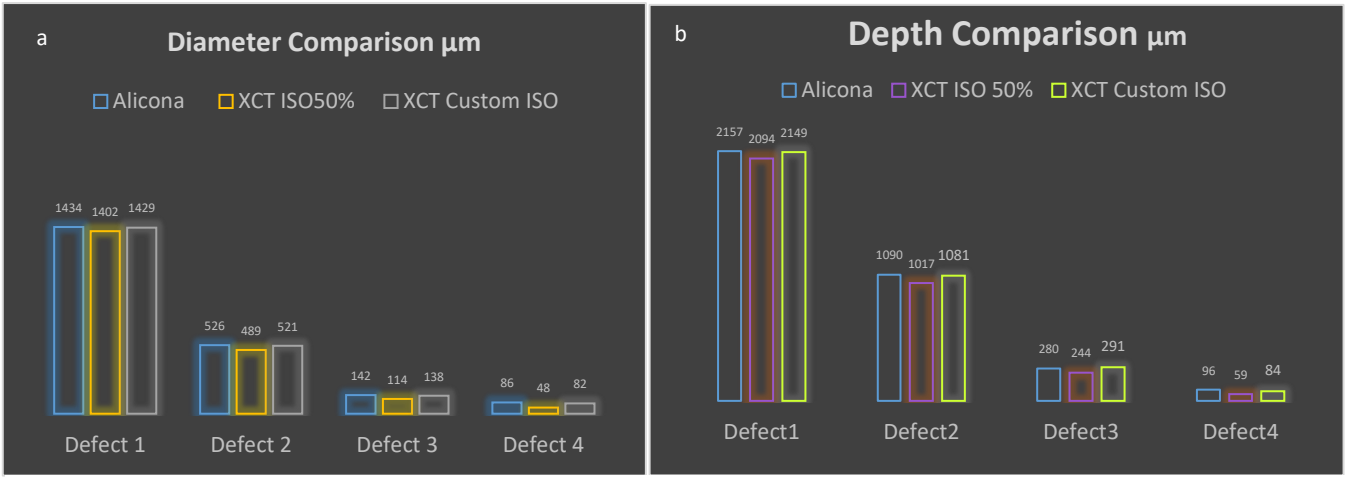

Figure 7-5 a) Defects diameter comparison µm b) Defects depth comparison µm

Figure 7-5 b) shows a comparison between the results of defect depths obtained with Alicona, XCT with ISO 50% surface determination and XCT with a custom ISO value. The differences between the Alicona and ISO 50% results for defect 1 and 2 are 3% and 6.7% respectively. For defect 3 the difference is 12.9% and for defect 4 39.5%. Comparing custom ISO to the Alicona results, the difference in defect 1 is 0.4%, defect 2 0.9%, defect 3 3.8% and defect 4 is 12.5%. It was noted that that the gray value threshold was 46, which corresponds to ISO 70%.

The results of this study confirm that the ISO 50% threshold is not appropriate for porosity analysis as the custom surface determination resulted in closer dimensional values to those obtained from the

alicona measurements. Visual inspection should be used to accurately identify the required threshold for surface determination. Optimisation of surface determination can enhance the capability of non-destructive inspection to detect defects with sub voxel accuracy.

It was noted that the surface threshold values required for accurate porosity detection are different than that needed for outer surface profile measuring. The threshold for surface determination is dependent on the material, material thickness and scanning parameters; scanning the same part with two different parameters will result in different ISO values. Further studies in this chapter will investigate ISO values for different materials and the impact of optimised ISO values on sub-voxel porosity detection.

7.2 Surface determination threshold optimisation for AM build artefact

There are big challenges for NDT regarding additive manufactured components. As previously mentioned in chapter 4, the pores in additive manufactured components are different in nature from those found in cast alternatives. In additive manufactured components, the pores could be hollow, filled with partially fused powder or unfused powder. Furthermore, porosity could be due lack of fusion of un-melted powder (low laser energy) or balling up effect (too high laser energy). There is also the possibility of unfused powder being present within the internal architecture of complex components. In such cases, XCT becomes an essential detection tool.

While XCT looks promising with various technologies available, one of the main obstacles that stops XCT from being accepted is the level of subjectivity within the process; allied to a lack of verification as the only way to verify internal features is by sectioning the part thus the process becomes destructive, losing time and costs. The challenges in inspecting AM components are quite different to cast ones, unfused powder detection is one of the biggest issues as the powder size used in sintering the AM component can be smaller than 20 µm. Detecting small pores or defects of such a size requires the use of high magnification and bespoke XCT settings.

A study carried out by Townsend et al [287], looked at the impact of surface determination on the surface extraction of a Rubert 50 plate. A plate was scanned with 12.9µm voxel size and compared to four other surface determination strategies; three global and one local.

The first method used was a manual one where the global surface determination was set by the user, optimising the surface location; which is explained in detail in VG Studio MAX 3.2 [288]. The second method was the standard ISO 50% surface determination method as explained previously. The third method was based on the Otsu method [289] used in ITK [290], this method identifies two clusters in the grey value histogram minimising the sum of within-class differences between the background and scanned materials. The final method used was a local iterative surface determination, examples of this method are shown in figure 7-6 [287]. This method enhances sub voxel detection by finding the max gradient in grey value and differentiating between the edge of the material and air. The results of this investigation proved that all the global surface determination methods achieve similar results.

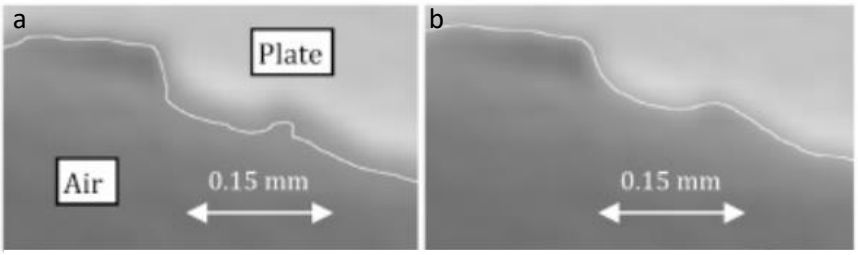

Figure 7-6 a) Iso50% surface b) local iterative surface determination

XCT settings have an important influence on the obtained results, but what makes the process subjective is the accuracy in identifying the grey value threshold for measuring the enclosed internal features and defects. The grey value of the enclosed internal surfaces is different from those exposed to the outer surface. This difference is primarily due to the difference in X-ray path length between the outer edge and the center section of the component.

7.2.1 Methodology

In this study the artefact used was the one discussed in chapter 5 section7 shown in figure 7-7 (a), which is an Aluminum (AlSi10Mg) AM artefact with built-in internal features containing unfused and semi fused powder. The built-in defects were used as markers to identify the powder's grey value.

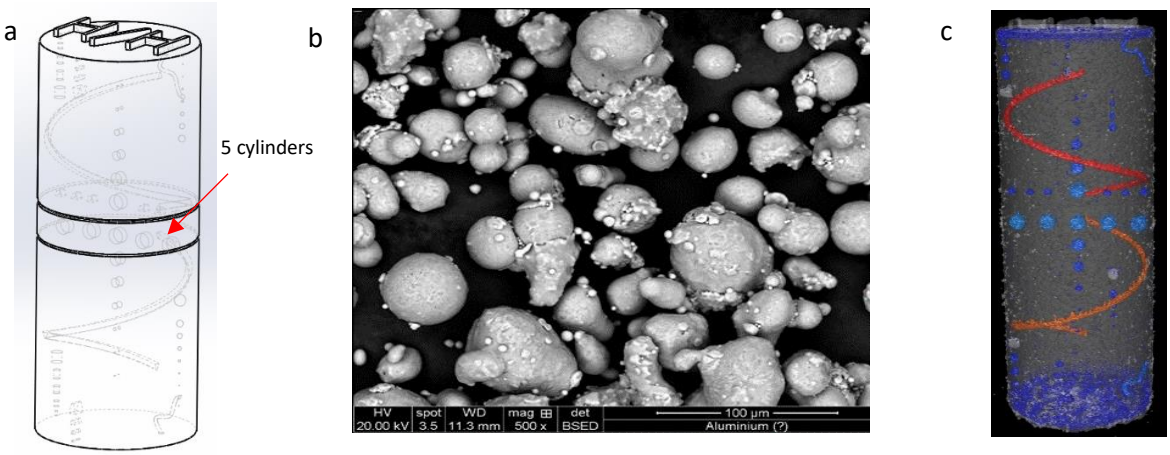

Figure 7-7 a) artefact 3D model b) AlSi10Mg alloy powder 15-45µm used in SLM process c) artefact XCT 3D image

A Nikon XTH225 industrial XCT was used to characterize an AlSi10Mg alloy 10mm diameter artefact shown in figure 7-7 (a) built using a Renishaw AM250 Selective laser melting (SLM). The sample contains several internal features designed to represent pores / defects; varying in size from 50µm to 1mm, located between 150µm and 5mm from the outer surface of the component. The features were designed as geometric features (spheres, cylinders, prisms and helical prisms). This study will focus on the four cylinders located in the middle of the part shown in figure 7-7 (a). The cylinders designed diameter is 1mm and depth is 500µm, the cylinders are spaced 2mm from the center of each other. The distance from the outer edge of the part to the closest cylinder edge is 500µm. The AlSi10Mg alloy powder used in this experiment had been recycled 7 times. Figure 7-7 (b) shows an SEM image of the powder used in which contamination is notable.

The artefact was scanned with a 26µm voxel size to create a volume file of the entire part. The XCT scanning parameters (shown in table 4) were optimized by reducing gain and fine-tuning the histogram by minimising beam filter and reducing filament current to ensure measurement noise was minimised without compromising X-ray beam penetration. Figure 7-7 (c) shows a CT image of the actual sample

Filter	Exposure	Filament Current	Acceleration Voltage	Voxel Size
0.25mm	4000ms	58µm	135 kV	26 µm

Table 4 XCT scan parameters

The data obtained was analyzed using Volume Graphics VG Studio Max 3.1 to quantify the unfused powder grey values and determine the optimum threshold.

The diameter and depth of each defect was evaluated using geometry measurements tools in the software. To determine the adequate ISO threshold three different methods were employed: manually selecting background and material, selecting automatic ISO 50 and manually identifying grey values of the pores/defects. To confirm the XCT results the part was sectioned by CNC machine and the features was measured with an Alicona G4 focus variation microscope. The location of the defects was compared to the design and XCT results.

The surface determination methodology used currently is uniquely optimised to detect and measure internal features/defects [10]. The method shown in figure 7-8 (a) is applied by identifying the grey value of the trapped air between the unfused powder within the denser section of the work piece (longest X-ray path) shown in figure 7-8 (b), this exact grey value is used as the threshold for the defect analysis.

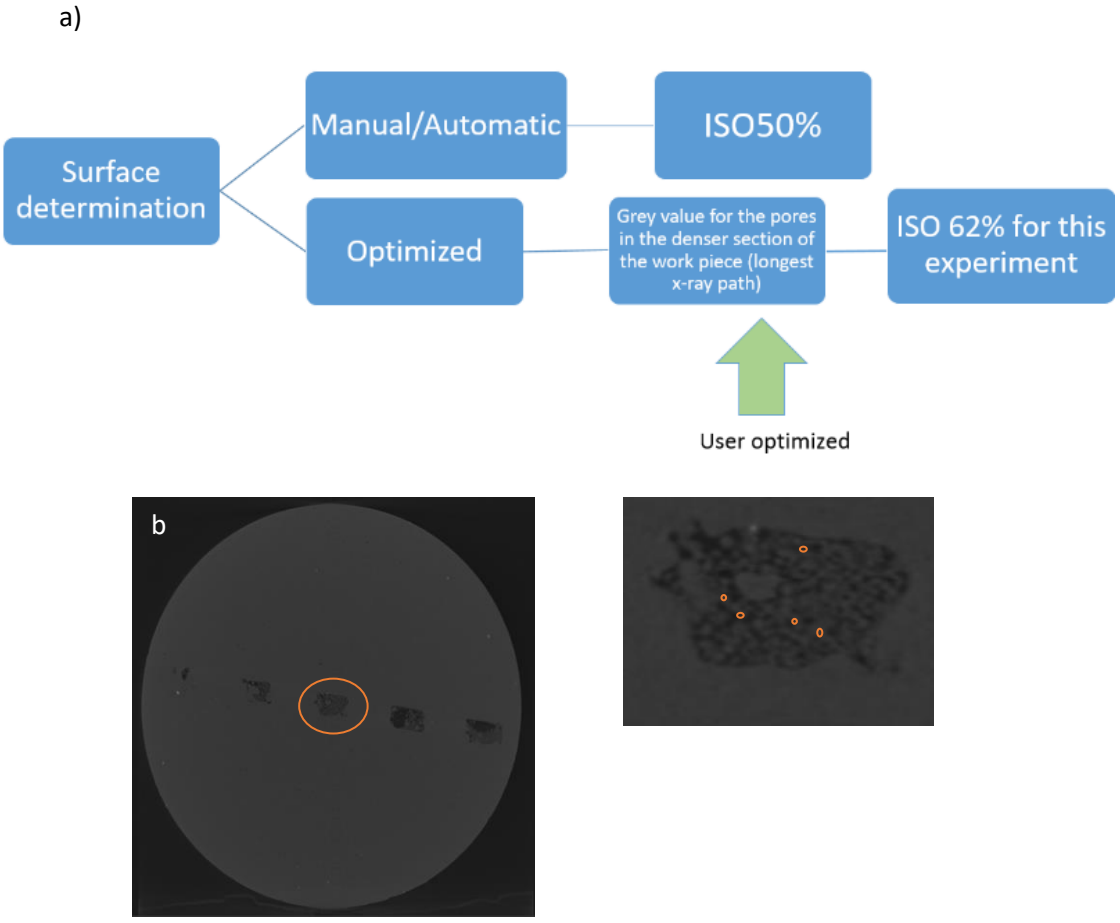

Figure 7-8 surface determination optimisation methods

This method enhances sub voxel detection by taking into consideration the voxels that contain air and material. Following the application of this method, shown in figure 5, this study adopted the surface determination threshold of 62 %.

7.2.2 Results

As previously discussed in section 5.7.2, there were two circumferential location marks printed in the middle of the artefacts, the indication marks were located in the central zones of the five cylinders. Figure 36 in chapter 5 discusses the location verification process; the centre of the cylinders was designed to be 14.40 mm from the base, the location was verified by the XCT and found to be 14.382mm from the base; 18µm lower than the designed location.

Another method used the upper and lower helix features to compare the angular position to the 3D model. Verification showed the angular location was identical to the model with the exact start and end locations within the XCT's resolution. The artefact was sectioned through the middle between the indication marks using a CNC machine.

The length and width of the five cylinders were verified using an Alicona G4 Focus Variation Microscope (Alicona Austria). The 5 cylinders are numbered 1 to 5 from left to right, the length is named as "major" axis and width as "minor" axis. The major and minor axis for the 5 cylinders shown in figure 7-9 was used for the methodology qualification by comparing the design dimensions to the Alicona based measurement and to the XCT ISO 50% threshold and custom threshold method.

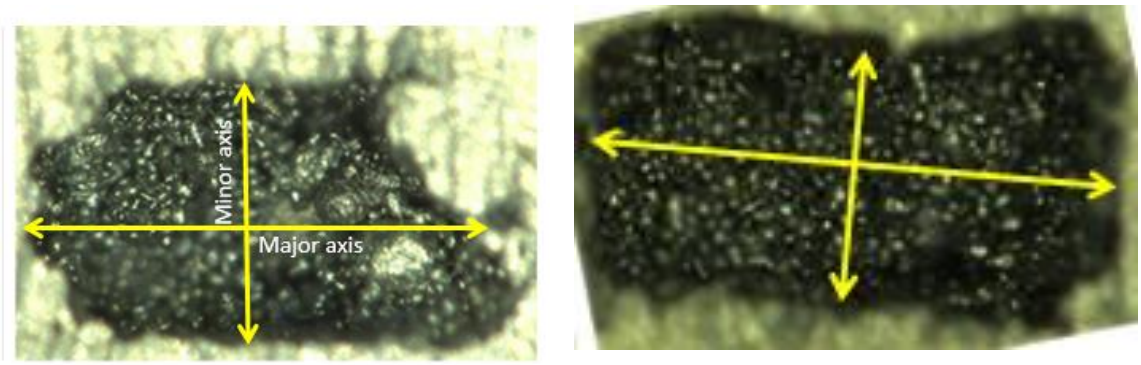

Figure 7-9 Minor and major axis of printed cylinders

The dimensional comparison is shown in figure 7-10, the minor (width) values were lower than the designed values, the only exception was cylinder 5 that was 1% more than the designed width. The difference between the reference Alicona results and custom threshold (surface determination) for cylinder 1 is 1.8%, cylinder 2 0.5%, cylinder 3 4.5% and cylinder 4 and 5 are 0.9% and 1% respectively. The difference between the Alicona reference values and ISO 50% threshold for cylinder 1 and 2 are 6% and 4.8%, cylinder 3 and 4 11.4% and 1.6% and cylinder 5 5.4%.

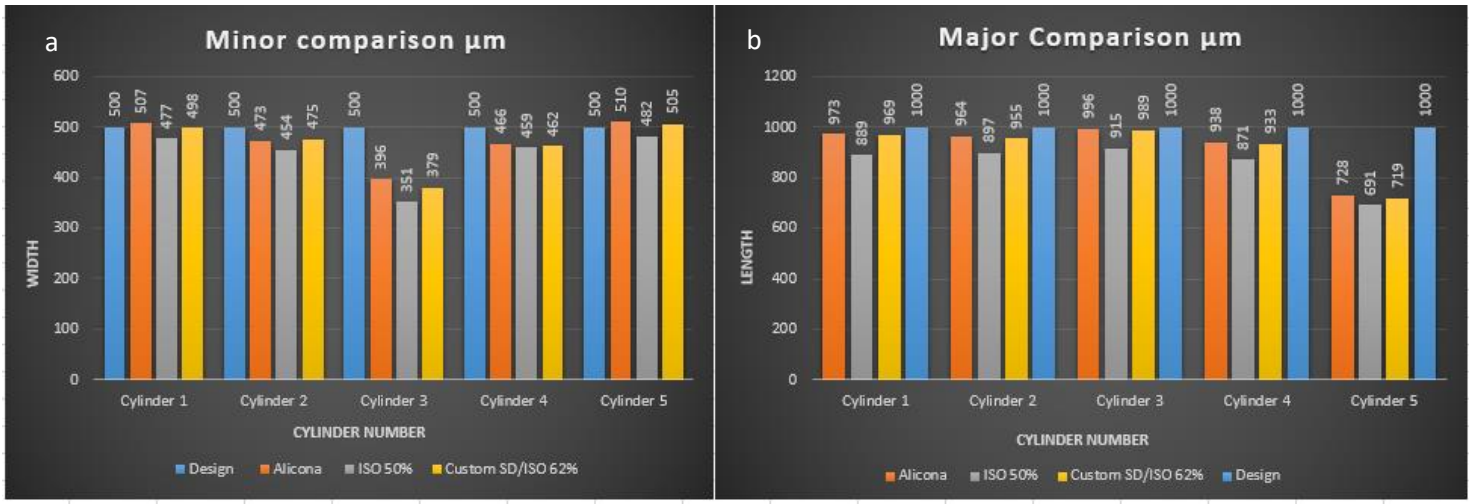

Figure 7-10 (a) Minor axis comparison (b) Major axis Comparison

In the case of major (length) comparison the custom threshold values were closer to the Alicona reference results than those obtained from ISO 50% threshold. The custom threshold value differences from Alicona for cylinder 1 and 2 are 0.5% and 0.9%, cylinder 3 and 4 are 0.3% and 0.4%. For the ISO 50% threshold the difference for cylinder 1 is 9%, cylinder 2 is 7% and cylinder 3 and 4 are 7.8% and 5.1% respectively. The lengths for cylinder 5 were not compared due to the presence of semi-fused powder. The results show that across all measurements the optimised surface determination method gave the least error compared to the verified values.

7.2.3 Powder detection discussion

The characterisation of semi fused and unfused powder is one of the biggest challenges in the metrology of AM components. This study highlighted the effect of semi fused and unfused powder presence on the part metrology.

It was noted during this study that the gray value threshold was 60.9, which corresponds to ISO 63.2%. The values for the threshold can vary while scanning the same part due to scanning parameters selected by the operator. Furthermore, scanning different shapes and dimensions of the same material will result in a different grey value. The threshold of the unfused powder will always be more than 50%. The grey value of the external background (air) for this investigation was different to the background found inside the features, the highest value for background was found inside the mid cylinder (3) and the lowest was inside cylinder 1 and 5.

Whilst the ISO 50% approach is widely cited and is a generally accepted method for XCT surface determination of single material components. This study showed that the grey values of pores and powder defects within additive manufactured components are such that they require a different, more bespoke approach to be adopted, such as manually defining the maximum grey value of the pore.

In this study, it was evident that the semi-fused particles were joined together in the areas closer to the melt pool creating large irregular particles, the particle grey values are very close to the solidified material, making it more difficult to threshold and quantify. A mean grey value analysis was carried out to assist in understanding the effect of the powder presence on the XCT histogram, and in identifying the appropriate threshold for powder detection.

Figure 7-11 shows the artefact mean grey value analysis, where figure a) shows the top view of the artefact with the five middle cylinders, figure b) shows a magnified front view of central cylinders. From the analysis, it can be concluded that the scan parameters are appropriate; this is proven by the consistency in the grey value across the entire artefact, with no unexpected dark or bright spots present.

In figure 7-11, the background/ air is light blue with a mean grey value under 25, whilst the solid material is deep red with a mean grey value above 64. The grey values of the internal features and defects/pores vary depending on size and shape.

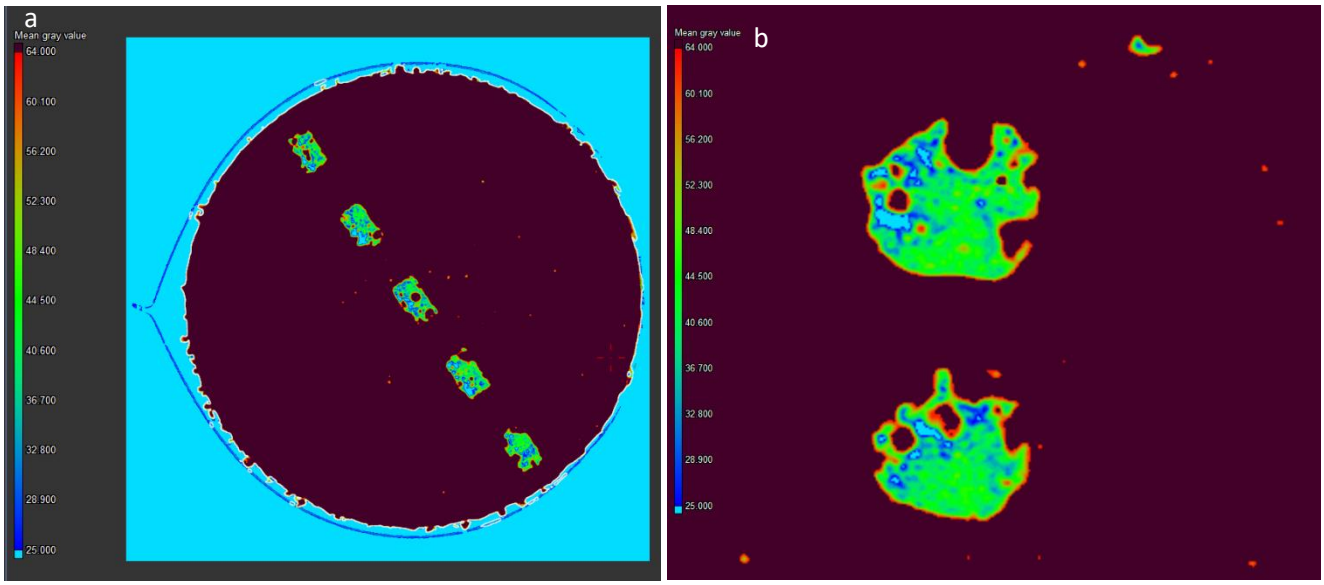

Figure 7-11 (a) Grey value analysis top view (b) Grey value analysis front view

The variation in grey value can be seen in figure 7-11 b), where the drop in the grey value increases with defect/pore size. The pores must be at least 3 times larger than the scanning voxel size to retain the background mean grey value. It was also noted that the grey value gradually reduces from the defect edge (highest value) to the core (lowest value).

The grey value of the semi-fused and un-fused powder is larger than the ISO 50% threshold and the large powder particles retain similar grey values to the solid materials.

The grey value of a material is related to the density of the material, this difference in grey value can be used to detect contamination within an AM build. Figure 7-12 a) show a top view of a section within the build with brighter particles. These particles have a grey value of 135 that is double the grey value of the background-solidified particles.

Figure 7-12 b) shows several bright spots with mean a grey value as high as 205. The solid material mean grey values range from 70 to 75. The small powder particle mean grey values range from 62 and 69, which is slightly lower than the solid material mean grey value, whilst the large particles retain the same mean grey value as the solid material.

It was noted that powder particles morphology could play an important role in detecting powder presence, which could compromise the defect characterisation process. Semi fused powder tends to retain a similar grey value as the solid material, whilst the un-fused powder grey value varies, depending mainly in the powder size and shape/sphericity.

Smaller size particles with regular shape fill the gaps and retain a mean grey value slightly less than the sold material. Whilst larger irregular particles retain a similar grey value to the solid material but they will usually have some relatively large air/background around them where the other particles are not filling the gaps.

Alternatively, if the small powder particles filled the air around the large particles the situation would be different because the grey values may be similar to the material. This situation requires further investigation.

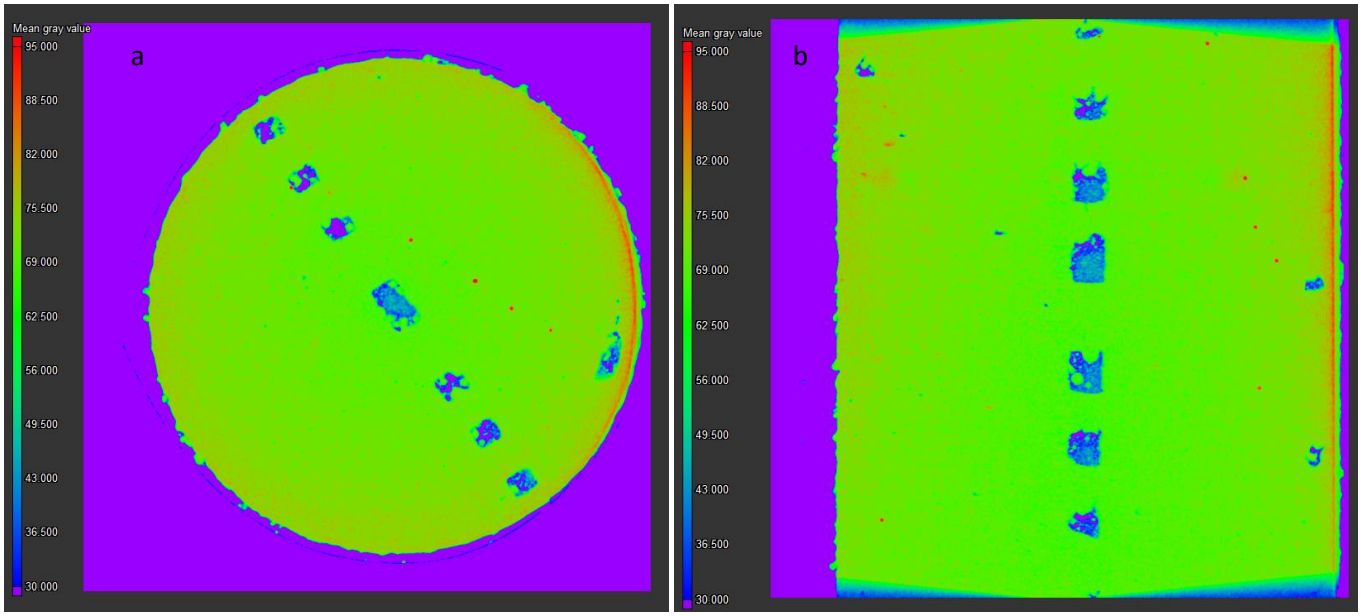

Figure 7-12(a) Grey value analysis top view (b) Grey value analysis front view

The results of the study confirm that ISO 50% is not the appropriate threshold for porosity analysis and for detecting unfused powder. The study has shown that to identify individual powder particles the exact gray value must be used. The gray value of the unfused powder tends to be closer to the material peak in the histogram.

Visual inspection should be used to accurately identify the required threshold for surface determination. Optimisation of surface determination can enhance the capability of non-destructive inspection to detect unfused or semi fused powder. It was also noted that the surface threshold values required for accurate porosity detection are different from that needed for outer surface profile measuring.

The threshold for surface determination is dependent on the material, material thickness and scanning parameters, therefore, scanning the same part with two different parameters will result in different ISO values.

7.3 Repeatability and Reproducibility

In this thesis two measurement systems were employed and XCT and Alicona Focus variation Microscope. In terms of uncertainty of the XCT there is much ongoing research including work by Affenzeller et al [291]. Essentially this work is still investigating sources of measurement uncertainty including material x-ray interaction and atomic density levels beam hardening effects and focal point drift. The sources of error are multiple and yet not fully quantified, alternative approaches such as Monte Carlo simulation are being considered but not reported in the literature [292]. Due to the above knowledge deficit, in the present work repeatability and reproducibility were considered adequate to demonstrate the applicability of the developed methodology for industrial users. A full consideration of uncertainty sources would have been outside of the scope of the PhD and would constitute a PhD project in itself.

The focus variation microscope (Alicona G4) used in the study was implemented due to its ability to characterise small surface defects below the resolution of conventional CMM machines available to the author. In terms of uncertainty of the optical FV technique this is the subject of research being carried out by Leach et al [293-295], and an ISO discussion paper is currently being prepared. However, given the lateral resolution of the FV approach is 1um (2 x10) it is considered that for artefacts of 50-1000um then measurement uncertainty should not be a factor.

Currently, XCT metrological capabilities require further enhancement, due to the absence of a full traceability chain and the presence of different scan parameters that can influence the process. In the last 10 years, substantial progress has been made towards an XCT standardised process for dimensional inspection, however AM surface measurement and porosity characterisation has been shown to be different from dimensional inspection. The scanned object dimensional inspection is affected by XCT measurement uncertainties. These are controlled by the scan voxel size (magnification) and scan parameters; however, porosity characterisation and surface measurement are also affected by the surface determination threshold, in addition to the material, magnification and scan parameters. Artefacts are used for performance verification of the measuring system and the identification of multiple errors, this is considered one of the essential steps in the metrological standardisation process.

Several researchers carried out different experiments to identify XCT dimensional metrology uncertainty [291,296]. It was shown that in order to achieve an accurate XCT dimensional measurement the material edge must be precisely differentiated from the background /air. As previously mentioned in chapter 3, XCT measurement accuracy is influenced by the accuracy of the 2D x-ray image and the process of reconstructing the 2D image into a 3D model.

The accuracy of the XCT 2D images are directly affected by the machine specification, scan parameters and target material, whilst the accuracy of the reconstruction process is influenced by the reconstruction algorithm (including edge detection), noise and beam hardening filtration algorithm, XCT kinematics repeatability and accuracy and correct identification of the rotational axis.

Measurement uncertainty is the main aspect that evaluates the quality of the measurement. In order to ensure measurement traceability, every result must be combined with its uncertainty [296]. However, several sources can cause uncertainty in the XCT measurements, making it very difficult to calculate the overall uncertainty. Furthermore, because the XCT system is a multi-purpose device that can be used for internal and external measurements, the uncertainty can vary significantly [296].

There is no guidance addressing XCT properties that affect measurement uncertainty. There are several aspects that cannot be taken in consideration, as they are variable and change from one machine to another, for example, the difference between high and low kV machines and the impact of beam spot size. In addition, the operator can play an important role in the overall accuracy of the XCT measurement, for example, an experienced operator that understands the influence of the scanned object material on result accuracy will select the appropriate parameters that produce good results and reduce scan time.

In these studies, the alicona was used for reference measurement to compare to the results obtained from the XCT. Several researchers have compared XCT results to CMM calibrated artefacts for uncertainty evaluation, this approach is impossible to adopt for internal features and enclosed defects, due to the requirement for probe access.

Another point to consider is the quantification of the systemic error, which can be estimated by the comparison of several measurements, Systematic error can be proportional or constant to the true value. The repeat of an XCT measurement does not take in consideration the impact of thermal expansion of the work piece, which can vary significantly depending on the scanned object material. The experimental use of a repeated measurement approach takes time to satisfy the number of repeats required for statistical validation.

In this study the precision of the XCT measurement were investigated by evaluating the reproducibility and repeatability of the internal feature characterisation process. Several sources of variability were used; two different machines, three different operators and surface determination threshold. The main aim of the repeatability study was to identify the confidence in the measurement results from successive measurements when scanning under the same conditions. The repeatability study was used to find the relationship between results when conditions are varied.

For the repeatability study, the artefact was scanned using the same parameters 10 times, to ensure the same position was used; the artefact was positioned on the rotating stage and not moved until the end of the experiment. The only influencing factors were filament degradation, expanding of the X-ray tube housing from temperature increase and the automatic shift of the center of rotation due to axis shift.

The impact of filament degradation is not fully quantified [297], but the filament tends to behave like any normal lamp filament that starts to fluctuate only very close to failure. To reduce the impact of filament degradation, shading correction was carried out before each scan and pre-scan histograms were inspected to ensure that the highest grey value for the air and the material was similar. In the reconstruction software the center of rotation was kept throughout the experiment; it was not possible to detect any shift.

In the reproducibility study, the operators were asked to select their own scan parameters after brief guidance on the best-recommended practice for parameters selection was given. The only fixed parameters were the magnification /voxel size, which was kept constant throughout the study. Four operators were used in this study, the scan arrangements are shown in figure 7-13.

Figure 7-13 scan arrangement for the reproducibility study

All four operators identified their own surface determination threshold based on the optimisation method shown in figure 7-8 and the dimension measurement results were compared to the reference values obtained from the Alicona measurement.

7.3.1 XCT defect analysis/internal features measurement good practice

The use of XCT as a dimensional measurement tool is subject to the procedures followed. Several conditions must be considered. The scanned object must be fixed on the rotary table to eliminate blurriness from movement. The scanned object fixture should be made from a low-density material to minimize beam absorption. When scanning an object, it is recommended to have some air/background voxels around it in the frame; not filling the frame with the object as this will enhance surface determination in the analysis process.

For high precision XCT measurements with a Nikon 225, it is always recommended if possible to minimize the spot size and compensate with a longer exposure time. To minimise noise presence, the gain should be under 18 and the acceleration voltage must be sufficient to penetrate the scanned material using a minimal thickness filter; this can be confirmed by inspecting the pre-scan histogram. The grey value of background/air must not exceed 63K and the minimum grey value for the material must not be lower than 7.5K.

7.3.2 Experiment setup

In this study the artefact used was the one discussed in section 5.7 shown in figure 7-7 (a), it is an Aluminum (AlSi10Mg) AM artefact / sample with built-in internal features, containing unfused and semi fused powder. The built-in defects were used as markers to fine tune the internal features grey value.

AS previously mentioned in chapter 5, there were two circumferential location marks printed in the middle of the artefacts; the indication marks were located in central zones of the five cylinders. Figure 7-14 (which is figure 5-32 and it reproduced here for convenience) shows the location indication marks and illustrates the location verification process; the centre of the cylinders was designed to be 14.40 mm from the base, the location was verified by the XCT and found to be 14382µm from the base, 18µm lower than the designed location.

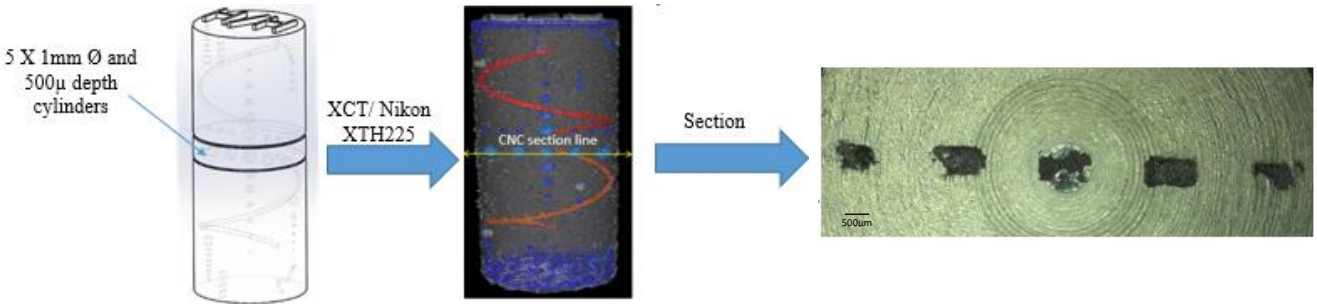

Figure 7-14 Location verification and physical section slice

Another method used for location verification used the lower and upper helix features and compared the angular position to the 3D model, the verification proved that the angular location was identical to model with the exact start and end location within the XCT resolution. The artefact was sectioned in the middle in-between the indication marks using a CNC machine. The sectioned slice is shown in figure 7-14, the length (major) and width (minor) of the five cylinders were verified using a Alicona G4 Focus Variation Microscope (Alicona Austria).

The 5 cylinders are numbered 1 to 5 from left to right, the length is named as “major” axis and width as “minor” axis. The major and minor axis for the 5 cylinders shown in figure 14 were used for the repeatability and reproducibility methodology qualification by comparing the design dimensions to the Alicona measurements using the custom surface determination threshold method.

A Nikon XTH225 industrial CT was used to scan the artefact with the same parameters consecutively 10 times. To ensure the same position was used, the artefact was positioned on the rotating stage and not moved till the end of the study, the scan parameters used in the repeatability study are shown in table 5.

Filter	Exposure	Filament Current	Acceleration Voltage	Voxel Size
0.25mm	4000ms	7.2W	140 kV	13µm

Table 5 XCT parameters

Data processing, surface determination and defect analysis was carried out using VG Studio Max 3.1 (Volume Graphics, Heidelberg). The previously discussed surface determination methodology was applied by identifying the grey value of the trapped air between the unfused powder within the denser section of the work piece (longest X-ray path); see figure 8. This exact grey value was used as the threshold for the defect characterisation. This method enhances sub voxel detection by taking into consideration the voxels that contain air and material.

7.3.3 Repeatability results

The artefact was scanned 10 times without moving the stage or moving the artefact. The acquired data was not filtered in the reconstruction process and the surface determination was selected manually with the aforementioned method. The results are shown in table 6 and 7, figure 14, 15, and 16.

Table 6 shows the results of the major measurements for the 5 cylinders, with the calculated average, standard deviation (SD) and standard error (SE). Cylinder 3 had the highest SD and SE with 4.6 and 1.4 respectively.

Cylinder number	1	2	3	4	5
Alicona	973	964	938	996	728
Average	966.8	955.9	929.1	987	721.6
Std dev.	2.780887149	4.01248053	4.653553003	4.027681991	2.75680975
Standard error	0.879393731	1.268857754	1.47158267	1.273664878	0.871779789

Table 6 Major results comparison

Cylinder 5 had the lowest SD and SE with 2.7 and 0.87 respectively. For the major measurements cylinder 1’S average is the closest to the Alicona reference value. Table 7 shows the results of the minor measurements, cylinder 5 hadthe highest SD and SE with 5.5 and 1.7 respectively, whilst cylinder 3 had the lowest SD and SE with 3.3 and 1.05 respectively.

Cylinder number	1	2	3	4	5
Alicona	507	473	396	466	510
Average	497.2	468.1	386.9	451.1	496.2
Std dev.	4.589843861	3.725288952	3.338091842	3.925648263	5.553313039
Std error	1.45143607	1.178039803	1.055597326	1.24139898	1.756111776

Table 7 Minor results comparison

Figure 7-15 below shows the XCT results compared to the Alicona measurement, where 7-15(a) is the major comparison and 7-15 (b) the minor comparison. The Alicona reference results are represented as red circles in the graphs. All the XCT results are lower than the reference Alicona measurements. For the major measurements, the mean value is within 0.5% from highest obtained value, however in some measurements like cylinder 2, 3 and 4 it was 1% from the lower obtained value.

Similarly, in the minor measurements, the Alicona reference values are higher than those obtained from the XCT; the highest difference is 3.3% in cylinder 4. The mean value was within 1.7 % from the highest obtained value and in some measurements like cylinder 4 it was 1.9% from the lower obtained value.

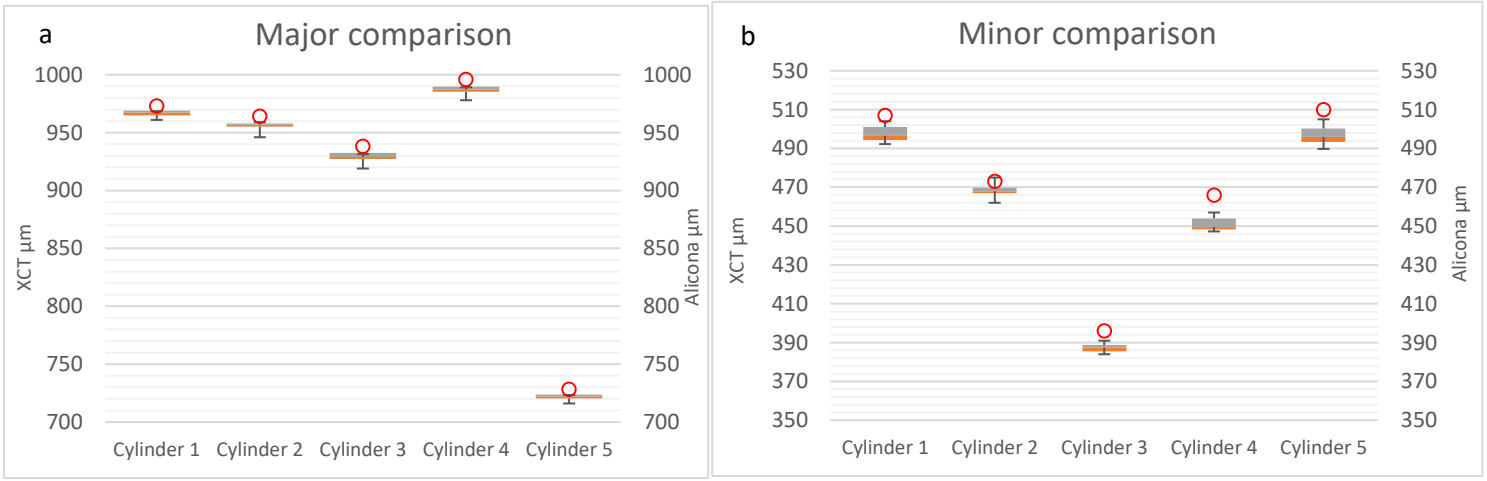

Figure 7-15 Repeatability results compared to Alicona reference values

The results of minor measurements are evenly spread; this is evident by the higher standard deviation value. This is also reflected in the standard error results, where cylinder 1 and 5 minor measurements are the highest with 4.5, 5.5 SD and 1.4, 1.7 SE, respectively.

Figure 7-16 shows the major measurement comparison where 7-16 a) is the deviation from the Alicona reference measurement in microns and 7-16 b) is the deviation from the Alicona in Voxels. All the measurements are within 19µm from the Alicona measurements; the closest measurement to the Alicona is 3µm.

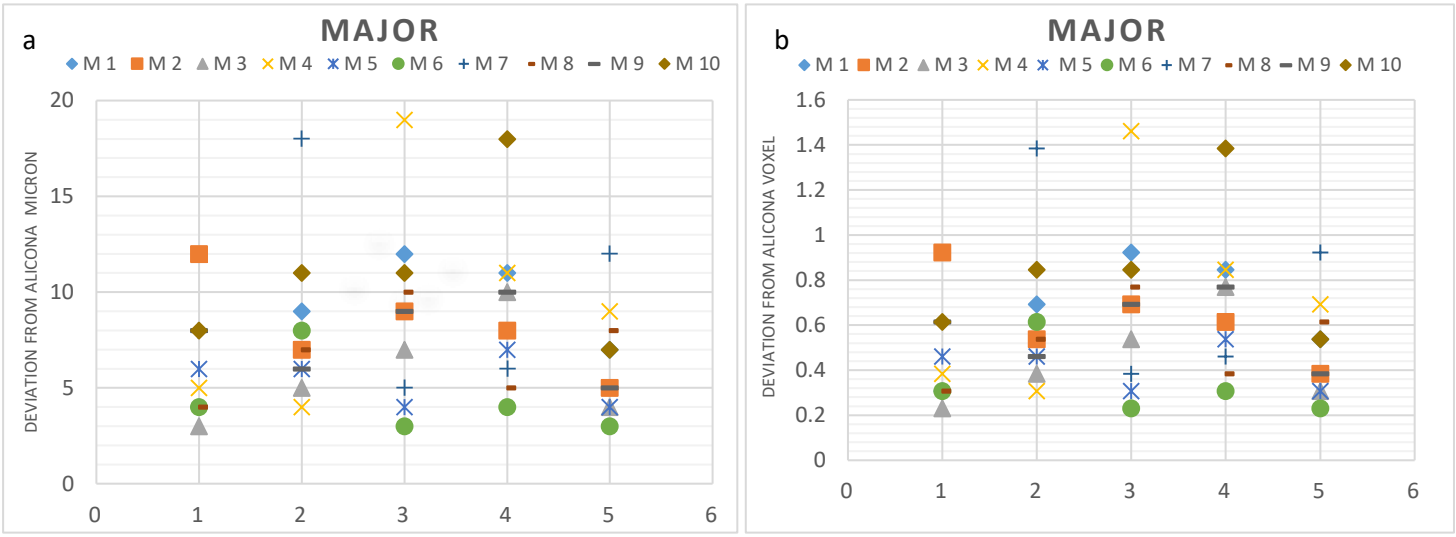

Figure 7-16Repeatability results for the major measurement compared to Alicona reference

There are only three measurements above 15µm and the majority of the measurements are under 12µm. In total 10 measurements are less than 5µm smaller than the Alicona reference values. The voxel size used in this study was 13µm, the smallest deviation was 0.2 voxels and the largest deviation was 1.5 voxels. The majority of the measurements vary less than one voxel from the reference values. The deviation results for cylinder 1 were between 0.2 and 0.9 voxels, cylinder 2 between 0.3 and 1.4 voxels, cylinder 3 between 0.2 and 1.5 voxels, cylinder 4 between 0.3 and 1.4 voxels and cylinder 5 between 0.25 and 0.95 voxels. The lowest measurement spread was in cylinder 1 and 5. Figure 7-17 shows the minor measurement comparison, where 7-17 a) is the deviation from the Alicona reference measurement in microns and 7-17 b) is the deviation from the Alicona in Voxels.

All the measurements are lower than the reference value apart from the first measurement of cylinder 2, which is 3 microns more than the reference value. In the case of the minor measurements, two are more than 20µm from the reference value. The majority of the measurements are between 2 and 20 microns from the reference values. Figure 7-17 b) shows the deviation from the reference values in voxels, the largest deviation is 1.8 voxels and 3 measurements are higher than 1.5 voxels. All the measurements are between 0.2 to 1.8 voxels less than the reference value. The only exception is measurement 1 in cylinder 2, which is 0.15 voxel more than the reference value.

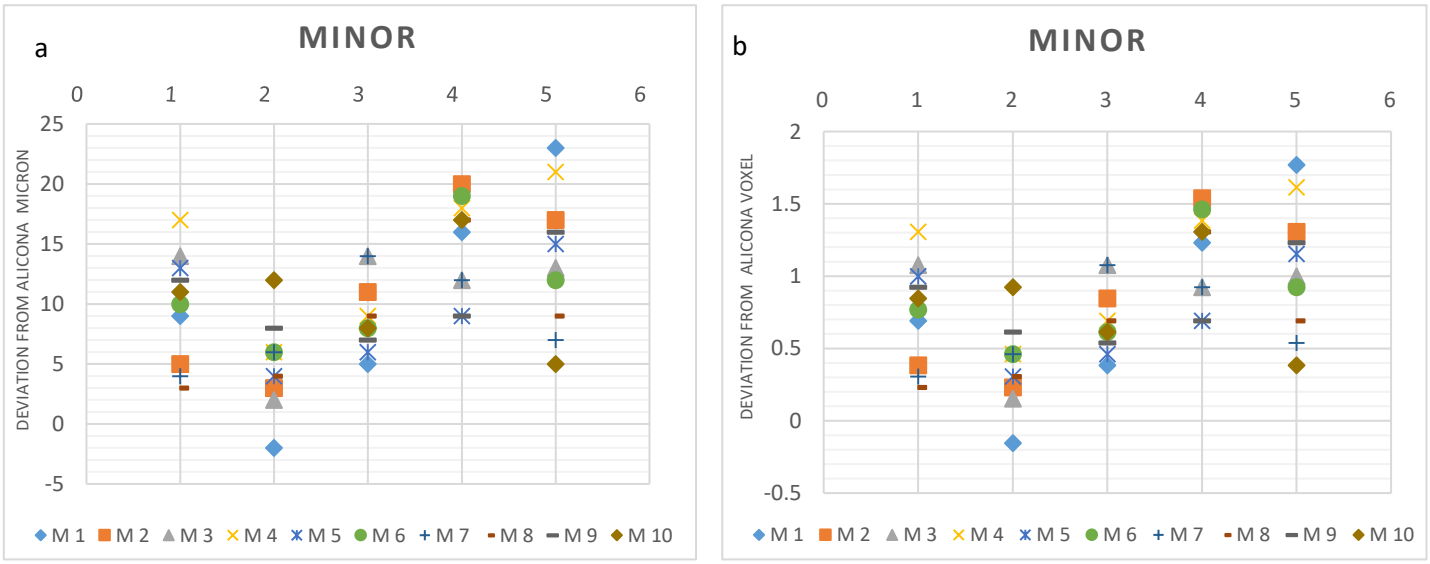

Figure 7-17 Repeatability results for the minor measurement compared to Alicona

The results deviation of cylinder 1 were between 0.2 and 1.3 voxels, cylinder 2 between -0.15 and 0.9 voxels, cylinder 3 between 0.4 and 1.1 voxels, cylinder 4 between 0.7 and 1.6 voxels and cylinder 5 between 0.4 and 1.8 voxels. The lowest measurements spread was in cylinder 3, and 80% of the results are different from the reference value. The repeatability study showed that by selecting the appropriate scan parameters, combined with the optimisation of surface determination it is possible to enhance the XCT defect characterisation process. The mean results are within 10 microns from the reference value, as the voxel size used was 13µm the measurements mean falls inside the sub voxel resolution. The highest standard deviation was 5.5, which was found in cylinder 5's minor measurement, the measurements mean for this cylinder was 14µm less than the Alicona reference value. In cylinder 5 the measurement results are well spread with no single repeated value.

7.3.4 Reproducibility results

In the reproducibility study the operators were asked to select their own scan parameters after a brief guidance on the best recommended practice for parameters selection (see 7.3.1). The voxel size used was 11µm and it was fixed throughout the study. Four operators were used in this study, the scan arrangements are shown in figure 13. The selected scan parameters and surface determination thresholds selected by each operator are shown in table 8.

Parameter\operator	1	2	3	4
Filter (mm)	0.25	0.1	0.25	0.25
Exposure (ms)	4000	2864	2864	4000
Filament current (w)	7.2	8	8.6	7.9
Acceleration voltage (kV)	140	150	145	145
Surface determination threshold	39.3	31.7	36.1	41.4

Table 8 scan parameters

After scanning the artefact, a mean grey value analysis was carried for each scan by the operators, which was used for identifying the surface determination threshold and assessing the quality of the scans. Figure 7-18 shows a top and front view of the grey value analysis used by the first operator.

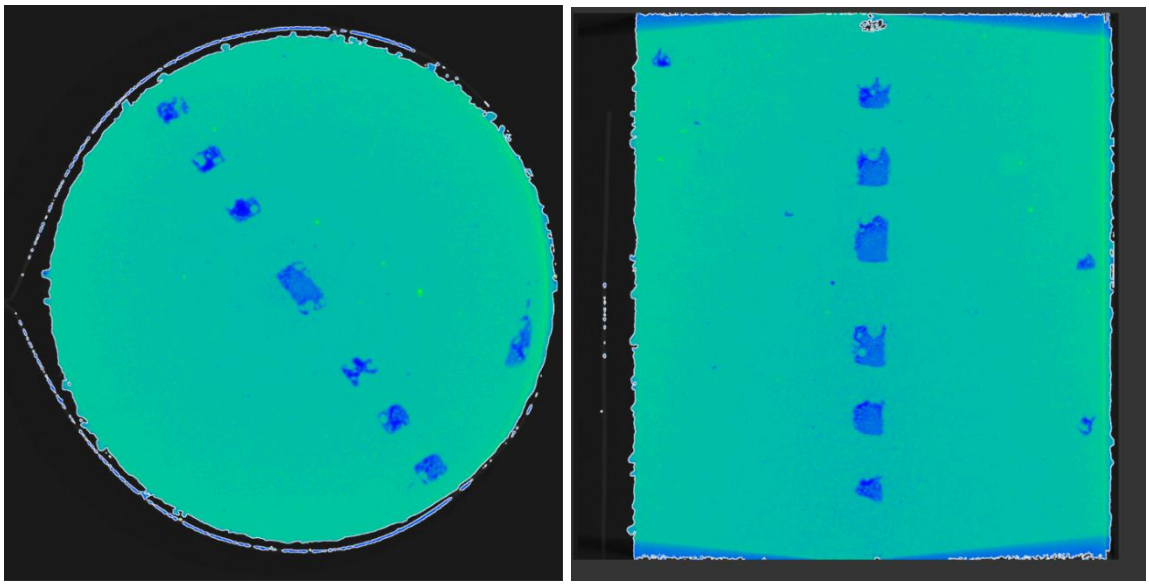

Figure 7-18 grey value comparison

Mean grey value analysis can be used in assessing scan parameters, for example in figure 18 there are no internal or external artefacts, also there is no noise present or any evidence of beam hardening or scatter. The grey value is consistent across the artefact, with an expected drop in the internal features between the semi-fused and unfused powder; deep blue. In addition, there are particles that indicate the presence of powder contamination; bright green.

Figure 7-19 shows the XCT major result deviation from the Alicona reference value a) is in microns (µm) and b) in Voxels. One of the operators XCT major measurement results are more than the alicona results and the other three operator measurements are less than these reference measurements.

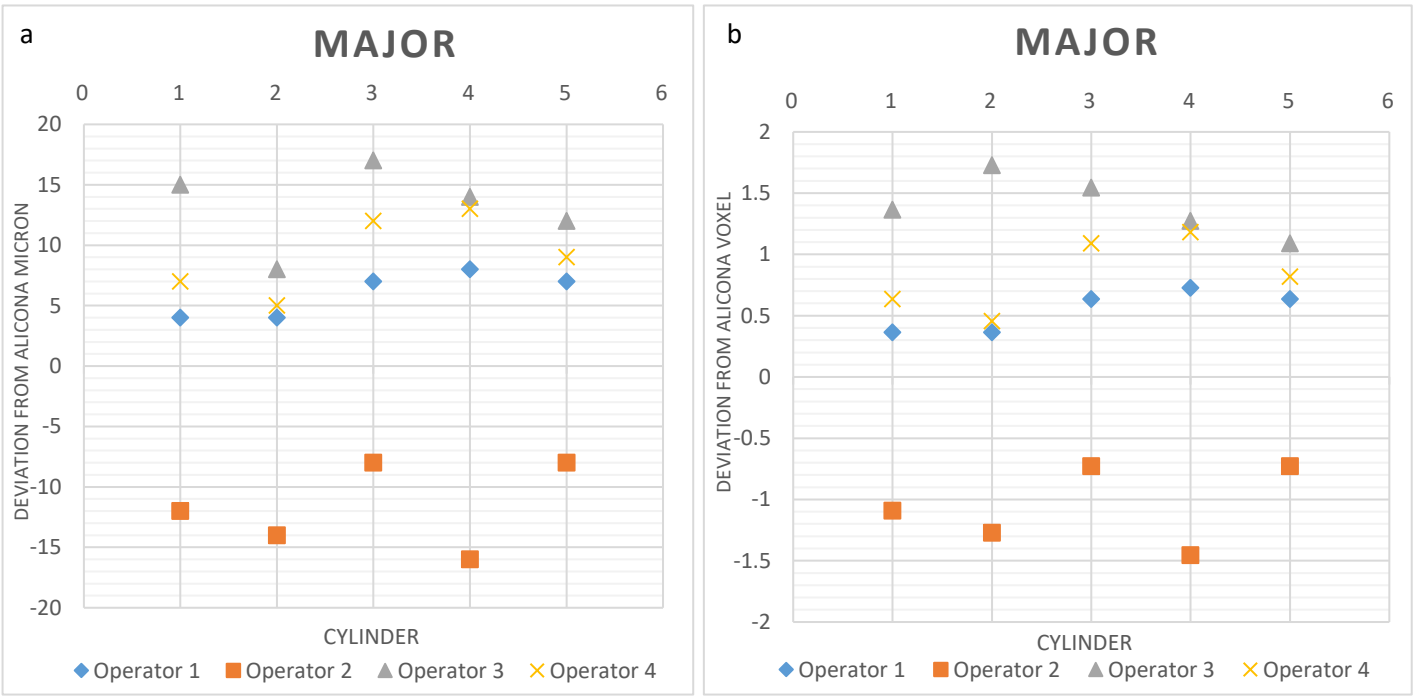

Figure 7-19Major XCT results deviation from Alicona a) in microns b) Voxels

The first operator's measurements are between 4 and 8 µm less the Alicona results, the second operator's measurements are between 3 and 16 µm greater than the reference measurements. The third operator's results are between 8 and 17µm less than the Alicona results and the fourth operator measurements are between 5 and 13µm less than the Alicona results.

Figure 7-19 b) shows the deviation from the reference measurements in voxels; all the scans were carried out with a fixed 11µm voxel size. The largest deviation is 1.7 voxels and the smallest is 0.3 voxels. The first operator measurements are 0.7 voxels or less than the alicona, the second operator's measurements are between 0.7 and 1.4 voxels greater than the reference values. The third operator's measurements are between 1.1 and 1.7 voxels less than the reference values and the fourth operator has three measurements less than one voxel and the other two are above 1 voxel less than the Alicona reference values.

Figure 7-20 shows the XCT minor results deviation from the Alicona reference value where a) is in microns (µm) and b) in Voxels. The first operator's measurements are between 2 and 9µm less than

the reference values, the second operator's measurements are between 4 and 16 µm greater than the alicona reference values. The third operator's results are between 13 and 20µm less than the alicona reference value, and the fourth operator's measurements are between 9 and 16µm less than the alicona measurement values.

Figure 7-20 b) shows the XCT minor results compared to the Alicona in voxels, the first operator's results are between 0.4 to 0.8 voxels less than reference values. The second operator's results are between 0.6 to 1.4 voxels greater than the alicona results. The third operator's results are between 1.1 to 1.8 voxels from those obtained from the alicona and the fourth operator's measurements are between 0.8 to 1.4 voxels less than the alicona reference values.

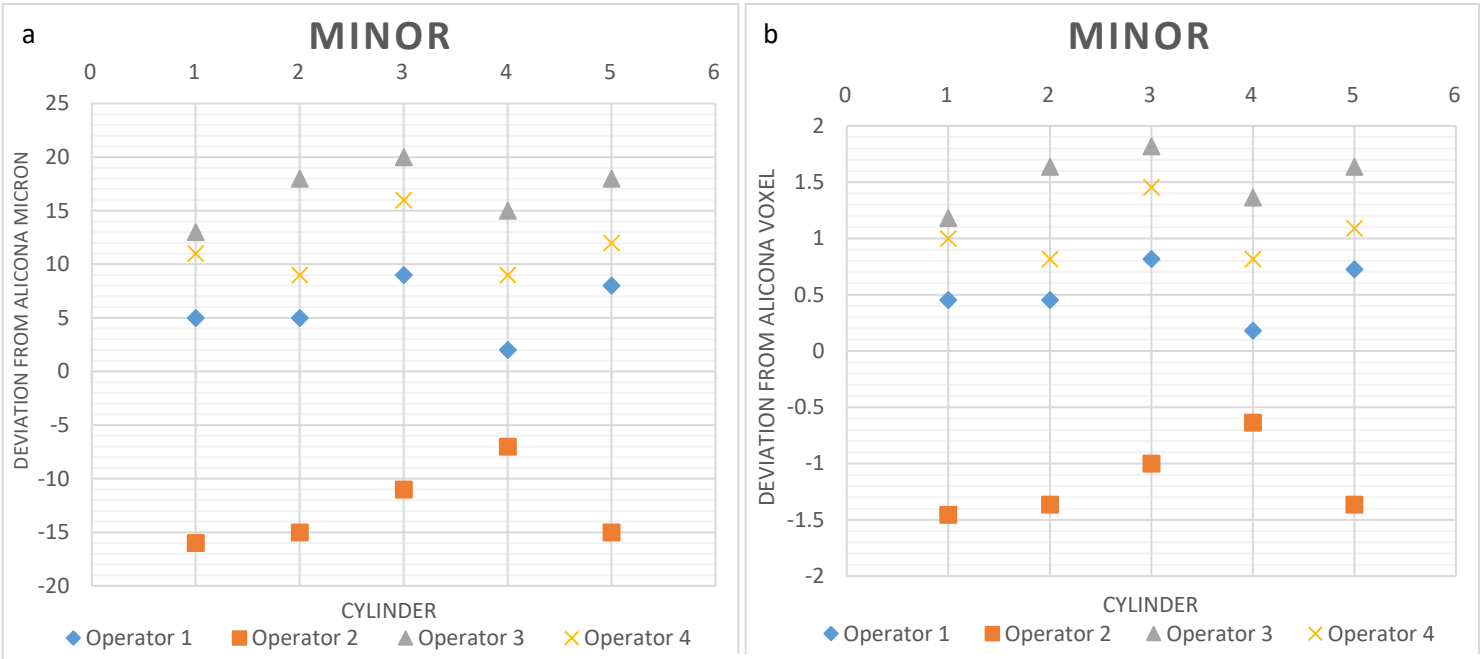

Figure 7-20minor XCT results deviation from Alicona a) in microns b) Voxels

Although all the operators selected their own individual scan parameters, the result total variation is less than 2 voxels. The four operators identified their own surface determination using the method shown in figure 8, using the highest grey value in the middle of the part trapped in-between un-fused powder, using this method only operator 2's measurements were more than the reference values.

Whilst the other three operators' measurements are less than the alicona reference results, the first operator results are the closest to the reference value, then the fourth and third operator respectively. The use of surface determination optimisation reduced the result variation from operator to operator, even when they used different parameters.

In this study, the results following a pattern; the variation between one operator to the other is consistent from dependant on the scan parameters and surface determination variation. This is shown in figure 20 where the major and minor XCT results are compared, it was noted that operator 1 and 4's results are close to each other across all the measurements, the second operator's measurements are the highest across all measurements.

In order to understand the cause of the variation the used threshold grey value was compared. Since each operator selected their individual scan parameters the grey value histogram varies from one operator to another. This resulted in different mean grey values for each scan, the first operator's threshold ISO value was 61%, the second operators were 53%, the third operator's was 64%, and the

fourth operator's was 65%. The first operator threshold resulted in the closest results to the Alicona reference values. All the operators used the same method for surface determination but the first operator used integrated mesh. Using the mesh can enhance the precision in the process of selecting the appropriate surface determination threshold. An integrated mesh can be applied on the 2D image as a pixel or the 3D model as a voxel, the operator can select the x, y and z values to match the required resolution, for example, in figure 7-22 (a) the object was scanned with a 15µm voxel size and the applied mesh used matches the voxel size. Figure 7-22 b) shows the same object scanned with the same voxel size but the mesh used was 5µm.

In figure 7-22 a) the drilled hole edge grey value changes from air/background to material in 2 pixels, whilst in figure 7-22 b) this area is coved by 6 pixels. Therefore, by using a higher definition mesh the operator can distinguish between, the gradual change in grey value from the material to the background/air to a sub voxel resolution by selecting the exact area where the grey value of the background ends and the material grey value starts.

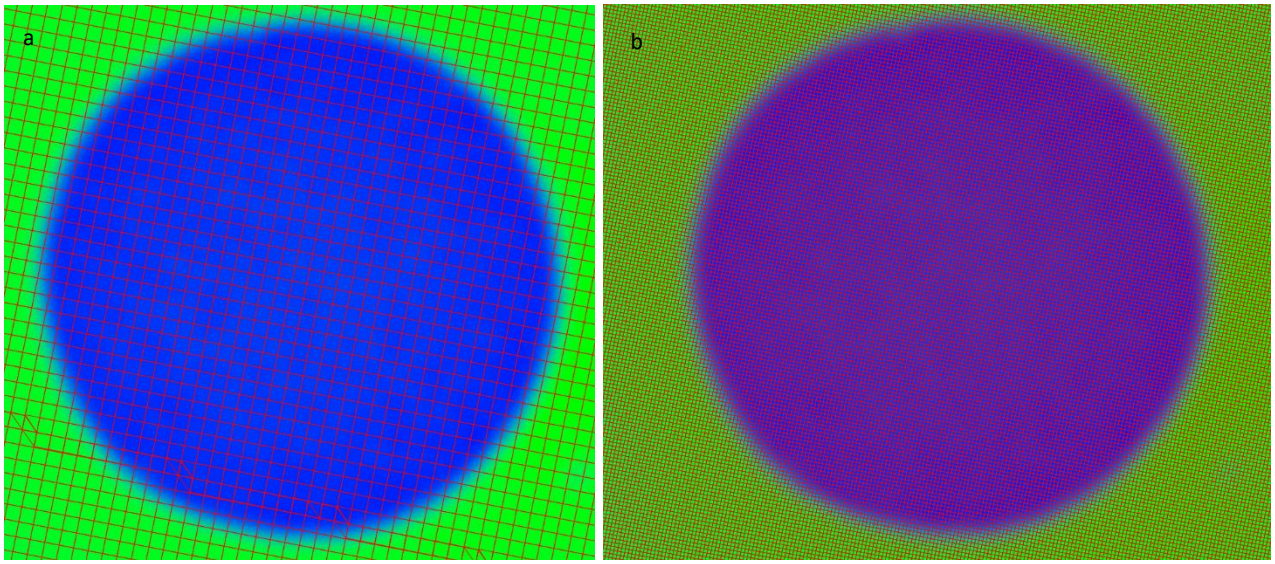

Figure 7-21a) grey value analysis with 15 µm integration mesh applies b) grey value analysis with 5µm

7.4 Summary and conclusion

The results of the reproducibility study have shown the deviation from the alicona reference value is within 1.6 voxels, with some operators results less than one voxel from the reference value. The use of different scan parameters and specifically different spot sizes can result in the results deviation. All the operators chose an optimum ISO threshold value which is more than 50%, the closest results to the reference value were obtained from a 61% surface determination threshold. The custom ISO threshold detected the cavities between the powder particles.

The results of this study confirm that ISO 50% is not the appropriate threshold for porosity analysis and for detecting unfused powder the exact gray value of the gap in-between the individual powder particles must be used. The grey value of the unfused powder tends to be closer to the material peak in the histogram.

Chapter 8 Porosity analysis case study

Statement of Publications Arising from This chapter

In this chapter, several collaborations with industrial partners have shown the requirement for a precise high-resolution porosity detection method. In some extreme critical components i.e. medical and aerospace applications, the resolution needs to be as small as 20µm (powder particle size). In this chapter, XCT powder characterisation is discussed and the effect of build location on internal feature printability in SLM AM technology is investigated.

Some of the work reported in the powder characterisation section of this chapter was presented at the Dimensional X-ray Computed Tomography Conference, 13 July 2017, University of Warwick, UK "Detection of unmelted powder in additive manufactured components using computed tomography" [1]. In the same section some of the work was presented at the 2018, ASPE and Euspen Summer Topical Meeting, United States, California, San Francisco. Advancing Precision in Additive Manufacturing, American Society for Precision Engineering, ASPE "Optimization of surface determination strategies to enhance detection of unfused powder in metal additive manufactured components" [4] .In addition, some of work was presented at 18th International Conference of the European Society for Precision Engineering and Nanotechnology (EUSPEN): June 4th-8th 2018, Venice, IT. "Development of an AM artefact to characterize unfused powder using computed tomography" [8]. A paper was published in the International Journal of Automation Technology, 14(3), 439-446 [259].

In the second section on powder analysis, this work was presented in the 4th ASTM Symposium on Structural Integrity of Additive Manufactured Materials and Parts (pp. 102-121). ASTM International." Challenges in Inspecting Internal Features for SLM Additive Manufactured Build Artifacts" [10]. The paper was selected as ASTM technical papers and was published in 2020.

In the AM study, section one the work was published in the International Journal of Automation Technology, 14(6), 1025-1035. "The Detection of Unfused Powder in EBM and SLM Additive Manufactured Components" [11]. In the AM dissimilar material section, the work was presented in EUSPEN 19th International Conference & Exhibition, 3-7 June 2019, Bilbao, Spain. "The challenges in edge detection and porosity analysis for dissimilar materials additive manufactured components" [9].

In these publications, the author performed all the experiments, research and wrote the entire manuscript with guidance and editorial changes from the co-author. It is indicated where text from this publication has been reproduced in this thesis.

8.1 Introduction

The mechanical properties of a given component can be assessed by destructive or non-destructive test methods, those methods are highlighted in chapter 2. Destructive testing methods often require long test times and by definition, the component cannot be used after testing. There are various non-destructive test methods to detect internal defects/pores for example: Archimedes, metallography and ultrasonic. As mentioned in chapter 2 those methods do not provide accurate information about pore size, shape or distribution.

The defects found in an additively manufactured component are different from those found in the cast alternatives. The pores in the cast component are usually hollow filled with air whilst in the AM components the pore could be hollow, filled with unfused powder or filled with partially fused powder. This chapter details the method for detecting semi-fused and unfused powder, comparing the lack fusion defects in aluminium SLM and titanium EBM manufactured components. A case study

about the challenges of porosity and edge detection in AM manufactured components using dissimilar metallic materials is discussed as well as several case studies regarding the defect characterisation in AM manufactured trabecular structures.

8.2 Powder detection

The main drive for this study was a resultant of an earlier NDT study involving the scan of a 16X16mm square titanium bar manufactured using an EBM machine. The specimen was scanned with a 38µm voxel size and the results from the subsequent porosity analysis failed to detect the presence of any unfused powder within the specimen[4].

To confirm the XCT results, the specimen was sectioned layer by layer in 20µm increments with a CNC machine. This found that some defects had not been detected, additionally the presence of unfused and semi-fused powder identified during microscope examination was not detected (8). The detection of unfused and semi-fused powder was found to be challenging due to the XCT process being governed by the component and pore size.

The artefact used in this experiment, previously discussed in chapter 5 section 4,a was a titanium artefact built using an Arcam Q10 electron beam-melting machine (EBM). Prior to measurement 500 and 1400µm holes were drilled onto the polished surface of the artefact using a CNC machine equipped with micro drills and end mills as shown in figure 8-1 a; the holes were selected to be representative of typical defects. The surface was machined using to a diamond cut finish and the mating part with the same diameter was designed to enclose the drilled holes thus creating internal defects/pores; which were filled with Ti6AL4V powder prior to assembly.

The principle of ringing the two surfaces together is like that employed for slip gauges, therefore, the XCT machine will consider the two halves as a single component with internal defects [3], the lower half with drilled holes powder filled is shown in figure 8-1 b).

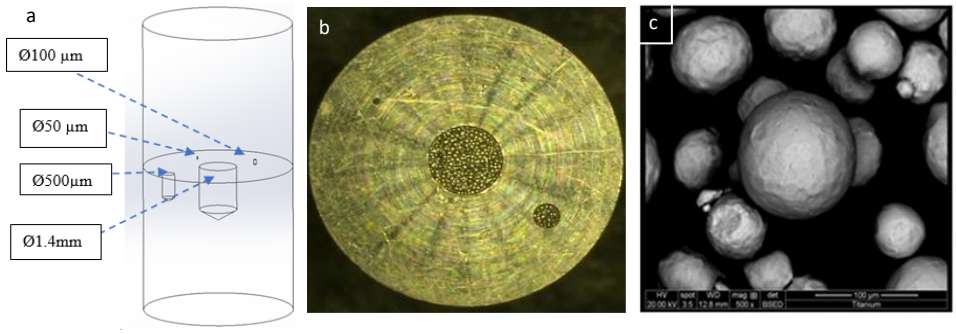

Figure 8-1 a) 3D model of the artefact with defects diameter; b) artefact lower half with defect 1 and 2 filled with powder; c) SEM image of virgin Ti6al4v powder (8)

The Ti6al4v powder used in the EBM process is spherical and uniform with sizes ranging from 40 to 105µm [298,299], the smaller powder particles can fill the gaps between the bigger ones; an SEM image of the used powder is shown in figure 8-1 c. The non-detection of these particles during the previous study has driven the requirement to carry out a further study to identify the voxel size threshold for detecting unfused powder.

8.2.1 Methodology

The artefact was scanned with the Nikon XTH 225, prior to filling with powder and then once filled the area of interest was rescanned at 38µm, 20µm, 15µm, 13µm and 7µm voxel sizes. The scans were repeated 3 times for each magnification. Figure 1a shows a 3D model of the artefact and figure 1b the defects filled with powder [3].

In the reconstruction process no beam hardening or noise filtration was used, the obtained results were analysed with VG Studio Max 3.1 and surface determination and porosity analysis parameters were kept constant for each voxel size scan to ensure that the results were comparable. The volume of the powder-filled defects was compared between different voxel sizes and the time taken for analysis was compared against voxel size.

The impact of voxel size on the image resolution and the overall accuracy of the CT scan has been widely investigated in the medical CT community. Cone-beam computed tomography (CBCT) used in medical applications has shown that micron resolution is achievable [300]. In the case of industrial CT, some work has been done in the past comparing submicron resolution to single figure micron resolution [301,302]. One of the main issues in scanning with ultra-high resolution is the sample size limitation, in most cases; it is not practical to section the sample for performing a CT scan.

In the artefact scanning process, the following settings were used: 0.5mm filter, 4000ms exposure time, 155Kv acceleration voltage and the filament current was 55 µA. Various inputs can have an impact on obtaining a high-definition X-ray image., one of these variables is the axis accuracy of the turntable.

The XTH 225 XCT uses a Newport high performance rotation stage with a guaranteed accuracy of ±7.5 mdeg. Another variable is nonhomogeneous shading; nonhomogeneous shading is a phenomenon where the image is corrupted by false intensity variations due to the integral imperfections in the image formation process. This phenomenon has a contrary impact on automatic image processing. There are several methods of shading correction, the one used in XCT is the prospective object-independent method; in this method, a background image is acquired and the shading is tuned according to the background grey value. In the study, the different magnifications were scanned one by one not by patch scan, to refresh the shading correction after each scan. In order to reduce experimental variables, the ISO 50% surface determination threshold was used to compare the results.

8.2.2 Results

The volume of each defect was calculated by assuming that each defect consists of a cylinder and a cone. The XCT data was analysed using Volume Graphics VG Studio Max 3.1. The surface determination and defect analysis settings were kept constant to make the results comparable. The diameter was determined using best-fit geometry measurements based on the surface determination.

Thirteen points were selected on the diameter to generate a circle. The depth was evaluated using the distance measurement by selecting the highest and lowest point in the defect. Figure 8-2 shows the region of interest (ROI) XCT 3D image where a) in an image of the ROI with voxel size 76µm, b) with 38µm voxel size and c) with 15µm voxel size.

The colour difference highlighted the variation in pore volume. The defect analysis has shown that at low magnification (76µm) he process failed to detect the presence of the unfused powder showing defect 1 as one large pore (the red colour indicates the volume is larger than 3.31mm^3 the blue colour is lower than 0.82mm^3). The 38µm defect analysis detected the variation in grey value, indicating the presence of air gaps between the powder particles.

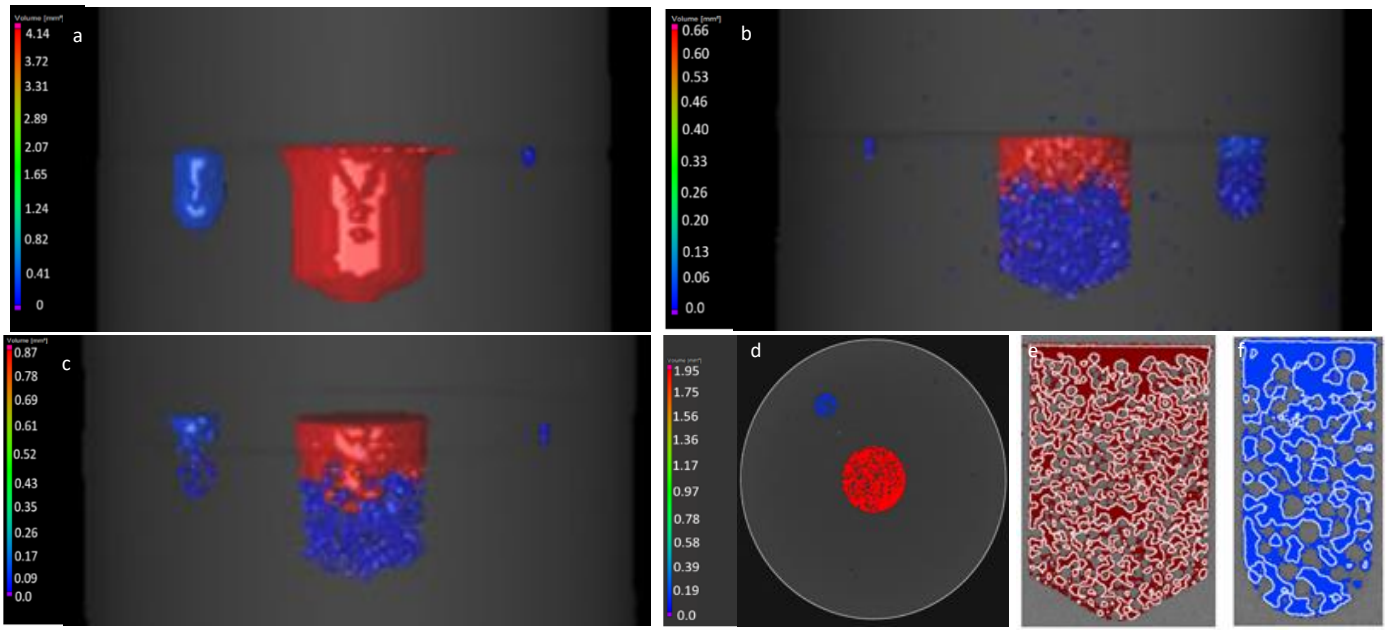

Figure 8-2 a) 76µm voxel size 3D image of defect analysis b) 38µm voxel size - 3D image of defect analysis c) 15µm voxel size - 3D image of defect analysis d) 13µm voxel size - 2D image of defect analysis. e) 7µm voxel size - 2D image of defects 1 filled

In the case of the 15µm voxel scan, the analysis process detected the presence of the powder particles and correctly identified the air gap between the particles. Figure 8-2) d shows the top view of the defect analysis for the 13µm scan where the powder particles are clearly visible at this voxel size. Figure 8-2 e) shows the largest two defects filled with unfused powder scanned at 7µm voxel size.

8.2.3 Discussion

The air gaps between the powder particles are not uniform owing to the difference in the diameter and shape of the powder particles. It is evident using the correct XCT settings that it is possible to identify the existence of powder and the overall shape of the defect as well as the size of some of the cavities between particles.

Figure 8-3 a) shows a volume comparison for defect 1 and 2 filled with unfused powder, the XCT results for different magnifications found that there is a 25.8% difference between voxel size 7.4µm and voxel size 38µm for defect 1. In the case of defect 2, the difference between voxel size 7.4µm and voxel size 38µm volume results was 23.4%.

The results of the low magnification cannot be compared due to failure in detecting the presence of unfused powder. The drop volume values from low to high magnification proved that the process can identify the difference in grey value between the powder particles and air gaps trapped in-between.

Virgin powder particles are generally spherically shaped, and vary in size between 15 to 45µm in diameter. To help understand the voids between the powder particles sphere-packing theory was used to calculate the air void radius; assuming the particles were of equal size. The gaps between the powder particles can be classified into 2 different types; Tetrahedral (see figure 8-3 b) and Octahedral shapes (see figure 8-3 c), the tetrahedral shape occur whenever 4 spheres contact each other.

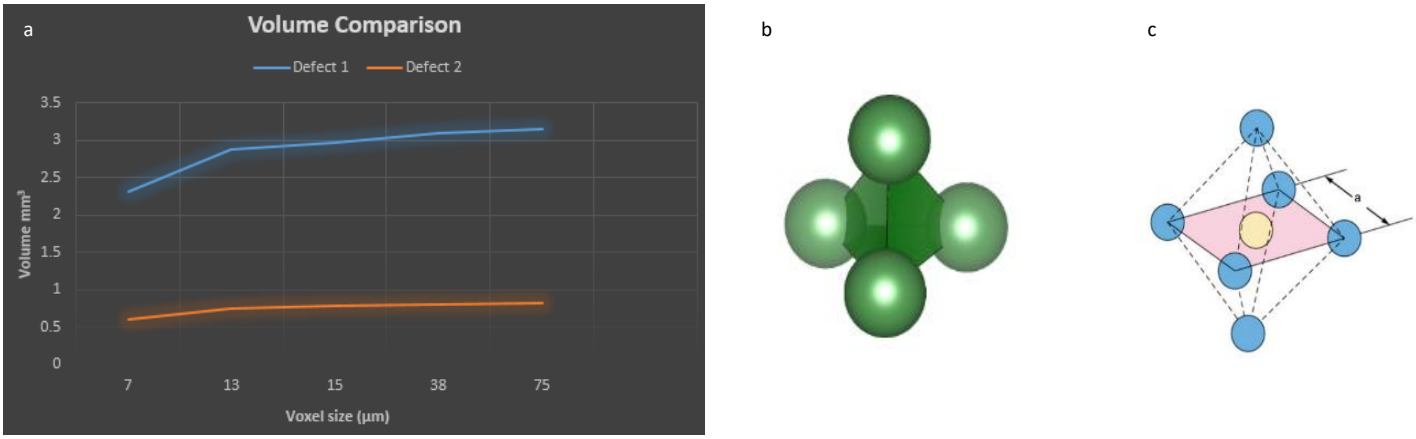

Figure 8-3 a) Defect 1 and 2-volume comparison b) tetrahedral pore c) octahedral pore

The Octahedral shape is formed whenever 6 spheres are contact each other. The radius of the largest sphere that can be placed in a tetrahedral pore can be calculated using the equation r/R= 0.225, where R is radius of the 4 spheres around the void and r is radius of the gap in-between the spheres.

In the case of octahedral shape, the pore between the spheres can be calculated by using the equation r/R= 0.414 where R is radius of the 6 spheres around the void and r is radius of the gap in-between the spheres. In the case of the tetrahedral arrangement the smallest sphere diameter was 22.5µm and largest sphere diameter was 45µm. Using the octahedral arrangement the smallest sphere was 41.4µm and largest sphere was 82.8µm.

The above values for pore diameter can only be considered accurate if the particles are placed regularly, the problem is the particles are irregularly packed (29-31). Furthermore, the large variation in powder particle size makes it impossible to calculate the pore diameter. Using the results obtained from a high resolution XCT scan (7µm voxel size) four random pore diameters were measured using the instrument distance measurement in VG Studio max software; figure 8-4 shows the values obtained. The smallest gap was 29.9µm and the largest was 93µm. The obtained values are not influenced by surface determination as the measurement were taken without applying surface determination.

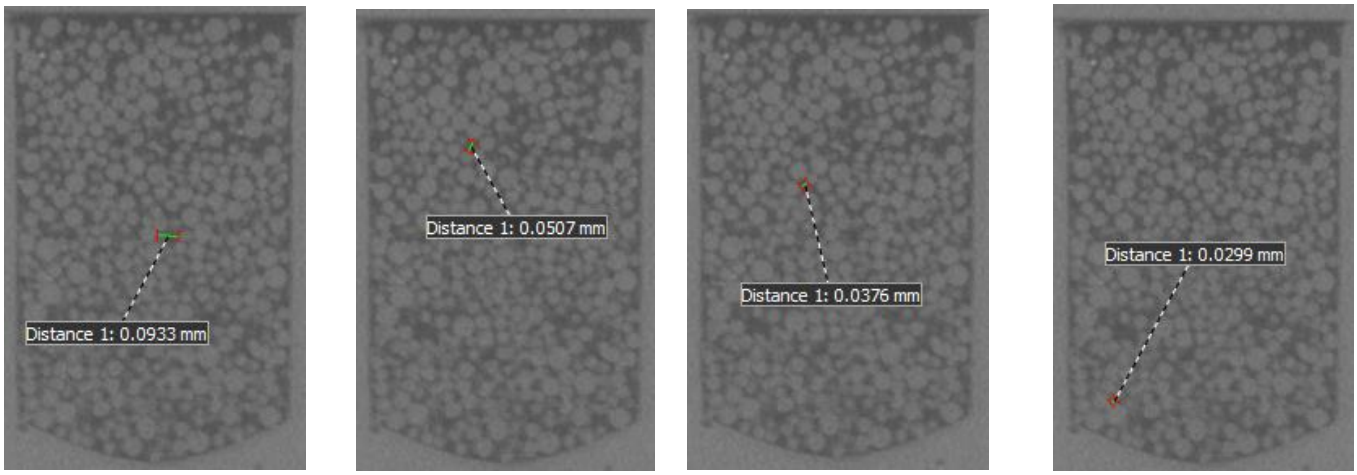

Figure 8-4 XCT images of different size pores between powder particles

The overall results of the analysis are highly dependent on the accuracy of surface determination and the surface determination is influenced by the scan resolution. Figure 5 shows the variation in the grey value for defect 1 containing powder; in this titanium artefact, the solid part grey value ranged from 165-340, the loose powder particles ranged from 165-250 and air gap between powder particles ranged from 40-160. The value range for the air gaps between the loose particles reduces with.resolution. Comparing the 7µm scan (figure 8-5 a) to the 38µm scan (figure 8-5 b) the solid part ranged from 205-250, the powder particles from 145-158 and the air gaps between particles from 130-143.

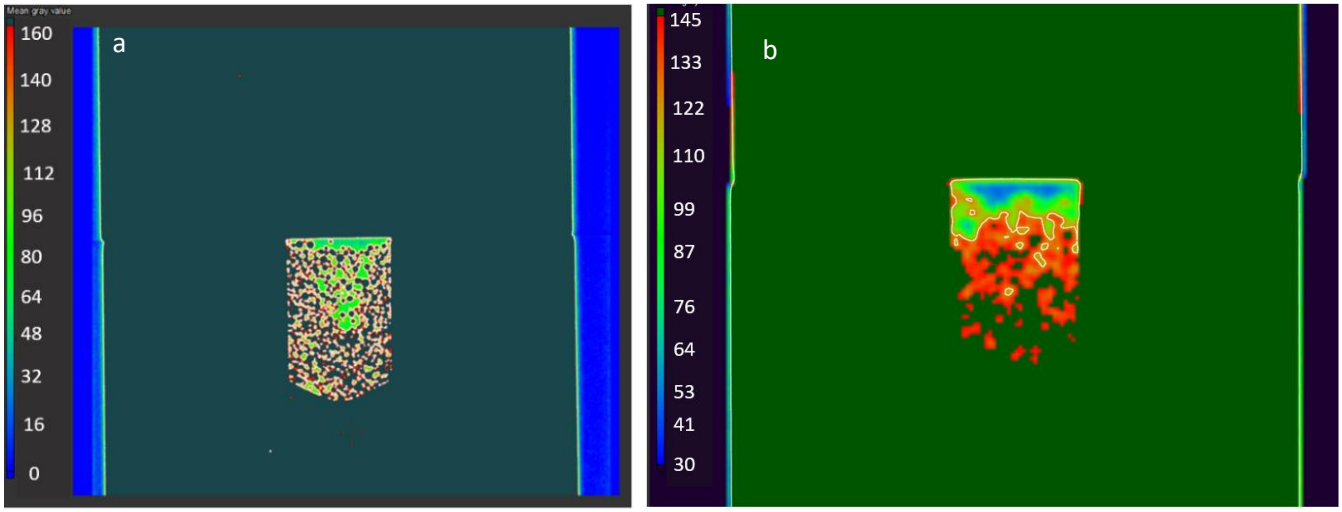

Figure 8-5 shows grey value variation for defect 1 filled with powder scanned with a)7µm b)38µm voxel size

The small variation in grey value in the lower resolution scan is due to the presence of background and material in the same voxel. The grey value for each voxel will decrease or increase depending on the percentage of the voxel containing air or material; if the material is more than air this will result in a higher grey value and vice versa.

To understand the impact magnification combined with surface determination optimisation had on un-fused powder characterisation, the 15µm, and 38µm and 76µm voxel size ISO 50% and optimised SD were compared. Figure 8-6 shows a top view slice of the 500µm defect filled with powder at three different magnifications and surface determination strategy. Figure 8-6 a) is the 15µm voxel size, b) is the 38µm voxel size and c) is the 76µm voxel size, all without surface determination. It was noted from these images that there was presence of blurring and the powder particles are faded. In figure 8-6 a) the 7 particles at the top can be seen, however the background is full of other powder particles that fill the holes.

Figure 8-6 d), e) and f) show the 15µm, 38µm, and 76µm voxel size with ISO 50% surface determination respectively. Figure 8-6 d) showed that the ISO 50% detected the powder particles but failed in detecting the gap between the three particles in the bottom of the hole, additionally the gap between the particles and the edge of the hole is not correctly identified. In figure 8-6 e) the surface determination threshold failed in detecting several particles and the detected ones are not highlighted correctly., In the low magnification image (figure 8-6 f) the ISO 50% threshold failed in detecting any powder particles and the drilled hole contour is not highlighted correctly.

Figure 8-6 shows the optimised surface determination results top view, where g) is the 15µm, h) 38µm, and i) is the 76µm. The optimised SD detected the gap between the three particles at the 15µm voxel size. In the 38µm image, the optimised SD detected the presence of all the powder particles and in

the low-resolution scan the optimised SD detected some of the powder and edge detection was vastly improved.

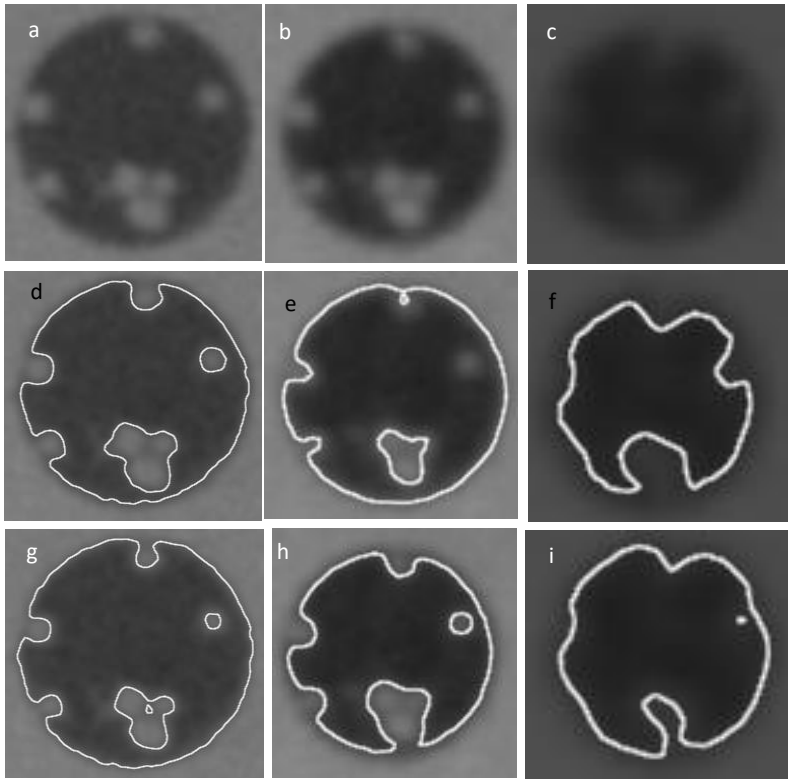

Figure 8-6 top view slice of defect 2 a) 15µm voxel size b) 38µm voxel size c) 76µm voxel size d) 15µm with ISO50% SD e) 38µm with ISO50% SD f) 76µm with ISO50% SD g) 15µm with optimised SD h) 38µm with optimised SD i) 76µm with optimised SD

The optimisation of surface determination shown in figure 8-6, improved the ability of the defect detection process in correctly distinguishing between unfused powder and the material. This is evident when figure 8-6 d) is compared to figure 8-6 h), where the 38µm image with optimised SD is comparable to the 15µm image with the ISO 50% SD. Figure 8-6 g) is the image with highest internal features definition, where all the particles and the gaps between them are highlighted.

8.2.4 Conclusion

The results of this study showed that the higher magnification scans provided better image resolution, which automatically led to a larger difference in the grey value of the unfused powder to the solid material, enabling the detection of unfused powder. The grey values measured by XCT for solid material, semi-fused and un-fused powder were previously shown to be different.

This study showed that detecting micro defects such as gaps between unfused powder does not require a high magnification. The best strategy is scanning the component with magnification as low as 38µm voxel size to identify the location of the defects, then to confirm the area where the defect is located with a higher magnification. As discussed previously this method will enable scanning larger components in a shorter time without compromising on the results accuracy.

8.3 Lack of fusion characterisation in SLM AM artefact

In the previous study the powder particles were placed in the drilled holes without any compressive force; the powder was not compacted; therefore, it is not representative of the rolling/spreading during the printing process. In most lack of fusion situations, the defects contain semi-fused and un-fused powder. A representative artefact with several internal features filled with semi-fused and un-fused powder (shown in figure 8-8 a)) was used to identify the appropriate XCT setting to enhance the accuracy in differentiating between unfused and semi fused powder. Understand the effect of semi fused and unfused powder on part metrology was the key driver for this reported research.

8.3.1Methodology

In this experiment the artefact used was the AM SLM AlSi10Mg alloy build artefact previously discussed in chapter 5 section 7. The artefact (figure 8-8 a) was 10 mm in diameter built using a Renishaw AM250 SLM. The sample contained several internal features designed to represent pores / defects; varying in size from 50µm to 1mm and located between 150µm and 5mm from the outer surface of the component. The features were designed as geometric features (spheres, cylinders, prisms and helical prisms). This study will focus on the four cylinders located in the middle of the part shown in figure 8-8 a).

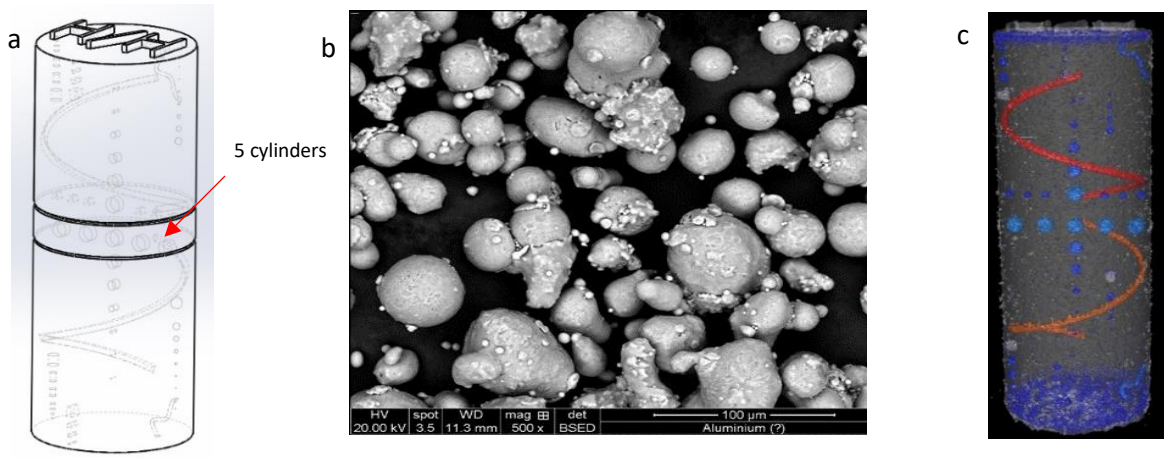

Figure 8-8a) artefact 3D model b) SEM image of AlSi10Mg alloy powder 15-45µm used in SLM process c) 3D CT image of the sample

The cylinder designed diameters were 1mm and the depths were 500µm, the cylinders are spaced 2mm from the center of each other. The distance from the outer edge of the part to the closest cylinder edge is 500µm. The AlSi10Mg alloy powder used in this study had been recycled 7 times. Figure 8-8 b) shows an SEM image of the powder used in which contamination is notable [7].

In this study a Nikon MCT 225 Metrology XCT was used, The XCT scanning parameters were optimized by reducing gain and fine-tuning the histogram by minimizing the beam filter and reducing filament current to ensure that measurement noise was minimized; without compromising X-ray beam penetration. Figure 3 c) shows a CT image of the actual sample. The scan parameters used are shown in table 1.

Filter	Exposure	Filament Current	Acceleration Voltage	Voxel Size
0.25mm	4000ms	7.8	135 kV	11 µm

Table 1 shows XCT scan parameters

The data obtained was analysed using Volume Graphics VG Studio Max 3.1 to quantify the unfused powder volume and determine the gray value threshold. The diameter and depth of each defect was evaluated using geometry measurements tools in the software and the results were shown previously in chapter 5. The surface determination methodology used was optimised to detect and measure internal features/defects [5]. The optimised SD method (discussed previously in figure 8 chapter 7) was applied by identifying the grey value of the trapped air between the unfused powder within the denser section of the work piece (longest X-ray path), this exact grey value was used as the threshold for defect analysis. This method enhances sub voxel detection by taking into consideration the voxels that contains air and material. Following the application of the method, this study adopted the surface determination threshold of 61%.

8.3.2 Results

The defect analysis detected the presence of the unfused powder, the pores in-between it and the hollow pores inside the semi fused powder. Figure 8-9 shows a top view of the middle cylinder, where a) is XCT image, b) the mean grey value analysis and c) the defect analysis. In figure 8-9 a), the powder particles are visible but the gap in-between them is not clear, it also identified the presence of a large pore inside the semi-fused powder, which is highlighted with an orange circle.

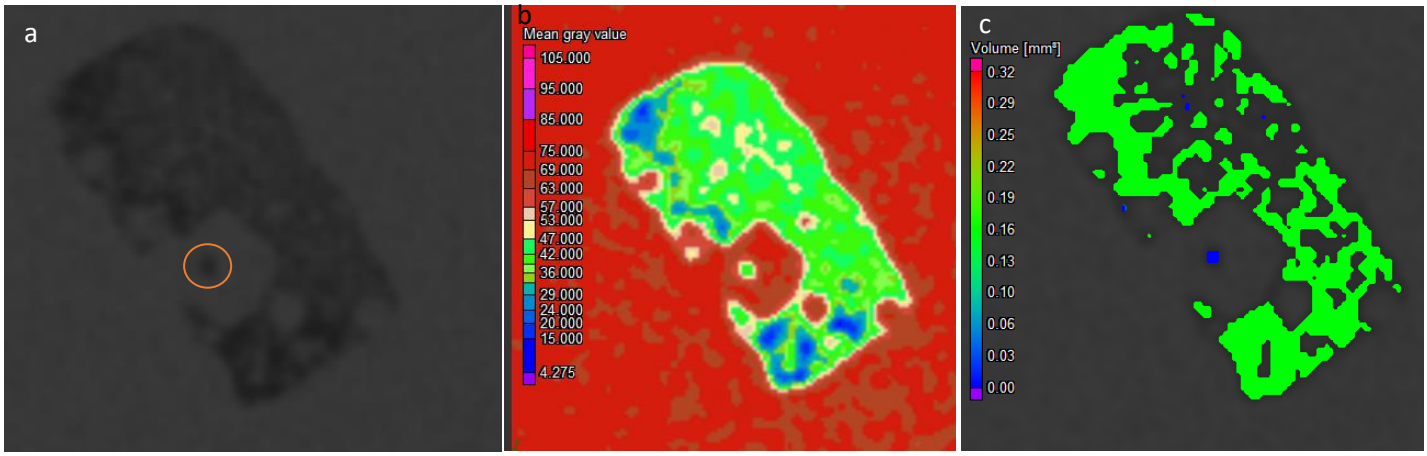

Figure 8-9 a) Top view XCT image of middle cylinder a) top view mean grey value XCT image of the middle cylinder c) top view XCT image of the defect analysis for the middle cylinder

In this study the ISO 50% threshold was 35.8, the mean grey value analysis in figure 8-9 b) shows that the ISO 50% value is not sufficient to detect gaps between the powder particles; using a higher threshold did identify the gaps between the particles. The use of mean grey value analysis assisted in the optimisation of the SD threshold by highlighting the gradual change in grey value between the air and material. The grey value analysis showed that the semi-fused powder grey value was the same as the solid material, whilst the unfused powder mean grey value was slightly less than the solid material. The mean grey value of the solid material in this study was 75, the mean grey value of semi-fused powder ranged from 69 to 75 and the unfused powder mean grey value ranged from 42 and 57.

Figure 8-9 c) show the defect analysis results; the process detected gaps between the particles and the pores inside the semi-fused powder. The threshold used for the defect detection was 39. The characterisation of semi fused and unfused powder is one of the biggest challenges in the metrology of AM components, this study highlighted the effect of semi fused and unfused powder presence on part metrology.

8.3.3 Powder characterisation

This study highlighted the role powder particle size plays in the additive manufacturing process. The presence of large powder particles, shown in figure 8-10 had a negative impact on the feature geometry, as shown in figure 8-12. Larger particles require higher energy to melt [303], the lack of the sufficient energy results in the smaller melted powder particles fusing to the bigger un-melted particles; creating semi or unfused powder zones within the build. This phenomenon will result in poor printing resolution for small (under 500µm) geometric features as well as poor overall structural integrity, due to the presence of internal pores/defects. The SEM images highlighted the presence of non-spherical particles as shown in figure 8-10 a) and c); the irregular shaped powder can cause packing pores between the powder particles.

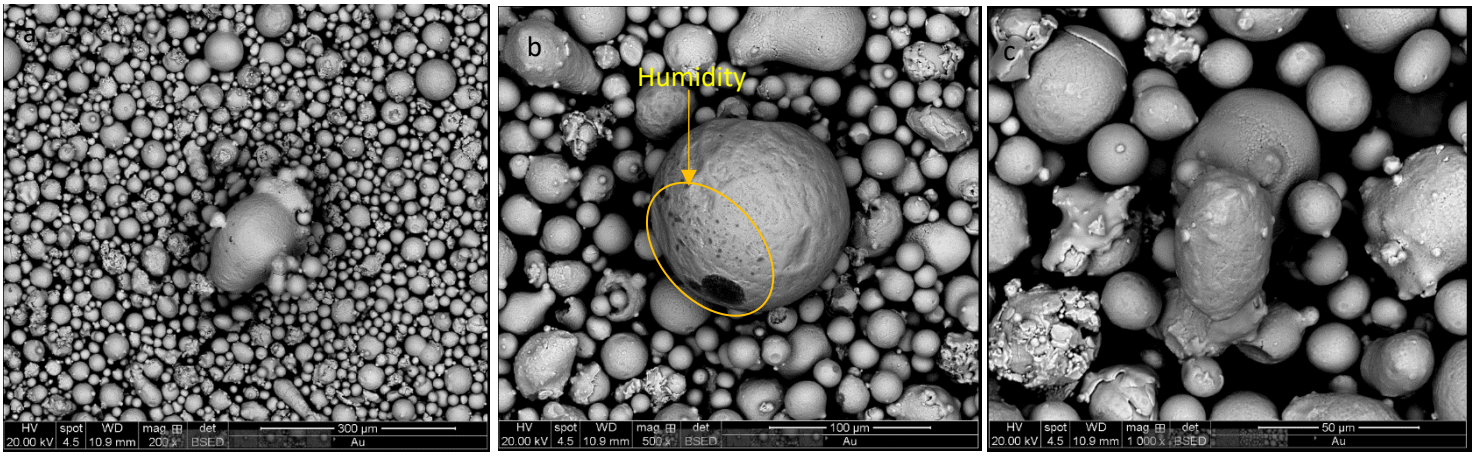

Figure 8-10 SEM image of the powder used a) 300µm magnification b) 100µm magnification c) 50µm

Figure 8-10 b) shows a powder particle with surface humidity (orange circle), the presence of humidity can cause splatter in the printing process. PBF splatter is a cause of porosity and also compromises powder quality and spreadability by introducing shape irregularity [304]; reducing its service life. The existence of humidity indicates the presence of a high oxygen content within the artefact, high oxygen levels will lead to decreases in ductility and impact toughness Typically recycled powder, as used in this study can contain 55% more oxygen than virgin powder [305-306].

Figure 8-11 a) shows a high magnification SEM image that focuses on the powder particle with surface humidity and figure 8-11 b) shows SEM quantitative analysis results. The SEM results found the oxygen level was above 13% in this specific particle, this level of oxygen could compromise the powder quality, resulting in the aforementioned issues in the build.

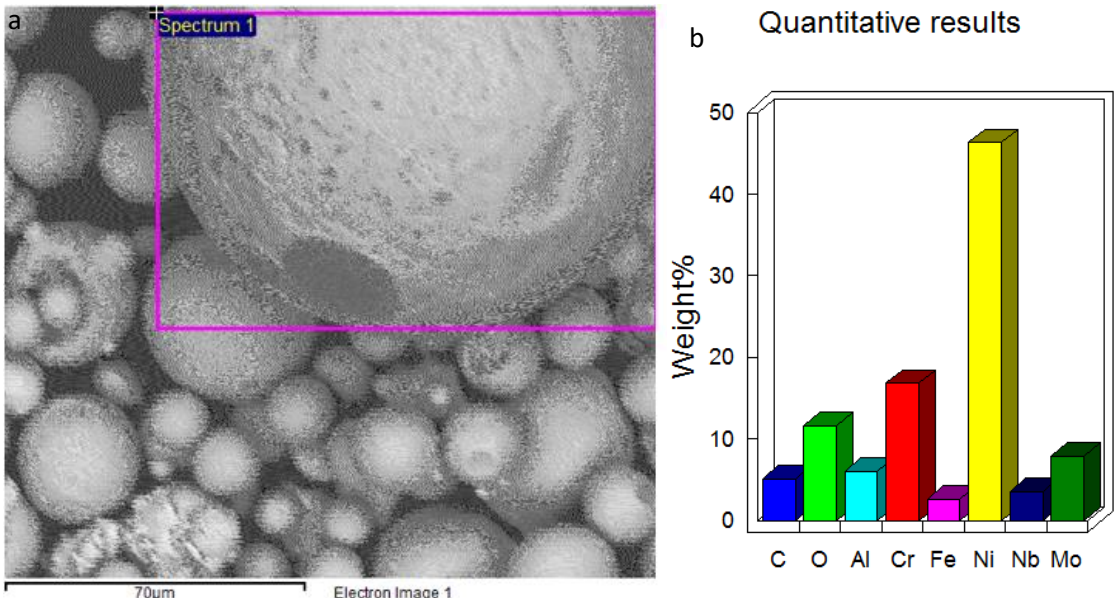

Figure 8-11 a) SEM image of a powder particle with surface humidity b) SEM quantitative analysis results

It was noted that virgin powder stored correctly would not suffer from humidity issues and feature resolution should be improved. It is possible the presence of humidity affected the results of this study through introduction of spherical shape irregularity, which compromised the printing resolution. Considering this, further investigation is required.

Figure 8-12 shows the internal features filled with un-fused and semi-fused powder. In figure a) and b) the large particles (greater than700µm) were present in the internal features. These particles were likely fused to the outer edge of the features, which have then detached.

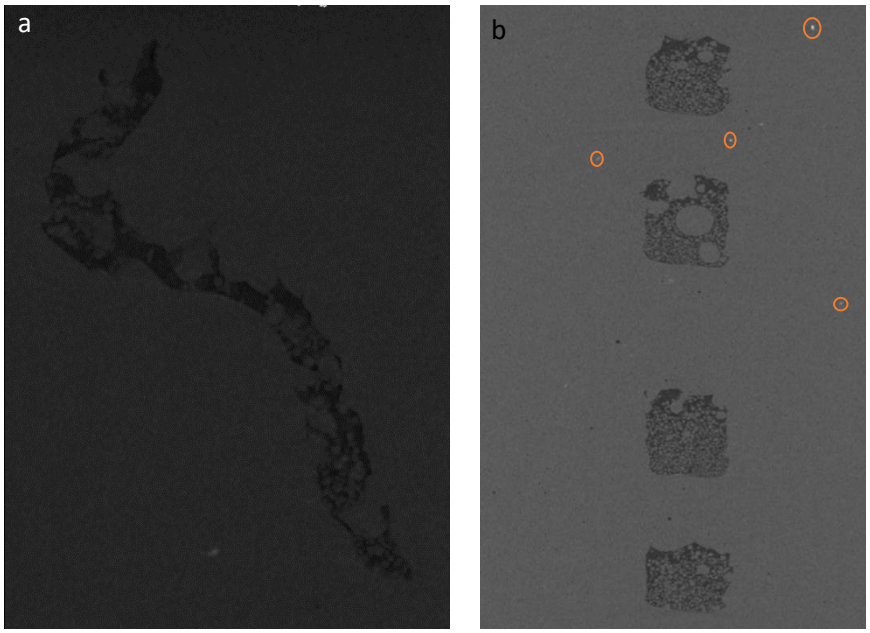

Figure 8-12 XCT images of the internal features containing semi-fused and unfused b) XCT image of with traces of powder contamination

Figure 8-12 b) shows an XCT image of the artefact with some traces of contamination, the mean grey value of the aluminium material in this experiment was 70; the highlighted bright spots in the artefact have a mean grey value above 320.

As previously discussed in chapter 4 section 5, powder contamination can be external or process related. External contamination also known as cross contamination, the presence of materials that are not present in the powder chemical composition. This is mainly due to either powder manufacturer or machine operator error during the powder changeover process. Powder contamination is a cause of defect formation in printed components, which result in mechanical failure.

Powder contamination in this case looks like metallic contamination, to understand the root cause of this contamination a sample of virgin powder used in this build was analysed. The sample was scanned with XCT and the powder was analysed with an SEM. The powder sample was placed in a plastic test tube, and then scanned with a XTH225 metrology CT at 4µm voxel size. The results of the scan are shown in figure 8-13, where 8-13 a) shows a top view of the powder and figure 8-13 b) shows an XCT image of the plastic test tube filled with the powder sample.

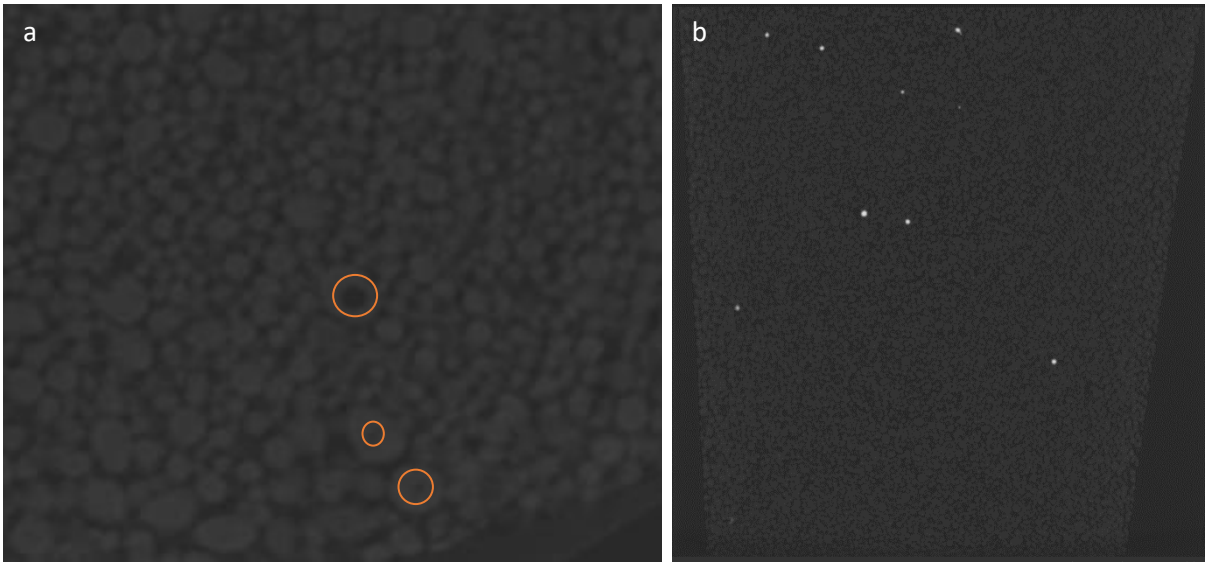

Figure 8-13 High-resolution XCT images of virgin aluminium powder b) High-resolution XCT image of the contaminated powder

The high magnification XCT scan showed the individual powder particles and the pores inside them, in figure 8-13 a) the pores inside the particles are highlighted with an orange circle. It was noted that several particles are not spherical; even in the virgin state. Furthermore, some particles are above the maximum acceptable diameter, which is 63µm. The powder contamination clearly visible in figure 8-13 b), where the (AlSi10Mg) aluminium mean grey value is 135 whilst the bright particles mean grey value is 1785.

The high mean grey value indicates that the contaminating material is much denser than the aluminium powder, most likely titanium or Inconel. The printing parameters required for melting aluminium powder particles are not sufficient for melting titanium or Inconel powder particles, the presence of a denser material in a light alloy matrix will cause lack of fusion around the denser particles. Because of this powder, contamination can compromise the mechanical properties of AM printed components due to the difference in thermal expansion characteristics of the contamination compared to the surrounding matrix.

In high-end applications such as medical or aerospace, it is a crucial requirement for the AM powder to be contamination free. This requirement is often underrated and is difficult to detect. The presence of a small quantity of contamination (less than 1%) most likely will not change the macroscopic and rheological of the powder. Techniques that are capable to characterise AM metal powder morphology include XCT and SEM.

In this study, SEM was found to be a powerful device, due to its ability in identifying the chemical composition of the scanned material. In order to confirm the chemical composition of the contaminating material, a sample of the powder scanned with the XCT was scanned with SEM. Figure 8-14 a) shows an SEM image of the contaminated powder and figure 8-14 b) shows the SEM chemical composition results.

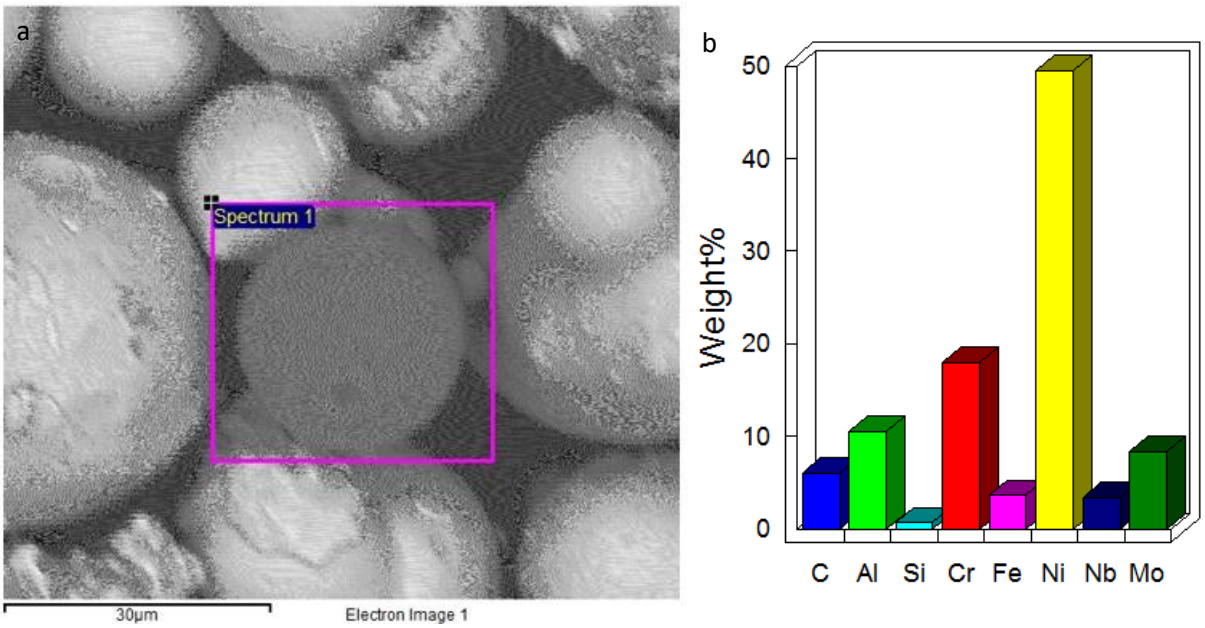

Figure 8-14 a) SEM image of the contaminating powder b) SEM chemical composition analysis results

The chemical composition results proved that the contaminating particles contained a high percentage of nickel, chromium and molybdenum, meaning the aluminium powder was contaminated with Inconel powder particles. The findings from this study resulted in the change of powder supplier as the powder was out of specification.

8.3.4 Conclusion

In the present study, the presence of semi-fused powder illustrated the minimal difference in grey value between semi fused powder and fully dense materials; similar grey values directly affect internal feature/defect detectability. A large difference in grey values result in better contrast, resulting in better surface determination and more accurate defect analysis.

The surface determination study proved that the ISO 50% threshold is not adequate for detecting semi-fused powder zones; consequently, a more bespoke approach is required. This approach acquires the grey value of the pores in the denser section of the part (longest x-ray path). The threshold can vary between scans due to different scanning parameters, part shape and dimensions. Furthermore, the grey value of the unfused powder and semi-fused powder will always be closer to the full dense material, even the air between the powder particles enclosed inside the part will have higher grey value than the background air found outside the part. These issues justify the use of the optimised surface determination method.

The XCT demonstrated to be a powerful tool in defect detection and powder cross- contamination characterisation; due to the effect of material density on x-ray attenuation, different materials will have different grey values. The contrast of low-density materials will be closer to background contrast; for example, in figure 13 (b) the background/air is black but the light grey aluminium powder particles are much darker than the Inconel particles bright spots, this difference in contrast can be used in contamination detection and characterisation.

8.4 EBM and SLM un-fused powder detection comparison

Selective laser melting (SLM) or electron beam melting (EBM) are two of the main technologies used for producing metal components through powder melting. The powder size varies, depending on the technology and manufacturer, from 20–50 µm for SLM and 45–100 µm for EBM [11]. This study presents a methodology to detect unfused powders in SLM- and EBM-manufactured components. Aluminum and titanium artefacts with designed internal defects filled with unfused powder were scanned with XCT and the results analysed with VG Studio Max 3.1 (Volume Graphics, Germany) software package.

A set of artefacts with designed internal defects filled with unfused powder were produced in both titanium and aluminum (popular AM materials), as previously discussed in chapter 5 section 5. The titanium artefact was built using an Arcam Q10 EBM machine using Ti6AL4V powder; the aluminum artefact was built using a Renishaw AM250 SLM and AlSi10Mg powder. The powder particle sizes were 45–10 µm for titanium and 15–45 µm for aluminum. The artifact 2D model is shown in Figure 8-15 a) and consisted of 2 cylindrical halves of 10.9 mm diameter with the lower half containing a 6 mm diameter machined hole followed by a subsequent 1.7 mm diameter drilled hole. The upper half was 10.9 mm in diameter with a 6.020 mm cylindrical protruding boss section used to enclose the designed 1.7 mm drilled hole/defect by means of interference fit. The tolerances were calculated to ensure a press fit to enclose the lower cavity and produce an internal defect. The present study presents the differences in requirements for detecting unfused powder in EBM- and SLM-manufactured components using XCT.

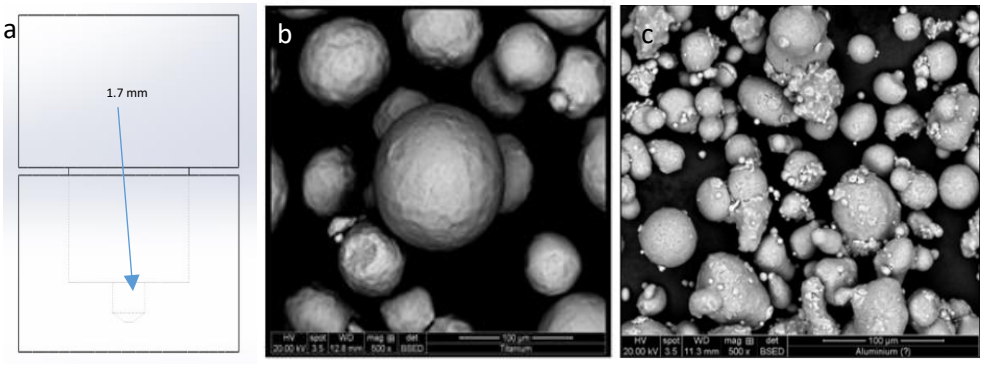

Figure 8-15 a) Artefact 3D model b) SEM image of titanium powder c) SEM image of the aluminium powder

SEM analysis was carried out initially to evaluate particle size and shape distribution differences between the titanium and aluminum AM powders used in this study. In the case of the titanium powder, the particles were uniform and generally of a larger size (see Figure 8-15 b), whereas the aluminum particles were generally smaller and non-uniform in morphology (see Figure 8-15 c); increasing the likelihood of any porosity being filled with these particles.

8.4.1 Methodology

Before assembling the artefacts and scanning them with the XCT, the diameter and depth of the defects were measured with an Alicona G4 non-contact instrument. The defect diameters were measured using a best-fit circle. The defect depths were measured by selecting the two highest points on the upper surface and selecting the lowest point in the drilled hole, creating a horizontal line.

Table 2 shows the Alicona values for diameter and depth for the titanium and aluminum artefacts. The defects were machined with a CNC machine, which is reflected in the results of the actual hole

dimension. The diameter was designed to be 1.7 mm; the actual diameters of the titanium and aluminum artefacts were 1.732 and 1.740 mm respectively.

Defect	Titanium EBM	Aluminum SLM
Diameter	1.732 mm	1.740 mm
Depth	2.368 mm	2.396 mm

Table 2 Alicona defects dimensions.

The depth of the defects was designed to be 2.4 mm, the actual depth was found to be 2.396 and 2.368 mm for titanium and aluminum respectively. The dimensions of the defects were considered acceptable as they fell within the 50-µm tolerance.

A Nikon XTH225 industrial XCT was used to scan the two AM artefacts. The XCT scanning parameters were optimised to ensure that noise was minimised; throughout the study, no noise or data filtration was utilised. This approach ensured that no useful data was omitted or discarded during the measurement process, guaranteeing that the operator had an unfiltered dataset for use in the analysis.

Filter	250 µm
Exposure	2000 ms
Filament current	9.1 W
Acceleration Voltage	175 Kv
Voxel size	9.7 µm
Gain	12

Table 3 XCT scan parameters- Titanium

Filter	100 µm
Exposure	2000 ms
Filament current	8.7 W
Acceleration Voltage	150 Kv
Voxel size	9.7 µm
Gain	12

Table 4 XCT scan parameters-Aluminium

After the 2 halves were assembled there was a 600 µm gap, as shown in Figure 8-16 a), which was used to fine-tune the XCT settings using the gray scale values to enhance the contrast between the enclosed air and material. This method of optimising the gray scale histogram was used to create a smooth transition between air/background, unfused powder and material; as shown in Figure 8-16 b), using the histogram for the titanium artefact.

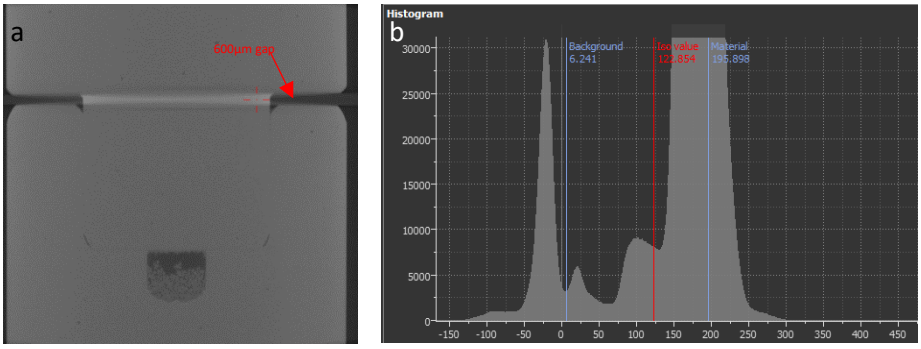

Figure 8-16 a) CT image of the artefact b) CT Histogram for the titanium artefact

The XCT result analysis was carried out using the standard ISO5 0% SD and was compared to the manual grey value identification. A Nikon 225 XTH was used and both the artefacts were scanned at 9.7µm voxel size, all the data analysis was carried out with Volume graphics VG studio max 3.1. The diameters and depths were evaluated using two different approaches, the first approach was based

on ISO 50% surface determination and the second manually identified the threshold for edge detection. The manual method can enhance the accuracy by increasing the probability of sub voxel detection. In this study, the adopted surface determination for the aluminum sample was ISO 59% and the titanium sample were ISO 63%.

After applying the surface determination, the diameter shown in figure 8-17 a) was evaluated using a best-fit circle via measurement instruments in the software. The depth shown in figure 8-17 b) was determined by using the highest 2 points of the defect and creating a horizontal line to the lowest point in the defect. To ensure the quality of the scans, a grey value analysis was carried out for both artefacts. In this study using the aforementioned scan parameters, the aluminium solid material mean grey value was 73 and the un-fused powder mean grey 67. The titanium mean grey value analysis results are shown in figure 8-17 c), the solid titanium mean grey was 178 and the titanium powder mean grey value was 134. Both the titanium and aluminium artefact defects are filled with the same powder that was initially used in the artefact manufacturing.

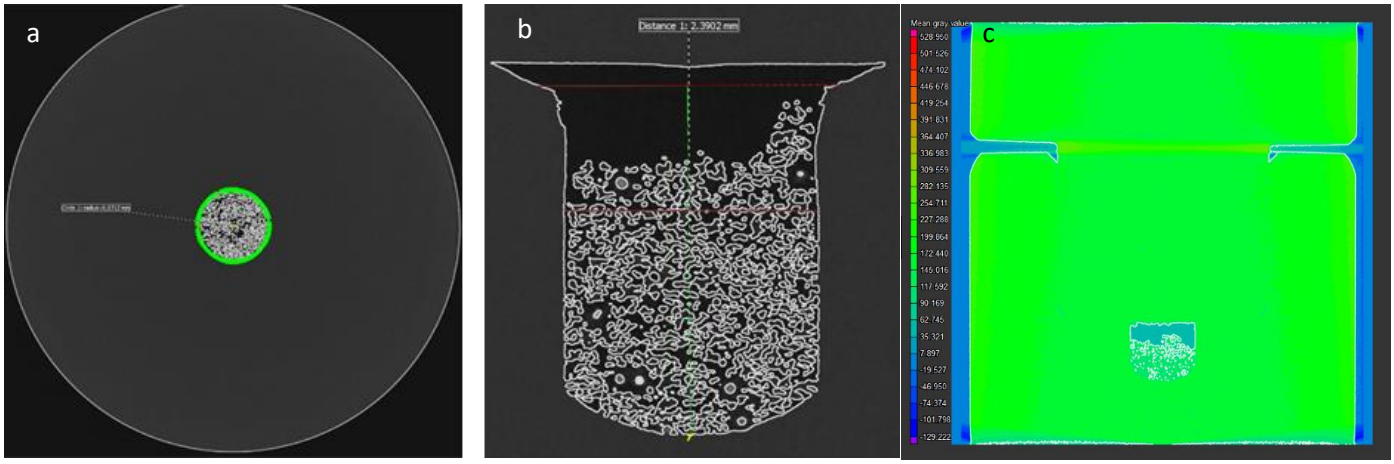

Figure 8-17 a) XCT defect diameter measurement b) defect depth measurement c) titanium artefact mean grey value analysis

8.4.2 Results

The obtained results of this study confirmed the ability of the XCT scan to characterise the internal defects. Furthermore, it proved that it is possible to image powder particles and air gaps between powder particles. In the case of the aluminium artefact, the powder is not uniform therefore, the gaps are much smaller.

Figure 8-18 a) shows the depth result comparison. The differences in the case of the aluminium artefact between the Alicona and ISO 50% results for Aluminium is 2.1% and the difference between Alicona and optimised surface determination is 0.1%. For the Titanium sample, the difference between Alicona and ISO 50% is 1.1% and the difference between optimised surface determination and Alicona is 0.1%.

Figure 8-18 b) shows the diameter result comparison for the Aluminium artefact, the difference in diameter value between Alicona and ISO 50% is 2.7% and difference between optimised surface determination and Alicona is 0.1%. For the titanium artefact, comparing custom ISO to the Alicona is so close such it required a different, more bespoke approach to be adopted. The depth results proved that the custom ISO values are closer to the Alicona values versus the ISO 50%. Results the difference 0.1% and the difference between Alicona and ISO 50% is 2%.

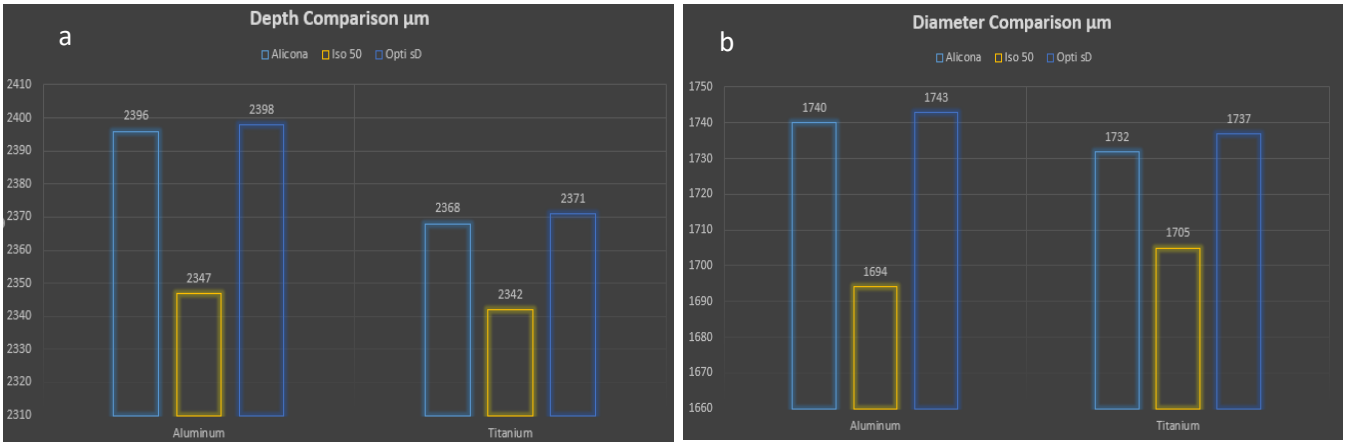

Figure 8-18 a) defect depth comparison b) diameter comparison

This study showed that the grey values of pores and powder-filled defects of additive manufactured components are so close they require a different, more bespoke approach to be adopted. The depth results proved that the custom ISO values are closer to the Alicona values than the ISO 50%.

Figure 8-19 shows the volume comparison between the results obtained from ISO 50% and the optimised threshold surface determination results strategy; the volume for the aluminium and titanium artefacts with ISO 50% threshold were 3.975 and 4.209 mm^3 respectively. Comparatively for the optimised threshold, the volumes were 3.376 and 3.975 for aluminium and titanium respectively.

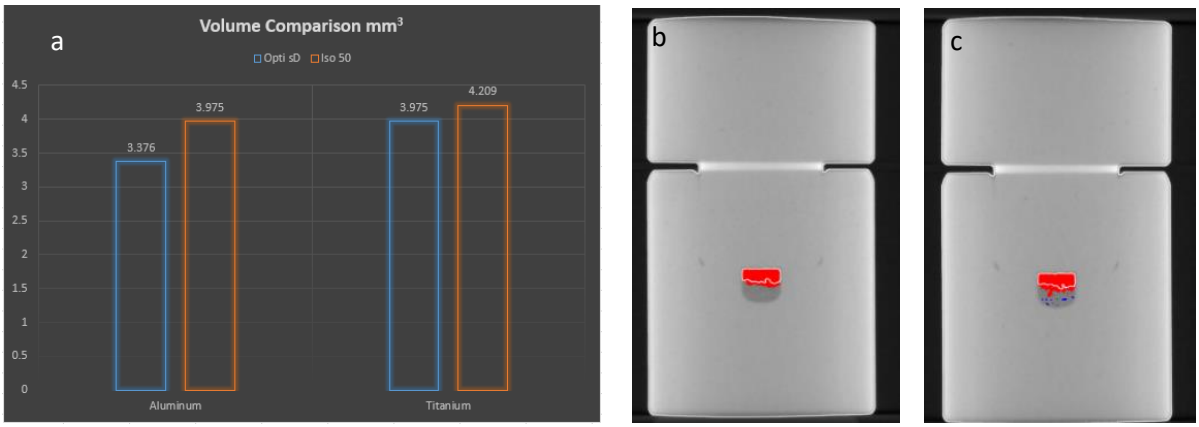

Figure 8-19 a) defect volume b) 21Titanium artefact 2D ISO50% surface determination c) Titanium artefact 2D optimized Surface determination

The results of the volume comparison show that the ISO 50% threshold failed to detect the individual contours of all the unfused powder particles therefore the volume for the optimised threshold is lower. One other comparison was carried out comparing the results of the titanium artefact scanned with 89µm voxel size (low magnification) and the 9.7µm voxel original scan. The diameter, depth and volume were compared. Figure 8-19 b) and 8-19 c) shows the ISO 50% threshold and optimised threshold respectively. It is clear from the images that again the ISO 50% detected the air gap on the top of the powder only and failed to detect any gaps within the unfused powder. The low magnification volume for ISO 50% and optimised threshold were 2.104mm^3 and 2.304mm^3 respectively. Furthermore, the optimised threshold detected some gaps between the powder particles; blue dots in figure 8-19 c). In the case of the dimensional differences, the low magnification diameter and depth were 31% lower than the high magnification results.

8.4.3 Conclusions

The artefact used in this study assisted in identifying the difference in detecting unfused powder in EBM- and SLM-AM components. SEM analysis for both powders found that the titanium EBM powder is spherical with uniform shape and the SLM aluminum powder is small and irregular; such powder can be hard to detect due to the shape of the powder particles minimising the air gaps. Conversely, detecting unfused titanium powder for EBM-manufactured components proved easier because of the powder's regular spherical shape and larger powder particles.

It is possible to detect every single powder particle, however, doing so requires high magnification and customized settings for surface determination; requiring the exact gray value to be identified. It was also noted that the gray value for the aluminum powder was much closer to that of the solid material in comparison to the titanium powder/solid values.

The threshold for surface determination is dependent on the material, material thickness and scanning parameters. Therefore, scanning the same part with two different parameters will result in different ISO values. Optimising surface determination can enhance the overall accuracy of the porosity analysis process; this was demonstrated in the defect dimensional comparison.

Visual inspection should be used to identify the required threshold for surface determination, whereby the exact gray value for each pixel in the defect is determined to enhance the results by accurately detecting the material edge.

Undoubtedly, scanning a component with high magnification improves the accuracy of the results. Unfortunately, in an industrial environment, it is not practical to utilise scanning strategies that have high acquisition times and small volumes. It was shown that detecting unfused powder is largely dependent on the scanning parameters; namely, it was found that reducing the X-ray spot size combined with low gain will result in natural noise reduction. In addition, well-defined peaks in the histogram will enable a high contrast where the typical histogram values for the material should be between 7K and 15K and the air/background values should be 49k to 62k.

8.5 Challenges in edge detection for dissimilar materials AM components

In recent years, additive manufacturing (AM) has changed the view of most manufacturers that utilise conventional subtractive machining for prototype testing. AM is being recognised as a core technology for producing complex and customised components. The demands for dissimilar materials has increased, with many industries seeking to optimise material properties by combining several alloys in one part to achieve the best performance possible. For example, in high-performance internal combustion engines, a piston head can be made from titanium and the skirt can be made with aluminium. Using this method, the structure will have excellent heat resistance and strength, combined with weight reduction for better inertia.

The advantage of using dissimilar materials enables the best properties in both materials to be utilised. There are several AM processes that can be used for bonding metallic dissimilar materials, two of these are direct energy deposition (DED) [307], and Ultrasonic additive manufacturing (UAM) [308]. There are several challenges in joining dissimilar materials, mainly in the transition from one material to the other; defined as the heat-affected zone (HAZ) and the thermo-mechanically affected zone (TMAZ) [309].

As previously discussed in chapter three, the mechanical properties of AM components are not well understood, furthermore non-destructive testing (NDT) and repeatability is not well established. X-ray computed tomography is one of the non-destructive testing methods that can be used to characterise porosity in dissimilar materials, XCT has already proven to be very effective in inspecting welds of similar and dissimilar materials. This section presents a case study that highlights the challenges in edge detection and porosity analysis for AM manufactured components using dissimilar metallic materials.

8.5.1 Methodology

The artefact used in this study was made from two sections, the upper section is Titanium made using the powder bed fusion (PBF) process and the lower section is Aluminium and made using the SLM process. The artefact 3D model is shown in figure 8-20 a) and consists of 2 cylindrical halves 10.9 mm in diameter, with the lower half containing a 6 mm diameter machined hole followed by a subsequent 1.7 mm diameter drilled hole filled with EBM Ti6Al4V unfused powder. Figure 8-20 b) shows a front view XCT image without surface determination, figure 8-20 c) shows a 3D image of defect analysis results. The upper half is 10.951 mm in diameter with a 6.020mm protruded cylindrical section; used to enclose the designed defect in the lower half by interference fit.

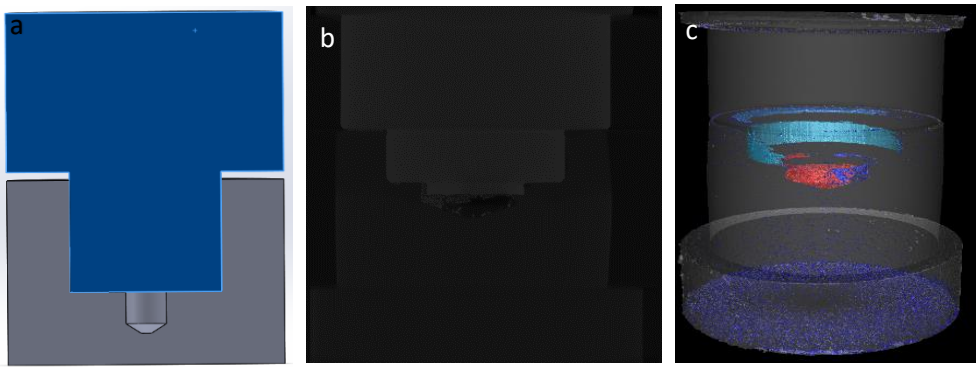

Figure 8-20 a) Artefact 3D model b) artefact front view XCT image c) Artefact XCT 3D Image

The tolerances were calculated to ensure a press fit to enclose the lower cavity and provide an internal defect. Prior to assembly the defects were characterised using a focus variation microscope (Alicona G4) in order to determine the reference values for diameter and depth. A Nikon XTH225 (Nikon Metrology, Tring) industrial XCT was used to analyse the pores/ defect locations and size. The XCT data was reconstructed and the analysis for surface determination and defect analysis was carried out using VG Studio Max 3.1 (Volume Graphics, Heidelberg). The purpose of the study was to provide guidelines for selecting the inspection parameters; optimising the surface determination to allow for porosity analysis and edge detection in AM dissimilar materials components. The artefact was CT scanned to create a volume file of the entire artefact. The XCT scanning parameters were optimised to ensure measurement noise was minimised. The XCT Settings are shown in table 1.

Filter	0.25mm copper
Exposure	2000 ms
Filament current	7.5 w
Acceleration Voltage	130 Kv
Voxel size	14 µm

Table 2 XCT scan parameters

Surface determination threshold identification is one of the biggest challenges in defect characterisation of dissimilar materials. When scanning different materials with large differences in X-ray attenuation, the difference in grey value is very large so the common single threshold SD method is not effective. Figure 24 shows the grey value histogram, due to the difference in material attenuation the histogram contains three peaks, where the first peak/air mean grey value is 0.145, the second peak/aluminium mean grey value is 91.278 and the third peak/titanium mean grey value is 215.392.

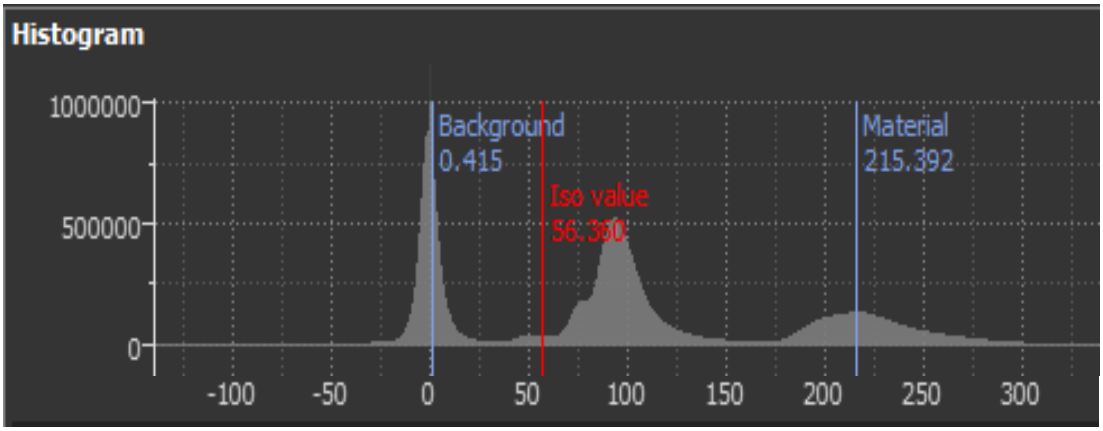

Figure 24 grey value histogram

The standard method used in the analysis software, known as advanced multi-material surface determination did not produce acceptable results; the software calculated threshold for this experiment was 91. This threshold value did not take into consideration the presence of several peaks in the grey value histogram.

In this study the method used in the surface determination threshold was to manually select the background/air and select both the materials as the main part, as shown in figure 8-21 a). The threshold was selected based on the optimised aluminium material value, in this experiment the threshold for internal feature measurement was 56.360. This threshold resulted in the optimum edge detection, without compromising image quality with noise or beam hardening, figure 8-21 b) shows an XCT image of the artefact with SD applied.

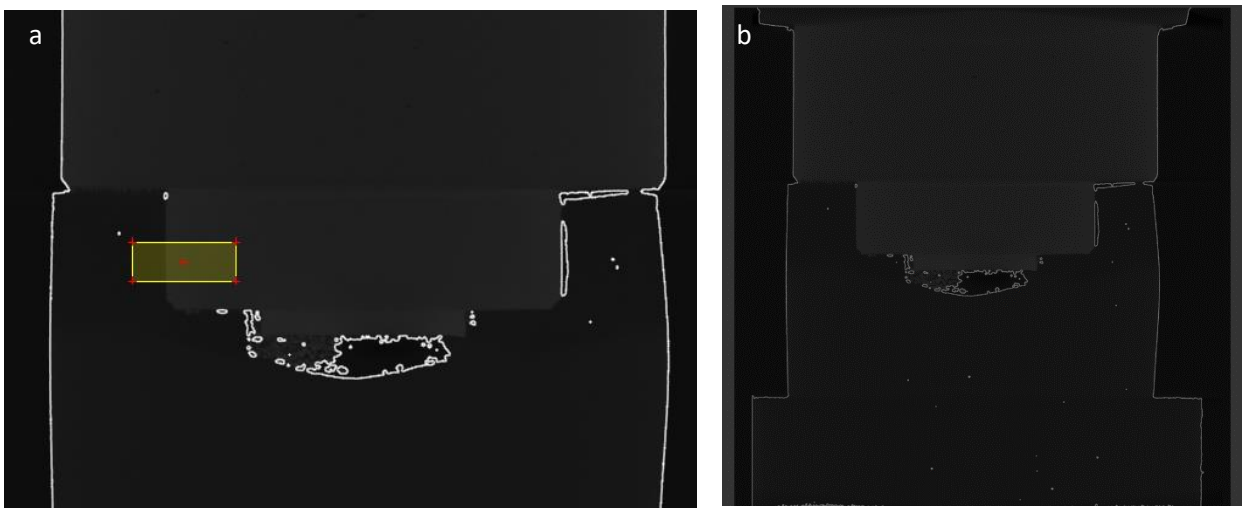

Figure 8-21 a) material selection b) XCT image of the artefact with the SD applied

8.5.2 Results

The diameter and depth of each material was evaluated using geometry measurement tools in the software. The results compared the outer bore diameter and depth for the titanium to the inner bore and depth of the aluminium as shown in figure 8-22 a) and b) respectively. In order to improve the result accuracy each dimension was measured 5 times and average was taken.

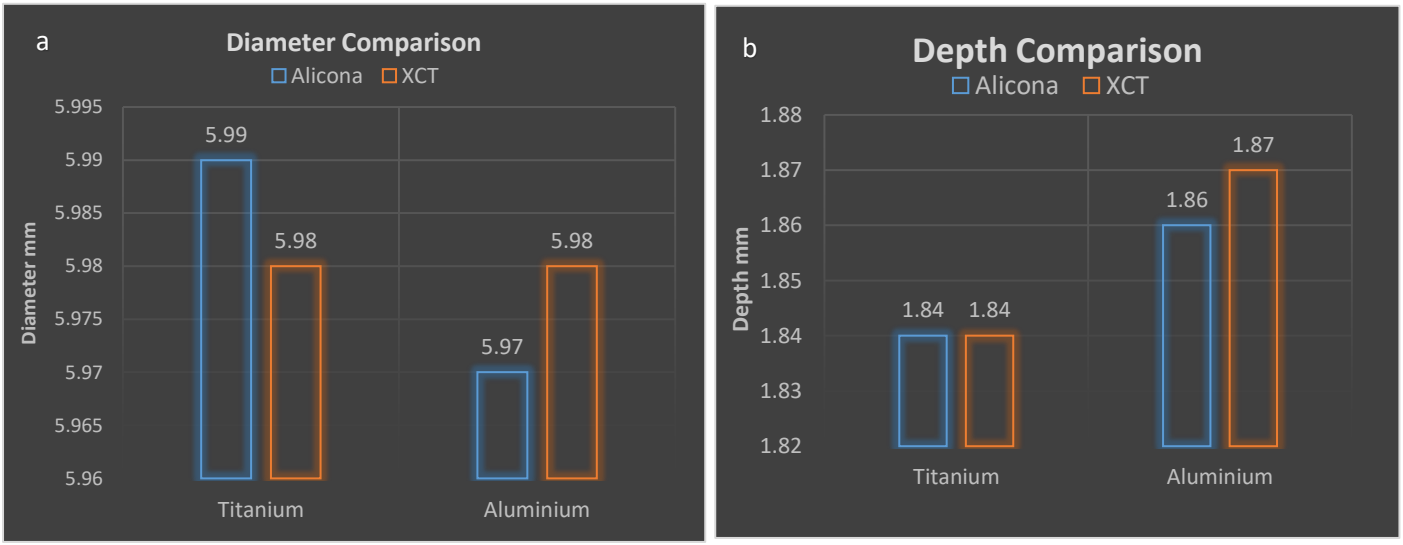

Figure 8-22 a) Diameter comparison b) Depth comparison

The difference in calculated diameter and depth values between the Alicona and XCT for the titanium and aluminium halves are within 2%. It was noted that the aluminium inner bore was deformed during the pressing process due to the interference fit design.

In the process of defect characterisation, a single highest value of the pore's grey value must be identified. For this study the highest pore grey value for titanium pores was similar to the aluminium solid material grey value, therefore, the normal defect method had a tendency to produce erroneous results. The use of XCT in scanning multi-material components has become a topic of increasing interest in industry over the last couple of years.

There are several challenges in the process of scanning and performing porosity characterisation on multi-material components. The difference in density of the scanned material requires bespoke XCT settings and cone beam filters. One other challenge is the threshold for surface determination; the correct threshold identification is the biggest challenge due to the presence of three peaks in the grey value histogram.

In this study, the scan parameters were setup mainly for the aluminium material; however, this did not affect the results due to the small artefact size. In order to assess the scan quality a grey value analysis was carried out, the results are shown in figure 8-23 where figure a) shows XCT front view of the grey value analysis and figure b) shows the top view of the drilled hole with titanium powder.

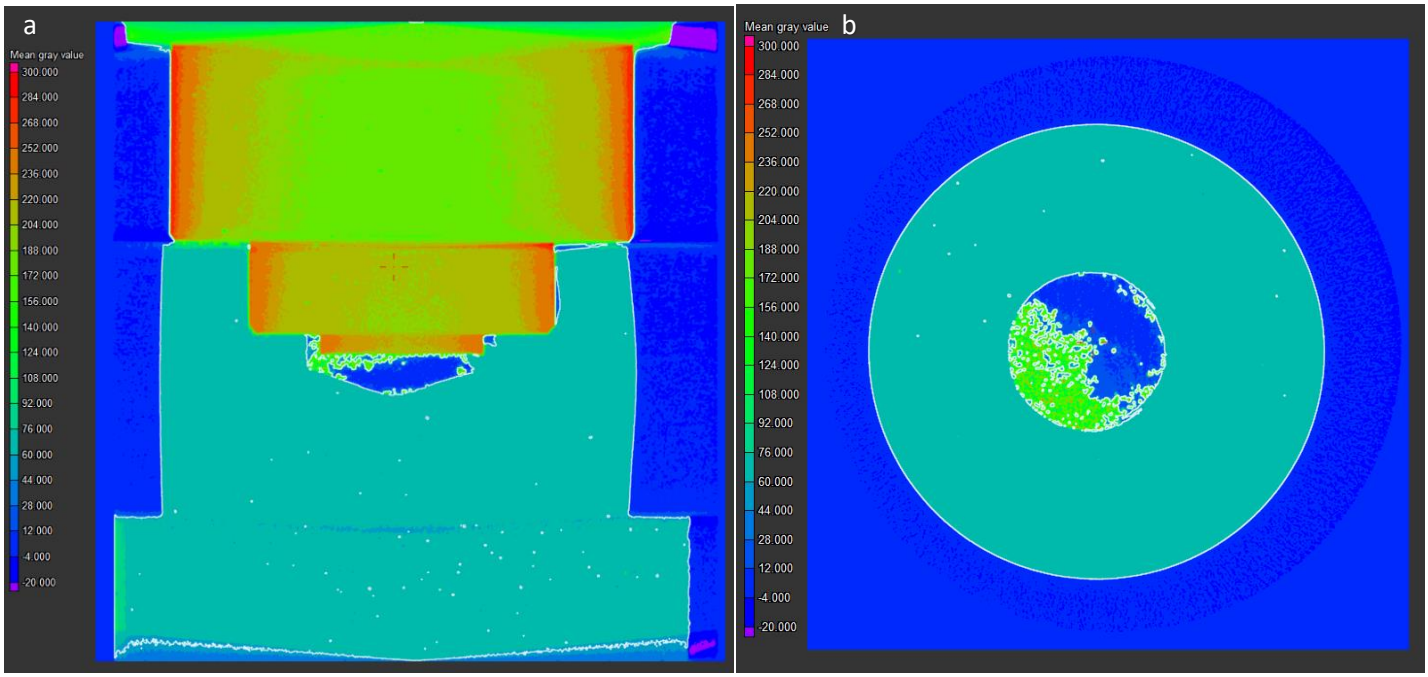

Figure 8-23 a) XCT front view grey value analysis b) XCT top view grey value analysis

In figure 8-23 a), it was noted that the scan parameters are sufficient for the lower aluminium section; this is evident by the consistent grey value (72) across the aluminium lower half. On the other hand, these parameters are not sufficient for the upper titanium half; this is evident by the grey value inconsistency in the titanium upper half, where the edges of the titanium mean grey value was 238, gradually reducing to 198 in the middle of the titanium half. The un-fused powder in figure 8-23 b) mean grey value is 185, which is closer to the mean grey value of the solid titanium material.

8.5.3 Discussion

In general, defect analysis is directly affected by the scan parameters and surface determination threshold. Consequently, if the scan parameters are setup for the lower density material the surface determination threshold will work effectively on the low-density material and the defect analysis results will distinguish correctly between defects/pores and the solid material.

If the scan parameters are not setup for high-density material and the material attenuation is not significantly higher, the surface determination threshold will possibly be sufficient for edge detection but it will not be effective for defect analysis; this is what happened in this study. The scan parameters were set for the aluminium and the surface determination was sufficient for edge detection, but not adequate for defect characterisation in the titanium solid section or the un-fused powder.

If when scanning dissimilar materials, the scan parameters were setup for the high density /high attenuation material, the surface determination will not be adequate for the low attenuation material edge detection. Defect analysis will detect defects within the dense material but will produce erroneous results in the low attenuation material. Figure 24 shows an example of dissimilar material assembly XCT scan, where the compressor wheel is made of aluminium and the shaft is made of steel. Figure 8-24 a) shows a 3D XCT image of the assembly, while figure 8-24 b) shows a front view 2D image with surface determination, c) figure 8-24 c) shows a front view 2D image with mean grey value analysis results.

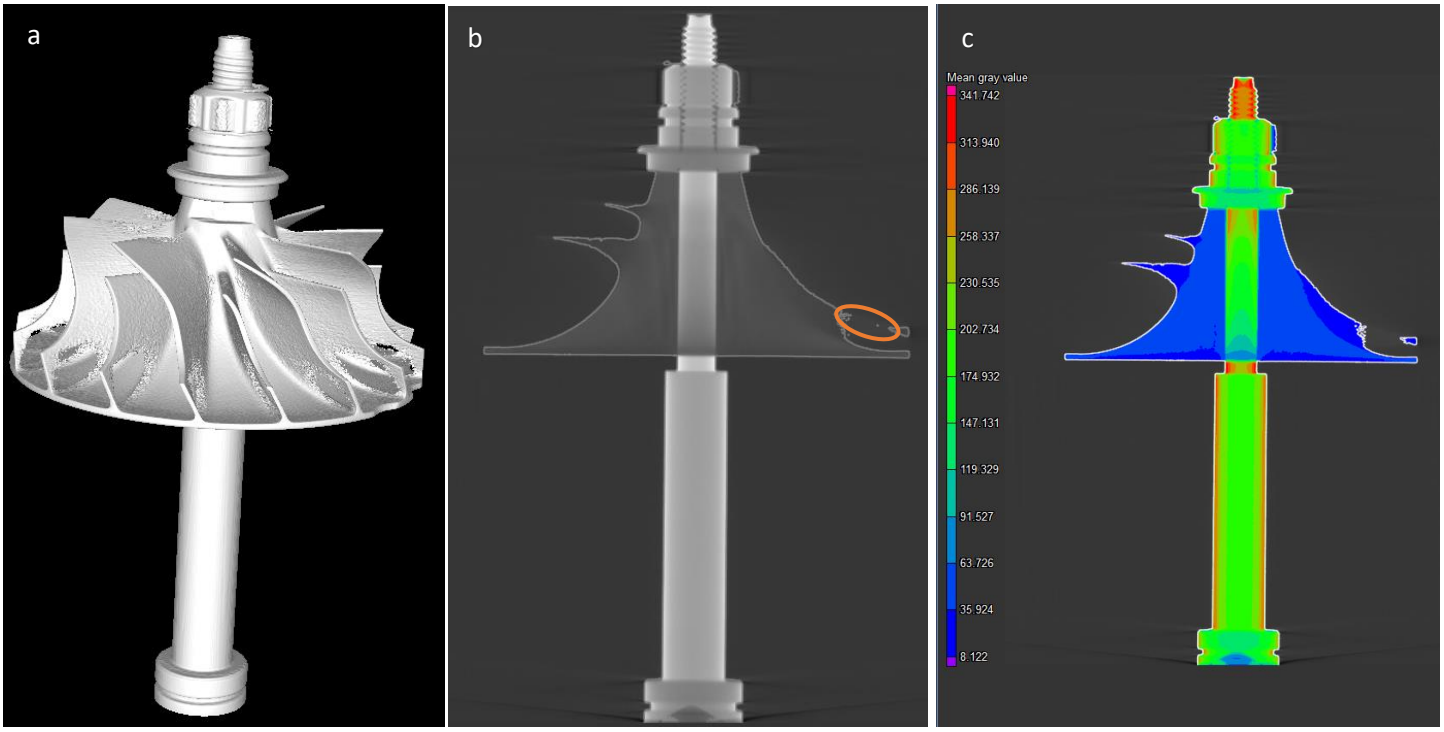

Figure 8-24 a) Multi material assembly 3D XCT image b) 2D front view XCT image c) Multi material XCT mean grey value results

The multi material assembly 3D image in figure 8-24 a) shows the complete assembly including the low and high material attenuation, but the root of an aluminium compressor wheel blade is not visible in the image. This is mainly due to the combination of a low attenuation material and blade root thickness, which resulted in a low mean grey value (15) in this section; the rest of the blade is between 28 and 35 and root of the compressor wheel, which is the thickest section of the wheel, is between 63 and 91. Figure 8-24 b) shows the front view of the assembly, where part of the blade edge is not visible, the grey value analysis in figure 8-24 c) shows that the high attenuation material (steel) ranges from 230 to 286.

This large difference in attenuation requires different scan strategies and data analysis methods; some machines have dual energy options, which enhances the material differentiation by combining two different X-ray spectra. The Dual-energy computed tomography (DECT) option is more effective when attenuation difference between the different scanned materials is small. Some machines only allow limited difference between the filament current and acceleration voltage settings, those machines are

usually utilise a single tube setup. The change in parameters will usually require beam filter change, which is not possible in a single tube machine without disturbing the scan.

In the DECT, the data is usually fused by linear or non-linear fusion methods pre-data reconstruction, however it is not possible to implement more than a single surface determination threshold, therefore the data processing and defect analysis can only be done for each material separately and the results merged.

As previously mentioned, the accuracy of the defect characterisation process is directly affected by scan parameters and SD threshold. In order to understand the impact of single beam spectra on multi material defect characterisation and unfused powder, the aluminium and titanium artefacts used previously in chapter 8 section 4 were scanned with a 29µm voxel. The titanium artefact was placed on top of the aluminium artefact, the scan parameters were optimised for the low density/aluminium material. The results of the scan are shown in figure 8-25, where a) shows an XCT image of artefacts with SD applied, b) shows the defect analysis results and c) shows the grey value analysis results.

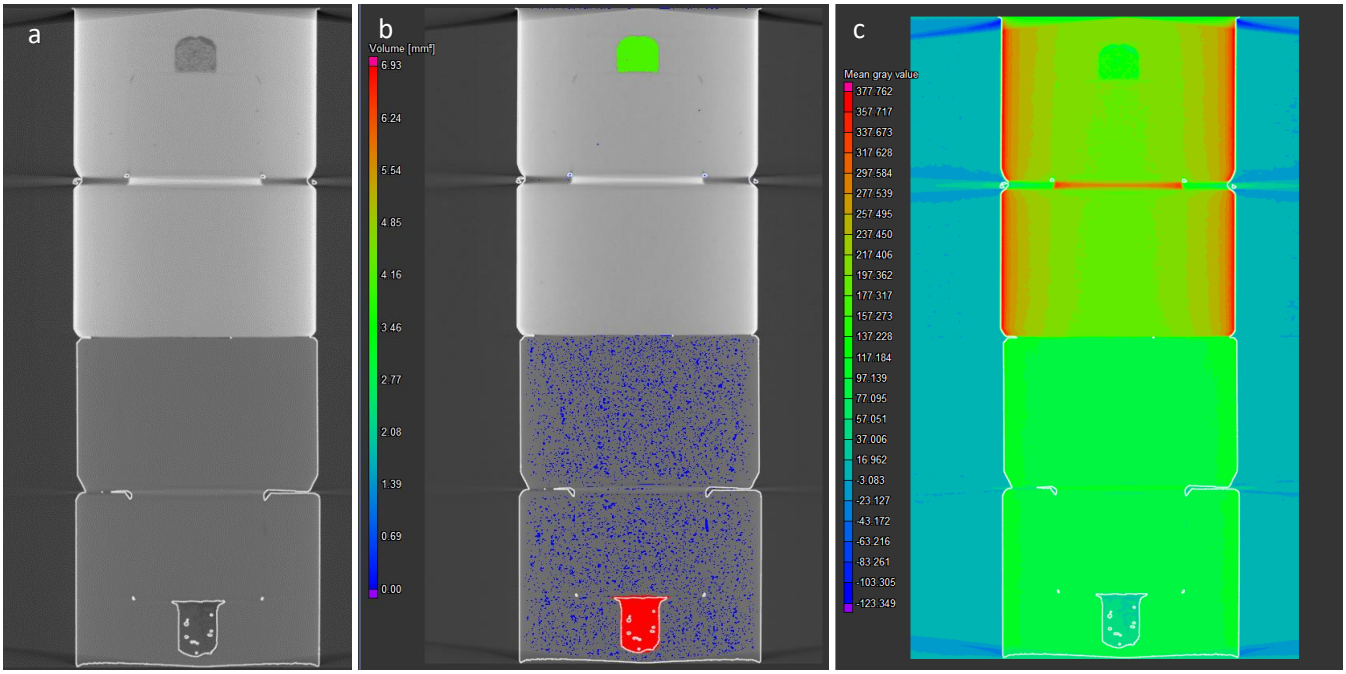

Figure 8-25 a) XCT front view with SD b) XC image of the defect analysis results grey value analysis b) XCT grey value analysis results

Figure 8-25 a) shows the scan results with SD threshold applied, the selected threshold successfully identified the outer edge of both materials and internal edges in the low attenuation material/aluminium only. The defect analysis results in figure 8-25 b) successfully detected both defects within the two different materials, but only detected the unfused powder presence in the aluminium artefact. The outer contour of the defect in the titanium artefact was detected but the unfused powder was not detected. Furthermore, the defect analysis results showed high noise intensity in the lower aluminium artefact, this noise could be easily controlled by result filtration in the defect analysis process.

The grey value analysis results showed a consistent mean grey value (97) across the aluminium artefact and the mean grey value of the enclosed aluminium unfused powder was 77. The titanium artefact mean grey value was not consistent with the high grey value on the outer edge (327) with a gradual decrease towards the middle of the artefact until it reached 212 in the centre of the artefact

the titanium unfused powder mean grey value was 150 and the air gaps between the particles mean grey value was 107. For best defect characterisation results the surface determination and defect analysis must be done for each material individually and then the results merged.

When both material densities are significantly different, the grey value of the defects within the denser section will mostly equal to or exceed the grey value of the lighter solid material. This large difference in attenuation requires special arrangement for scan parameter settings, beam filtration and subsequent surface determination.

The developed methodology was proven to be effective for edge detection of dissimilar materials. The porosity analysis was the biggest challenge in this study. Porosity analysis must be assessed separately for each material for accurate analysis. Whilst scanning the specimen at high magnification improves the accuracy of the obtained results; due to the larger voxel size, there are substantial practical limitations in doing so. It is surmised that in the case of large volume samples XCT settings and beam filtration will be a significant challenge.

8.6 Effect of build location on internal features printability in SLM AM technology

Selective laser melting (SLM) technology is widely adapted in many industries; several industrial applications are using SLM technology in manufacturing prototypes and low volume, high value components. As previously mentioned in chapter 4 section 3.1, that SLM is one of the PBF processes, which uses 15-45µm powder particles. The small powder particles combined with high ability of laser control enables the production of a smaller melt pool and smaller internal features versus the EBM process.

In literature, there are several studies looking into the impact of employing different printing parameters, build up direction and scan strategies on printed component properties. On the other hand, limited information is available on the impact of build location on internal feature printability. In this study, the artefact used was the SLM artefact discussed in section 5.7. The design for the artefact used is shown in figure 8-26 a) and figure 8-26 b) shows the position of each artefact in the build chamber. In total four artefacts were built, one in each corner, the artefacts were numbered from 1 to 4 as shown in 8-26 b).

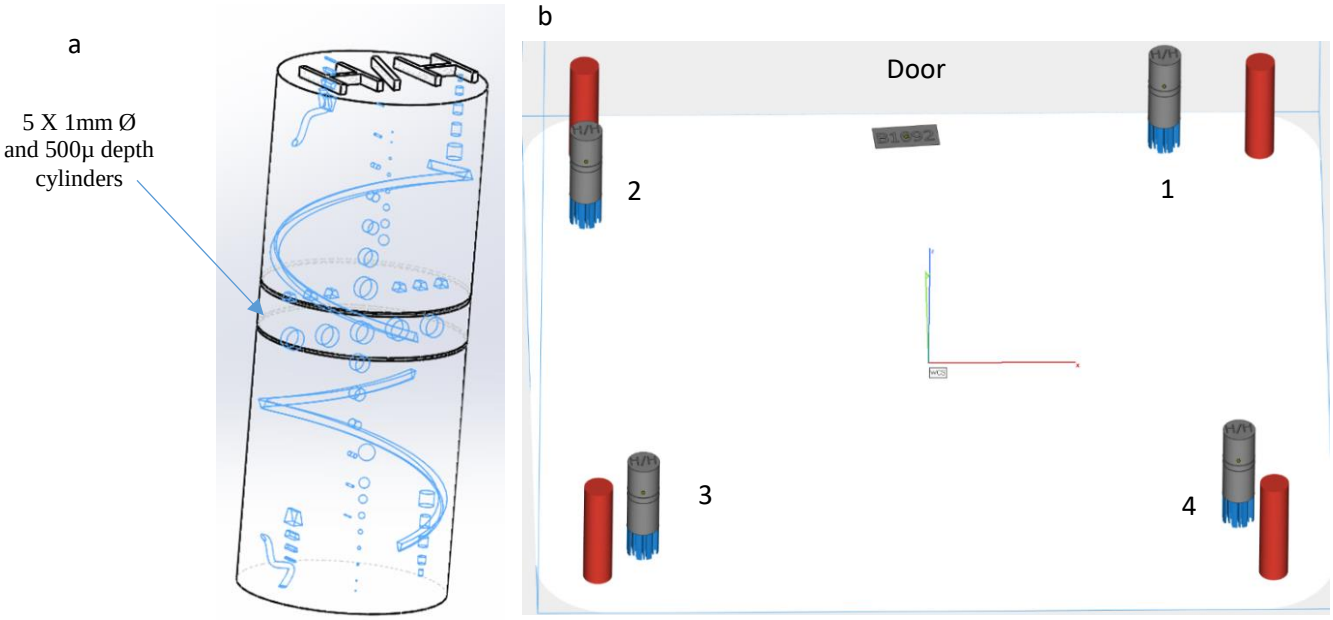

Figure 8-26 a) Artefact 3D model b) Artefact location on the build plate

In the SLM AM community it is known that printing resolution is directly related to the laser spot size and it is not possible to print smaller than the laser spot. However, this is not entirely correct; several layers underneath the surface can be re-melted from the melt pool. The secondary driver for developing this artefact was to identify the limitation in manufacturing capability of geometrical and internal features as they approach the laser spot size or powder particle size [10].

As previously mentioned in chapter 5 section 7, the artefact contains various geometries with different sizes; some of the features were designed as close as 50µm from the surface to duplicate subsurface pores. The artefacts used in the experiment contained 64 internal features ranging from 50µm up to 1mm. The geometrical features included centre located cylinders and prisms, spheres, surface cylinders, edge truncated prisms, two truncated prism helix/spirals and two 350µm internal cylindrical channels. The artefact length was 24mm and outer diameter was 11mm, there are two circumferential marks on the outer middle section of the artefact that were used as physical sectioning marks for location verification.

These four artefacts will be used later for understanding the repeatability in printing internal features within the build chamber volume and identifying the relationship between artefact printing location within the build volume and internal feature printability.

8.6.1 Methodology

The machine used for manufacturing the artefacts was a Renishaw AM 250 using Aluminium AlSi10Mg powder that had been recycled 8 times. A sample of the used powder was analysed by SEM. The build parameters used on the AM250 are shown in table 7.

Laser Power	Laser Focus	Laser Speed	Point Distance	Exposure Time	Point Jump Delay	Jump Speed	Jump Delay
200 W	0 mm	0.55 m/s	80 µm	140 µs	NULL	NULL	NULL

Table 7 AM250 build parameters [10]

Figure 8-27 a) shows the laser beam-scanning pattern used in this build, the pattern was an outer contour with hatches and arrays in parallel stripes [315]. Figure 8-27 (a) shows the middle slice obtained from Quantum software; the middle slice shows the five cylinders top view. Figure 8-27 (b) shows an XCT image of the middle slice with the 5 cylinders.

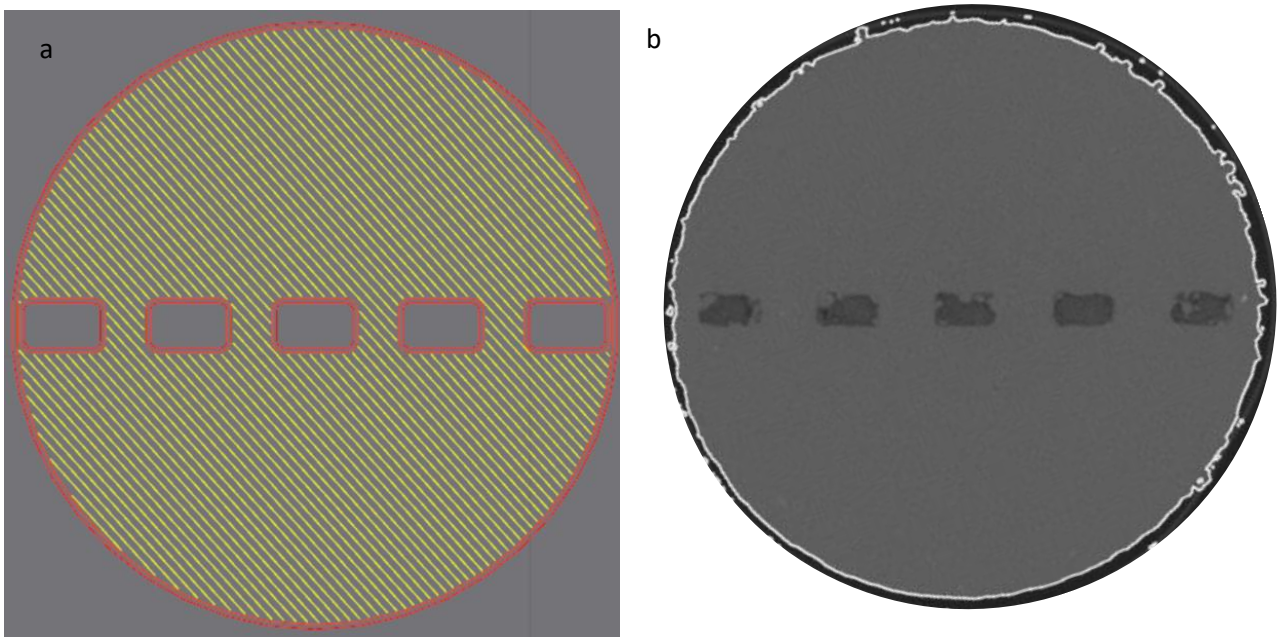

Figure 8-27 a) Quantum software middle slice b) XCT image of the artefact with internal features highlighted

The four artefacts were scanned with a Nikon XTH225 industrial CT with 26µm voxel size; the XCT settings used are shown in table 8 below, the scan results was reconstructed by CT-PRO software. Data processing, surface determination processes and defect analysis were carried out using VG Studio Max 3.1 (Volume Graphics, Heidelberg). The surface determination threshold was kept constant throughout the experiment to ensure result comparability.

Filter	Exposure	Filament Current	Acceleration Voltage	Voxel Size
0.1mm	4000ms	50µA	135 kV	26 µm

Table 8 XCT scan parameters

8.6.2 Results

In the designed artefacts, several cylinders and prisms were designed close to the outer surface/edge of the part. The feature distance from the surface varied from 50µ to 350µm; any feature closer than 100µm from the surface was not designed to be enclosed. Figure 8-28 shows an XCT image of the edge cylinders, where figure 8-28 a) shows artefact 1, b) artefact 2, c) artefact 3, and d) artefact 4.

The slicing software predicted that the edge features would not be enclosed, figure 8-28 confirmed that the edge cylinders closer than 100µm from surface in all four artefacts were not enclosed Although all the edge cylinders were not enclosed they varied in size and shape. It was noted from the XCT results that cylinder 1's four edge cylinders are 20-30% less than cylinder 2 and 3 cylinder. Furthermore, the surface entrance for the upper cylinders were less than all the lower cylinders in all four artefacts.

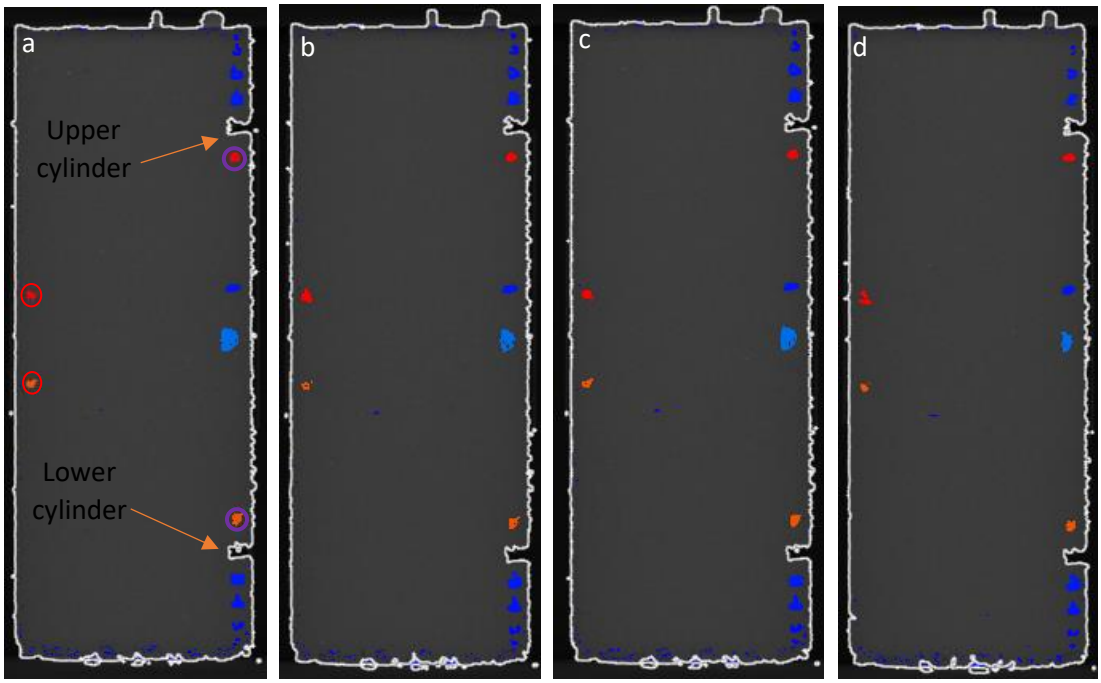

Figure 8-28 a) artefact 1 b) artefact 2 c) artefact 3 d) artefact 4

Figure 8-26 a) shows the two circumferential location marks printed in the middle of the artefacts, located in the central zone of the five cylinders. The centre of the cylinders was designed to be 14.40 mm from the base, the location was verified by the XCT and found to be 14362µm from the base in artefact 1, 14383µm in artefact 2, 14297 in artefact 3 and 14348 in artefact 4. The largest differences were in Artefact 3 and 4; 103 and 52µm respectively.

Another method used for location verification was the lower and upper helix features, the angular positions were compared to the CAD drawing; the verification proved that the angular location was identical to the CAD design with the exact start and end location within the XCT's resolution. As the features were mirrored, the start location of the lower spiral/helix should have been identical to the top helix end location. In figure, 8-28 a) the lower helix feature start location is marked with a purple circle and the end location is marked with red circle. The upper helix start location is marked with a red circle and the end location is marked with a purple circle. In all four artefacts, the helix feature was symmetric with the same start and end location.

The 5 cylinders (see figure 8-26 (a)) located between the two circumferential location marks are numbered 1 to 5, from left to right. The length is named as the "major" axis and width as the "minor" axis. Figure 8-29 shows the five cylinders in each artefact, where a) is artefact 1, b) is artefact 2, c) artefact 3 and d) artefact 4. The 5 cylinders shown in figure 8-29 were used for comparing between the four artefacts internal feature dimensions.

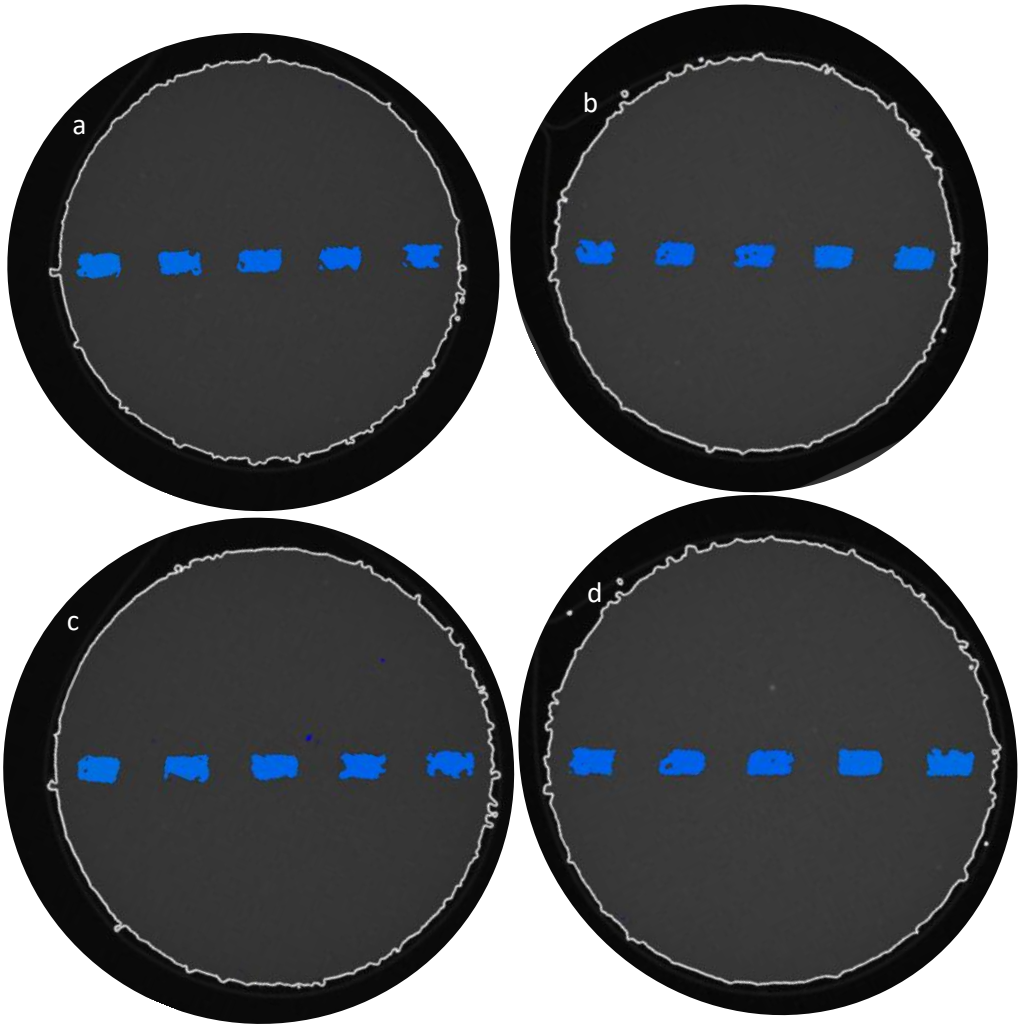

Figure 8-29 middle cylinders a) artefact 1 b) artefact 2 c) artefact3 d) artefact 4

While comparing the five cylinders in the four artefacts in figure 8-29 it was noted that cylinder 5 in artefact 1 and cylinder 1 in artefact 4 are smaller than the other cylinders. Although all cylinders were printed, the edges (length and width) are not uniform. The spacing between the cylinders are matching in all artefacts and the distance between the edge cylinders and the artefact outer edge are uniform across the four artefacts within 100µm.

Figure 8-30 a) shows the major dimension comparison and figure 8-30 b) shows the minor dimension comparison for 5 cylinders across the four artefacts. The major dimensions were designed to be 1mm and the minor were designed to be 500µm. In figure 8-30 a) the lowest major value was cylinder 5 in artefact 1 which was 729 µm, then cylinder 1 in artefact 4 which was 794µm. All the remaining major dimensions are between 873µm and 987µm, with six measurements under 900µm. In the minor comparison, the lowest measurements are found in artefact 2 cylinder 3 (383µm) and artefact 4 cylinder 1 (386µm), all the remaining measurements are between 407 and 487µm.

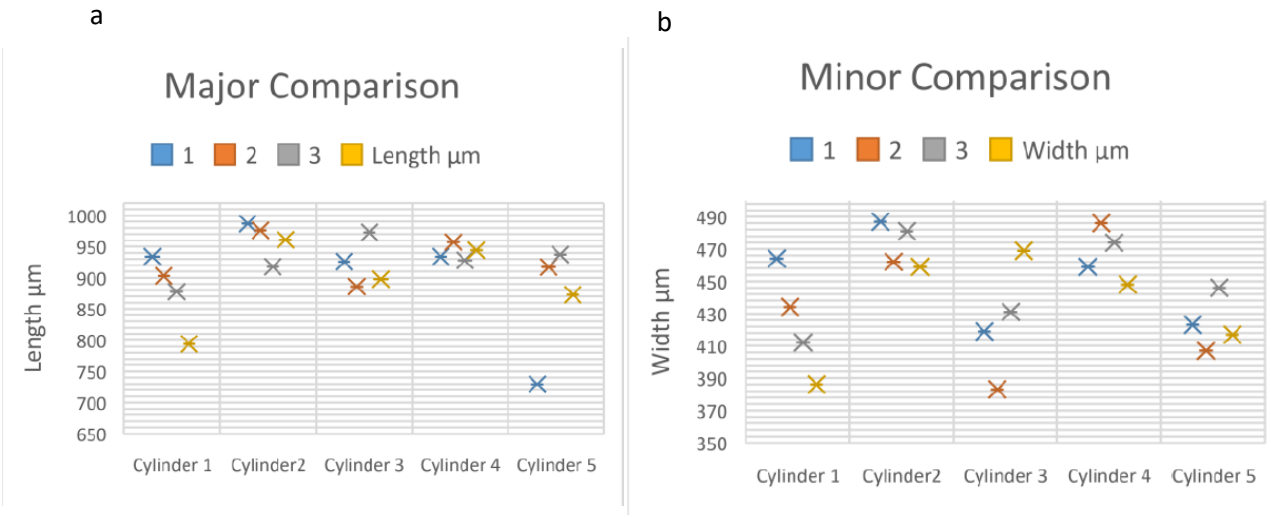

Figure 8-31 a) Major comparison b) Minor comparison

8.6.3 Discussion

Across the four artefacts the sphere minimum resolution was 100µm, the 50µm spheres were not seen to be present within in the build. The smallest truncated prisms were designed with a 100µm base and 50µm top face; these prisms were not present in any of the four artefacts. The smallest truncated prism found had a 150µm base and 100µm top face. The vertical cylinders with diameter less than 150µm were not present.

In the case of the horizontal cylinders, any cylinder with a diameter less than 100µm was not present. Finally, the helix and spiral features were present and high-resolution scans revealed that the start and end angular positions accurately matched the designed locations.

Figure 8-31 a) shows an XCT image of the printed internal features in artefact 4, figure 8-31 b) shows the upper spheres, figure 8-31 c) shows the lower spheres and figure 8-31 d) shows two cylinders in the upper half. While figure 8-31 e) shows the upper truncated prism helix, figure 8-31 f) shows a truncated prism, figure 8-31 g) shows the upper internal channels and figure 8-31 h) shows one of the upper edge cylinders.

In was noted in artefact 4 that the internal feature resolution is lower than the other artefacts, this can be seen in figure 8-31. Where the two upper edges spheres were linked to each other, in the original design the 500µm and 400µm diameter spheres should have been separated with a 350µm gap. In 8-31 b) it can be seen that the spheres are connected. On the contrary, the mirrored spheres in the lower half (see 8-31 c)) did not suffer the same issue, although the designed spheres and the space between them are identical, the only difference is in the lower half the 400µm sphere was

printed first then the 500µm sphere. In the upper half, the 500µm sphere was printed first, then the 400µm sphere.

It was also noted that there is a 220µm height and 90µm depth triangular shaped geometry on the top of several features, like those appearing on the top of the central cylinders shown in figure 8-31 d). These also appeared on some sections of the spiral helix truncated prisms shown in figure 8-31 e) and on the top of the 400µm diameter edge cylinder shown in figure 8-31 h). Those triangular shapes were much less in the internal channels as shown in figure 8-31 g).

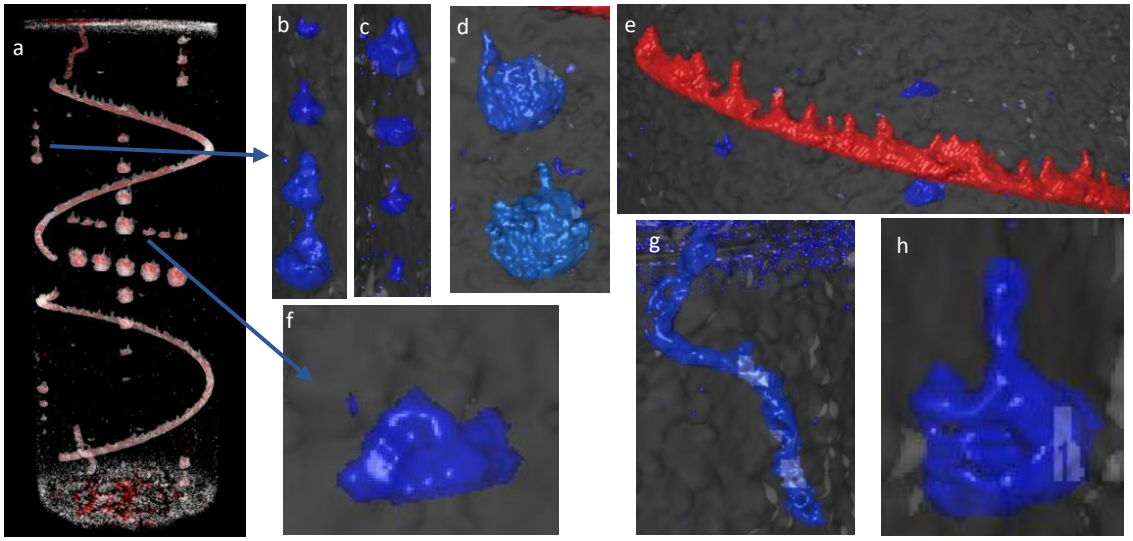

Figure 8-32 a) internal features XCT image b) upper spheres c) lower spheres d) central cylinders e) upper helix f) truncated prisms g) internal channel h) edge cylinder

In this study, the designed internal features have shown that the melt pool dimensions directly affect AM internal features printability. As any feature, less than 150µm did not produce the designed shape, and any feature closer than 100µm from surface was not enclosed; one of the main reasons for this was that the melt pool dimensions were larger than the spot size. The printing parameters used produced a melt pool with 150µm length, 90µm width and in some locations; the melt pool depth was more than 200µm.

The results of this study show that the lowest internal feature resolution was found in artefact 1 and 4, those two artefacts were located opposite to the re-coater filling point. The powder re-coater carries a limited amount of powder that decreases during the spreading process, so the powder bulk density is decreasing from the re-coater start line to the end line; reducing the compactness of the layer towards the end line. This could be one of the factors, which contributed to the drop in the internal feature resolution in artefact 1 and 4.

The melt pool dimensions and material solidification behaviour are directly affected by the laser-scanning pattern, in this study the scan pattern used was outer contour with hatches in arrays of parallel strips. When using this scan pattern the max melt pool temperature will always be in the middle of the internal feature, leading to re-melt of lower layer. In this study, the feature geometry was not large enough to cause re-melting of the lower layers; this was evident by good consistency in the internal features base. However, the top of the internal features was not consistent and this was evident by the connection between the upper spheres and the triangular shaped geometry on the top of several features.

As previously discussed in chapter 4 section 5, powder morphology affects several aspects of the AM process; some powder characteristics like shape and size distribution can introduce lack fusion, which compromises the structural integrity in the printed component. In the SLM process virgin powder particle size ranges between 15-45µm, large irregular shape powder particles cause irregular powder compaction, which decreases flowability and increases defects in the component.

When comparing virgin powder particles to the particles obtained after 10 prints, it was noted that the particle size distribution increased by 3%, this change in size distribution would cause uneven heat distribution during energy deposition; introducing lack fusion in the printed components [331].

The powder used in this experiment was recycled eight times, figure 8-32 shows an SEM image of the powder used, where figure a) is a low magnification image and b) is a focused high magnification SEM image for the largest particle. The powder used in this experiment contained several large irregular satellite powder particles, the particles shown in figure 8-32 b) are irregularly shaped and were 4X the upper limit of the virgin powder particle size, with several smaller particles fused to it.

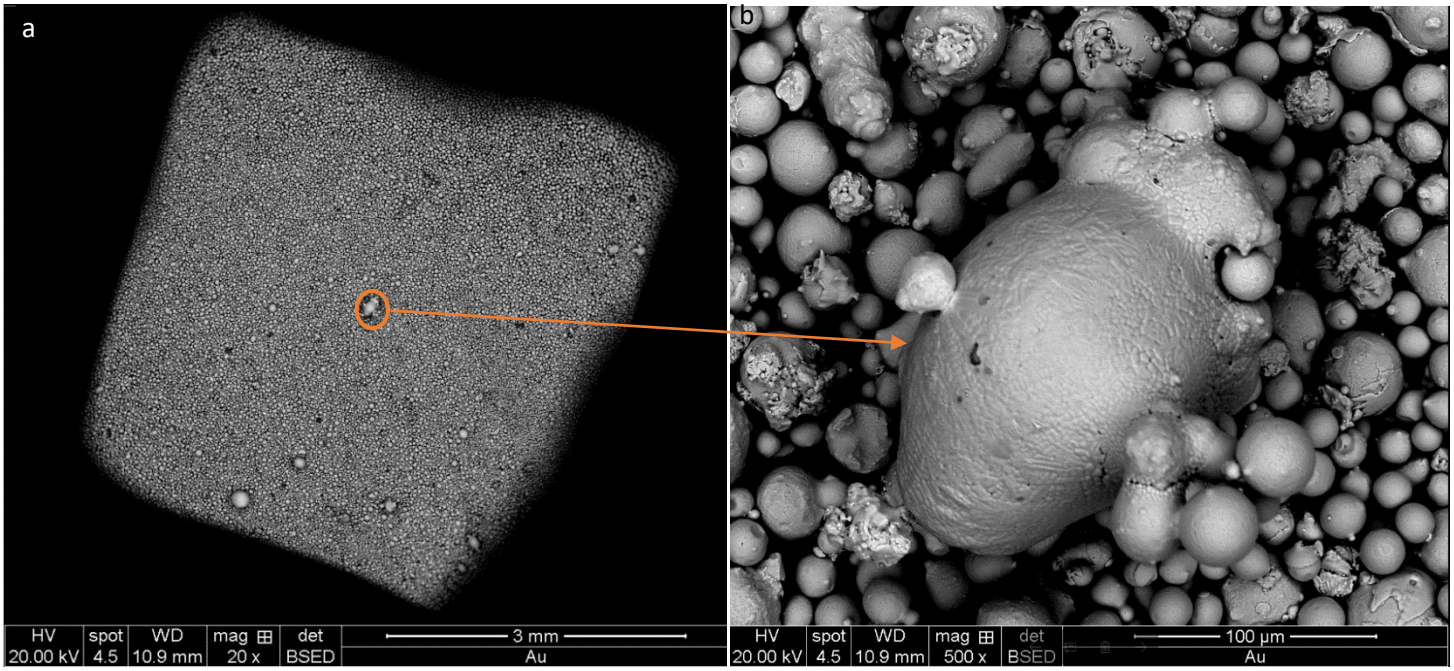

Figure 8-33 8X recycled powder a) low magnification 3mm b) high magnification 100µm

The presence of those particles increased the overall powder size distribution and reduced the overall powder sphericity by around 30%. Powder recycled 10 times increased the largest defect size by 50% [310-312]. To fully melt large particles high energy is required, on the other hand, smaller particles require lower energy levels. In the SLM process, virgin powder ranges from 15-45µm, the size distribution is consistent but after recycling some particles can be very large, similar to the one shown in figure 8-32 b) which is in excess of 200µm.

In this study, most of the internal features are more than 150µm greater than the designed dimensions; recycled powder degradation is contributing to the difference, as the AM machine slicing software did not consider powder quality and condition when selecting the optimum printing parameters. Furthermore, the internal feature resolution was directly affected by the print parameters and laser scan pattern, in this study the parameters was not optimised for internal features; a reduction in laser speed was required to improve the feature resolution. In the AM process,

printing internal features with heavily recycled powder requires sophisticated process parameters that are optimised to internal geometries and the spaces between them. The impact of powder morphology and melt pool dimensions requires further investigation. For the presently used slicing software there appears to be shortcomings in determining the manufacturability of parts containing small intricate features near the surface. In this instance, care/experience is needed to realise such features.

Unfortunately, there is no information recorded about inert gas flow velocity. Melt pool dimensions are affected by inert gas characteristics; reduced gas flow could result in ejecting powder spatter from upstream locations, which lands in random locations on the powder bed. The impact of gas flow on internal features printability is one of the important points that requires further investigation.

8.7 Chapter Summary & Conclusions

In this chapter the challenges in characterising unfused and semi-fused power using XCT was discussed. The magnification study proved that a 38µm voxel size is sufficient to detect the unfused/semi-fused powder defect outer contours. To characterise the powder, a sub 30µm voxel size is required.

In the second study, the results confirmed that un-fused powder detectability is difficult due to grey value similarity to the solid material, furthermore, the ISO 50% threshold is not adequate for detecting semi-fused powder zones; consequently, a more bespoke approach is required. This approach encompasses acquiring the grey value of the pores in the denser section of the part (longest x-ray path). The threshold can vary between scans due to different scanning parameters, parts shape and dimensions.

The XCT demonstrated to be a powerful technique in defect detection and powder cross-contamination characterisation due to the effect of material density on x-ray attenuation; different materials will have different grey values.

In the third study, two artefacts from aluminum and titanium were developed to assess the difference in detecting unfused powder in EBM- and SLM-AM components. The SEM analysis for both powders proved that the titanium EBM powder is spherical with uniform shape and SLM aluminum powder is small and irregular; such powder can be hard to detect. It is possible to detect every single powder particle however; doing so requires high magnification and customised settings for surface determination, requiring the exact gray value to be identified.

In the fourth experiment, a multi material artefact was developed to investigate the optimum method for edge detection in a multi material artefact. From this study, it was concluded that when both material densities are significantly different, the grey value of the defects within the denser section would be equal to or exceed the grey value of the lighter solid material. Subsequently, porosity analysis for dissimilar materials must be assessed separately for each material in order to produce accurate analysis. Whilst scanning a specimen at high magnification improves the accuracy of the obtained results due to the larger voxel size, there are substantial practical limitations in doing so.

In the build plate position study, the developed artefacts were manufactured to understand the impact of component position on the build plate on internal feature printability. These artefacts established process capability of the SLM AM for manufacturing small internal features for this powder condition. The study highlighted the limitation in manufacturing capability for specific geometrical features i.e. internal features approaching the size of laser spot/powder size and the relationship between internal feature dimensional resolution and position on the build plate.

From this study, it can be concluded that features placed opposite to the re-coater powder filling point will have a lower internal feature resolution than those placed closer to re-coater filling point. All the internal features are affected directly by the melt pool dimensions, any feature less than 150µm did not conform the designed shape and any feature closer than 100µm from surface was not enclosed. In this study the melt pool dimensions were 150µm length, 90 µm width and 180µm height.

Powder size and quality directly affects internal feature resolution and overall AM part structural integrity. It is clear from the results of this study that slicing software currently does not take in consideration powder particle size and degradation from recycling, which in this case presented as internal feature geometry errors.

Chapter 9 Overall Conclusions

The evolution of industrial computed tomography in recent years has enabled inspection of mechanical component integrity without sectioning or destroying them. For many valuable components and prototypes, non-destructive inspection (NDI) can save time and costs, allowing for pre-failure detection and accurate finite element analysis.

In the chapter, the overall conclusions of the present study. These conclusions are divided into primary and secondary conclusions.

9.1 Primary Conclusions

- **The developed custom surface determination resulted in closer dimensional values to those obtained from the benchmark mark Alicona measurements.** In section 7.1, it was reported that **ISO 50% is not** the appropriate threshold for porosity analysis across a range of sample parts and hence should be avoided for detailed porosity analysis.

- **A methodology to efficiently detect internal porosity/defects down to the build powder size has been demonstrated using the surface determinations and grey level discriminator methodologies and a via series of bespoke artefacts.**

- **A best practice guide for use of the XCT to detect powder scale defects has been developed and is applicable across a range of end users**

9.2 Secondary Conclusions

9.2.1 XCT

- **The best scan strategy for a component made by PBF is to scan with a magnification as low as 38 µm voxel size**, this is mainly to identify the location of the defects and then confirm the area where the defect is located using a high magnification scan. Using this strategy permits scanning relatively large components in a shorter period without compromising the precision of the results; this was highlighted in section 6.1.

- **Surface determination threshold is affected by XCT image blur**, High magnification will improve the resolution and reduce image blur, enhancing the defect analysis results.

- **Surface determination threshold values required for accurate porosity detection are different from that needed for outer surface profile measurement**; this is mainly due to the difference in grey value between the outer edge and inner core of the scanned object.

- **It is always recommended to start defect detection analysis on a new data set with a probability threshold of zero to avoid filtering real defects.** VG studio max manual states “There is no absolute value for the threshold applicable to all data sets”.

- **The beam filtration study reported that dark areas created by beam hardening could be minimised by using an appropriate beam filtration material**. The use of an Aluminium detector filter gave better contrast than a beam source filter. Generally, the filters used in this study showed a gradual change in the grey value, which enhanced edge detection.

- **Currently, XCT metrological capabilities require further enhancement,** this is mainly due to the absence of a full traceability chain and the presence of different scan parameters, which can influence the process. However, in the last 10 years substantial progress has been made towards an XCT standardised process for dimensional inspection but not internal defects analysis, this was discussed in section 7.3.

- The grey value of the defects in assembly with significantly different densities within the denser section will mostly equal to or exceed the grey value of the lighter solid material; this was reported in the dissimilar material study in section 8.5.

- **In order to obtain the best defect characterisation results the surface determination and defect analysis must be done for each material individually and the results merged,** the biggest challenge in the dissimilar material scan was the porosity analysis; to ensure the reliability of the results porosity analysis must be assessed separately for each material.

- When scanning a multi material assembly, the difference in attenuation requires different scan strategies and data analysis methods, some machines have a dual energy option, which enhances the material differentiation by combining two different X-ray spectra. The problem with Dual-energy computed tomography (DECT) is the requirement for beam filter change this is not possible in a single tube machine without disturbing the scan.

9.2.2 Lessons learned from artefacts

- **Scan parameters and object size affect the XCT scan process**; the percentage of error in internal defect dimensional measurements are significantly reduced at higher resolution but the noise presence compromised the defect analysis process by showing false non-present defects.

- **There is a relationship between the x-ray beam being perpendicular or parallel to the pore.** This was confirmed by the results of the interference fit forged titanium artefact in section 5.8, where the error percentage in the internal dimensional measurements were lower when the measured geometry was perpendicular to X-ray beam, compared to those that were parallel to X-ray beam.

- **The optimisation of surface determination combined with the appropriate scan parameters, enhanced the XCT defect characterisation process,** this was proved in the repeatability study in section 7.3

- **Different scan parameters resulted in a maximum deviation of 1.6 voxels from the Alicona reference value, with a minimum deviation of 0.4 voxels.** this was highlighted by the results of reproducibility study in section 7.3.4.

9.2.3 Powder characterisation

- **In order to detect un-fused powder, the air gaps between the powder particles must be detected.** Those gaps are not uniform owing to the differenced in the diameter and shape of the powder particles, this was highlighted in in section 8.2

- **The sufficient voxel size for detecting un-fused powder presence was found to be 38µm.**When the voxel size is equal to or exceeds the size of the air gaps between the powder particles, the defect analysis process fails to detecting unfused powder.

- **The presence of large/satellite powder particles had a negative impact on the internal features printing resolution.**

- **XCT could be used for detecting powder contamination**; this is highlighted by the presence of bright spots in the scanned object. The contamination was distinguished from the material by the excessive mean grey value. In high-end applications such as medicine or

aerospace, it is a crucial requirement for the AM powder to be contamination free. This requirement is often underrated and has proved to be quite difficult to detect. The techniques that are capable of characterising the AM metallic powder morphology include XCT and SEM.

- **The slicing software does not consider powder quality and condition when selecting the optimum printing parameters.** This was noted by the deviation in the internal feature dimensions.

9.2.4 Contribution to Knowledge

Overall, this work has contributed to the subject in area in several aspects

- Highlighting the challenges and pit falls of porosity defect detection using XCT.
  Any XCT user will benefit from this knowledge specifically the user of high-end applications that requires 100% inspection. The appreciation of these pitfalls will improve the overall efficiency of NDT process.

- Development of a methodology for porosity characterisation, which removes many elements of user subjectivity.
  XCT users that focus on defects analysis will benefit from this knowledge. The removal of user subjectivity will enhance the defect characterisation process leading to reproducible results.

- Development of an artefact that is capable of identifying PBF AM machine printable internal features resolution.
  The artefact will benefit AM machine users that are interested in identifying the minimum printable resolution of the machine.

- The micro drilled defect artefacts that contained un-fused powder, discussed in chapter five section four are currently used by Volume graphics as a case study demonstrating the ability of the software in characterising un-fused powder and detecting powder contamination.

- The results of the powder investigation study helped AM machine manufacturer in changing their powder supplier due to the powder being produced outside of specification. This knowledge will benefit any PBF AM machine users that are concerned about the powder degradation and morphology.

9.3 Future work

The studies carried out as part of this thesis have highlighted several areas that require further investigation this chapter outlines this work.

9.3.1 XCT system comparison

A comparison of different XCT machines using similar voxel size and scan parameters is required to understand the advantages and disadvantages of each machine relating to scan setup, acquisition time, reconstruction software, final data accuracy, cost of purchase, repeatability, and overall performance.

9.3.2 Software comparison

Currently there are several different options for XCT data processing software; VG studio max 3 software was used throughout the research. VG studio is very capable and includes several add-ons that aid in converting XCT data to formats to be used in other software packages as well as analysing the results independently. The cost of the software purchasing and licence renewal is considerably high and it requires high computing power to properly. Further work is required to compare all available software on the market and rationalise them in terms of ease of use, process capability, repeatability, cost, accuracy and overall performance.

9.3.3 Dissimilar material

This thesis has highlighted the challenges presented in porosity characterisation of dissimilar materials and assemblies with different attenuation materials. A method was developed for edge detection in dissimilar materials, which proved to be effective for edge detection, but failed to detect defects in high attenuation material, specifically when the SD threshold was set for the low attenuation material. This method will work in case of multiple component assemblies; however, it is ineffective in AM application when dissimilar materials are fused together. To help resolve this issue future work aim the develop a defect analysis method for fused dissimilar materials.

9.3.4 Dual-energy computed tomography (DECT) filtration strategy

There are several machines, which have the capability of utilising dual energy source to scan multi attenuation components. Beam filtration strategies for dual energy scans can be challenging, especially if the difference in attenuation is large. Therefore, future work will investigate beam filtration strategies for dual energy scans.

9.3.5 High voltage XCT

225kV machines were used throughout this research; these machines are limited in terms of beam penetration, which is especially important in the case of large components or dense materials with a large wall thickness. High power XCT machines with micro focus capabilities are available and future work will look to investigate the resolution of defects characterisation using high-powered XCT and the impact of beam spot size on internal feature characterisation.

9.3.6 Round robin

Four operators from the same lab participated in the reproducibility study; to add more confidence in the results a wide variety of participants is required. Future work will focus on conducting a round robin defect characterisation investigation. In this round robin, several labs will participate from locations around the globe.

9.3.7 Voxel signature

The powder analysis investigation highlighted the ability of the XCT in differentiating between different materials based on their density, it was noted that Inconel particles contaminating

aluminium powder could easily be detected due to their higher mean grey value. Future work will investigate the voxel grey value signature for each material; this will help in using the XCT for material analysis.

It was noted in the surface determination experiment that the edge voxel grey value changes with the percentage of air in it. Future work will investigate the relationship between the grey value and percentage of air and material in this specific voxel. The aim is to enhance the accuracy of surface determination and improve defect characterisation results.

9.3.8 AM machine resolution

An SLM artefact with internal features showed that AM machine printing resolution varies between 150 and 200µm. Future work will aim to improve print resolution by:

- using virgin powder
- increasing internal feature dimensions
- increasing the spacing between features
- increasing laser speed

Future work will focus on establishing the relation between the preprint large irregular powder particles and those found in the post build internal features, and whether the machine parameters requires optimisation that takes in consideration the increase in the overall powder size distribution. Another points that requires further investigation, is the impact of gas flow on internal features printability and defining is the appropriate parameters for printing internal features.

Chapter 10 Reference

1. *Tawfik, A., Racasan, R., Bills, P. J., & Blunt, L. (2017). Detection of unmelted powder in additive manufactured components using computer tomography.*
2. *Blunt, L., Tawfik, A., Racasan, R., & Bills, P. (2017, October). Method for characterizing defects/porosity in additive manufactured components using computer tomography. In Joint Special Interest Group Meeting between EUSPEN and ASPE Dimensional Accuracy and Surface Finish in Additive Manufacturing (pp. 188-189). euspen.*
3. *Tawfik, A., Bills, P., Blunt, L., & Racasan, R. (2018, February). Characterisation of powder-filled defects in additive manufactured surfaces using X-ray CT. In 8th Conference on Industrial Computed Tomography. NDT.net Issue - 2018-02*
4. *Tawfik, A., Bills, P., Blunt, L., & Racasan, R. (2018). Optimization of surface determination strategies to enhance detection of unfused powder in metal additive manufactured components. In Proceedings - 2018 ASPE and euspen Summer Topical Meeting: Advancing Precision in Additive Manufacturing (pp. 281-285). American Society for Precision Engineering, ASPE.*
5. *Tawfik, A., Bills, P., Blunt, L., & Racasan, R. (2018, June). Development of an AM artefact to characterize unfused powder using computer tomography. In European Society for Precision Engineering and Nanotechnology 18th International Conference & Exhibition (pp. 97-98). euspen.*
6. *Tawfik, S. Nicholson, R. Racasan, L. Blunt, and P. Bills, "Utilizing Detector Filters for Noise Reduction in X-Ray Computer Tomography Scanning for the Inspection of the Structural Integrity of Additive Manufactured Metal Parts," Smart and Sustainable Manufacturing Systems 3, no. 1 (2019): 18-30. https://doi.org/10.1520/SSMS20180042.*
7. *Tawfik, A., Bills, P., & Blunt, L. (2019, February). Optimisation of surface determination to improve the accuracy and repeatability of detecting unfused powder in AM Aluminum component. In Proc. of Conf. on Industrial Computed Tomography (iCT2019), Padova, Italy (pp. 1-7).*
8. *Tawfik, A., Bills, P., Blunt, L., & Racasan, R. (2018, June). Development of an AM artefact to characterize unfused powder using computer tomography. In European Society for Precision Engineering and Nanotechnology 18th International Conference & Exhibition (pp. 97-98). euspen.*
9. *Tawfik, A., Racasan, R., Bacheva, D., Blunt, L., & Bills, P. (2019). The challenges in edge detection and porosity analysis for dissimilar materials additive manufactured components. In 19th International Conference of the European Society for Precision Engineering and Nanotechnology (pp. 350-351). Euspen.*
10. *Tawfik, A., Racasan, R., Bacheva, D., Blunt, L., Beerlink, A., & Bills, P. (2020). Challenges in Inspecting Internal Features for SLM Additive Manufactured Build Artifacts. In 4th ASTM Symposium on Structural Integrity of Additive Manufactured Materials and Parts (pp. 102-121). ASTM International.*
11. *Tawfik, A., Radwan, M., Attia, M. A., Bills, P., Racasan, R., & Blunt, L. (2020). The Detection of Unfused Powder in EBM and SLM Additive Manufactured Components. International Journal of Automation Technology, 14(6), 1025-1035.*
12. *Mahmood, A., n.d. About Eureka!. [online] Bellarmine.edu. Available at: <https://www.bellarmine.edu/learningcommunity/eureka/about/> [Accessed 4 January 2022].*
13. *Thibaut de Terris, Olivier Andreau, Patrice Peyre, Frédéric Adamski, Imade Koutiri, et al.. Optimization and comparison of porosity rate measurement methods of Selective Laser Melted metallic parts. Additive Manufacturing, Elsevier, 2019, 28, pp.802-813. 10.1016/j.addma.2019.05.035. hal02292119*
14. *Spierings, A. B., Schneider, M., & Eggenberger, R. (2011). Comparison of density measurement techniques for additive manufactured metallic parts. Rapid Prototyping Journal.*
15. *Slotwinski, J. A., Garboczi, E. J., & Hebenstreit, K. M. (2014). Porosity measurements and analysis for metal additive manufacturing process control. Journal of research of the National Institute of Standards and Technology, 119, 494.*
16. *Wessel W. Wits, Simone Carmignato, Filippo Zanini, Tom H.J. Vaneker,Porosity testing methods for the quality assessment of selective laser melted parts,CIRP Annals,Volume 65, Issue 1,2016,Pages 201-204,ISSN 0007-8506,https://doi.org/10.1016/j.cirp.2016.04.054.*
17. *Density: Helium Pycnometry | There are two types of density associated with powders: envelope (or bulk) density and skeletal density. (2020). Retrieved 4 December 2020, from*

https://www.mri.psu.edu/materials-characterization-lab/characterization-techniques/density-helium-pycnometry.

18. *Electromagnetic Testing. (2020). Retrieved 25 December 2020, from https://www.nasa.gov/centers/wstf/supporting_capabilities/nondestructive_evaluation/electromagnetic_testing.html*
19. *Electromagnetic testing (2020). Retrieved 26 December 2020, from https://www.skillscommons.org/bitstream/handle/taaccct/8674/8%20Electromagnetic%20Testing%20%28ET%29.pdf?sequence=17&isAllowed=y*
20. *Ivor Hughes. "The AWA Review: Professor David Edward Hughes", 2009, retrieved July 1, 2015.*
21. *Helle H. Rasmussen, Hans Kristensen & Leif Jeppesen, Birring, Anmol (March 2001). "Selection of NDT Techniques for Heat Exchanger Tubing". Materials Evaluation*
22. *Eddy Current Testing - A Definitive Guide. (2020). Retrieved 26 December 2020, from https://www.twi-global.com/technical-knowledge/job-knowledge/eddy-current-testing-123.*
23. *Pulsed Eddy Current (PEC). (2020). Retrieved 26 December 2020, from https://www.eddyfi.com/en/technology/pulsed-eddy-current-pec*
24. *H M Sadek. "NDE technologies for the examination of heat exchangers and boiler tubes – principles, advantages and limitations", Insight vol. 48 no. 3, March 2006, retrieved July 1, 2015.*
25. *Rossetto, L., Tenti, P., & Zuccato, A. (1999). Electromagnetic compatibility issues in industrial equipment. IEEE Industry Applications Magazine, 5(6), 34-46.*
26. *Ma, M. T., Kanda, M., Crawford, M. L., & Larsen, E. B. (1985). A review of electromagnetic compatibility/interference measurement methodologies. Proceedings of the IEEE, 73(3), 388-411.*
27. *Krautkrämer, J., & Krautkrämer, H. (2013). Ultrasonic testing of materials. Springer Science & Business Media.*
28. *Szilard, J. (1982). Ultrasonic testing: Non-conventional testing techniques. JOHN WILEY & SONS, INC., 605 THIRD AVE., NEW YORK, NY 10158, 1982, 640.*
29. *Pros, A. (2008). The Power of Ultrasonic Inspection. Aviation Pros. Retrieved 13 January 2021, from https://www.aviationpros.com/home/article/10377226/the-power-of-ultrasonic-inspection.*
30. *"Diagnostic Ultrasound -- Proceedings of the first International Conference, University of Pittsburg, 1965. Edited by CC Grossman, JH Holmes, C Joyner and EW Purnell. Plenum Press, New York. 1066.*
31. *“This Month in Physics History: November 8, 1865: Roentgen’s discovery of X-Rays.” Ed. Alan Chodos. American Physical Society. Web. 1 Jan. 2015 <http://www.aps.org/publications/apsnews/200111/history.cfm>*
32. *“Wilhelm Conrad Röntgen – Biographical”. Nobelprize.org. Nobel Media AB 2014. Web. 4 Jan 2015. <http://www.nobelprize.org/nobel_prizes/physics/laureates/1901/rontgen-bio.html>*
33. *Kevles, Bettyann Holtzmann. Naked to the Bone: Medical Imaging in the Twentieth Century. New Brunswick, N.J.: Rutgers University Press, 1997.*
34. *"Marie Curie Facts". Nobelprize.org. Archived from the original on 6 March 2019. Retrieved 2 March 2019*
35. *"Marie Curie and the radioactivity, The 1903 Nobel Prize in Physics". nobelprize.org. Archived from the original on 30 July 2018. Marie called this radiation radioactivity—"radio" means radiation.*
36. *Gillet, K. (2021). Romanian company develops scanners that will make airline heads explode | bne. Intellinews.com. Retrieved 2 January 2021, from https://www.intellinews.com/romanian-company-takes-aim-at-terrorism-with-world-s-first-aircraft-scanner-98700/.*
37. *PH Tool Standards for Radiographic Testing (RT). Ndt.net. (2021). Retrieved 2 January 2021, from https://www.ndt.net/search/docs.php3?id=21252.*
38. *S., W., 2021. Non Destructive Testing - Radiographic Testing (RT). [online] Wermac.org. Available at:<http://www.wermac.org/others/ndt_rt.html#:~:text=The%20history%20of%20radiographic%20testing,radioactive%20material%20called%20%22Radium%22.> [Accessed 2 January 2021].*
39. *Radiography Testing - NDT Inspection. Twi-global.com. (2021). Retrieved 2 January 2021, from https://www.twi-global.com/what-we-do/services-and-support/asset-management/non-destructive-testing/ndt-techniques/radiography-testing.*
40. *ASTM E2104-01, Standard Practice for Radiographic Examination of Advanced Aero and Turbine Materials and Components, ASTM International, West Conshohocken, PA, 2001, www.astm.org*
41. *ISO 10675-1, Non-destructive testing of welds - Acceptance levels for radiographic testing - Part 1: Steel, nickel, titanium and their alloys*
42. *EN 444, Non-destructive testing; general principles for the radiographic examination of metallic materials using X-rays and gamma-rays.*

43. *S. Amin Yavari, S.M. Ahmadi, R. Wauthle, B. Pouran, J. Schrooten, H. Weinans, A.A. Zadpoor, Relationship between unit cell type and porosity and the fatigue behavior of selective laser melted meta-biomaterials, Journal of the Mechanical Behavior of Biomedical Materials, Volume 43, 2015, Pages 91-100, ISSN 1751-6161, https://doi.org/10.1016/j.jmbbm.2014.12.015.*
44. *Inglis, C.E., "Stresses in Plates Due to the Presence of Cracks and Sharp Corners," Transactions of the Institute of Naval Architects, Vol. 55, pp. 219-241, 1913.*
45. *Anderson, T.L., "Fracture Mechanics: Fundamentals and Applications," 3rd Edition*
46. *Sanford, R.J., "Principles of Fracture Mechanics," 1st Edition.*
47. *Dowling, Norman E., "Mechanical Behavior of Materials: Engineering Methods for Deformation, Fracture, and Fatigue," 3rd Edition.*
48. *F Gieras, J. (2013). Analysis of Accidents of the Tu-154 Aircraft. In 2nd Smolensk Conference (II Konferencja Smolenska). Warsaw. Retrieved 3 January 2021, from https://www.researchgate.net/publication/277077227_Analysis_of_Accidents_of_the_Tu-154_Aircraft.*
49. *Campbell, J. (2015). Complete casting handbook: metal casting processes, metallurgy, techniques and design. Pages 506-509 Butterworth-Heinemann.*
50. *Luke Sheridan, Onome E. Scott-Emuakpor, Tommy George, Joy E. Gockel, Relating porosity to fatigue failure in additively manufactured alloy 718, Materials Science and Engineering: A, Volume 727, 2018, Pages 170-176, ISSN 0921-5093, https://doi.org/10.1016/j.msea.2018.04.075.*
51. *Smith, E. W. and Pascoe, K. J., Fatigue crack initiation and growth in a high strength ductile steel subject to in phase biaxial loading. Multiaxial Fatigue, ASTM STP 853, ed. K. J. Miller and M. W. Brown. American Society for Testing and Materials, Philadelphia, PA, 1985, pp. 111-134*
52. *Miyazaki, T., Kang, H., Noguchi, H., & Ogi, K. (2008). Prediction of high-cycle fatigue life reliability of aluminum cast alloy from statistical characteristics of defects at meso-scale. International Journal of Mechanical Sciences, 50(2), 152-162.*
53. *J.Z. Yi, P.D. Lee, T.C. Lindley, T. Fukui, Statistical modeling of microstructure and defect population effects on the fatigue performance of cast A356-T6 automotive components, Materials Science and Engineering: A, Volume 432, Issues 1–2, 2006, Pages 59-68, ISSN 0921-5093, https://doi.org/10.1016/j.msea.2006.07.003.*
54. *P.J Laz, B.M Hillberry, Fatigue life prediction from inclusion initiated cracks, International Journal of Fatigue, Volume 20, Issue 4, 1998, Pages 263-270, ISSN 0142-1123, https://doi.org/10.1016/S0142-1123(97)00136-9.*
55. *Gruenberg, K. M., Craig, B. A., & Hillberry, B. M. (1999). Probabilistic method for predicting the variability in fatigue behavior of 7075-T6 aluminum. AIAA journal, 37(10), 1304-1310.*
56. *Murat Tiryakioğlu, Pore size distributions in AM50 Mg alloy die castings, Materials Science and Engineering: A, Volume 465, Issues 1–2, 2007, Pages 287-289, ISSN 0921-5093, https://doi.org/10.1016/j.msea.2007.02.008.*
57. *Tiryakioğlu, M. Weibull Analysis of Mechanical Data for Castings II: Weibull Mixtures and Their Interpretation. Metall Mater Trans A 46, 270–280 (2015). https://doi.org/10.1007/s11661-014-2610-9*
58. *Przystupa, M.A., Bucci, R.J., Magnusen, P.E., Hinkle, A.J. 6701744011;7006240329;6602874594;7003485826;Microstructure based fatigue life predictions for thick plate 7050-T7451 airframe alloys (1997) International Journal of Fatigue, 19 (SUPPL.1), pp. S285-S288.*
59. *Y. Murakami, M. Endo, Effects of defects, inclusions and inhomogeneities on fatigue strength, International Journal of Fatigue, Volume 16, Issue 3, 1994, Pages 163-182, ISSN 0142-1123, https://doi.org/10.1016/0142-1123(94)90001-9.*
60. *Murat Tiryakioğlu, On the size distribution of fracture-initiating defects in Al- and Mg-alloy castings, Materials Science and Engineering: A, Volume 476, Issues 1–2, 2008, Pages 174-177, ISSN 0921-5093, https://doi.org/10.1016/j.msea.2007.04.088.*
61. *Spera, D. A. (1976). What is thermal fatigue. In Thermal fatigue of materials and components. ASTM International.*
62. *K. Miller, J. (2021). Turbocharger Failure Analysis. Muscle Car Diy. Retrieved 4 January 2021, from https://www.musclecardiy.com/performance/turbocharger-failure-analysis-went-wrong-fix/.*
63. *Carley, L. (2012). Cylinder Head Repair Methods. Engine Builder.*
64. *H. Arami, R. Khalifehzadeh, M. Akbari, F. Khomamizadeh, Microporosity control and thermal-fatigue resistance of A319 aluminum foundry alloy, Materials Science and Engineering: A, Volume 472, Issues 1–2, 2008, Pages 107-114, ISSN 0921-5093, https://doi.org/10.1016/j.msea.2007.03.031.*

65. *Mark E Seniw, James G Conley, Morris E Fine, The effect of microscopic inclusion locations and silicon segregation on fatigue lifetimes of aluminum alloy A356 castings, Materials Science and Engineering: A, Volume 285, Issues 1–2, 2000, Pages 43-48, ISSN 0921-5093, https://doi.org/10.1016/S0921-5093(00)00663-8.*
66. *A.A Dabayeh, A.J Berube, T.H Topper, An experimental study of the effect of a flaw at a notch root on the fatigue life of cast Al 319, International Journal of Fatigue, Volume 20, Issue 7, 1998, Pages 517-530, ISSN 0142-1123, https://doi.org/10.1016/S0142-1123(98)00020-6.*
67. *J-Y. Buffière, S. Savelli, P.H. Jouneau, E. Maire, R. Fougères, Experimental study of porosity and its relation to fatigue mechanisms of model Al–Si7–Mg0.3 cast Al alloys, Materials Science and Engineering: A, Volume 316, Issues 1–2, 2001, Pages 115-126, ISSN 0921-5093, https://doi.org/10.1016/S0921-5093(01)01225-4.*
68. *J.H. Elsner, E.P. Kvam, A.F. Grandt Metall. Mater. Trans. A, 28A (1997), pp. 1157-1167.*
69. *M.E. Seniw, M.E. Fine, E.Y. Chen, M. Meshli, J. Gray, Relationship of Defect Size and Location to Fatigue Failure in Al Alloy A356 Cast Specimens, Prepared for the Paul C. Paris International Symposium 'Fatigue of Materials', TMS-ASM Fall Meeting, 1997.*
70. *Mark E Seniw, James G Conley, Morris E Fine, The effect of microscopic inclusion locations and silicon segregation on fatigue lifetimes of aluminum alloy A356 castings, Materials Science and Engineering: A, Volume 285, Issues 1–2, 2000, Pages 43-48, ISSN 0921-5093, https://doi.org/10.1016/S0921-5093(00)00663-8.*
71. *J.A. Ødegard, K. Pedersen, Report No. 940811, Society of Automotive Engineers, Warrendale, PA, 1984.*
72. *Webb, S. (1992). Historical experiments predating commercially available computed tomography. The British journal of radiology, 65(777), 835-837.*
73. *Nobelprize.org. (2021, 02 Jan 2021). The Nobel prize in physiology or medicine 1979. Available: https://www.nobelprize.org/nobel_prizes/medicine/laureates/1979/.*
74. *What is Computed Tomography? | FDA. U.S. Food and Drug Administration. (2021). Retrieved 15 January 2021, from https://www.fda.gov/radiation-emitting-products/medical-x-ray-imaging/what-computed-tomography.*
75. *Tawfik, S. Nicholson, R. Racasan, L. Blunt, and P. Bills, "Utilizing Detector Filters for Noise Reduction in X-Ray Computer Tomography Scanning for the Inspection of the Structural Integrity of Additive Manufactured Metal Parts," Smart and Sustainable Manufacturing Systems 3, no. 1 (2019): 18-30. https://doi.org/10.1520/SSMS20180042.*
76. *Berrington de González A, Mahesh M, Kim K-P, Bhargavan M, Lewis R, Mettler F and Land C 2009 Projected cancer risks from computed tomographic scans performed in the United States in 2007 Arch. Intern. Med. 169 2071-77.*
77. *Herman, G. T. (2009). Fundamentals of computerized tomography: image reconstruction from projections. Springer Science & Business Media.*
78. *Cal-Gonzalez, J., Rausch, I., Shiyam Sundar, L. K., Lassen, M. L., Muzik, O., Moser, E., ... & Beyer, T. (2018). Hybrid imaging: instrumentation and data processing. Frontiers in Physics, 6, 47.*
79. *S., W. (2021). Non Destructive Testing - Radiographic Testing (RT). Wermac.org. Retrieved 18 January 2021, from http://www.wermac.org/others/ndt_rt.html#:~:text=The%20history%20of%20radiographic%20testing,radioactive%20material%20called%20%22Radium%22.*
80. *Chesler DA, Riederer SJ, Pelc NJ. Noise due to photon counting statistics in computed X-ray tomography. J Comput Assist Tomogr. 1977 Jan;1(1) 64-74. PMID: 615896.*
81. *Mittal, B., Rana, N., Rawat, D., Parmar, M., Dhawan, D. and Bhati, A. (2015). Evaluation of external beam hardening filters on image quality of computed tomography and single photon emission computed tomography/computed tomography. Journal of Medical Physics, 40(4), p.198.*
82. *Radiologymasterclass.co.uk. (2020). Basics of X-ray Physics - X-ray production. [online] Available at: https://www.radiologymasterclass.co.uk/tutorials/physics/x-ray_physics_production [Accessed 16 Oct. 2020].*
83. *2007 Industrial radiography image forming techniques (General Electric Company) GEIT 30158EN.*
84. *Kruth J P, Bartscher M, Carmignato S, Schmitt R, De Chifffre L and Weckenmann A 2011 Computed tomography for dimensional metrology Ann. CIRP 60 821-42*
85. *1980 Radiography in modern industry (Eastman Kodak Company) Quinn R A and Sigl C C 4th Edition.*
86. *ISO 15708-1:2002(E) Non-destructive testing – Radiation methods – Computed tomography - Part 1: Principles, International Organization for Standardization.*

87. *Thompson A, Lindau I, Attwood D, Liu Y, Pianetta E G, Howells M, Robinson A, Kim K-J, Scofield J, Kirz J, Underwood J, Kortright J, Williams G and Winick H 2009 X-ray data booklet Lawrence Berkeley National Laboratory, University of California, Berkeley LBNL/PUB-490 Rev. 3*
88. *Sun, W., Brown, S. B., & Leach, R. K. (2012). An overview of industrial X-ray computed tomography.*
89. *Noel, A. and Fabienne Thibault (2004). "Digital detectors for mammography: The technical challenges". In: European Radiology 14, pp. 1990–1998.*
90. *Marimón Muñoz, E. (2019). Digital radiography: image acquisition and scattering reduction in x-ray imaging (Doctoral dissertation, Bournemouth University).*
91. *Bick, Ulrich and Felix Diekmann (2007). "Digital mammography: what do we and what don't we know?" In: European radiology 17.8, pp. 1931–1942.*
92. *Konstantinidis, Anastasios C. et al. (2013). "X-ray Performance Evaluation of the Dexela CMOS APS X-ray Detector Using Monochromatic Synchrotron Radiation in the Mammographic Energy Range". In: IEEE Transactions on Nuclear Science 60.5, pp. 3969–3980.*
93. *ASTM E2597-07, Standard Practice for Manufacturing Characterization of Digital Detector Arrays, ASTM International, West Conshohocken, PA, 2007, www.astm.org.*
94. *Vareximaging 2520DX Data sheet. Vareximaging.com. (2021). Retrieved 22 January 2021, from https://www.vareximaging.com/sites/default/files/datasheets/vic/2520DX-I%20Industrialpds.pdf.*
95. *Nikon specifications. Nikonmetrology.com. (2021). Retrieved 22 January 2021, from https://www.nikonmetrology.com/images/brochures/xt-h-series-en.pdf.*
96. *Varex XRD 1611 Data sheet. Vareximaging.com. (2021). Retrieved 22 January 2021, from https://www.vareximaging.com/sites/default/files/datasheets/vic/XRD%201611.pdf.*
97. *Varex XRD1620 data sheet.. Vareximaging.com. (2021). Retrieved 22 January 2021, from https://www.vareximaging.com/sites/default/files/datasheets/vic/XRD%201620.pdf.*
98. *ASTM E1441-19, Standard Guide for Computed Tomography (CT), ASTM International, West Conshohocken, PA, 2019, www.astm.org.*
99. *Schörner, K. (2012). Development of methods for scatter artifact correction in industrial x-ray cone-beam computed tomography (Doctoral dissertation, Technische Universität München).*
100. *Sprawls, P. (2021). Blur, Resolution, and Visibility of Detail. Sprawls.org. Retrieved 24 January 2021, from http://www.sprawls.org/ppmi2/BLUR/.*
101. *Bushberg, J. T. et al. (2012). "The Essential Physics of the Medical Imaging, 3rd ed". Lippincott Williams & Wilkins, p. 1048.*
102. *Sprawls, P. (2021). CT Image Quality and Dose Management. Sprawls.org. Retrieved 25 January 2021, from http://www.sprawls.org/resources/CTIQDM/.*
103. *Mulder, M. J., Keuken, M. C., Bazin, P. L., Alkemade, A., & Forstmann, B. U. (2019). Size and shape matter: The impact of voxel geometry on the identification of small nuclei. PloS one, 14(4), e0215382.*
104. *Shepp, L. A., & Vardi, Y. (1982). Maximum likelihood reconstruction for emission tomography. IEEE transactions on medical imaging, 1(2), 113-122.*
105. *R. Gordon, R. Bender, and G.T. Herman. Algebraic Reconstruction Techniques (ART) for three-dimensional electron microscopy and X-ray photography. J. Theor. Biol. 29 (1970), 471–481.*
106. *Kak, A. C., Slaney, M., & Wang, G. (2002). Principles of computerized tomographic imaging.*
107. *Feldkamp, L. A., Davis, L. C., & Kress, J. W. (1984). Practical cone-beam algorithm. Josa a, 1(6), 612-619.*
108. *Reinhart, T. Günther, and C. Poliwoda. VGStudio Max 3.1. Volume Graphics GmbH, Heidelberg. 2021. url: www.volumegraphics.com.*
109. *Townsend, A. (2018). Characterisation of the Surface Topography of Additively Manufactured Parts (Doctoral dissertation, University of Huddersfield).*
110. *Barrett J F and Keat N 2004 Artifacts in CT: recognition and aviodance Radio Graphics 24 1679-91.*
111. *Katić, M., Ferdelji, N., & Šestan, D. (2020). Investigation of Temperature-Induced Errors in XCT Metrology. International Journal of Automation Technology, 14(3), 484-490.*
112. *Muralikrishnan, B., Shilling, M., Phillips, S., Ren, W., Lee, V., & Kim, F. (2019). X-ray computed tomography instrument performance evaluation, Part I: Sensitivity to detector geometry errors. Journal of Research of the National Institute of Standards and Technology, 124, 1-16.*
113. *Hanson K M 1981 Radiology of the skull and brain, Vol. 5: Technical aspects of computed tomography 113 Noise and contrast discrimination in computed tomography Newton T H and Potts D G.*
114. *Lida H, Sasaki H, Inoue H, Kanno I, Miura S, Okuyama D and Uemura K 1986 A simulation study to evaluate the statistical noise and spatial resolution in image reconstruction of emission computed*

tomography--with respect to the optimization of the filter function in the convolution integral Radioisotopes 35 589-94.

115. *Sprawls P The web-based edition of the physical principles of medical imaging Website: www.sprawls.org/ppmi2/XRAYHEAT/ Accessed on 24th Jan 2021.*
116. *Vogeler F, Verheecke W, Voet A, Kruth J-P and Dewulf W 2011 Positional stability of 2D X-ray images for computed tomography Proc. of International Symposium on Digital Industrial Radiology and Computed Tomography (Berlin, Germany).*
117. *Steffen J P and Froba T 2011 Reducing the focal spot shift of microfocus X-ray tubes to increase the accuracy of CT-based dimensional measurement Proc. of International Symposium on Digital Industrial Radiology and Computed Tomography (Berlin, Germany).*
118. *Sijbers J and Postnov A 2004 Reduction of ring artefacts in high resolution micro-CT reconstructions Phys. Med. Biol. 49 247-53.*
119. *Bock R, Hoppe S, Scherl H and Hornegger J 2007 Beam hardening correction with an iterative scheme using an exact backward projector and a polychromatic forward projector Proc. of Bildverarbeitung für die Medizin (Munich, Germany: Springer) pp46-50.*
120. *(4) (PDF) An overview of industrial X-ray computed tomography. Available from: https://www.researchgate.net/publication/323547274_An_overview_of_industrial_X-ray_computed_tomography [accessed Jan 28 2021].*
121. *J. Hsieh. Computed tomography: principles, design, artifacts, and recent advances. 1st edition. SPIE Press, Bellingham, 2003.*
122. *T.M. Buzug. Computed tomography: from photon statistics to modern conebeam CT. 1st edition. Springer, Berlin, 2008.*
123. *P. Hammersberg and M. Mangard. Correction for beam hardening artefacts in computerised tomography. J. X-Ray Sci. Technol. 8 (1998), 75–93.*
124. *J. Hsieh, R.C. Molthen, C.A. Dawson, and R.H. Johnson. An iterative approach to the beam hardening correction in cone beam CT. Med. Phys. 27 (2000), 23–29.*
125. *Alvarez R E and Macovski A 1976 Energy-selective reconstruction in X-ray computerized tomography Phys. Med. Biol. 21 733-44.*
126. *H. Yan, X. Mou, S. Tang, Q. Xu, and M. Zankl. Projection correlation based view interpolation for cone beam CT: primary fluence restoration in scatter measurement with a moving beam stop array. Phys. Med. Biol. 55 (2010), 6353–6375.*
127. *Peterzol, J.M. Létang, and D. Babot. A beam stop based correction procedure for high spatial frequency scatter in industrial cone-beam X-ray CT. Nucl. Instr. Meth. B 266 (2008), 4042–4054.*
128. *ISO 9000:2005 Quality management systems — Fundamentals and vocabulary, International Organization for Standardization.*
129. *LaMarr B, Bautz M, Kissel S, Prigozhin G, Hayashida K, Tsuru T and Matsumoto H 2004 Ground calibration of X-ray CCD detectors with charge injection for the X-ray imaging spectrometer on Astro-E2 Proc. of SPIE Vol15501 pp385-91.*
130. *CBCT electron density and image quality phantom (Computer Imaging Reference Systems, Inc) Website: www.imagingequipment.co.uk/downloadfile/742 Accessed on 3rd August 2011.*
131. *JCGM 200:2008 International vocabulary of metrology - basic and general concepts and associated terms, International Organization for Standardization.*
132. *Hull, C. W. (1993). U.S. Patent No. 5,236,637. Washington, DC: U.S. Patent and Trademark Office.*
133. *Gibson, I., Rosen, D., Stucker, B., & Khorasani, M. (2021). Design for additive manufacturing. In Additive manufacturing technologies (pp. 555-607). Springer, Cham.*
134. *Thompson, M. K., Moroni, G., Vaneker, T., Fadel, G., Campbell, R. I., Gibson, I., ... & Martina, F. (2016). Design for Additive Manufacturing: Trends, opportunities, considerations, and constraints. CIRP annals, 65(2), 737-760.*
135. *Susman, G. I. (Ed.). (1992). Integrating design and manufacturing for competitive advantage. Oxford University Press.*
136. *CoreLink Surpasses 5,000 Implants With Proprietary 3D Printed Technology. https://orthospinenews.com/. (2021). Retrieved 2 February 2021, from https://orthospinenews.com/2020/01/16/corelink-surpasses-5000-implants-with-proprietary-3d-printed-technology/.*
137. *White, M. (2021). 3D printed bone implants could revolutionise medical industry. https://www.themanufacturer.com/. Retrieved 3 February 2021, from*

https://www.themanufacturer.com/articles/3d-printed-bone-implants-could-revolutionise-medical-industry/.

138. *Everett, H., & Magrone, I. (2021). LimaCorporate breaks ground for first on-site hospital 3D printing facility - 3D Printing Industry. 3D Printing Industry. Retrieved 2 February 2021, from https://3dprintingindustry.com/news/limacorporate-breaks-ground-for-first-on-site-hospital-3d-printing-facility-157524/.*
139. *Industrial Applications of 3D Printing: The Ultimate Guide - AMFG. AMFG. (2021). Retrieved 3 February 2021, from https://amfg.ai/industrial-applications-of-3d-printing-the-ultimate-guide/.*
140. *Sedlak, J., Zemčík, O., Slaný, M., Chladil, J., Kouřil, K., Sekerka, V., & Rozkošný, L. (2015). Production of Prototype Parts Using Direct Metal Laser Sintering Technology. Acta Polytechnica, 55(4), 260-266.*
141. *Carey, B. (2021). Solid Concepts 3-D Printed Components Take Flight. Retrieved 3 February 2021, from https://www.ainonline.com/aviation-news/aerospace/2013-10-20/solid-concepts-3-d-printed-components-take-flight.*
142. *Mueller, B. (2012). Additive manufacturing technologies–Rapid prototyping to direct digital manufacturing. Assembly Automation.*
143. *Pour, M. A., & Zanoni, S. (2017). Impact of merging components by additive manufacturing in spare parts management. Procedia Manufacturing, 11, 610-618.*
144. *Gaining A Competitive Edge With Additive Manufacturing - Asia Pacific Metalworking Equipment News | Manufacturing | Automation | Quality Control. Asia Pacific Metalworking Equipment News | Manufacturing | Automation | Quality Control. (2021). Retrieved 4 February 2021, from https://www.equipment-news.com/gaining-competitive-edge-additive-manufacturing/.*
145. *O'Kane, T. (2021). Here's how 3D printing is changing the automotive industry. WhichCar. Retrieved 4 February 2021, from https://www.whichcar.com.au/car-style/3d-printing-and-the-automotive-industry.*
146. *O'Connor, D. (2021). The Ultimate Printing Machine - How BMW is applying 3D printing to commercial vehicles. TCT Magazine. Retrieved 5 February 2021, from https://www.tctmagazine.com/additive-manufacturing-3d-printing-news/the-ultimate-3d-printing-machine-bmw/.*
147. *Fickerl, A. (2021). 3D printing in the BMW Individual M850i NIGHT SKY. Bmw-m.com. Retrieved 5 February 2021, from https://www.bmw-m.com/en/topics/magazine-article-pool/3d-printing-in-the-bmw-individual-m850i-night-sky.html.*
148. *Watkin, H. (2021). Michelin and GM Unveil 3D Printed Puncture Proof Tire Prototype Called Uptis | All3DP. All3dp.com. Retrieved 5 February 2021, from https://all3dp.com/4/michelin-and-gm-unveil-3d-printed-puncture-proof-tire-prototype-called-uptis/.*
149. *Markstedt K, Mantas A, Tournier I, Martínez Ávila H, Hägg D, Gatenholm P. 3D Bioprinting Human Chondrocytes with Nanocellulose-Alginate Bioink for Cartilage Tissue Engineering Applications. Biomacromolecules. 2015 May 11;16(5):1489-96. doi: 10.1021/acs.biomac.5b00188.*
150. *ASTM F2792-12a, Standard Terminology for Additive Manufacturing Technologies, (Withdrawn 2015), ASTM International, West Conshohocken, PA, 2012, www.astm.org.*
151. *J. Anderson, J. Wealleans, J. Ray, Endodontic applications of 3D printing, Int. Endod. J. 51 (9) (2018) 1005–1018.*
152. *L. Rony, R. Lancigu , L. Hubert. Intraosseous metal implants in orthopedics: A review Morphologie. 2018(102), 339,231-242 doi.org/10.1016/j.morpho.2018.09.003.*
153. *Paulo G. Coelho, Ryo Jimbo. Osseointegration of metallic devices: Current trends based on implant hardware design Archives of Biochemistry and Biophysics. 2014(561) 99-108. doi.org/10.1016/j.abb.2014.06.033*
154. *F. Asa'ad, G. Pagni, S.P. Pilipchuk, A.B. Giannì, W.V. Giannobile, G. Rasperini, 3D-printed scaffolds and biomaterials: review of alveolar bone augmentation and periodontal regeneration applications, Int. J. Dent 2016 (2016).*
155. *R. Van Noort, The future of dental devices is digital, Dent. Mater. 28 (1) (2012)\ 3–12.*
156. *S.B. Patzelt, S. Vonau, S. Stampf, W. Att, Assessing the feasibility and accuracy of digitizing edentulous jaws, J. Am. Dent. Assoc. 144 (8) (2013) 914–920.*
157. *Li J, Yin X, Huang L, Mouraret S, Brunski JB, Cordova L, Salmon B, Helms JA. Relationships among Bone Quality, Implant Osseointegration, and Wnt Signaling. J Dent Res. 2017 Jul;96(7):822-831. doi: 10.1177/0022034517700131.*
158. *Johnson TB, Siderits B, Nye S, Jeong YH, Han SH, Rhyu IC, Han JS, Deguchi T, Beck FM, Kim DG. Effect of guided bone regeneration on bone quality surrounding dental implants. J Biomech. 2018 Oct 26;80:166-170. doi: 10.1016/j.jbiomech.2018.08.011.*

159. *H.J. Nickenig, M. Wichmann, J. Hamel, K.A. Schlegel, S. Eitner, Evaluation of the difference in accuracy between implant placement by virtual planning data and surgical guide templates versus the conventional free-hand method–a combined in vivo–in vitro technique using cone-beam CT (Part II), J. Cranio- Maxillofac. Surg. 38 (7) (2010) 488–493.*
160. *Vayre B, Vignat F, Villeneuve F. Metallic additive manufacturing: state-of-the-art review and prospects. Mech Ind 2012;13:89–96.*
161. *Pugliese L, Marconi S, Negrello E, Mauri V, Peri A, Gallo V, Auricchio F, Pietrabissa A. The clinical use of 3D printing in surgery. Updates Surg. 2018 Sep;70(3):381-388. doi: 10.1007/s13304-018-0586-5. Epub 2018 Aug 30.*
162. *Mandrycky C, Wang Z, Kim K, Kim DH. 3D bioprinting for engineering complex tissues. Biotechnol Adv. 2016 Jul-Aug;34(4):422-434. doi: 10.1016/j.biotechadv.2015.12.011.*
163. *Markstedt K, Mantas A, Tournier I, Martínez Ávila H, Hägg D, Gatenholm P. 3D Bioprinting Human Chondrocytes with Nanocellulose-Alginate Bioink for Cartilage Tissue Engineering Applications. Biomacromolecules. 2015 May 11;16(5):1489-96. doi: 10.1021/acs.biomac.5b00188.*
164. *T.D. Ngo, A. Kashani, G. Imbalzano, K.T.Q. Nguyen, D. Hui, Additive manufacturing (3D printing): a review of materials, methods, applications and challenges, Compos. Part B Eng. 143 (2018) 172–196, https://doi.org/10.1016/j.compositesb. 2018.02.012.*
165. *Ma Y, Xie L, Yang B, Tian W. Three-dimensional printing biotechnology for the regeneration of the tooth and tooth-supporting tissues. Biotechnol Bioeng. 2019 Feb;116(2):452-468. doi: 10.1002/bit.26882. Epub 2018 Dec 14.*
166. *Vyas, G. Poologasundarampillai, J. Hoyland, P. Bartolo, 12 - 3D printing of biocomposites for osteochondral tissue engineering, Editor(s): Luigi Ambrosio, In Woodhead Publishing Series in Biomaterials, Biomedical Composites (Second Edition), Woodhead Publishing, 2017, Pages 261-302, ISBN 9780081007525,https://doi.org/10.1016/B978-0-08-100752-5.00013-5.*
167. *Ana Rita C. Santos, Henrique A. Almeida & Paulo J. Bártolo (2013) Additive manufacturing techniques for scaffold-based cartilage tissue engineering, Virtual and Physical Prototyping, 8:3, 175-186, DOI: 10.1080/17452759.2013.838825*
168. *Castells, R. (2021). DMLS vs SLM 3D Printing for Metal Manufacturing. Element. Retrieved 8 February 2021, from https://www.element.com/nucleus/2016/06/29/dmls-vs-slm-3d-printing-for-metal-manufacturing.*
169. *Sing, S. L., An, J., Yeong, W. Y., & Wiria, F. E. (2016). Laser and electron-beam powder-bed additive manufacturing of metallic implants: A review on processes, materials and designs. Journal of Orthopaedic Research, 34(3), 369-385.*
170. *Buchbinder, H. Schleifenbaum, S. Heidrich, W. Meiners, J. Bültmann,High Power Selective Laser Melting (HP SLM) of Aluminum Parts, Physics Procedia, Volume 12, Part A, 2011, Pages 271-278, ISSN 1875-3892, https://doi.org/10.1016/j.phpro.2011.03.035.*
171. *Anilli, M., Demir, A.G. and Previtali, B. (2018), "Additive manufacturing of laser cutting nozzles by SLM: processing, finishing and functional characterization", Rapid Prototyping Journal, Vol. 24 No. 3, pp. 562-583. https://doi.org/10.1108/RPJ-05-2017-0106.*
172. *Zhang, L. C., Klemm, D., Eckert, J., Hao, Y. L., & Sercombe, T. B. (2011). Manufacture by selective laser melting and mechanical behavior of a biomedical Ti–24Nb–4Zr–8Sn alloy. Scripta Materialia, 65(1), 21-24.*
173. *Clijsters, S., Craeghs, T., Buls, S., Kempen, K., & Kruth, J. P. (2014). In situ quality control of the selective laser melting process using a high-speed, real-time melt pool monitoring system. The International Journal of Advanced Manufacturing Technology, 75(5-8), 1089-1101.*
174. *Mercelis, P., & Kruth, J. P. (2006). Residual stresses in selective laser sintering and selective laser melting. Rapid prototyping journal.*
175. *Rombouts, M., Kruth, J. P., Froyen, L., & Mercelis, P. (2006). Fundamentals of selective laser melting of alloyed steel powders. CIRP annals, 55(1), 187-192.*
176. *Olakanmi, E. O., Cochrane, R. F., & Dalgarno, K. W. (2015). A review on selective laser sintering/melting (SLS/SLM) of aluminium alloy powders: Processing, microstructure, and properties. Progress in Materials Science, 74, 401-477.*
177. *Craeghs, T., Clijsters, S., Yasa, E., & Kruth, J. P. (2011). Online quality control of selective laser melting. In Proceedings of the 20th Solid Freeform Fabrication (SFF) symposium, Austin (Texas), 8-10 august (pp. 212-226).*
178. *Arun Ramanathan Balachandramurthi, Johan Moverare, Nikhil Dixit, Robert Pederson, Influence of defects and as-built surface roughness on fatigue properties of additively manufactured Alloy 718,*

Materials Science and Engineering: A, Volume 735, 2018, Pages 463-474, ISSN 0921-5093, https://doi.org/10.1016/j.msea.2018.08.072.

179. *Bi, G., Gasser, A., Wissenbach, K., Drenker, A., & Poprawe, R. (2006). Characterization of the process control for the direct laser metallic powder deposition. Surface and Coatings Technology, 201(6), 2676-2683.*
180. *What is Directed Energy Deposition additive manufacturing and how does it work?. Engineering Product Design. (2021). Retrieved 10 February 2021, from https://engineeringproductdesign.com/knowledge-base/direct-energy-deposition/.*
181. *Alexandrea, P. (2019). The Complete Guide to Binder Jetting in 3D printing - 3Dnatives. 3Dnatives. Retrieved 11 February 2021, from https://www.3dnatives.com/en/powder-binding100420174/.*
182. *Bournias Varotsis, A. (2021). Introduction to binder jetting 3D printing | 3D Hubs. 3D Hubs. Retrieved 11 February 2021, from https://www.3dhubs.com/knowledge-base/introduction-binder-jetting-3d-printing/.*
183. *HP Binding jet. Www8.hp.com. (2021). Retrieved 11 February 2021, from https://www8.hp.com/h20195/v2/GetPDF.aspx/4AA7-3333EEW.pdf.*
184. *Truong Do, Patrick Kwon, Chang Seop Shin,Process development toward full-density stainless steel parts with binder jetting printing, International Journal of Machine Tools and Manufacture, Volume 121, 2017, Pages 50-60, ISSN 0890-6955, https://doi.org/10.1016/j.ijmachtools.2017.04.006.*
185. *All You Need to Know About Metal Binder Jetting - AMFG. AMFG. (2021). Retrieved 11 February 2021, from https://amfg.ai/2019/07/03/metal-binder-jetting-all-you-need-to-know/.*
186. *Jinqiang Ning, Daniel E. Sievers, Hamid Garmestani, Steven Y. Liang, Analytical modeling of part porosity in metal additive manufacturing, International Journal of Mechanical Sciences, Volume 172, 2020, 105428, ISSN 0020-7403, https://doi.org/10.1016/j.ijmecsci.2020.105428.*
187. *Nesma T. Aboulkhair, Nicola M. Everitt, Ian Ashcroft, Chris Tuck, Reducing porosity in AlSi10Mg parts processed by selective laser melting, Additive Manufacturing, Volumes 1–4,2014, Pages 77-86, ISSN 2214-8604, https://doi.org/10.1016/j.addma.2014.08.001.*
188. *Alexander M. Rubenchik, Wayne E. King, Sheldon S. Wu, Scaling laws for the additive manufacturing, Journal of Materials Processing Technology, Volume 257, 2018, Pages 234-243, ISSN 0924-0136, https://doi.org/10.1016/j.jmatprotec.2018.02.034.*
189. *Joni Reijonen, Alejandro Revuelta, Tuomas Riipinen, Kimmo Ruusuvuori, Pasi Puukko, On the effect of shielding gas flow on porosity and melt pool geometry in laser powder bed fusion additive manufacturing, Additive Manufacturing,Volume 32, 2020, 101030, ISSN 2214-8604,https://doi.org/10.1016/j.addma.2019.101030.*
190. *Barua, S., Liou, F., Newkirk, J., & Sparks, T. (2014). Vision-based defect detection in laser metal deposition process. Rapid Prototyping Journal.*
191. *Carter, L. N., Attallah, M. M., & Reed, R. C. (2012). Laser powder bed fabrication of nickel-base superalloys: influence of parameters; characterisation, quantification and mitigation of cracking. Superalloys, 2012(6), 2826-2834.*
192. *Donachie, M. J., & Donachie, S. J. (2002). Superalloys: a technical guide. ASM international.*
193. *Lippold, J. C., Kiser, S. D., & DuPont, J. N. (2011). Welding metallurgy and weldability of nickel-base alloys. John Wiley & Sons.*
194. *Kou, S. (2003). Welding metallurgy. New Jersey, USA, 431-446.*
195. *Dye, D., Hunziker, O., & Reed, R. C. (2001). Numerical analysis of the weldability of superalloys. Acta Materialia, 49(4), 683-697.*
196. *Zhong, M., Sun, H., Liu, W., Zhu, X., & He, J. (2005). Boundary liquation and interface cracking characterization in laser deposition of Inconel 738 on directionally solidified Ni-based superalloy. Scripta materialia, 53(2), 159-164.*
197. *Sidhu, R. K., Ojo, O. A., & Chaturvedi, M. C. (2009). Microstructural response of directionally solidified René 80 superalloy to gas-tungsten arc welding. Metallurgical and Materials Transactions A, 40(1), 150-162.*
198. *Egbewande, A. T., Buckson, R. A., & Ojo, O. A. (2010). Analysis of laser beam weldability of Inconel 738 superalloy. Materials characterization, 61(5), 569-574.*
199. *Henderson, M. B., Arrell, D., Larsson, R., Heobel, M., & Marchant, G. (2004). Nickel based superalloy welding practices for industrial gas turbine applications. Science and technology of welding and joining, 9(1), 13-21.*

200. *Li, R., Liu, J., Shi, Y. et al. Balling behavior of stainless steel and nickel powder during selective laser melting process. Int J Adv Manuf Technol 59, 1025–1035 (2012). https://doi.org/10.1007/s00170-011-3566-1.*
201. *Sames, W. J., Medina, F., Peter, W. H., Babu, S. S., & Dehoff, R. R. (2014, November). Effect of process control and powder quality on Inconel 718 produced using electron beam melting. In 8th Int. Symp. Superalloy 718 Deriv (pp. 409-423).*
202. *Darvish, K., Chen, Z. W., & Pasang, T. (2016). Reducing lack of fusion during selective laser melting of CoCrMo alloy: Effect of laser power on geometrical features of tracks. Materials & Design, 112, 357-366.*
203. *Mukherjee, T., Zuback, J. S., De, A., & DebRoy, T. (2016). Printability of alloys for additive manufacturing. Scientific reports, 6(1), 1-8.*
204. *Bauereiß, A., Scharowsky, T., & Körner, C. (2014). Defect generation and propagation mechanism during additive manufacturing by selective beam melting. Journal of Materials Processing Technology, 214(11), 2522-2528.*
205. *Rai, R., Elmer, J. W., Palmer, T. A., & DebRoy, T. (2007). Heat transfer and fluid flow during keyhole mode laser welding of tantalum, Ti–6Al–4V, 304L stainless steel and vanadium. Journal of physics D: Applied physics, 40(18), 5753.*
206. *Madison, J. D., & Aagesen, L. K. (2012). Quantitative characterization of porosity in laser welds of stainless steel. Scripta Materialia, 67(9), 783-786.*
207. *King, W. E., Barth, H. D., Castillo, V. M., Gallegos, G. F., Gibbs, J. W., Hahn, D. E., ... & Rubenchik, A. M. (2014). Observation of keyhole-mode laser melting in laser powder-bed fusion additive manufacturing. Journal of Materials Processing Technology, 214(12), 2915-2925.*
208. *T. DebRoy, H.L. Wei, J.S. Zuback, T. Mukherjee, J.W. Elmer, J.O. Milewski, A.M. Beese, A. Wilson-Heid, A. De, W. Zhang, Additive manufacturing of metallic components – Process, structure and properties, Progress in Materials Science, Volume 92, 2018, Pages 112-224, ISSN 0079-6425, https://doi.org/10.1016/j.pmatsci.2017.10.001.*
209. *Cordova, L., Campos, M., & Tinga, T. (2019). Revealing the effects of powder reuse for selective laser melting by powder characterization. Jom, 71(3), 1062-1072.*
210. *Svensson, M., Ackelid, U., & Ab, A. (2010). Titanium alloys manufactured with electron beam melting mechanical and chemical properties. In Proceedings of the materials and processes for medical devices conference (pp. 189-194). ASM International.*
211. *Sola, A., & Nouri, A. (2019). Microstructural porosity in additive manufacturing: The formation and detection of pores in metal parts fabricated by powder bed fusion. Journal of Advanced Manufacturing and Processing, 1(3), e10021.*
212. *Iebba, M., Astarita, A., Mistretta, D., Colonna, I., Liberini, M., Scherillo, F., ... & Squillace, A. (2017). Influence of powder characteristics on formation of porosity in additive manufacturing of Ti-6Al-4V components. Journal of Materials Engineering and Performance, 26(8), 4138-4147.*
213. *Sames, W. (2015). Additive manufacturing of inconel 718 using electron beam melting: processing, post-processing, & mechanical properties (Doctoral dissertation).*
214. *Amir Mostafaei, Amy M. Elliott, John E. Barnes, Fangzhou Li, Wenda Tan, Corson L. Cramer, Peeyush Nandwana, Markus Chmielus, Binder jet 3D printing—Process parameters, materials, properties, modeling, and challenges,Progress in Materials Science,2020,100707,ISSN 0079-6425, https://doi.org/10.1016/j.pmatsci.2020.100707.*
215. *ASTM F3049-14, Standard Guide for Characterizing Properties of Metal Powders Used for Additive Manufacturing Processes, ASTM International, West Conshohocken, PA, 2014, www.astm.org.*
216. *Seki, Y., Okamoto, S., Takigawa, H., & Kawai, N. (1990). Effect of atomization variables on powder characteristics in the high-pressured water atomization process. Metal Powder Report, 45(1), 38-40.*
217. *Antony, L. V., & Reddy, R. G. (2003). Processes for production of high-purity metal powders. Jom, 55(3), 14-18.*
218. *Lagutkin, S., Achelis, L., Sheikhaliev, S., Uhlenwinkel, V., & Srivastava, V. (2004). Atomization process for metal powder. Materials Science and Engineering: A, 383(1), 1-6.*
219. *Heim, K., Bernier, F., Pelletier, R., & Lefebvre, L. P. (2016). High resolution pore size analysis in metallic powders by X-ray tomography. Case Studies in Nondestructive Testing and Evaluation, 6, 45-52.*
220. *Mikli, V., Kaerdi, H., Kulu, P., & Besterci, M. (2001). Characterization of powder particle morphology. Proceedings of the Estonian Academy of Sciences: Engineering (Estonia), 7(1), 22-3*
221. *Torralba, J. D., Da Costa, C. E., & Velasco, F. (2003). P/M aluminum matrix composites: an overview. Journal of Materials Processing Technology, 133(1-2), 203-206.*

222. *Yujie Cui, Yufan Zhao, Haruko Numata, Huakang Bian, Kimio Wako, Kenta Yamanaka, Kenta Aoyagi, Chen Zhang, Akihiko Chiba, Effects of plasma rotating electrode process parameters on the particle size distribution and microstructure of Ti-6Al-4 V alloy powder, Powder Technology, Volume 376, 2020, Pages 363-372, ISSN 0032-5910, https://doi.org/10.1016/j.powtec.2020.08.027.*
223. *Simpson, J., Haley, J., Cramer, C., Shafer, O., Elliott, A., Peter, W., ... & Dehoff, R. (2019). Considerations for application of additive manufacturing to nuclear reactor core components. ORNL/TM-2019-1190, Oak Ridge National Laboratory.*
224. *T. DebRoy, H.L. Wei, J.S. Zuback, T. Mukherjee, J.W. Elmer, J.O. Milewski, A.M. Beese, A. Wilson-Heid, A. De, W. Zhang, Additive manufacturing of metallic components – Process, structure and properties, Progress in Materials Science, Volume 92, 2018, Pages 112-224, ISSN 0079-6425, https://doi.org/10.1016/j.pmatsci.2017.10.001.*
225. *Simonelli, M., Tse, Y. Y., & Tuck, C. (2014). Effect of the build orientation on the mechanical properties and fracture modes of SLM Ti–6Al–4V. Materials Science and Engineering: A, 616, 1-11.*
226. *Lutter-Günther, M., Bröker, M., Mayer, T., Lizak, S., Seidel, C., & Reinhart, G. (2018). Spatter formation during laser beam melting of AlSi10Mg and effects on powder quality. Procedia Cirp, 74, 33-38.*
227. *Jamshidinia, M., & Kovacevic, R. (2015). The influence of heat accumulation on the surface roughness in powder-bed additive manufacturing. Surface Topography: Metrology and Properties, 3(1), 014003.*
228. *Ahmed, F., Ali, U., Sarker, D., Marzbanrad, E., Choi, K., Mahmoodkhani, Y., & Toyserkani, E. (2020). Study of powder recycling and its effect on printed parts during laser powder-bed fusion of 17-4 PH stainless steel. Journal of Materials Processing Technology, 278, 116522.*
229. *Sivasankaran, S., Sivaprasad, K., Narayanasamy, R., & Iyer, V. K. (2010). An investigation on flowability and compressibility of AA 6061100− xx wt.% TiO2 micro and nanocomposite powder prepared by blending and mechanical alloying. Powder technology, 201(1), 70-82.*
230. *Ali, U., Mahmoodkhani, Y., Shahabad, S. I., Esmaeilizadeh, R., Liravi, F., Sheydaeian, E., ... & Toyserkani, E. (2018). On the measurement of relative powder-bed compaction density in powder-bed additive manufacturing processes. Materials & Design, 155, 495-501.*
231. *Esmaeilizadeh, R., Ali, U., Keshavarzkermani, A., Mahmoodkhani, Y., Marzbanrad, E., & Toyserkani, E. (2019). On the effect of spatter particles distribution on the quality of Hastelloy X parts made by laser powder-bed fusion additive manufacturing. Journal of Manufacturing Processes, 37, 11-20.*
232. *Kennedy, S. K., Dalley, A. M., & Kotyk, G. J. (2019). Additive manufacturing: Assessing metal powder quality through characterizing feedstock and contaminants. Journal of materials engineering and performance, 28(2), 728-740.*
233. *Brandão, A. D., Gerard, R., Gumpinger, J., Beretta, S., Makaya, A., Pambaguian, L., & Ghidini, T. (2017). Challenges in additive manufacturing of space parts: powder feedstock cross-contamination and its impact on end products. Materials, 10(5), 522.*
234. *Gatto, A., Bassoli, E., & Denti, L. (2018). Repercussions of powder contamination on the fatigue life of additive manufactured maraging steel. Additive Manufacturing, 24, 13-19.*
235. *Santecchia, E., Mengucci, P., Gatto, A., Bassoli, E., Defanti, S., & Barucca, G. (2019). Cross-Contamination Quantification in Powders for Additive Manufacturing: A Study on Ti-6Al-4V and Maraging Steel. Materials, 12(15), 2342.*
236. *Sutton, A. T., Kriewall, C. S., Leu, M. C., & Newkirk, J. W. (2017). Powder characterisation techniques and effects of powder characteristics on part properties in powder-bed fusion processes. Virtual and physical prototyping, 12(1), 3-29.*
237. *Slotwinski, J. A., Garboczi, E. J., Stutzman, P. E., Ferraris, C. F., Watson, S. S., & Peltz, M. A. (2014). Characterization of metal powders used for additive manufacturing. Journal of research of the National Institute of Standards and Technology, 119, 460.*
238. *Strondl, A., Lyckfeldt, O., Brodin, H., & Ackelid, U. (2015). Characterization and control of powder properties for additive manufacturing. Jom, 67(3), 549-554.*
239. *Tofail, S. A., Koumoulos, E. P., Bandyopadhyay, A., Bose, S., O'Donoghue, L., & Charitidis, C. (2018). Additive manufacturing: scientific and technological challenges, market uptake and opportunities. Materials today, 21(1), 22-37.*
240. *Sutton, A. T., Kriewall, C. S., Leu, M. C., & Newkirk, J. W. (2016). Powders for additive manufacturing processes: Characterization techniques and effects on part properties. Solid Freeform Fabrication, 1, 1004-1030.*
241. *Neuschaefer-Rube, U., Neugebauer, M., Ehrig, W., Bartscher, M., & Hilpert, U. (2008). Tactile and optical microsensors: test procedures and standards. Measurement Science and Technology, 19(8), 084010.*

242. *Bartscher, M., Hilpert, U., Goebbels, J., & Weidemann, G. (2007). Enhancement and proof of accuracy of industrial computed tomography (CT) measurements. CIRP annals, 56(1), 495-498.*
243. *Bartscher, M., Neukamm, M., Koch, M., Neuschaefer-Rube, U., Staude, A., Goebbels, J., ... & Knoch, A. (2010). Performance assessment of geometry measurements with micro-CT using a dismountable work-piece-near reference standard. In 10th European Conference on Non-Destructive testing.*
244. *Carmignato, S., Pierobon, A., & Savio, E. (2011). CT audit interlaboratory comparison of CT systems for dimensional metrology. University of Padova, Project report.*
245. *Carmignato, S., Dreossi, D., Mancini, L., Marinello, F., Tromba, G., & Savio, E. (2009). Testing of x-ray microtomography systems using a traceable geometrical standard. Measurement Science and Technology, 20(8), 084021.*
246. *Schmitt, R., & Niggemann, C. (2010). Uncertainty in measurement for x-ray-computed tomography using calibrated work pieces. Measurement Science and Technology, 21(5), 054008.*
247. *Sun, W., Brown, S. B., & Leach, R. K. (2012). An overview of industrial X-ray computed tomography.*
248. *Nikishkov, Y., Airoldi, L., & Makeev, A. (2013). Measurement of voids in composites by X-ray Computed Tomography. Composites Science and Technology, 89, 89-97.*
249. *Hermanek, P., & Carmignato, S. (2016). Reference object for evaluating the accuracy of porosity measurements by X-ray computed tomography. Case studies in nondestructive testing and evaluation, 6, 122-127.*
250. *Krolczyk, G., Raos, P., & Legutko, S. (2014). Experimental analysis of surface roughness and surface texture of machined and fused deposition modelled parts. Tehnički vjesnik, 21(1), 217-221.*
251. *Triantaphyllou, C. L. Giusca, G. D. Macaulay, F. Roerig, M. Hoebel, R. K. Leach, et al., "Surface texture measurement for additive manufacturing," Surface Topography: Metrology and Properties, vol. 3, p. 024002, 2015.*
252. *Townsend, A., Senin, N., Blunt, L., Leach, R. K., & Taylor, J. S. (2016). Surface texture metrology for metal additive manufacturing: a review. Precision Engineering, 46, 34-47.*
253. *Alicona. (2021). InfiniteFocus. Available: http://www.alicona.com/products/infinitefocus/*
254. *Reese, Z., Fox, J., Taylor, J., & Evans, C. (2019). Evolution of Cooling Length in Parts Created Through Laser Powder Bed Fusion Additive Manufacturing. Retrieved 9 December 2019, from https://www.nist.gov/publications/evolution-cooling-length-parts-created-through-laser-powder-bed-fusion-additive*
255. *Roberts, I. (2019). Investigation of residual stresses in the laser melting of metal powders in additive layer manufacturing. (Doctoral Thesis) Indiana University of Pennsylvania, University of Wolverhampton, Wolverhampton Retrieved 9 December 2019, from https://wlv.openrepository.com/handle/2436/254913.*
256. *Xiao Ding, Yuichiro Koizumi, Daixiu Wei, Akihiko Chiba,Effect of process parameters on melt pool geometry and microstructure development for electron beam melting of IN718: A systematic single bead analysis study, Additive Manufacturing, Volume 26, 2019, Pages 215-226, ISSN 2214-8604, https://doi.org/10.1016/j.addma.2018.12.018.*
257. *Abolhasani, D., Seyedkashi, S. M., Kang, N., Kim, Y. J., Woo, Y. Y., & Moon, Y. H. (2019). Analysis of melt-pool behaviors during selective laser melting of AISI 304 stainless-steel composites. Metals, 9(8), 876.*
258. *Withers, P. J., Bouman, C., Carmignato, S., Cnudde, V., Grimaldi, D., Hagen, C. K., ... & Stock, S. R. (2021). X-ray computed tomography. Nature Reviews Methods Primers, 1(1), 1-21.*
259. *Tawfik, A., Bills, P., Blunt, L., & Racasan, R. (2020). Development of an additive manufactured artifact to characterize unfused powder using computed tomography. International Journal of Automation Technology, 14(3), 439-446.*
260. *J. Yag¨ue-Fabra, S. Ontiveros, R. Jim´enez, S. Chitchian, G. Tosello, and S. Carmignato, "A 3D edge detection technique for surface extraction in computed tomography for dimensional metrology applications,"CIRP Annals, Vol.62, Issue 1, pp. 531-534, 2013.*
261. *F. B. de Oliveira, A. Stolfi, M. Bartscher, L. De Chiffre, and U. Neuschaefer-Rube, "Experimental investigation of surface determination process on multi-material components for dimensional computed tomography," Case Studies in Nondestructive Testing and Evaluation, Vol.6, Part B, pp. 93-103, 2016.*
262. *Chesler DA, Riederer SJ, Pelc NJ. Noise due to photon counting statistics in computed X-ray tomography. J Comput Assist Tomogr. 1977 Jan;1(1) 64-74. PMID: 615896.*

263. *Mittal, B., Rana, N., Rawat, D., Parmar, M., Dhawan, D. and Bhati, A. (2015). Evaluation of external beam hardening filters on image quality of computed tomography and single photon emission computed tomography/computed tomography. Journal of Medical Physics, 40(4), p.198.*
264. *Radiologymasterclass.co.uk. (2018). Basics of X-ray Physics - X-ray production. [online] Available at: https://www.radiologymasterclass.co.uk/tutorials/physics/x-ray_physics_production [Accessed 16 Oct. 2018].*
265. *Orau.org. (2018). Coolidge X-ray Tubes - General Information. [online] Available at: https://www.orau.org/ptp/collection/xraytubescoolidge/coolidgeinformation.html [Accessed 2 Nov. 2018].*
266. *Radiology Mnemonics,Editor(s): Dennis M. Marchiori,Clinical Imaging (Third Edition),Mosby,2014,Pages IBC1-IBC3,ISBN 9780323084956.*
267. *Lifton, J. J. and S. Carmignato (2017). "Simulating the influence of scatter and beam hardening in dimensional computed tomography." Measurement Science and Technology 28(10): 104001.*
268. *K. Schörner, M. Goldammer, and J. Stephan, Scatter Correction by Modulation of Primary Radiation in Industrial X-ray CT: Beam-hardening Effects and their Correction, in Proceedings 'International Symposium on Digital Industrial Radiology and Computed Tomography 2011', Berlin, Germany (2011).*
269. *Hubbell, J. H., & Seltzer, S. M. (2004). X-ray mass attenuation coefficients. NIST Standard Reference Database, 126, 20899.*
270. *TOLLEY, G. and YUE, S., 2021. BEAM HARDENING – WHAT IS IT AND HOW TO REDUCE IT | North Star Imaging. [online] 4nsi.com. Available at: <https://4nsi.com/blog/2016/02/12/beam-hardening/> [Accessed 25 April 2021].*
271. *Salzali Mohd, Jaafar Abdullah, & Mohamad Rabaie Shari (2011). Comparison Types of Filter Used in Viewing Inner Structure of Materials Using X-Ray Computed Tomography. NTC 2011: Nuclear Technical Convention 2011, Malaysia*
272. *Nivedita Rana (2015). Evaluation of external beam hardening filters on image quality of computed tomography and single photon emission computed tomography/computed tomography. Journal of Medical Physics, 40(4), p.198.*
273. *Kueh, A., Warnett, J. M., Gibbons, G. J., Brettschneider, J., Nichols, T. E., Williams, M. A., & Kendall, W. S. (2016). Modelling the penumbra in Computed Tomography1. Journal of X-ray science and technology, 24(4), 583–597.*
274. *N. Kourra, J. A. Warnett, A. Attridge and M. A. Williams, "Metrological investigation of radiation filtration in x-ray computed tomography," 2017 IEEE International Instrumentation and Measurement Technology Conference (I2MTC), Turin, 2017, pp. 1-6.*
275. *Etter, B. (2019). Measurement Science & Standards in Forensic Firearms Analysis. Retrieved from https://www.nist.gov/sites/default/files/documents/oles/Etter-Brad-Presentation.pdf.*
276. *Alicona G4 InfiniteFocus | Engineering | University of Southampton. (2019). Retrieved from https://www.southampton.ac.uk/engineering/research/facilities/360/nCATS_facility/alicona.page#technical_specifications*
277. *M. Reiter, D. Weiss, C. Gusenbauer, J. Kastner, M. Erler, S. Kasperl - Evaluation of a histogram-based image quality measure for X-ray computed tomography - Proceedings of Conference on Industrial Computed Tomography (iCT2014), Wels, Austria, 2014.*
278. *TOLLEY, G. (2018). BEAM HARDENING – WHAT IS IT AND HOW TO REDUCE IT | North Star Imaging. [online] 4nsi.com. Available at: https://4nsi.com/blog/2016/02/12/beam-hardening/ [Accessed 16 Nov. 2020].*
279. *Catheryn M. Yashar,Chapter 23 - Basic Principles in Gynecologic Radiotherapy,Editor(s): Philip J. Di Saia, William T. Creasman,Clinical Gynecologic Oncology (Eighth Edition),Mosby,2012,Pages 659-680.e3,ISBN 9780323074193.*
280. *J. Daniel Bourland,Chapter 6 - Radiation Oncology Physics, Editor(s): Leonard L. Sourcederson, Joel E. Tepper, Clinical Radiation Oncology (Third Edition),W.B. Saunders, 2012,Pages 95-152,ISBN 9781437716375,https://doi.org/10.1016/B978-1-4377-1637-5.00006-7.*
281. *James A. Patton and Timothy G. Turkington, SPECT/CT Physical Principles and Attenuation Correction, J. Nucl. Med. Technol. March 2008 36:1-10 published ahead of print February 20, 2008 (10.2967/jnmt.107.046839).*
282. *Cooper, M., Mijnarends, P. and Shiotani, N. (2004). X-Ray Compton Scattering. Chapter 1 ISBN-13: 9780198501688.*

283. *de Oliveira, F. B., Stolfi, A., Bartscher, M., De Chiffre, L., & Neuschaefer-Rube, U. (2016). Experimental investigation of surface determination process on multi-material components for dimensional computed tomography. Case studies in nondestructive testing and evaluation, 6, 93-103.*
284. *Yagüe-Fabra, J., Ontiveros, S., Jiménez, R., Chitchian, S., Tosello, G. and Carmignato, S. (2013). A 3D edge detection technique for surface extraction in computed tomography for dimensional metrology applications. CIRP Annals.*
285. *Kowaluk, T., & Wozniak, A. (2017). A new threshold selection method for X-ray computed tomography for dimensional metrology. Precision Engineering, 50, 449-454.*
286. *Kruth, J. P., Bartscher, M., Carmignato, S., Schmitt, R., De Chiffre, L., & Weckenmann, A. (2011). Computed tomography for dimensional metrology. CIRP annals, 60(2), 821-842.*
287. *Townsend, A., Pagani, L., Blunt, L., Scott, P. J., & Jiang, X. (2017). Factors affecting the accuracy of areal surface texture data extraction from X-ray CT. CIRP Annals, 66(1), 547-550.*
288. *Volume Graphics GmbH, VGStudio MAX.*
289. *N. Otsu, A Threshold Selection Method from Gray-level Histograms, Automatica, 11 (285–296) (1975), pp. 23-27.*
290. *T.S. Yoo, M.J. Ackerman, W.E. Lorensen, W. Schroeder, V. Chalana, S. Aylward, D. Metaxas, R. Whitaker, Engineering and Algorithm Design for an Image Processing API: A Technical Report on Itk-the Insight Toolkit, Studies in Health Technology and Informatics (2002), pp. 586-592.*
291. *Affenzeller, C., Gusenbauer, C., Reiter, M., & Kastner, J. (2015). Measurement uncertainty evaluation of an X-ray computed tomography system. Digital Industrial Radiology and Computed Tomography.*
292. *Sánchez, Á. R., Thompson, A., Körner, L., Brierley, N., & Leach, R. (2020). Review of the influence of noise in X-ray computed tomography measurement uncertainty. Precision Engineering.*
293. *Gao, F., Leach, R. K., Petzing, J., & Coupland, J. M. (2007). Surface measurement errors using commercial scanning white light interferometers. Measurement Science and Technology, 19(1), 015303.*
294. *Newton, L., Senin, N., Gomez, C., Danzl, R., Helmli, F., Blunt, L., & Leach, R. (2019). Areal topography measurement of metal additive surfaces using focus variation microscopy. Additive Manufacturing, 25, 365-389.*
295. *Newton, L., Senin, N., Chatzivagiannis, E., Smith, B., & Leach, R. (2020). Feature-based characterisation of Ti6Al4V electron beam powder bed fusion surfaces fabricated at different surface orientations. Additive Manufacturing, 35, 101273.*
296. *J.P. Kruth, M. Bartscher, S. Carmignato, R. Schmitt, L. De Chiffre, A. Weckenmann, Computed tomography for dimensional metrology, CIRP Annals, Volume 60, Issue 2, 2011, Pages 821-842, ISSN 0007-8506, https://doi.org/10.1016/j.cirp.2011.05.006.*
297. *Slocombe, J., Townsend, A., Addinall, K., & Blunt, L. (2019). The effects of x-ray computed tomography filament degradation on extracted areal surface texture data. In R. K. Leach, D. Billington, C. Nisbet, & D. Phillips (Eds.), European Society for Precision Engineering and Nanotechnology, Conference Proceedings - 19th International Conference and Exhibition, EUSPEN 2019 (pp. 346-349). euspen.*
298. *O. Riemer, E. Savio, D. Billington, R. K. Leach, & D. Phillips (Eds.), Proceedings of the 18th International Conference of the European Society for Precision Engineering and Nanotechnology (EUSPEN): June 4th-8th 2018, Venice, IT (pp. 97-98). euspen. https://www.euspen.eu/knowledge-base/ICE18289.pdf*
299. *Vock, S., Klöden, B., Kirchner, A. et al. Powders for powder bed fusion: a review. Prog Addit Manuf 4, 383–397 (2019). https://doi.org/10.1007/s40964-019-00078-6.*
300. *Scarfe WC, e. (2019). Clinical applications of cone-beam computed tomography in dental practice. - PubMed - NCBI. [online] Ncbi.nlm.nih.gov. Available at: https://www.ncbi.nlm.nih.gov/pubmed/16480609 [Accessed 10 Dec. 2020].*
301. *Johann Kastner, Bernhard Harrer, Guillermo Requena, Oliver Brunke, A comparative study of high resolution cone beam X-ray tomography and synchrotron tomography applied to Fe- and Al-alloys, NDT & E International, Volume 43, Issue 7, 2010,Pages 599-605.*
302. *Brunke, K Brockdorf, S Drews, B Müller, T Donath, J Herzen, et al. Comparison between X-ray tube based and synchrotron radiation based µCT, Development in X-ray tomography VI,S.R. Stock (Ed.), Proceedings of SPIE, 7078 (2008), pp. 1-12.*
303. *A.B. Spiering, N. Herres , G. Levy "Influence of the Particle Size Distribution on Surface Quality and Mechanical Properties in AM Steel Parts." Rapid Prototyping Journal., MCB University Press, ISSN: 1355-2546, doi:10.1108/13552541111124770.*

304. *Ahmad Bin Anwar, Quang-Cuong Pham, Study of the spatter distribution on the powder bed during selective laser melting, Additive Manufacturing, Volume 22,2018,Pages 86-97,ISSN 2214-8604,https://doi.org/10.1016/j.addma.2018.04.036.*
305. *Strondl, A., Lyckfeldt, O., Brodin, H., Ackelid, U. "Characterization and Control of Powder Properties for Additive Manufacturing." JOM 67(3): 549-554. ISSN: 1543-1851, DOI: 10.1007/s11837-015-1304-0.*
306. *Vladimir V. Popov, Alexander Katz-Demyanetz, Andrey Garkun, Menachem Bamberger, The effect of powder recycling on the mechanical properties and microstructure of electron beam melted Ti-6Al-4 V specimens, Additive Manufacturing, Volume 22, 2018, Pages 834-843,ISSN 2214-8604,https://doi.org/10.1016/j.addma.2018.06.003.*
307. *Takeyuki Abe, Hiroyuki Sasahara, Dissimilar metal deposition with a stainless steel and nickel-based alloy using wire and arc-based additive manufacturing, Precision Engineering, Volume 45, 2016, Pages 387-395, ISSN 0141-6359.*
308. *R.J. Friel, R.A. Harris, Ultrasonic Additive Manufacturing – A Hybrid Production Process for Novel Functional Products, Procedia CIRP, Volume 6, 2013, Pages 35-40, ISSN 2212-8271.*
309. *Alejandro Hinojos, Jorge Mireles, Ashley Reichardt, Pedro Frigola, Peter Hosemann, Lawrence E. Murr, Ryan B. Wicker, Joining of Inconel 718 and 316 Stainless Steel using electron beam melting additive manufacturing technology, Materials & Design, Volume.*
310. *Esmaeilizadeh, R., Ali, U., Keshavarzkermani, A., Mahmoodkhani, Y., Marzbanrad, E., & Toyserkani, E. (2019). On the effect of spatter particles distribution on the quality of Hastelloy X parts made by laser powder-bed fusion additive manufacturing. Journal of Manufacturing Processes, 37, 11-20.*
311. *Ahmed, F., Ali, U., Sarker, D., Marzbanrad, E., Choi, K., Mahmoodkhani, Y., & Toyserkani, E. (2020). Study of powder recycling and its effect on printed parts during laser powder-bed fusion of 17-4 PH stainless steel. Journal of Materials Processing Technology, 278, 116522.*
312. *Ali, U., Mahmoodkhani, Y., Shahabad, S. I., Esmaeilizadeh, R., Liravi, F., Sheydaeian, E. & Toyserkani, E. (2018). On the measurement of relative powder-bed compaction density in powder-bed additive manufacturing processes. Materials & Design, 155, 495-501.*

Appendices

XCT Specification

SPECIFICATIONS

Microfocus source	Max. kV	Max. power	Focal spot size		XT H 160	XT H 225	XT H 225 ST	XT H 320	XT H 450	Custom cabinet
160 kV Xi, Reflection target	160 kV	60 W	3 µm up to 7 W	60 µm at 60 W	●					○
160 kV Reflection target	160 kV	225 W	3 µm up to 7 W	225 µm at 225 W	○					○
180 kV Transmission target	180 kV	20 W	1 µm up to 3 W	10 µm at 10 W		○	○			○
225 kV Reflection target	225 kV	225 W	3 µm up to 7 W	225 µm at 225 W		●	●	○		○
225 kV Rotating target option	225 kV	450 W	10 µm up to 30 W	113 µm at 450 W			○	○		○
320 kV Reflection target	320 kV	320 W	30 µm up to 30 W	300 µm at 320 W				●		○
450 kV Reflection target	450 kV	450 W	80 µm up to 200 W	320 µm at 450 W					●	○
450 kV High brilliance source	450 kV	450 W	80 µm up to 200 W	113 µm at 450 W					○	○
750 kV with integrated generator	750 kV	750 W	30 µm up to 70 W	190 µm at 750 W						○

Detectors	# Bits	Active pixels	Pixel Size	Max. frame rate at 1x1 binning	Max. frame rate at 2x2 binning					
Varian 1313	14-bit	1000 x 1000	127 µm	10 fps	30 fps	○					○
Varian 2520	14-bit	1900 x 1516	127 µm	7.5 fps	15 fps	○	○	○	○ (1)		○
Varian 4030	14-bit	2300 x 3200	127 µm	3 fps	7 fps		○	○			○
Perkin Elmer 0820	16-bit	1000 x 1000	200 µm	7.5 fps	15 fps	○	○	○	○		○
Perkin Elmer 1620	16-bit	2000 x 2000	200 µm	3.75 fps	7.5 fps			○	○	○	○
Perkin Elmer 1621 EHS	16-bit	2000 x 2000	200 µm	15 fps	30 fps			○	○	○	○
Nikon Metrology CLDA	16-bit	2000	415 µm	50 fps						○	○
Combination PE162x & CLDA	Configuration with both Flat panel and Curved Linear Diode Array detector									○	○

(1) only with 225 kV source ● Basic configuration ○ Alternative configuration

	XT H 160	XT H 225	XT H 225 ST	XT H 320	XT H 450
Manipulator					
# Axes	5	5	5	4 (optional 5th axis)	4 (optional 5th axis)
Axes travel	(X) 185 mm (Y) 250 mm (Z) 700 mm (Tilt) +/- 30° (Rotate) n*360°	(X) 185 mm (Y) 250 mm (Z) 700 mm (Tilt) +/- 30° (Rotate) n*360°	(X) 450 mm (Y) 350 mm (Z) 750 mm (Tilt) +/- 30 (Rotate) n*360°	(X) 510 mm (Y) 610 mm (Z) 800 mm (Rotate) n*360°	(X) 400 mm (Y) 600 mm (Z) 600 mm (Rotate) n*360°
Max. sample weight	15 kg	15 kg	50 kg	100 kg	100 kg
General specifications					
Cabinet dimensions (LxWxH)	1,830 mm x 875 mm x 1,987 mm	1,830 mm x 875 mm x 1,987 mm	2,414 mm x 1,275 mm x 2,202 mm	2,695 mm x 1,828 mm x 2,249 mm	3,613 mm x 1,828 mm x 2,249 mm
Weight	2,400 kg	2,400 kg	4,200 kg	8,000 kg	14,000 kg
Safety	All systems are manufactured to IRR99				
Control software	All systems are controlled by Nikon Metrology's in-house Inspect-X software				

NIKON METROLOGY NV
Geldenaaksebaan 329
B-3001 Leuven, Belgium
phone: +32 16 74 01 00 fax: +32 16 74 01 03
Sales.NM@nikon.com

NIKON CORPORATION
Shinagawa Intercity Tower C, 2-15-3, Konan,
Minato-ku, Tokyo 108-6290 Japan
phone: +81-3-6433-3701 fax: +81-3-6433-3784
www.nikon-instruments.jp/eng/

NIKON METROLOGY EUROPE NV
tel. +32 16 74 01 01
Sales.Europe.NM@nikon.com

NIKON METROLOGY GMBH
tel. +49 6023 91733-0
Sales.Germany.NM@nikon.com

NIKON METROLOGY SARL
tel. +33 1 60 86 09 76
Sales.France.NM@nikon.com

NIKON METROLOGY, INC.
tel. +1 810 2204360
Sales.US.NM@nikon.com

NIKON METROLOGY UK LTD.
tel. +44 1332 811349
Sales.UK.NM@nikon.com

NIKON INSTRUMENTS (SHANGHAI) CO. LTD.
tel. +86 21 5836 0050
tel. +86 10 5869 2255 (Beijing office)
tel. +86 20 3882 0550 (Guangzhou office)

NIKON SINGAPORE PTE. LTD.
tel. +65 6559 3618

NIKON MALAYSIA SDN. BHD.
tel. +60 3 7809 3609

NIKON INSTRUMENTS KOREA CO. LTD.
tel. +82 2 2186 8400

More offices and resellers at **www.nikonmetrology.com**

InfiniteFocus G5

Optical micro coordinate measurement and surface finish measurements in one system

InfiniteFocus is a highly accurate, fast and flexible optical 3D measurement system. Users benefit from a 3D micro coordinate measurement machine and surface roughness measurement device combined in one system. The range of measurable surfaces is almost unlimited. All relevant surface features of micro precision components are measured using only one multifunctional measurement sensor. Users achieve traceable measurement results in a high repeatability and a vertical resolution of up to 10nm. The robust measurement principle of Focus-Variation in combination with a vibration-isolating hardware enables the form and roughness measurement of also large and heavy components. All axes of InfiniteFocus are equipped with highly accurate encoders ensuring precise stage movement. With an automation interface, InfiniteFocus is also applied for fully automatic measurement in production.

AdvancedReal3D RotationUnit G2

Real3D Rotation Unit G2

RotationGrip

RinglightHP

AdvancedInsertGrip

InsertGrip G2

ToolGrip

alicona

GENERAL SPECIFICATIONS

Positioning volume (X x Y x Z)	100 mm x 100 mm x 100 mm = 1000000 mm³ 200 mm x 200 mm x 100 mm = 4000000 mm³ 200 mm x 200 mm x 200 mm = 8000000 mm³
Max. specimen weight	30 kg; more on request

OBJECTIVE SPECIFIC FEATURES

Objective magnification (*)		**2.5x**	**5x**	**10x HX (**)**	**10x**	**20x HX(**)**	**20x**	**50x**	**100x**
Numerical aperture		0.075	0.15	0.2	0.3	0.3	0.4	0.6	0.8
Working distance	mm	8.8	23.5	37	17.5	30	19.0	11	4.5
Lateral measurement range (X,Y) (X x Y)	mm	5.63	2.82	1.62	1.62	0.7	0.81	0.32	0.16
	mm²	31.7	7.95	2.62	2.62	0.49	0.66	0.10	0.03
Extended lateral measurement range (X x Y)	mm²	6195.26	1548.42	387.30	387.30	96.83	96.83	15.49	3.87
Measurement point distance	µm	3.52	1.76	0.88	0.88	0.44	0.44	0.18	0.09
Calculated lateral optical limiting resolution	µm	4.35	2.18	1.64	1.09	1.09	0.82	0.54	0.41
Finest lateral topographic resolution	µm	7.04	3.51	1.76	1.76	1.17	0.88	0.64	0.44
Measurement noise	nm	800	120	75	30	20	10	3	1
Vertical resolution	nm	2300	410	250	100	80	50	20	10
Vertical measurement range	mm	8	22.5	36	16.5	29	18	10	4
Vertical scanning speed	µm/s	3000	3000	1000 - 3000	1000 - 3000	500 - 3000	500 - 3000	200 - 2000	100 - 1000
Measurement speed	≤ 1.7 million measurement points/sec.								

(*) Objectives with longer working distance available upon request (**) Objective available in special objective configuration
(***) Larger measurement areas possible with data reduction (primarily limited by positioning volume)

RESOLUTION AND APPLICATION SPECIFICATIONS

Objective magnification		**2.5x**	**5x**	**10x HX**	**10x**	**20x HX**	**20x**	**50x**	**100x**
Min. measurable height	µm	2.3	0.41	0.25	0.1	0.08	0.05	0.02	0.01
Max. measurable height	mm	8	22.5	36	16.5	29	18	10	4
Height step accuracy (1 mm)	%	n.a.	0.05	0.05	0.05	0.05	0.05	0.05	0.05
Max. measurable area Optional	mm²	10000 40000	10000 40000	10000 40000	10000 40000	10000 24780	10000 24780	3965 3965	990 990
Max. measurable profile length Optional	mm	100 200							
Min. measurable roughness (Ra)	µm	7	1.2	0.75	0.3	0.24	0.15	0.06	0.03
Min. measurable roughness (Sa)	µm	3.5	0.6	0.375	0.15	0.12	0.075	0.03	0.015
Min. measurable radius	µm	20	10	5	5	3	3	2	1
Min. measurable wedge angle	°	20							
Max. measurable slope angle	°	87							

ACCURACY

Flatness deviation	1.6 mm x 1.6 mm with 10x objective	U = 0.1 µm
Max. deviation of a height stepmeasurement	height step 10000µm height step 1000µm height step 100µm height step 10µm height step 1µm	$E_{Sa,3c,020,MPE}$ = 0.8 µm, σ = 0.4 µm $E_{Sa,3c,020,MPE}$ = 0.5 µm, σ = 0.1 µm $E_{Sa,3c,020,MPE}$ = 0.4 µm, σ = 0.05 µm $E_{Sa,3c,020,MPE}$ = 0.3 µm, σ = 0.025 µm $E_{Sa,3c,020,MPE}$ = 0.15 µm, σ = 0.01 µm
Profile roughness	Ra = 0.1 µm Ra = 0.5 µm	U = 0.025 µm, σ = 0.002 µm U = 0.04 µm, σ = 0.002 µm
Area roughness	Sa = 0.1 µm Sa = 0.5 µm	U = 0.02 µm, σ = 0.002 µm U = 0.03 µm, σ = 0.002 µm
Distance measurement	XY up to 1 mm XY up to 10 mm XY up to 20 mm	$E_{Bi,Tr,020,MPE}$ = 0.7 µm $E_{Bi,Tr,020,MPE}$ = 1.0 µm $E_{Bi,Tr,020,MPE}$ = 2.0 µm
Wedge angle	β = 70 ° - 110 °	U = 0.15 °, σ = 0.02 °
Edge radius	R = 5 µm - 20 µm R > 20 µm	U = 1.5 µm, σ = 0.15 µm U = 2 µm, σ = 0.3 µm

$E_{Sa,3c,020,MPE}$ & $E_{Bi,Tr,020,MPE}$ conform to ISO 10360-8

Initiative Fair Data Sheet
Specifications in blue mark Alicona specific values.